AD-A212 232

WRDC–TR–89–2077

ANALYSIS OF THE PERFORMANCE OF HEAT PIPES AND PHASE–CHANGE MATERIALS WITH MULTIPLE LOCALIZED HEAT SOURCES FOR SPACE APPLICATIONS

Amir Faghri, Ph.D.
Brage Golding Distinguished Professor of Research

MECHANICAL SYSTEMS ENGINEERING
WRIGHT STATE UNIVERSITY
DAYTON, OH 45435

Won Soon Chang, Ph.D., Edward T. Mahefkey, Ph.D.

WRIGHT RESEARCH AND DEVELOPMENT CENTER
WRIGHT–PATTERSON AIR FORCE BASE, OHIO 45433

MAY 1989

FINAL REPORT FOR PERIOD JANUARY 1988 – DECEMBER 1988

DTIC
S **ELECTF**
SEP 11 1989
B **D**

REPORT DOCUMENTATION PAGE

Form Approved
OMB No. 0704-0188

1a. REPORT SECURITY CLASSIFICATION Unclassified	1b. RESTRICTIVE MARKINGS N/A

2a. SECURITY CLASSIFICATION AUTHORITY N/A	3. DISTRIBUTION / AVAILABILITY OF REPORT
2b. DECLASSIFICATION / DOWNGRADING SCHEDULE N/A	Approved for public release; distribution is unlimited.

4. PERFORMING ORGANIZATION REPORT NUMBER(S) WSU-TR-88-001	5. MONITORING ORGANIZATION REPORT NUMBER(S) WRDC-TR-89-2077

6a. NAME OF PERFORMING ORGANIZATION Wright State University	6b. OFFICE SYMBOL (If applicable)	7a. NAME OF MONITORING ORGANIZATION Wright Research Development Center

6c. ADDRESS (City, State, and ZIP Code) Department of Mechanical & Materials Engineering Wright State University Dayton, Ohio 45435	7b. ADDRESS (City, State, and ZIP Code) Aero Propulsion and Power Laboratory (WRDC/POOS) Wright-Patterson AFB, OH 45433-6563

8a. NAME OF FUNDING / SPONSORING ORGANIZATION Wright Research Development Center	8b. OFFICE SYMBOL (If applicable) WRDC/POOS	9. PROCUREMENT INSTRUMENT IDENTIFICATION NUMBER F-33615-86-C-2720

8c. ADDRESS (City, State, and ZIP Code) Aero Propulsion and Power Laboratory Wright-Patterson AFB, OH 45433-6563	10. SOURCE OF FUNDING NUMBERS			
	PROGRAM ELEMENT NO.	PROJECT NO.	TASK NO	WORK UNIT ACCESSION NO.
	62203F	3145	20	06

11. TITLE (Include Security Classification)
Analysis of the Performance of Heat Pipes and Phase-Change Materials with Multiple Localized Heat Sources for Space Applications

12. PERSONAL AUTHOR(S)
Amir Faghri, Won Soon Chang and Edward T. Mahefkey

13a. TYPE OF REPORT Final Report	13b. TIME COVERED FROM 22Jan88 TO Dec 88	14. DATE OF REPORT (Year, Month, Day) 1989 May	15. PAGE COUNT 244

16. SUPPLEMENTARY NOTATION

17. COSATI CODES			18. SUBJECT TERMS (Continue on reverse if necessary and identify by block number)
FIELD	GROUP	SUB-GROUP	Heat Pipes; Phase Change; Thermal Control.

19. ABSTRACT (Continue on reverse if necessary and identify by block number)
The objective of this report is to examine the performance characteristics of heat pipes and phase-change materials with multiple localized heat sources as well as the fundamental problems related to their specific applications. A numerical analysis is presented for the overall performance of heat pipes with single or multiple heat sources. The analysis includes the heat conduction in the wall and liquid-wick regions as well as the compressibility effect of the vapor flow inside the heat pipe. The solutions are compared with existing experimental data for the vapor and wall temperatures at both low and high temperatures. In addition, the performance of heat pipes with localized heat input including the effects of axial and circumferential heat conduction under high and low working temperatures was investigated. The numerical results for block heating a heat pipe with low working temperatures indicate a good agreement with existing experimental data.

20. DISTRIBUTION / AVAILABILITY OF ABSTRACT ☒ UNCLASSIFIED/UNLIMITED ☐ SAME AS RPT. ☐ DTIC USERS	21. ABSTRACT SECURITY CLASSIFICATION Unclassified
22a. NAME OF RESPONSIBLE INDIVIDUAL Won S. Chang	22b. TELEPHONE (Include Area Code) (513) 255-2922	22c. OFFICE SYMBOL WRDC/POOS

DD Form 1473, JUN 86   Previous editions are obsolete.   SECURITY CLASSIFICATION OF THIS PAGE

Block 19-Continued

Various technologies which protect a wall from being burned out by an intense localized moving heat source have been reviewed and a solution to this problem is proposed in which a phase-change material (PCM) is placed underneath the wall to absorb the high heat flux. The three-dimensional melting problem is nondimensionalized and modeled with a new enthalpy transforming scheme. The numerical results show that the proposed solution reduces the peak wall temperature significantly.

FOREWORD

The information in this report was assembled for the SCEEE contract F33615-86-C-2720 with the Aero Propulsion and Power Laboratory, Wright Research and Development Center and NASA Lewis Research Center as the sponsoring agencies. The work was carried out at the Department of Mechanical Systems Engineering at Wright State University. Technical assitance from Mr. Albert Juhasz of NASA Lewis Research Ceanter is appreciated.

During FY 1988, five tasks were performed as outlined in the table of contents. The various tasks dealt with the performance characteristics of heat pipes and phase-change materials with multiple localized heat sources as well as the fundamental problems related to their specific applications. Five technical publications were produced from the present work. Three graduate research assistants were involved in the preparation of this work: Mr. Yiding Cao, Mr. Ming-Ming Chen and Mr. Scott Thomas. Professor Mohammad Faghri from the University of Rhode Island provided technical assistance on some of the computational work presented in this report.

Accession For		
NTIS GRA&I	☑	
DTIC TAB	☐	
Unannounced	☐	
Justification		
By		
Distribution/		
Availability Codes		
Dist	Avail and/or Special	
A-1		

iii

TABLE OF CONTENTS

SECTION   PAGE

Table of Contents (continued)

LIST OF FIGURES

List of Figures (continued)

List of Figures (continued)

List of Figures (continued)

List of Figures (continued)

List of Figures (continued)

LIST OF TABLES

NOMENCLATURE

A surface area of pipe wall (m^2), Sections I and II

A radiation surface area, m^2, Section III

A_H heated area, m^2

a coefficient in the power-law equation for boiling, Section III

a coefficient, Sections IV and V

b source term in the discretization equation, Sections IV and V

b exponent in the power-law equation for boiling, Section III

C specific heat per unit volume, $J/(m^3\text{-}K)$, Section V

c specific heat, J/kg-K, Sections IV and V

c speed of sound, m/s, Sections I and II

$C_{\ell w}$ dimensionless number, C_ℓ/C_w

c_p specific heat at constant pressure, J/kg-K

C_{sw} dimensionless number, C_s/C_w

c_v specific heat at constant volume, J/kg-K

D diagonal distance, m

E enthalpy, J/kg

F flow rate through a control-volume face, kg/s

H latent heat, J/kg, Sections IV and V

H heat transfer coefficient, $W/(m^2\text{-}K)$, Section III

h enthalpy, J/kg, Sections I and II

h height of the spot heated heat pipe, m, Section III

h total thickness, $\delta_p + \delta$, m, Section V

h^* dimensionless number, h/R_h

Nomenclature (continued)

h_{fg} latent heat of evaporation, J/kg

h_i heat transfer coefficient at interface, W/m^2-K

K   ratio of the thermal conductivities of the wall to the fluid,

       k_w/k_f

k   thermal conductivity, W/m-K

$k_{\ell w}$ dimensionless number, k_ℓ/k_w

k_{sw} dimensionless number, k_s/k_w

K_{w1} solid wall and effective liquid thermal conductivity ratio,

       k_s/k_{eff}

K_{1v} effective liquid and vapor thermal conductivity ratio,

       k_{eff}/k_v

L   total length of the pipe, m, Sections I and II

L   reference length, m, Section IV

L_C condenser length, m

L_E evaporator length, m

L_H length of heated block, m

L_1, L_2 length of spot heated heat pipe, m

ℓ interface position along the diagonal, m, Sections IV and V

$\dot{m}$ mass flux, kg/m^2-s

M   Mach number

N_Q dimensionless number, $q_h R_h/(T_m-T_i)k_w$

N_r dimensionless number, $R_h(T_m-T_i)^3 \sigma \epsilon/k_w$

N_t dimensionless number, $T_i/(T_m-T_i)$

N_v dimensionless number, $UC_w(T_m-T_i)k_w$

Nomenclature (continued)

Nu_z local Nusselt number at the solid-fluid interface, $2r_i h_i/k_f$

n normal outward direction

n^* dimensionless normal outward direction, n/R_h

P pressure of fluid, N/m^2

P_0 datum pressure at the end cap of the evaporator at the liquid-vapor interface, N/m^2

Pr Prandtl number, $\mu c_p/k$

Pe Peclet number, $PrRe$

Q heat source power, W, Sections IV and V

Q total heat input rate at evaporator outer pipe wall, W Section I

Q_H input heat, W

Q_R radiation heat transfer to surroundings, W

q heat flux, W/m^2

q_H heat flux, W/m^2

R radius of heat pipe, m, Section III

R gas constant in Eq.(1.5a), J/kg-K

Re inlet axial Reynolds number, $2r_i w_{in}/\nu$

Re_a axial Reynolds number at the adiabatic section, $2R_v \bar{w}_a/\nu$

Re_i radial Reynolds number at the solid-fluid interface, $v_i r_i/\nu$

R_h heat source radius, m

R_0 radius of the numerical domain, m

R_v vapor space radius, m

Nomenclature (continued)

R_w outer pipe wall radius, m

Re_r average radial Reynolds number at the liquid-vapor interface, $\rho_0 v_0 R_v / \mu_v$

r radial coordinate, m

S coefficient in Eq. (4.7) or Eq. (5.19)

S_h source term in the energy equation

St Stefan number, $c_s(T_m - T_w)/H$ or $c_s(T_m - T_i)/H$

s circumferential distance coordinate, m, Section III

s dimensionless interface position along the diagonal, ℓ/D Section IV

s_H $W_H / 2\pi R$

T temperature, K

T^* $(T - T_s)/T_H$, Section III

T^* dimensionless temperature, $(T-T_i)/(T_m - T_i)$, Section V

T^+ The "Kirchoff" temperature

T_H reference temperature, K

T_i initial temperature, K

T_m melting temperature, K, Sections IV and V

T_0 temperature of environment, K

T_0 temperature of evaporator end cap at liquid-vapor interface, K

T_s vapor temperature, K

T_w wall temperature, K

Nomenclature (continued)

T_1 the temperature defined in Fig. 4.2, K

T_2 the temperature defined in Fig. 4.2, K

t   time, s

t^* dimensionless number, $tk_w/(C_wR_h^2)$

ΔT $T - T_s$, $^{\text{o}}$C, Section III

ΔT temperature range $T_2 - T_1$, K, Sections IV and V

ΔT_c critical temperature difference, K

Δt time step, s

U   heat source velocity, m/s

U^* dimensionless velocity, C_wUR_h/k_w

u,v,w   velocities, m/s

v_0 evaporation or condensation velocity at the vapor-liquid interface, m/s

v_n normal melting/freezing speed, m/s

ΔV volume of the control volume, m^3

$\bar{w}_a$ average axial velocity in the adiabatic section, m/s

W_H width of heated block, m

$\bar{w}_z$ average local axial velocity over the cross section at any axial location, m/s

W_1,W_2 width of spot heated pipe, m

x $x/\pi R$, Section III

x_1 distance of the edge of heated block from the origin, m

x,y,z   moving coordinate directions in Section V and general coordinate directions in other sections

Nomenclature (continued)

x′,y′,z′   fixed coordinate directions, Section IV

x^*, y^*, z^* dimensionless distances, x/R_h, y/R_h, z/R_h

X-X   the plane indicated in Fig. 5.4 and Fig. 5.14

Y $s/\pi R$

Greek Symbols

α thermal diffusivity, m^2/s

Γ coefficient in Eq. (4.7) or (5.19) and exchange coefficient k,

           Sections I and II

γ ratio of specific heats, c_p/c_v

δ wall thickness, m, Sections III, IV and V

ε wall or liquid-wick thickness, m, Section I

δ^* dimensionless wall thickness, δ/R_h

δ_m maximum melting front depth, m

δ_m^* dimensionless maximum melting front depth, δ_m/R_h

δ_p thickness of the PCM, m

δ_p^* dimensionless thickness of the PCM, δ_p/R_h

δx x-direction distance between two adjacent grid points

Δ dimensionless wall or liquid-wick thickness, $\delta/2R_v$, Section

           I; $(r_o - r_i)/2r_i$,   Section II

Δx x-direction width of the control volume

$\Delta y, \delta y$ similar to Δx, δx

$\Delta z, \delta z$ similar to Δx, δx

Nomenclature (continued)

η dummy variable

ϵ emissivity

ϵ wick porosity, Sections I and II

θ dimensionless temperature, Section I and II; coordinate direction, Sections IV and V

θ_d dimensionless temperature, $(T - T_m)/(T_m - T_i)$

θ_o dimensionless temperature, $(T_i - T_w)/(T_m - T_w)$

μ dynamic viscosity of fluid, kg/m-s

ρ density of fluid, kg/m^3

ϕ viscous dissipation term in the energy eqn. (1.4), Section I; dummy variable, Section IV

τ dimensionless time, ta/L^2

σ Stefan-Boltzmann constant, W/(m^2-K^4)

Subscripts

a   adiabatic

B   "Bottom" neighbor of grid P

b   control-volume face between P and B, Sections IV and V

b   bulk condition, Sections I and II

C   condensation

c   condenser

E   evaporation

E   "East" neighbor of grid P, Sections IV and V

Nomenclature (continued)

e   control volume face between P and E, Sections IV and V

e   evaporator

eff   effective

f   fluid

h   harmonic mean

i   initial condition, Sections IV and V

i   vapor-liquid interface for Section I, solid fluid interface for Section I

in   entrance condition to the pipe

l   liquid

lw   liquid-wick

m   mean value in Section I and II

m   mushy pahse in Section IV and V

N   "North" neighbor of grid P

n   contol-volume face between P and N

o   variable at outer pipe wall

P   grid point

r   radial direction

S   "South" neighbor of grid P

s   control-volume face between P and S, Sections IV and V

T   "Top" neighbor of grid P

Nomenclature (continued)

t   control-volume face between P and T

v   vapor

W   "West" neighbor of grid P

w   control-volume face between P and W

w   wall

z   at z location

0   variable with initial value before iteration and the
        properties corresponding to T_0

Superscripts

+   dimensionless variable

-       average variable

*   dimensionless variable

I. NUMERICAL ANALYSIS OF THE VAPOR FLOW AND THE HEAT CONDUCTION THROUGH THE LIQUID-WICK AND THE WALL IN A HEAT PIPE

1.1 Summary

A numerical analysis is presented for the overall performance of heat pipes with single or multiple heat sources. The analysis includes the heat conduction in the wall and liquid-wick regions as well as the compressibility effect of the vapor flow inside the heat pipe. The two-dimensional elliptic governing equations in conjunction with the thermodynamic equilibrium relation and appropriate boundary conditions are solved numerically for the whole domain. The solutions are compared with existing experimental data for the vapor and wall temperatures at both low and high operating temperatures. The effects of conjugate axial conduction, vapor compressibility, flow reversal, and viscous dissipation are discussed as well as the accuracy of the parabolic version versus the elliptic version. The results show that the axial wall conduction tends to distribute the temperature more uniformly for the heat pipe with large solid wall and effective liquid thermal conductivity ratios. The compressible and incompressible models show a very close agreement for the total pressure drop while the local pressure variations along the heat pipe are quite different for these two models for the cases with high radial Reynolds numbers at the interface. Also, the partially parabolic solution provides fairly accurate results compared with the elliptic solution except

for the cases with a large radial Reynolds number at the interface or large solid wall and effective liquid thermal conductivity ratios.

1.2 Introduction

The heat pipe is a device which has a very high thermal conductance. It is a closed vacuum tube or chamber of different shapes whose inner surfaces are lined with a porous capillary wick (Fig. 1.1). The wick is saturated with the liquid phase of a working fluid, and the remaining volume of the tube contains the vapor phase. Heat applied at the evaporator causes the liquid to vaporize and the vapor to move to the cold end of the tube where it is condensed. The condensate is returned to the evaporator by capillary forces. The amount of heat that can be transported as the latent heat of vaporization is usually several orders of magnitude larger than that which can be transported in a conventional convective heat transfer system. Thus, a small heat pipe can transport a large amount of heat.

The first recorded patent of a device similar to the heat pipe was by Perkins and Buck (1892). It is called a Perkins tube which is actually a wickless heat pipe. It relies on gravitational forces to return the liquid from the condenser to the evaporator. In 1942, Gaugler applied a wick structure to the Perkins tube and invented the heat pipe which can operate at different orientations. However, it was not widely publicized until 1964 when Grover et al. at the Los Alamos Scientific Laboratory independently reinvented the concept. Grover (1963) included a theoretical

3
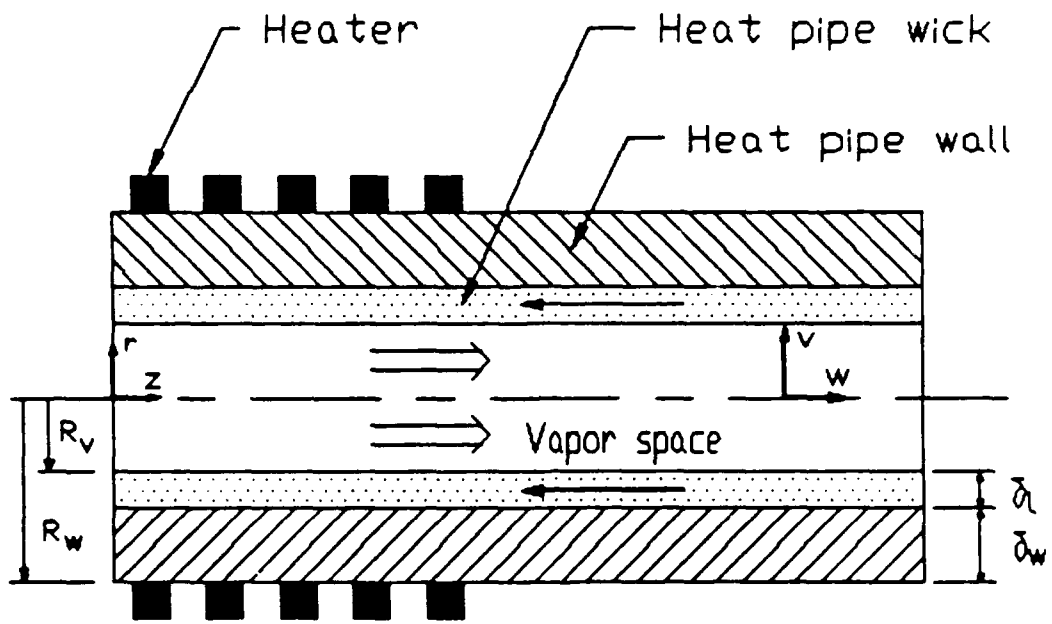
Figure 1.1   The Multiple Evaporator Heat Pipe
and Coordinate System.

analysis and experimental results in his patent. The demonstration heat pipe was made from a stainless steel pipe incorporating a wire mesh wick and sodium as the working fluid, although lithium and silver were also mentioned as possible working fluids. Since then, the heat pipe has gained ever increasing development and applications.

The performance of heat pipes is restricted by several limitations, namely, (1) vapor flow limit: sonic and viscous limits; (2) liquid flow limit: capillary, entrainment, and boiling limits. The sonic limit is defined as when the vapor velocity is so high that it reaches the speed of sound ($M=1$), thus affecting the overall heat pipe performance because of poor temperature uniformity. The viscous limit usually occurs at low working temperatures where the viscous forces are dominant in the vapor flow. As described by Busse (1973), the maximum heat flux due to the viscous limit occurs when the vapor pressure is reduced to zero ($P=0$). The capillary limit is the wicking limitation whenever the capillary forces are insufficient to overcome the vapor and liquid pressure losses (e.g., $\Delta P_c \leq \Delta P_l + \Delta P_v$, where ΔP_c is the capillary pressure, and ΔP_l and ΔP_v are the liquid and vapor pressure losses, respectively). The entrainment limit represents an interaction between the countercurrent vapor and liquid that leads to the entrainment of liquid droplets from the wick structure, which leads to an insufficient amount of liquid returning to the evaporator which limits the heat pipe operation. The boiling limit is a limitation of the radial heat flux density. For a considerably high radial heat flux at the

5

evaporator, vapor bubbles may be formed in the evaporator wick. The formation of vapor bubbles in the wick structure can cause hot spots and obstruct the circulation of the liquid.

A common type of heat pipe which meets the growing needs in space applications (e.g., transportation of energy in the reactor core of nuclear power systems (Koening, 1985) and supersonic jet surface cooling (Silverstein, 1971)) is a liquid metal heat pipe, which uses a liquid metal for the working fluid such as sodium. The major concern for this type of heat pipe is the sonic limit during the starting period of operation, i.e., at the lower working temperature range for a certain working fluid. This is because the vapor has a low density and a high viscosity. In this case, the compressibility of the vapor and the viscous dissipation may have a significant effect on the performance of the heat pipe. Also, the high vapor velocity and viscosity may cause a significant pressure drop which is related to the temperature profile by the thermodynamic equilibrium at the vapor-liquid interface, thus affecting the overall heat pipe performance. The purpose of the present study is to determine the effects of conjugate heat transfer and vapor compressibility for liquid metal heat pipes by solving the complete conservation of mass, Navier-Stokes, and conservation of energy equations by using a computer code called PHOENICS. The present analysis includes the conjugate heat conduction through the wall and the liquid-wick matrix, which is usually neglected but is very important for heat pipes with multiple heat sources. The investigation is also extended

to lower temperature heat pipes such as those using water as the working
fluid.

Literature Review

Since 1964, many experimental, analytical, and numerical investigations
were made on heat pipes. The related work presented here is grouped into
the following three categories: (1) vapor dynamics, (2) coupled temperature
field and vapor dynamics, and (3) experimental studies. A brief
description of the previous theoretical and experimental work is also
summarized in Tables 1.1 and 1.2.

Vapor Dynamics

The prediction of the vapor pressure distribution in heat pipes was
first studied by Cotter (1965) for incompressible flow and the limiting
cases of $Re_r \ll 1$ and $Re_r \gg 1$. He concluded that for $Re_r \ll 1$, the
viscous effects dominate, and the pressure gradient is the same as in a
Poiseuille flow while for $Re_r \gg 1$, the flow is dominated by inertial
effects. The pressure recovery in the condenser was $4/\pi^2$ of the pressure
drop at the evaporator.

Busse (1967) further analyzed the hydrodynamics of laminar
incompressible flow in long cylindrical heat pipes. An analytical approach

TABLE 1.1 Related Numerical or Analytical Work on Heat Pipes

References	Analysis	1-D or 2-D (Vapor)	Equations Solved	Elliptic or Parabolic	Compressible or Incompressible	Geometry	Flow Type	Comments
Cotter (1965)	Analytical No Wall	1-D	Mass + Momentum	Parabolic	Incompressible	Cylinder	Laminar, Steady	Analytical expressions for pressure drop with limiting cases $Re_r \ll 1$ and $Re_r \gg 1$
Busse (1967)	Analytical No Wall	1-D	Mass + Momentum	Parabolic	Incompressible	Cylinder	Laminar, Steady	Analytical expressions for vapor pressure drop were obtained
Levy (1968)	Analytical No Wall	1-D	Mass + Momentum + Energy	NA	Compressible (equilibrium two-phase)	Cylinder	Laminar, Steady	Numerical results for pressure, velocity and sonic heat transfer rate were presented for high temperature liquid metal heat pipes
Bankston and Smith (1973)	Numerical & Analytical (slow motion) No Wall	2-D	Mass + Momentum	Elliptic	Incompressible	Cylinder	Laminar, Steady	The governing equations in terms of stream function and vorticity were solved numerically. Analytical results were obtained for low Reynolds number cases
Rohani and Tien (1973)	Numerical (finite diff.) No Wall	2-D	Mass + Momentum + Energy + Species	Elliptic	Compressible (perfect gas law)	Cylinder	Laminar, Steady	The stream function and vorticity type of equations were solved. The effect of gas loaded heat pipe is analyzed.
Busse (1973)	Analytical No Wall	2-D	Mass + Momentum	Parabolic	Compressible	Cylinder	Laminar, Steady	An approximate methodology was developed. Ultimate limits of heat pipes were discussed and analyzed.
Tien and Rohani (1974)	Numerical (finite diff.) No Wall	2-D	Mass + Momentum + Energy	Elliptic	Compressible (perfect gas law)	Cylinder	Laminar, Steady	Elliptic energy equation was solved simultaneously with the stream function and vorticity equations
Kadaner and Rassadkin (1975)	Analytical No Wall	1-D	Mass + Momentum	Parabolic	Incompressible	Cylinder	Laminar, Steady	Pressure drop and friction coeff. vs. Reynolds number and axial distance were presented
Bystrov and Popov (1976)	Analytical No Wall	1-D	Mass + Momentum	NA	Compressible (equilibrium two-phase)	Cylinder	Laminar, Steady	The pressure profile and the sonic limit in terms of temperature were presented for high temperature liquid metal heat pipes

8

(TABLE 1.1   continued)

Reference	Method / Wall	Dimension	Equations	Type	Compressibility	Geometry	Flow	Comments
Ooijen and Roogendoorn (1979)	Numerical (finite diff.) No Wall	2-D	Mass + Momentum	Elliptic	Incompressible	Rectangle	Laminar, Steady	Comparison was made with flat simulated heat pipe
Bystrov and Mikhailov (1982)	Analytical No Wall	1-D	Mass + Momentum	Parabolic	Incompressible	Cylindrical Condenser	Laminar, Steady	Parametric method was used
Busse and Prenger (1984)	Analytical No Wall	1-D	Mass + Momentum	Parabolic	Compressible (perfect isothermal gas)	Cylinder	Laminar, Steady	A generalized code was developed for gas dynamics. The isothermal perfect gas was chosen for analysing heat pipes with organic working fluids
Faghri (1986)	Numerical (finite diff.) No Wall	2-D	Mass + Momentum	Parabolic	Incompressible	Annulus	Laminar, Steady	Numerical analysis for annular heat pipe
Narayana (1986)	Numerical (finite diff.) No Wall	2-D	Mass + Momentum	Parabolic	Incompressible	Cylinder	Laminar, Steady	The results for pressure drop were presented for $Re_r = 2 \sim -5.0$
Colwell, Jang and Carmada (1987)	Analytical (vapor) + finite element (wall + wick)	1-D	Mass + Momentum + Energy	N/A	Compressible (equilibrium two-phase)	Rectangle	Laminar, Steady	Analysis was related to the start-up of a frozen heat pipe
Bianchi (1987)	Numerical (finite element) No Wall	2-D	Mass + Momentum + Energy	Elliptic	Incompressible	Cylinder	Laminar, Steady	Comparison with experimental data using water as working fluid. The viscous dissipation is included in the energy equation
Ismail, Zanardi and Liu (1987)	Numerical (finite diff.) No Wall	2-D	Mass + Momentum + Energy	Elliptic	Incompressible	Cylinder	Laminar, Steady	No discussion of the solution procedure is given. The governing equation is given with some general trends of the results
Busse (1987)	Analytical No Wall	2-D	Mass + Momentum	Parabolic	Compressible (perfect isothermal gas)	Cylinder	Laminar, Steady	A logical criteria for determining the flow type was presented for the heat pipe condenser
Faghri and Parvani (1988)	Numerical (finite diff.) No Wall	2-D	Mass + Momentum	Elliptic & Parabolic	Incompressible	Annulus	Laminar, Steady	Comparison between elliptic and parabolic solutions for $Re_r \leq 1000$ using water as working fluid
Faghri (1988)	Analytical + Numerical No Wall	1-D & 2-D	Mass + Momentum + Energy	Elliptic & Parabolic	Incompressible (2-D) Compressible (1-D)	Annulus & Cylinder	Laminar, Steady	Analytical expressions for pressure drop at each section of the heat pipe were given both for conventional and annular heat pipes. The results for 1-D were in good agreement with 2-D model

9

(TABLE 1.1 continued)

Reference	Method	Dim.	Equations	Flow	Gas	Geometry	Regime	Remarks
Isaacci, Catton, Reiss and Ghoniem (1988)	Numerical (finite diff.) No Wall	2-D	Mass + Momentum + Energy	Elliptic	Compressible (perfect gas law)	Rectangle	Laminar, Transient	Only velocity profile was presented. The numerical results were presented at low temperature
Bowman and Ritchcock (1988)	Numerical (finite diff.) No Wall	2-D	Mass + Momentum	Elliptic	Compressible (perfect gas law)	Cylinder	Laminar, Turbulent & Transient	Comparison was made with experimental data of simulated heat pipe using air as a working fluid
Seo and El-Genk (1988)	Numerical (finite diff.) With Wall	1-D	Mass + Momentum + Energy	N/A	Compressible (perfect gas law)	Cylinder	Laminar, Steady	The effect of porosity in the liquid wick is neglected. The energy due to mass injection and suction to the vapor region is also neglected.
Busse and Loehrke (1989)	Analytical + Numerical No Wall	2-D	Mass + Momentum	Parabolic	Compressible (perfect isothermal gas)	Cylinder	Laminar, Steady	Emphasis on flow reversal and pressure recovery. An empirical wall-friction parameter was also obtained for the prediction of subsonic turbulent pressure recovery
Jang, Faghri and Chang (1989)	Numerical No Wall	1-D	Mass + Momentum + Energy	N/A	Compressible (perfect gas law)	Cylinder	Laminar, Turbulent & Transient	The transient behavior of vapor flow under subsonic, sonic and supersonic speeds are successfully predicted
Jang, Faghri, Chang and Mahefkey (1989)	Numerical With Wall and Wick	1-D	Mass + Momentum + Energy	N/A	Compressible (perfect gas law)	Cylinder	Laminar, Turbulent & Transient	Analysis related to the start-up from frozen state. The wall and wick are modelled as two-dimensional
Cao and Faghri (1989)	Numerical (finite diff.) With Wall	2-D	Mass + Momentum + Energy	Elliptic	Compressible (perfect gas law)	Cylinder	Laminar, Transient	A complete transient model analysis for high Mach numbers for high temperature heat pipes with a pulsed heat input.
Chen and Faghri (present)	Numerical (finite diff.) With Wall	2-D	Mass + Momentum + Energy	Elliptic	Compressible (perfect gas law)	Cylinder	Laminar, Steady	The energy due to mass injection and suction to the vapor region is included. The numerical results are compared with both low and high temperature experimental data

TABLE 1.2 Some Related Experimental Work on Heat Pipes

References	heat pipe or simulation	working fluid	geometry	wick type	data reported	steady or transient	comments
Kemme (1969)	conventional heat pipe	sodium potassium	cylinder	screen mesh	outer wall temperature	steady state	$M \approx 1$
Quaile and Levy(1972)	simulation of heat pipe condenser	silicon oil	cylinder	sintered bronze powder	vapor pressure	steady state	$2.21 \leq Re_{r,c} \leq 5.0$
Ivanovskii et al (1982)	conventional heat pipe	sodium	cylinder	ring-shaped gap with screen mesh	vapor saturation temperature	steady state	heat pipe wall thickness was not reported
Ponnappan and Mahefkey (1984)	double-wall artery heat pipe	water	cylinder	double-wall artery screen mesh	outer wall temperature	steady state	high capacity heat pipe
Bianchi (1986)	conventional heat pipe	water	cylinder	phosphorus-bronze screen	vapor temperature along centerline	steady state	wick mesh size was missing
Gernert (1986)	heat pipe with multiple heat sources	water	cylinder	sintered copper powder	vapor and outer wall temperature	steady state	two heat sources were used
Merrigan et al (1986)	conventional heat pipe	lithium	cylinder	annular passage covered with screen wick	outer wall temperature	transient	radiation cooling
Bowman and Hitchcock (1988)	simulation of heat pipe	air	cylinder	polyethylene porous pipe	vapor pressure and velocity	steady state	laminar and turbulent vapor flow
Faghri and Thomas (1988)	annular heat pipe	water	annulus	axial grooves	outer wall temperature	steady state	capillary limit was measured

was used to solve the momentum and continuity equations. The heat pipe under consideration had three distinct sections with constant mass injection in the evaporator and extraction in the condenser. The length of each section was assumed to be much larger than the diameter of the vapor channel. To solve the momentum equation, the axial velocity profile was approximated by a fourth-order polynomial with respect to the radius and a correction function. He found that the normalized axial velocity component is constant along the evaporator, approaches the Poiseuille profile in the adiabatic section, and varies strongly along the condenser. The expression for the pressure distributions along the evaporator, adiabatic, and condenser sections were derived separately.

Bankston and Smith (1973) analyzed the incompressible two-dimensional laminar vapor flow in a heat pipe. The solution was presented for the pressure variation along the pipe for various evaporator and condenser lengths at steady-state operation. The finite difference scheme was employed to solve the momentum equation in terms of the stream function and vorticity. In addition, a new series solution for the slow-motion case was also obtained, and it confirms numerical results in the limit of low Reynolds numbers. Various cases with different radial Reynolds number were analyzed, and they concluded that flow reversal in the condenser may occur when the condenser radial Reynolds number exceeds 2.

Kadaner and Rassadkin (1975) studied the laminar vapor flow along the heat pipe. The problem was solved by using a parametric method which introduces a velocity profile in terms of two unknown functions. The integrated momentum equation was then solved in terms of these functions.

12

The functions were determined by analyzing the limiting situation, and the results were presented in a graphic manner for the determination of the vapor pressure loss along the pipe. The dimensionless pressure drop and friction coefficient were presented in terms of the radial Reynolds numbers and the dimensionless axial distance.

Bystrov and Mikhailov (1982) also studied the laminar vapor flow in the heat pipe condenser using the parametric method. The axial velocity profile was approximated by a fourth-order polynomial with respect to the radius and an unknown parameter which was later determined by the boundary conditions. The results were presented for pressure and velocity variations with the Reynolds number in the range of 1 to 30. The comparison of the theoretical results with the experimental data by Quaile and Levy (1972) showed a good agreement under the conditions studied.

Faghri (1986) solved the 2-D incompressible laminar vapor flow in the concentric annular heat pipe. The parabolic Navier-Stokes equation plus the continuity equation were solved by using the finite difference numerical scheme. The pressure drops and velocity profiles were presented for symmetric and asymmetric heating and cooling cases. He concluded that for radial Reynolds numbers much less than 1, viscous effects dominate, and the axial velocity profile throughout the heat pipe is close to the Poiseuille flow conditions. For radial Reynolds numbers greater than 1, the evaporation and condensation cases become qualitatively different. Flow reversal was also noticed in the condenser section for high condensation cooling rates. The observations obtained here for an annular

13

heat pipe are similar to what Busse (1967) concluded for a cylindrical heat pipe.

Narayana (1986) studied the 2-D steady, incompressible laminar vapor flow in a heat pipe. The continuity and Navier-Stokes equations with the boundary layer assumptions were solved. The effect of frictional and inertial pressure drops on the static pressure is compared for the values of the wall Reynolds number in the range of 2 to -5.

Busse (1987a) presented a logical criterion for axisymmetric internal flows which indicates whether or not a given velocity profile tends to develop into a separation profile. He found that the reversal of the profile depends on the profile shape and the Mach number. The extraction of mass usually leads to a much stronger profile variation than injection. The viscous forces and mass injection tend to establish an equilibrium profile while mass extraction is an inherently unstable process which promotes a run-away from the equilibrium condition. It is still not certain, however, whether viscous forces can also cause a flow reversal.

Busse (1987b) studied laminar subsonic flow in cylindrical heat pipes. The vapor was modeled as a 2-D isothermal perfect gas with a constant heat of vaporization. The approach involves the use of the boundary layer approximation and a noncontinuous power series to describe the velocity profile. Based on the analytical method, the numerical results for the pressure recovery in the condenser were compared to experimental measurements. He found that significant flow reversal at the condenser wall first appears at $-6.0 \geq Re_{r,c} \geq -10.0$ giving rise to pressure recovery

14

in the condenser. Also confirmed, is that the onset of turbulence is at $Re_{r,c} \approx -6$ at axial Reynolds numbers of only a few hundred. This phenomenon coincides with the appearance of significant reversal flow. The restriction for the boundary layer approximation is that L_c/D should not be too small. The results presented in this report give a fairly good comparison with experimental measurements with $L_c/D = 4.4$. This work is an extension of the work by Busse and Prenger (1984) using a similar model, but the more recent analysis emphasizes identifying the influence of transition to turbulence on the condenser pressure recovery.

Recently, Bowman and Hitchcock (1988) modeled the unsteady vapor flow in a heat pipe. The vapor was assumed to be compressible, viscous and changing from laminar to turbulent. The Navier-Stokes equations were solved numerically using the MacCormack explicit finite difference method. Both transient and steady-state results were obtained. The experimental data for the pressure variation was obtained by using a porous pipe with air blowing along half of the pipe wall and suction along the other half of the pipe which simulates the heat pipe vapor flow. The pressure variation of both subsonic and supersonic vapor flow was measured and compared with the numerical results and a fairly good agreement was found. The experiment also demonstrated that the vapor flow in the heat pipe can be accurately modeled using the steady-state governing equations because the time period of the vapor transient is very short when compared to the heat pipe wall and wick transients.

Faghri and Parvani (1988) further analyzed the gas dynamics of annular heat pipes. The vapor was modeled as laminar incompressible flow. The

elliptic and partially parabolic Navier-Stokes equations were solved numerically and compared for the pressure drop and velocity profile along the pipe. For the cases presented, only a small deviation was found between these two solutions. Flow reversal was also noticed at high radial Reynolds numbers in the condenser and long condenser lengths. Based on the observation of a very short hydrodynamic entry length for the evaporator section, a similarity solution was also proposed for the prediction of the pressure drop and velocity profile for both conventional and annular heat pipes.

The investigators mentioned above only studied the vapor gas-dynamics by solving the mass and momentum conservation equations. The analyses with the coupling of the energy equati will be presented below.

Coupled Temperature Field and Vapor Dynamics

Levy (1968) analyzed the one-dimensional compressible vapor flow in the evaporator section of a heat pipe. He assumed a uniform temperature distribution and averaged the vapor velocity along the radial direction. The analysis was started from the mass, momentum and energy differential equations incorporating the Clausius-Clapeyron equation, the two-phase equilibrium relations and the Clapeyron-Mendeleev equation ($v_{sat} = \frac{RT}{P}$) for the specific volume of the saturated vapor. The vapor quality, velocity, and pressure differential equations were obtained with respect to the axial distance. These equations were integrated by using the Runge-Kutta method, and the results under the choking condition were presented for sodium heat pipes. Comparing the theoretical calculations with existing data suggests

16

that at sufficiently low vapor pressures, it is the choking phenomenon of the vapor flow rather than the capillary limit of the wick which will limit the maximum heat flux of the device. Bystrov and Popov (1976) performed a similar analysis by including the effect of friction along the pipe.

Rohani and Tien (1973) studied the heat and mass transfer in the vapor-gas region of a gas-loaded heat pipe. The elliptic governing equations were solved in conjunction with the overall energy and mass conservation balances and the thermodynamic equilibrium condition for three cases with different working fluids. They found that in liquid metal gas-loaded heat pipes, the vapor-gas two-dimensional diffusion must be considered in the analysis. A simple numerical framework to include the axial conduction in the wall and liquid-wick matrix was also proposed in that paper but no results were presented.

In 1974, Tien and Rohani solved th e2-D elliptic coupled momentum and energy equations with the thermodynamic equilibrium relation at the interface for the heat pipe vapor flow. The model was laminar, compressible and steady state with sodium as the working fluid. They used a vorticity-stream-function approach similar to the incompressible flow model used by Bankston and Smith (1973). For the boundary conditions, they specified that the evaporator and condenser are surrounded by constant but different ambient temperatures and have uniform overall heat transfer coefficients between the vapor-liquid interface and the ambient. The pressure and temperature variations were presented in terms of five different radial Reynolds numbers: $|Re_{r,e}| = 2, 4, 8, 24, 36$ or $|Re_{r,c}| = 1.33, 2.66, 5.33, 16.0, 24.0$. A large deviation was found for the elliptic

17

and parabolic pressure drop results at high radial Reynolds numbers. No comparison was made with experimental data.

Bianchi (1987) performed a similar analysis by using the finite element method, but he modeled the vapor flow as 2-D and incompressible with water as the working fluid for the presentation of the results. No pressure recovery in the condenser was observed for the cases presented.

Ismail et al. (1987) investigated the vapor and liquid flows inside the heat pipe. The finite difference method was used to solve this problem. The liquid and vapor were both assumed to be 2-D laminar and incompressible. The thermodynamic equilibrium relation linked the temperature and pressure at the liquid-vapor interface. The liquid flow in the porous medium is assumed to be one phase and covers the whole wick matrix, so the liquid flow was treated like pipe flow in a porous annulus with blowing and suction at the boundary. The overall pressure effect was considered rather than considering the pressure difference at each meniscus. Flow reversal of the vapor was observed in the evaporator, adiabatic and condenser regions, which usually only happens in the condenser region.

Colwell et al. (1987) modeled a liquid metal heat pipe start-up from frozen state. The heat pipe under consideration was rectangular in geometry. The finite element method was used to solve the transient two-dimensional solid wall and frozen liquid regions. A one-dimensional analytical approach similar to that of Levy (1968) was employed to solve the steady-state vapor flow. The transient temperature variation along the

18

liquid-vapor interface was presented at different time intervals. The results showed that it would take about 150 seconds for a heat pipe to get to the normal operation state from the frozen state. Since the 1-D analytical solution for vapor flow is easy to use and gives quite accurate results, it was a good approach to combine this method together with the 2-D unsteady solution of the wall-liquid regions. This is because the approaches for the 1-D vapor and 2-D solid regions are well established, and therefore a converged solution is ensured.

A transient heat pipe model with the wall, liquid-wick and vapor regions was proposed by Seo and El-Genk (1988). This model solves the quasi-steady-state, one-dimensional mass, momentum and energy conservation equations in the vapor region and a two-dimensional transient model is used in the wall and liquid-wick regions. This model assumes a compressible laminar vapor flow and an incompressible liquid flow in the porous medium with the capillary relationship as a link between the two fluids, but the effect of porosity in the liquid-wick region was neglected. Furthermore, the energy due to mass injection and suction to and from the vapor region was not considered. The thermophysical properties were assumed to be temperature dependent for both the liquid and vapor. The solution gives the temperature, pressure, and velocity distributions in the heat pipe, as well as the predictions of the heat pipe operational limits during both steady and transient operations. The numerical predictions of the temperatures of a lithium heat pipe with a radiative boundary condition in the condenser were in good agreement with experimental data.

19

Issacci et al. (1988) studied the transient behavior of the vapor flow in a rectangular heat pipe. The time dependent viscous compressible elliptic 2-D continuity, momentum and energy conservation equations were solved numerically. The ideal gas law is used to model the compressibility of the vapor and the pressure and temperature are linked by thermodynamic equilibrium at the interface. The "SIMPLE" numerical scheme developed by Patankar (1980) was used for the computations. Flow reversal was detected in the condenser and adiabatic regions with water as working fluid, but no comparison was made with experimental data.

Faghri (1988) extended the solution derived by Levy (1968) to annular heat pipes by using a similar approach. The annular heat pipe under consideration has two concentric pipes of unequal diameters attached by end caps which create an annular vapor space between the two pipes. The heat input and cooling were supplied to both the inner and outer walls. Similar results as obtained by Levy (1968) and Bystrov and Popov (1976) were obtained for the pressure and temperature variation along the pipe at the sonic limit. It was confirmed that the friction along the pipe will accelerate the vapor flow and make the sonic limit occur at a smaller heat input. A simple equation was also proposed for the prediction of the sonic limit of the annular heat pipe. In addition, the two-dimensional numerical parabolic and elliptic solutions were also obtained for the pressure drop along the pipe. Based on the observation that the vapor flow becomes fully developed in a very short distance from the evaporator end cap, three analytical similarity expressions were obtained for the pressure drop in the three different sections of conventional and annular heat pipes.

20

Experimental Studies

A number of experiments have been performed both on actual and simulated heat pipes and are summarized in Table 1.2. The experimental data on the actual heat pipes are usually obtained for the vapor or wall temperature variations along the heat pipe. The pressure profile along the pipe, which is usually difficult to obtain for actual heat pipes, is measured by using simulated heat pipes.

Kemme (1969), Ivanovskii et al. (1982) and Merrigan et al. (1986) investigated the performance of liquid metal heat pipes. Kemme's experiment was focused on the situation when a sodium heat pipe is working close to the sonic limit (M = 1). Ivanovskii et al. studied the sodium heat pipe performance at different working temperatures by measuring the vapor saturation temperature. For space applications, Merrigan et al. (1986) performed an experiment on the transient performance of the lithium heat pipe with radiation cooling at the condenser.

For low temperature heat pipes, Ponnappan and Mahefkey (1984), Bianchi (1987), Gernert (1986) and Faghri and Thomas (1988) used water as the working fluid. Ponnappan and Mahefkey (1984) studied a heat pipe with a double-wall artery wick structure while Bianchi (1987) studied a conventional heat pipe with a screen mesh wick. Gernert's experiment on the heat pipe with multiple heat sources found a very small difference in temperature for the wall and vapor temperatures along the heat pipe. Faghri and Thomas (1988) performed an experiment on an annular heat pipe which has axial grooves on the inner and outer pipe walls for the capillary

wick.   The purpose was to measure the capillary limit and compare the results with a conventional heat pipe with the same outer dimensions.

The most widely referenced experiment on a simulated heat pipe is that done by Quaile and Levy (1972).   The experiment simulated the vapor flow in a heat pipe condenser. The tube was closed at the downstream end and the fluid was removed uniformly by suction through the porous wall. They measured the axial pressure drop in a porous pipe as well as the radial variations of the axial velocity at several axial locations. The pressure recovery phenomenon was observed in that experiment. The experimental data from the pressure profile showed a very good agreement with the theoretical solution by Weissberg (1959) and Busse (1967) in the range $2.21 < Re_r < 5.0$.   Recently, Bowman and Hitchcock (1988) simulated a whole heat pipe by employing air flow with injection and extraction in a porous pipe.   The results were given for the pressure and velocity variations while the flow changed from laminar to turbulent.

1.3. Mathematical Formulation

The heat pipe model under consideration (Fig. 1.1), has three distinct regions in the radial direction (wall, liquid-wick and vapor) as well as three different types of sections in the axial direction (evaporator, adiabatic and condenser). This model solves the two-dimensional conservation of mass, momentum and energy equations for the heat pipe with single and multiple heat sources under the following assumptions:

a. The compressible vapor flow is laminar and steady.

b. The heat transfer through the liquid-wick is modeled as pure conduction with an effective thermal conductivity.

c. The properties of the vapor, the liquid and the solid in each region are constant with the vapor density following the perfect gas law.

d. Both evaporation and condensation are considered to occur at the inner radius of the porous medium.

e. At the vapor-liquid interface, the vapor is at its thermodynamic equilibrium temperature corresponding to the local saturation vapor pressure.

f. At the liquid-vapor and wall-liquid interfaces, the harmonic mean of the thermal conductivity is used for the energy equation.

g. The flow is axisymmetric.

23

1.3.1. Vapor Region:

The conservation of mass and momentum equations given by Bird et al. (1960) and the energy equation given by Bejian (1984) after some simplification are as follows:

mass:

$$\frac{\partial}{\partial z}(\rho_v w_v) + \frac{1}{r}\frac{\partial}{\partial r}(\rho_v r v_v) = 0 \qquad (1.1)$$

r-component momentum:

$$\rho_v(v_v\frac{\partial v_v}{\partial r} + w_v\frac{\partial v_v}{\partial z}) = -\frac{\partial P_v}{\partial r} + \mu_v\left[\frac{4}{3r}\frac{\partial}{\partial r}(r\frac{\partial v_v}{\partial r}) - \frac{1}{3}\frac{v_v}{r^2} + \frac{1}{3}\frac{\partial^2 w_v}{\partial z\partial r} + \left\{\frac{\partial^2 v_v}{\partial z^2}\right\}\right]$$

$$\qquad (1.2)$$

z-component momentum:

$$\rho_v(v_v\frac{\partial w_v}{\partial r} + w_v\frac{\partial w_v}{\partial z}) = -\frac{\partial P_v}{\partial z} + \mu_v\left[\frac{1}{r}\frac{\partial}{\partial r}(r\frac{\partial w_v}{\partial r}) + \frac{1}{r}\frac{\partial}{\partial r}(r\frac{\partial v_v}{\partial z})\right.$$

$$\left. - \frac{2}{3}\frac{\partial}{\partial z}(\frac{1}{r}\frac{\partial}{\partial r}(rv_v)) + \left\{\frac{4}{3}\frac{\partial^2 w_v}{\partial z^2}\right\}\right] \qquad (1.3)$$

energy conservation:

$$\rho_v c_p(v_v\frac{\partial T_v}{\partial r} + w_v\frac{\partial T_v}{\partial z}) = k_v\left[\frac{1}{r}\frac{\partial}{\partial r}(r\frac{\partial T_v}{\partial r}) + \left\{\frac{\partial^2 T_v}{\partial z^2}\right\}\right] + v_v\frac{\partial P_v}{\partial r} + w_v\frac{\partial P_v}{\partial z}$$

$$+ \mu_v\phi \qquad (1.4)$$

24

where:

$$\phi = 2\left[\left(\frac{\partial v_v}{\partial r}\right)^2 + \left(\frac{v_v}{r}\right)^2 + \left(\frac{\partial w_v}{\partial z}\right)^2 + \frac{1}{2}\left(\frac{\partial v_v}{\partial z} + \frac{\partial w_v}{\partial r}\right)^2 - \frac{1}{3}(\nabla \cdot v)^2\right]$$

$$\nabla \cdot v = \frac{1}{r}\frac{\partial}{\partial r}(rv_v) + \frac{\partial w_v}{\partial z}$$

The viscous dissipation, ϕ, is included in the present analysis. We should mention here that in equations (1.2-1.4), the terms in braces {} are associated with axial diffusion terms. These terms are neglected when the partially parabolic version is considered but are included in the elliptic version.

Compressibility of Vapor:

The perfect gas law is employed to account for the compressibility of the vapor. The vapor density is obtained from the following equation:

$$\rho_v = \frac{P_v}{RT_v} \tag{1.5a}$$

where R is the gas constant.

Since

$$\frac{P_v}{\rho_v} = RT_v$$

and

$$\frac{\gamma P_v}{\rho_v} = \gamma RT_v$$

we have

$$\frac{\gamma P_v}{\rho_v} = c^2$$

where c is the velocity of sound and γ is the ratio of specific heats. Usually the velocity of sound changes very little under the normal working conditions of a heat pipe, so we can write the derivative of the above equation in the following form:

$$\frac{1}{\rho_v} \frac{\partial \rho_v}{\partial P_v} = \frac{1}{P_v} \qquad (1.5b)$$

Equation (1.5b) is used in the density correction formula $\rho = \rho^* + \rho'$, where ρ' is the density correction and is equal to $\frac{\partial \rho}{\partial P} P'$, P' is the pressure correction, ρ^* is the guessed density and is obtained from ρ of the previous iteration. As long as a converged solution can be obtained, P' approaches zero, therefore the approximate ρ' equation (i.e., Eq. (1.5b)) is sufficient.

1.3.2 Wall and Liquid-Wick Regions

In these regions, only heat conduction is considered and the energy conservation equation is as follows:

$$\frac{1}{r} \frac{\partial}{\partial r}\left[rk\frac{\partial T}{\partial r}\right] + \frac{\partial}{\partial z}\left[k\frac{\partial T}{\partial z}\right] = 0 \qquad (1.6)$$

where the thermal conductivity k of the wall is different from that of the liquid-wick structure.

The equation for the effective thermal conductivity proposed by Chi (1976) is used here for the liquid saturated screen wicks, and is as

26

follows:

$$k_{eff} = \frac{k_l[k_l + k_s - (1-\epsilon)(k_l-k_s)]}{k_l + k_s + (1-\epsilon)(k_l-k_s)} \qquad (1.7)$$

In the above equation, the ϵ is the wick porosity and is given by Chang (1987):

$$\epsilon = 1 - \frac{\pi AB}{2(1+A)}$$

where $A = d/w$ and $B = d/t$. The wire diameter is d, the screen thickness is t, and the opening width of the screen is w. The liquid and solid wick thermal conductivities are k_l and k_s, respectively.

For the sintered powder wick, the following equation proposed by Dunn and Reay (1982) is used to calculate the effective thermal conductivity.

$$k_{eff} = k_s \left[\frac{2 + k_l/k_s - 2\epsilon(1-k_l/k_s)}{2 + k_l/k_s + \epsilon(1-k_l/k_s)} \right] \qquad (1.8)$$

For the concentric annulus wick, the effective thermal conductivity is obtained from the following equation proposed by Dunn and Reay (1982).

$$k_{eff} = k_l$$

27

1.3.3. The Boundary Conditions

At either end of the heat pipe ($z = 0$, $z = L$), the radial and axial velocities and the axial temperature gradient are zero.

$$w = v = \frac{\partial T}{\partial z} = 0 \tag{1.9}$$

The pressure is fixed to zero at the end cap of the evaporator at the liquid-vapor interface for the elliptic solution and the datum pressure, P_0, is added to get the absolute value.

The uniform heat flux boundary condition is specified at the outer pipe wall surface ($r = R_w$) of the evaporator and condenser sections. For the evaporator section ($0 \leq z \leq L_e$) or each of the evaporator sections in the case of multiple heat sources, the constant heat flux boundary condition is as follows:

$$-k_w \frac{\partial T_w}{\partial r} = q_{o,e}$$

For the adiabatic section ($L_e \leq z \leq L_e + L_a$) at the outer pipe wall surface ($r = R_w$), we have

$$\frac{\partial T_w}{\partial r} = 0 \tag{1.10}$$

and for the condenser section ($L_e + L_a \leq z \leq L$), the constant heat flux boundary condition is:

28

$$-k_w \frac{\partial T_w}{\partial r} = q_{o,e} \frac{A_e}{A_c}$$

At the wall and liquid-wick interface $(r = R_v + \delta_1)$, the temperature and heat flux at both sides of the interface should be the same.

$$T_{lw} = T_w \qquad (1.11)$$
$$k_w \frac{\partial T_w}{\partial r} = k_{eff} \frac{\partial T_{lw}}{\partial r}$$

The symmetry boundary conditions are applied along centerline of the pipe $(r=0)$:

$$\frac{\partial w_v}{\partial r} = v_v = \frac{\partial T_v}{\partial r} = 0 \qquad (1.12)$$

Along the liquid-vapor interface $(r = R_v)$, the following boundary conditions are specified: no slip boundary condition, thermodynamic equilibrium, energy balance heat source, and blowing and suction velocities.

For the no slip boundary condition at the liquid-vapor interface

$$w_v = 0 \qquad (1.13)$$

For thermodynamic equilibrium, the Clapeyron equation is used in the following form:

$$\frac{dP_v}{P_v} = \frac{dT_v}{T_v^2} \frac{h_{fg}}{R}$$

29

or it can be integrated in terms of T_0 and P_0, which results in

$$T_v = \frac{1}{\frac{1}{T_0} - \frac{R}{h_{fg}} \ln \frac{P_v}{P_0}} \tag{1.14}$$

The above equation is used to determine the vapor temperature at the vapor-liquid interface.

Making an energy balance at the interface results in

$$q_i = \dot{m} h_{fg} = k_v \frac{\partial T_v}{\partial r} - k_{eff} \frac{\partial T_{lw}}{\partial r} \tag{1.15}$$

or

$$\dot{m} = \frac{k_v \frac{\partial T_v}{\partial r} - k_{eff} \frac{\partial T_{lw}}{\partial r}}{h_{fg}} \tag{1.16}$$

and

$$v_i = \frac{\dot{m}}{\rho_v} \qquad \begin{cases} v_i > 0 & \text{Suction (condensation)} \\ v_i < 0 & \text{Blowing (evaporation)} \end{cases} \tag{1.17}$$

A summary of the boundary conditions are also listed in Table 1.3.

Table 1.3 Boundary Conditions for Heat Pipe Analysis

	evaporator $(0 \leq z \leq L_e)$	adiabatic $(L_e \leq z \leq L_e + L_a)$	condenser $(L_e + L_a \leq z \leq L)$
outer pipe wall $(r = R_w)$	$-k_w \dfrac{\partial T_w}{\partial r} = q_{o,e}$	$\dfrac{\partial T_w}{\partial r} = 0$	$-k_w \dfrac{\partial T_w}{\partial r} = q_{o,e} \dfrac{A_e}{A_c}$
wall and liquid-wick interface $(r = R_v + \delta_1)$	$T_{lw} = T_w, \quad k_w \dfrac{\partial T_w}{\partial r} = k_{eff} \dfrac{\partial T_{lw}}{\partial r}$		
liquid-vapor interface $(r = R_v)$	$w_v = 0, \quad v_i = \dfrac{\dot{m}}{\rho_v}, \quad q_i = \dot{m} h_{fg} = k_v \dfrac{\partial T_v}{\partial r} - k_{eff} \dfrac{\partial T_{lw}}{\partial r},$ $$T_i = \cfrac{1}{\dfrac{1}{T_0} - \dfrac{R}{h_{fg}} \ln \dfrac{P_v}{P_0}}$$		
centerline of the pipe $(r = 0)$	$\dfrac{\partial w_v}{\partial r} = v_v = \dfrac{\partial T_v}{\partial r} = 0$		
both ends of the pipe $(z = 0, L)$	$w = v = \dfrac{\partial T}{\partial z} = 0$		

1.3.4. The Dimensionless Variables

The solution for the parametric study will be presented for the following dimensionless dependent variables:

$$w^+ = \frac{w}{\bar{w}_z}, \quad P^+ = \frac{2(P - P_0)}{\rho_0 \bar{w}_a^2}, \quad T^+ = \frac{T}{T_0}, \quad q^+ = \frac{q_i}{q_m},$$

where ρ_0 is obtained at T_0 and P_0. The mean heat flux at the liquid-vapor interface without considering the axial heat conduction in the wall and liquid-wick regions is q_m, which is specified as follows:

at the evaporator and adiabatic sections,

$$q_{m,e} = q_{0,e}\left[\frac{R_w}{R_v}\right]$$

and at the condenser section,

$$q_{m,c} = q_{0,c}\left[\frac{R_w}{R_v}\right]$$

where $q_{0,e}$ and $q_{0,c}$ are the heat fluxes specified at the outer pipe wall of the evaporator and condenser sections. The heat flux across the liquid-vapor interface, q_i, is calculated from equation (1.15).

These results are presented in terms of the dimensionless independent variables and parameters as follows:

$$z^+ = \frac{z}{L}, \quad r^+ = \frac{r}{R_v}, \qquad K_{wl} = \frac{k_w}{k_{eff}}, \quad K_{lv} = \frac{k_{eff}}{k_v},$$

$$\Delta_w = \frac{\delta_w}{2R_v}, \quad \Delta_l = \frac{\delta_l}{2R_v}, \qquad Re_r = \frac{\rho_0 v_0 R_v}{\mu_v}, \quad \text{or}$$

$$Re_{r,e} = \frac{QR_v}{\mu_v h_{fg} A_e} \qquad\qquad Re_{r,c} = \frac{QR_v}{\mu_v h_{fg} A_c}$$

The dimensionless parameters proposed here are based on the conjugate heat transfer analysis of flow in a pipe (Section II) and the annular heat pipe analysis by Faghri and Parvani (1988).

1.4 Solution Procedure

The heat pipe problem is solved as a convection-conduction problem throughout the entire domain by solving one generalized energy equation with different thermal diffusion coefficients. The velocity in the solid wall and the liquid-wick matrix is specified to be zero so that the analysis in these two regions becomes purely a conduction problem. Since the liquid velocity in the porous medium is much slower compared to the vapor flow, the zero vapor velocity boundary condition at the liquid-vapor interface and neglecting the convective term in the energy equation of the liquid-wick region should not cause a large accuracy problem. The validity of the results will be checked with experimental data.

The generalized PHOENICS computer code is used in the present analysis, which employs the finite-difference iterative method of solution developed by Spalding et al (1980). The elliptic solutions of the mass, momentum and energy conservation equations with boundary conditions given in equations (1.9-1.17) were obtained. The partially parabolic solution was also obtained by neglecting the axial diffusion terms in the momentum and energy equations. The solution procedure is based on a line-by-line iteration method in the axial direction and the Jacobi point-by-point procedure in the radial direction. The "SIMPLEST" method is employed for the momentum equations, in which the finite-domain coefficients contain only diffusion contributions, and where the convection terms are added to the linearised source term of the equations.

The pressure field is solved by the whole-field pressure correction

algorithm derived by Markatos et al. (1982). The pressure correction equation is deduced from the finite-domain form of the continuity equation, which assumes that the flow coming into the system is due to the pressure difference. The pressure field is first assumed and then the velocities and temperatures are solved. This step is repeated line-by-line to the completion of a sweep. The pressure correction equation is then solved using the mass errors that have been calculated during the sweep and other variables are updated accordingly. A new sweep will start until convergence is attained. In this numerical scheme, once the velocity boundary condition is specified no pressure boundary condition is needed. For compressible vapor flow, the mass and momentum equations are coupled with the energy equation by the perfect gas law. These four equations are solved sequentially by iteration.

Since there is a change of phase at the liquid-vapor interface, the energy equation is no longer continuous due to the latent heat of evaporation or condensation. To make an energy balance, we can include the term $\dot{m}h_{fg}$ as a heat sink at the liquid-vapor interface in the evaporator and as a heat source at the interface in the condenser section. Therefore, the sign of q_i in the evaporator should be negative and positive in the condenser.

The governing equation of the vapor flow is first solved by assuming that the heat flux is uniform at the liquid-vapor interface based on the total heat input at the outer wall. The rate of evaporation, condensation and the velocity are then calculated by $\dot{m} = q_i/h_{fg}$ and $v_i = \dot{m}/\rho_v$. These values are used in the vapor mass and momentum conservation equations.

35

Once the converging solution is obtained after a few iterations, a new q_i is calculated through equation (1.15) and used for further iterations. At the same time, the thermodynamic equilibrium is checked and corrected during each iteration. The iteration will continue until fully converged results are obtained. The pressure at the liquid-vapor interface at the end of the evaporator, P_0, is taken as the datum pressure and does not change. The corresponding saturation temperature T_0 is assumed to be the initial temperature for the whole calculation domain.

The accuracy of the numerical solution is checked with experimental data and the convergence is assured in two ways:

1) The sum of the absolute value of the residuals should decrease as the sweep number increases.

2) The spot value should approach a constant value as the sweep number increases.

For each grid point, a residual is defined as the error that occurs when the current values of the dependent variables are inserted into the discretization equation. The error is due to the fact that the current values of the dependent variables do not satisfy the discretization equation exactly. The number of sweeps changes from 150 to 350 based on each different case. The spot value was used to monitor the change of each variable with the increase of the sweep number at one particular location in the domain. The location of the spot value was chosen in the vapor region of the condenser section next to the adiabatic section.

As a common approach, a course grid size is first chosen to test the program, and a fine grid spacing is employed for the final solution. A uniform grid size is used for the axial direction, and three different uniform grid sizes are used for the vapor, liquid-wick, and wall regions. For the numerical results presented for the parametric study, the grid sizes for the cases presented are chosen as follows:

30 x 20 x 10 x 10 = (axial) x (radial vapor) x (radial liquid-wick) x (radial solid wall).

1.5 Model Verification Versus Experimental Data

To verify the numerical predictions, the results are compared to four cases of existing experimental data reported by several investigators as listed in Table 1.4. The related experimental specifications and properties for the numerical computations are also listed in Tables 1.4 and 1.5, respectively.

The numerical model was first compared to the experimental data reported by Ivanovskii et al. (1982) for a cylindrical sodium heat pipe (Case 1). The heat pipe was provided with a compound wick of the type with a ring-shaped gap for the flow of liquid. The effective thermal conductivity for the computation is chosen to be equal to the liquid thermal conductivity proposed by Dunn and Reay (1982). The method of measuring the temperature distribution was to place a movable micro-thermocouple directly in the vapor channel. The thermocouple was provided with a special capillary device to keep it wetted by the condensate, so the temperature readings correspond to the saturation temperature which matches the numerical model at the interface. For the numerical computation, the constant heat flux with a total heat input of 560 W is specified at the outer wall of the evaporator. The pipe wall is assumed to be made of stainless steel and has a thickness of $\delta_w = 1$ mm. At the condenser, a constant heat flux based on the total heat input at the outer wall of the evaporator section is also specified. Fig. 1.2 compares the numerical results and the experimental data for the vapor saturation

38

TABLE 1.4 Experimental Heat Pipe Specifications

Case No.	1	2	3	4
References	Ivanovskii et al. (1982)	Ivanovskii et al. (1982)	Kemme (1969)	Gernert (1986)
Working Fluid	Sodium	Sodium	Sodium	Water
L_e(m)	0.1	0.1	0.143	0.1, 0.1
L_a(m)	0.05	0.05	0.06	0.4, 0.3
L_c(m)	0.35	0.55	1.08	0.6
Vapor Channel Radius (mm)	7.0	7.0	5.7	11.0
Wick Type	Ring-Shaped Gap(screen mesh)	Ring-Shaped Gap(screen mesh)	Screen Mesh	Sintered Powder
Mesh Number (per in²)	not reported	not reported	400	325
Wick Thickness (δ_1,mm)	0.5	0.5	0.15	0.76
Wall Material	Stainless Steel(assumed)	Stainless Steel(assumed)	Stainless Steel	Copper
Wall Thickness (δ_w,mm)	1.0 (assumed)	1.0 (assumed)	0.9	1.6
Total Heat Input (Q,W)	560	1000	6400	200 + 800

TABLE 1.5 Experimental Heat Pipe Properties

Case No. Properties	1	2	3	4
$T_0(^\circ C)$	545	583	692	94
$P_0(N/m^2)$	1300	2476	12,460	85,710
$h_{fg} \times 10^{-6} (J/kg)$	4.22	4.182	4.08	2.27
$\rho_v \times 10^2 kg/m^3)$	0.461	0.843	3.857	51.06
$\mu_v \times 10^7 N\ s/m^2)$	194.9	191.43	192.89	121.42
$c_{p_v} (J/kg\text{-}K)$	2583.0	2648.0	2710.0	2010.1
$k_s(W/m\text{-}K)$	19.0	19.0	19.0	394.0
$k_l(W/m\text{-}K)$	66.18	66.18	59.54	0.682
$k_{eff}(W/m\text{-}K)$	66.18	66.18	45.45	240.2
$k_v(W/m\text{-}K)$	0.0352	0.0353	0.044	0.0244
ϵ	0.33	0.33	0.74	0.30
grid number (radial x axial)	35 x 50	35 x 70	35 x 50	40 x 60

temperature along the heat pipe for Case 1. These particular experimental data were chosen for comparison because they were more readable than other data presented by Ivanovskii et al. (1982). As the results show, the present compressible elliptic and partially parabolic models give accurate predictions of the temperature profile compared to the experimental data with a maximum deviation of $3^{0}C$. According to Ivanovskii et al. (1982), the experimental data for the heat transfer rate were measured with an accuracy of 6 to 10%, so the deviations of the present compressible models are within the range of experimental accuracy. For the incompressible model, however, there is a maximum deviation of about $6^{0}C$ at the inlet of the condenser section. Therefore, we need to include the effect of the compressibility of the vapor in the analysis.

Figure 1.3 shows the variation of the pressure drop distribution along the liquid-vapor interface for Case 1. The pressure drop reaches its maximum value at the exit of the adiabatic section and then recovers about 55% in the condenser. Since the Clapeyron equation is the link between the temperature and the pressure at the liquid-vapor interface, the pressure profile is similar to the temperature distribution. The trend of the pressure profile also agrees with the existing numerical results obtained by Tien and Rohani (1974).
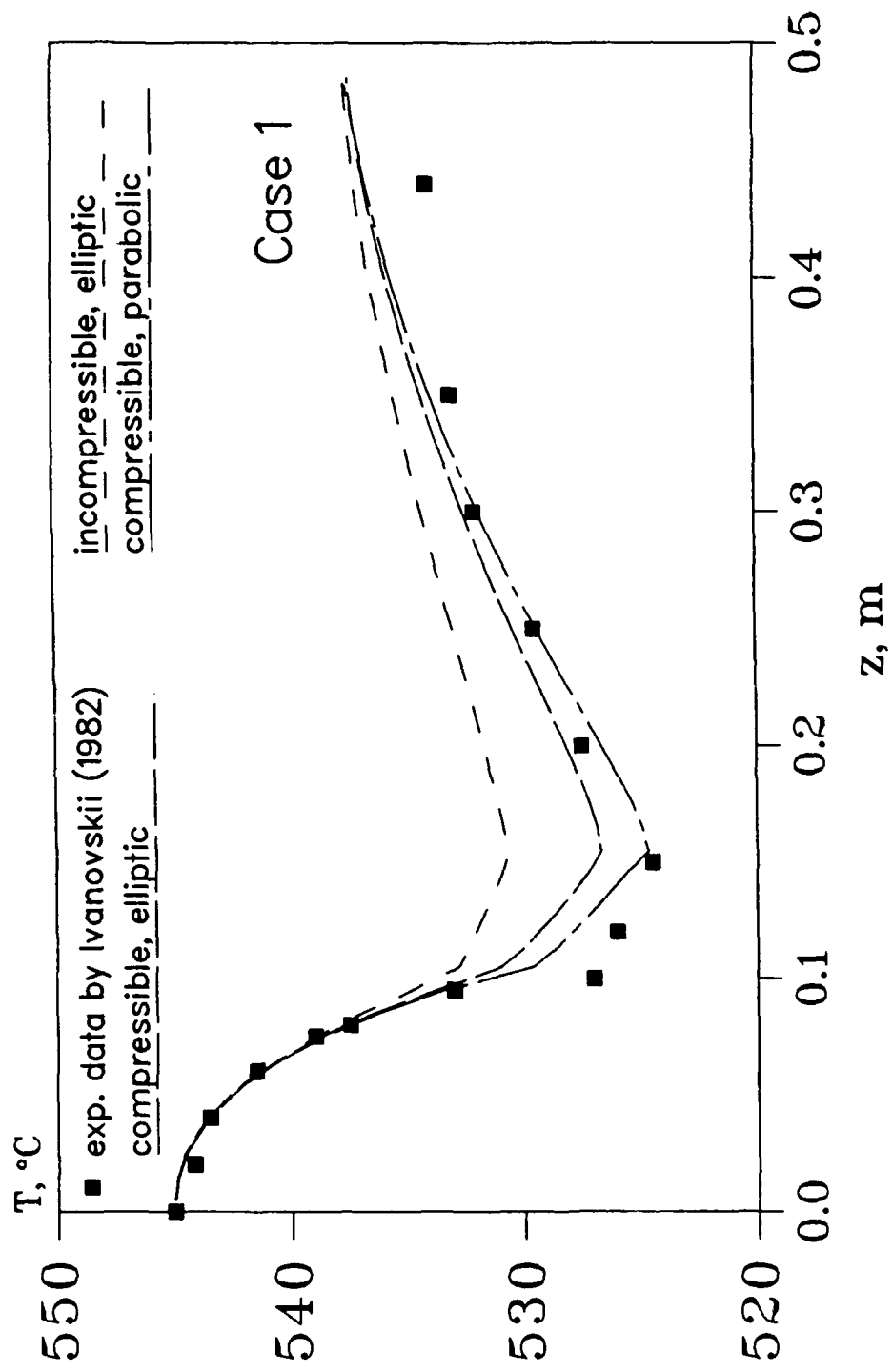
Fig. 1.2 The axial interface temperature profile along the sodium heat pipe
with Q=560 W, R_v=0.007 m, L_e=0.1 m, L_a=0.05 m, L_c=0.35 m
k_l=66.2 W/m^2-K, k_s=19.0 W/m-K, δ_l=0.0005 m, δ_w=0.001 m
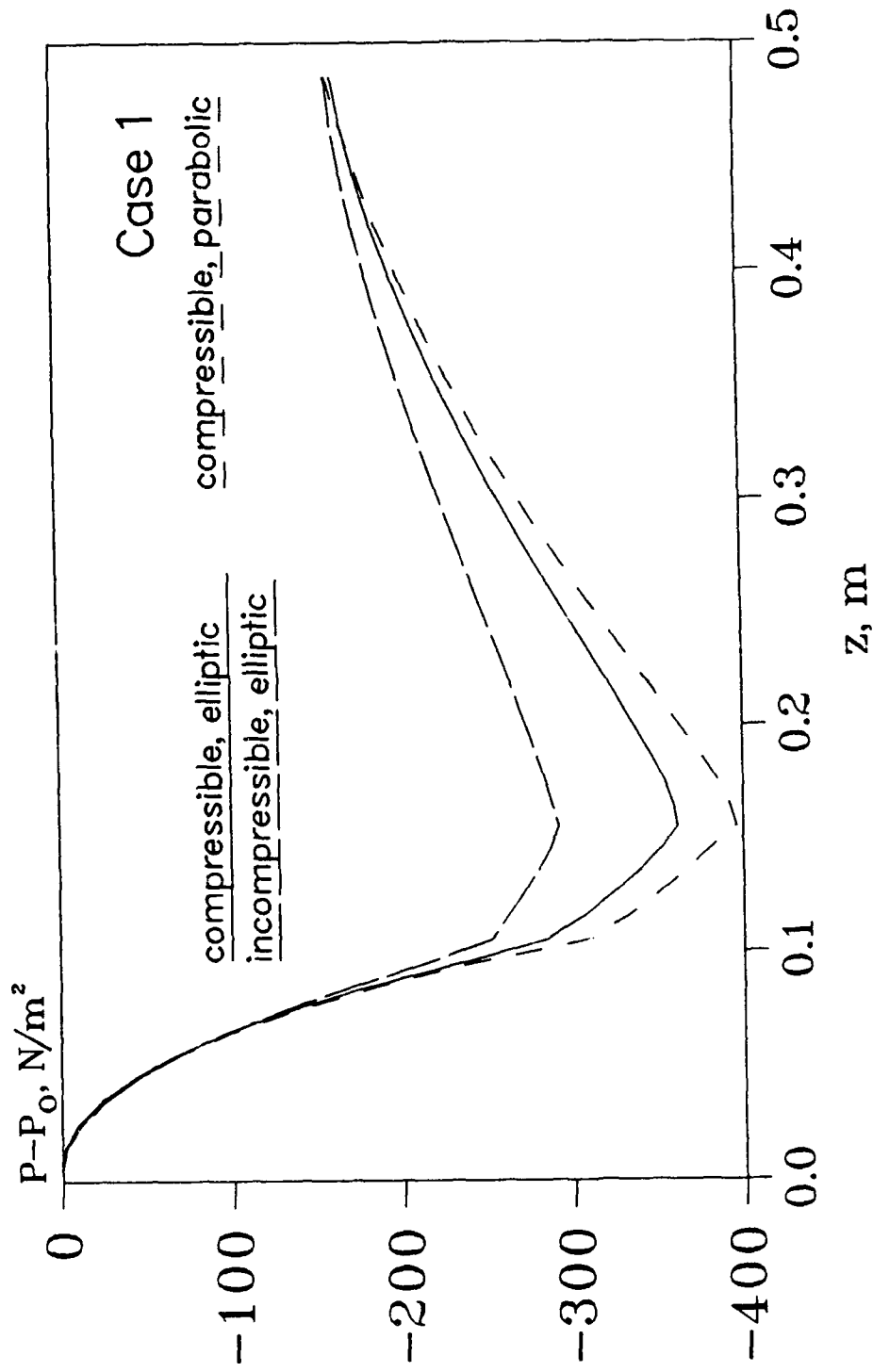
Fig. 1.3 The axial interface pressure profile along the sodium heat pipe with Q=560 W, R_v=0.007 m, L_e=0.1 m, L_a=0.05 m, L_c=0.35 m, k_l=66.2 W/m²-K, k_s=19.0 W/m²-K, δ_l=0.0005 m, δ_w=0.001 m

Fig. 1.4 shows the variation of the Mach number along the centerline of the pipe with a maximum value of 0.6 at the inlet of the condenser for the compressible elliptic model. The trend is generally in agreement with the results obtained by Levy (1968) for a cylindrical heat pipe and Faghri (1988) for an annular heat pipe with a 1-D compressible model.

Figures (1.5-1.7) shows the numerical results for the axial temperature, pressure and Mach number variations, respectively, which correspond to Case 2 of the experimental data by Ivanovskii (1982). For this case, the heat input was Q=1000 W and other geometric parameters are indicated in Table 1.4. Since the thickness of the wall and the type of materials were not mentioned in the reference, numerical calculations were made with two different thermal conductivities and thicknesses for the pipe wall which are believed to be commonly used by heat pipe manufacturers. The results showed that the effect of axial conduction inside the wall and liquid-wick is not important in this range, so only the results for the thermal conductivity and wall thickness reported in Tables 1.4 and 1.5 are given. The results of the compressible and incompressible models for the vapor flow are presented versus the experimental data for the interface temperature in Fig. 1.5. It shows that both models give a very good prediction in the evaporator region, but the incompressible model overpredicts the data in the adiabatic and condenser regions while the compressible model underpredicts the data in the start of the condenser region and overpredicts it near the end. In general, the compressible model gives a better prediction. Fig. 1.6 shows the pressure variation along the heat pipe for the compressible and incompressible models for Case 2. The incompressible model gives a maximum deviation of about 18%

44
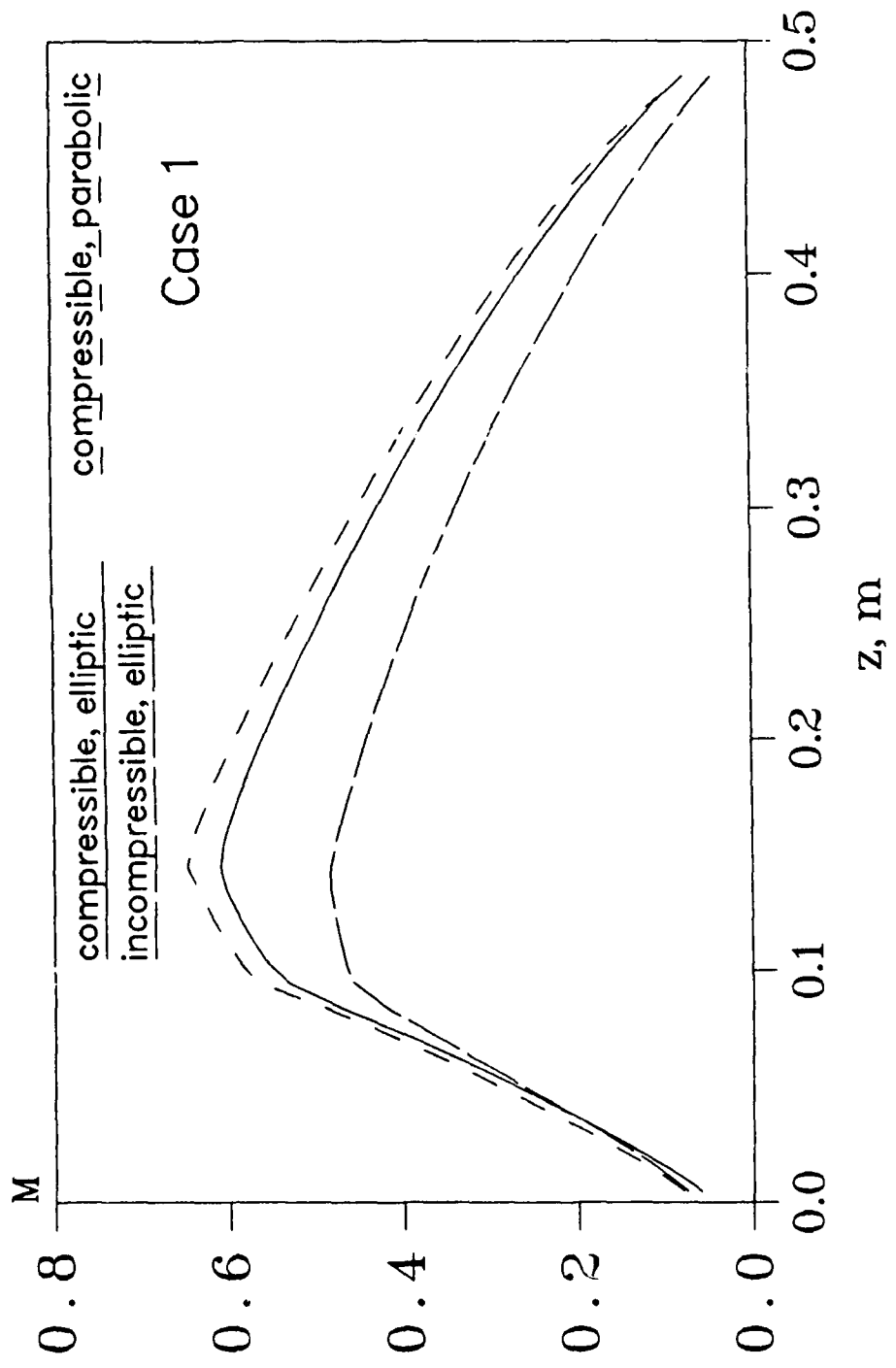
Fig. 1.4 The axial Mach number along the centerline of the sodium heat pipe with $Q=560$ W, $R_v=0.007$ m, $L_e=0.1$ m, $L_a=0.05$ m, $L_c=0.35$ m, $k_l=66.2$ W/m^2–K, $k_s=19.0$ W/m–K, $\delta_l=0.0005$ m, $\delta_w=0.001$ m
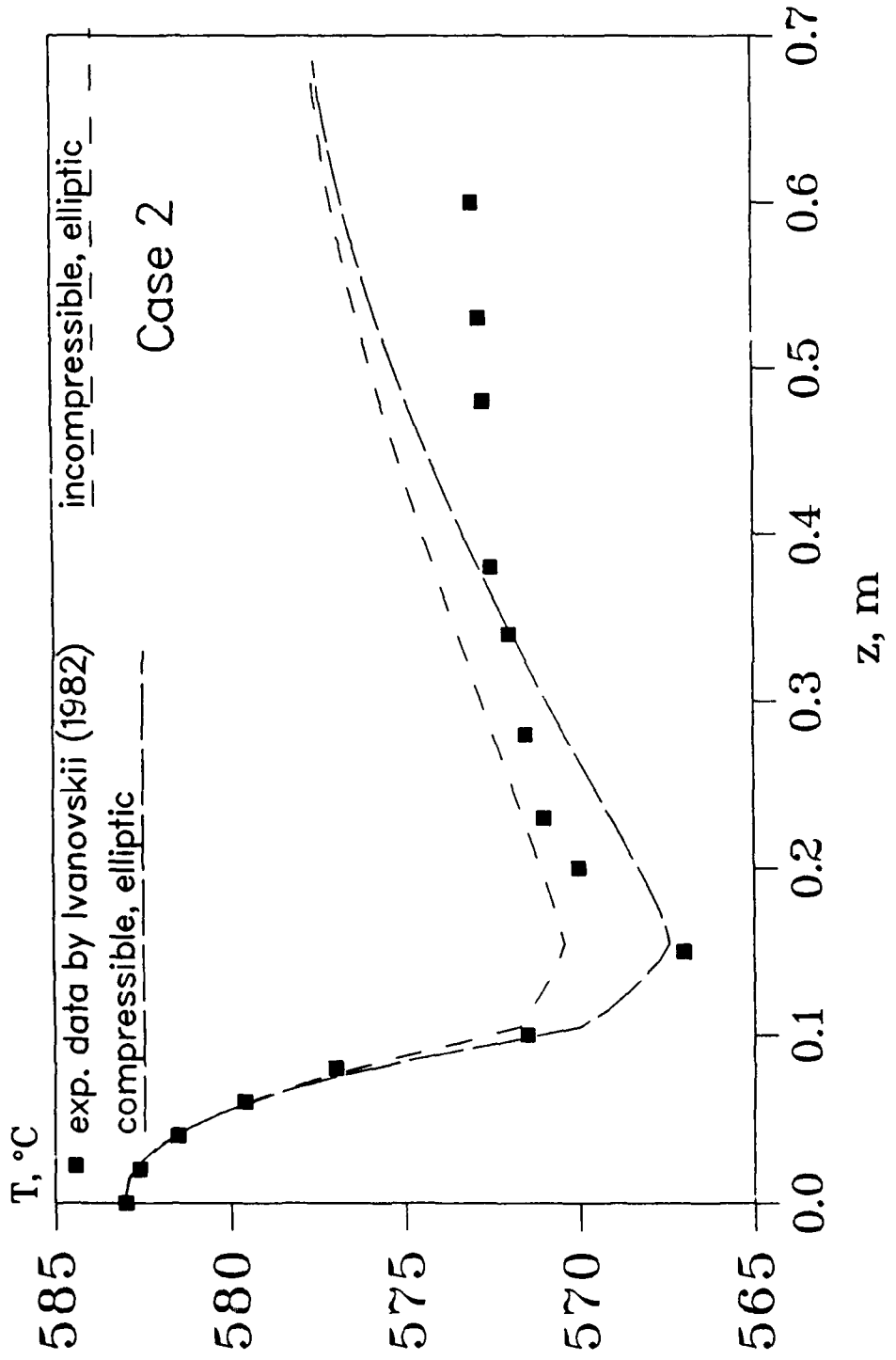
Fig. 1.5 The axial interface temperature profile along the sodium heat pipe with Q=1000 W, R_V=0.007 m, L_e=0.1 m, L_a=0.05 m, L_c=0.55 m k_l=66.2 W/m²-K, k_s=19.0 W/m-K, δ_l=0.0005 m, δ_w=0.001 m
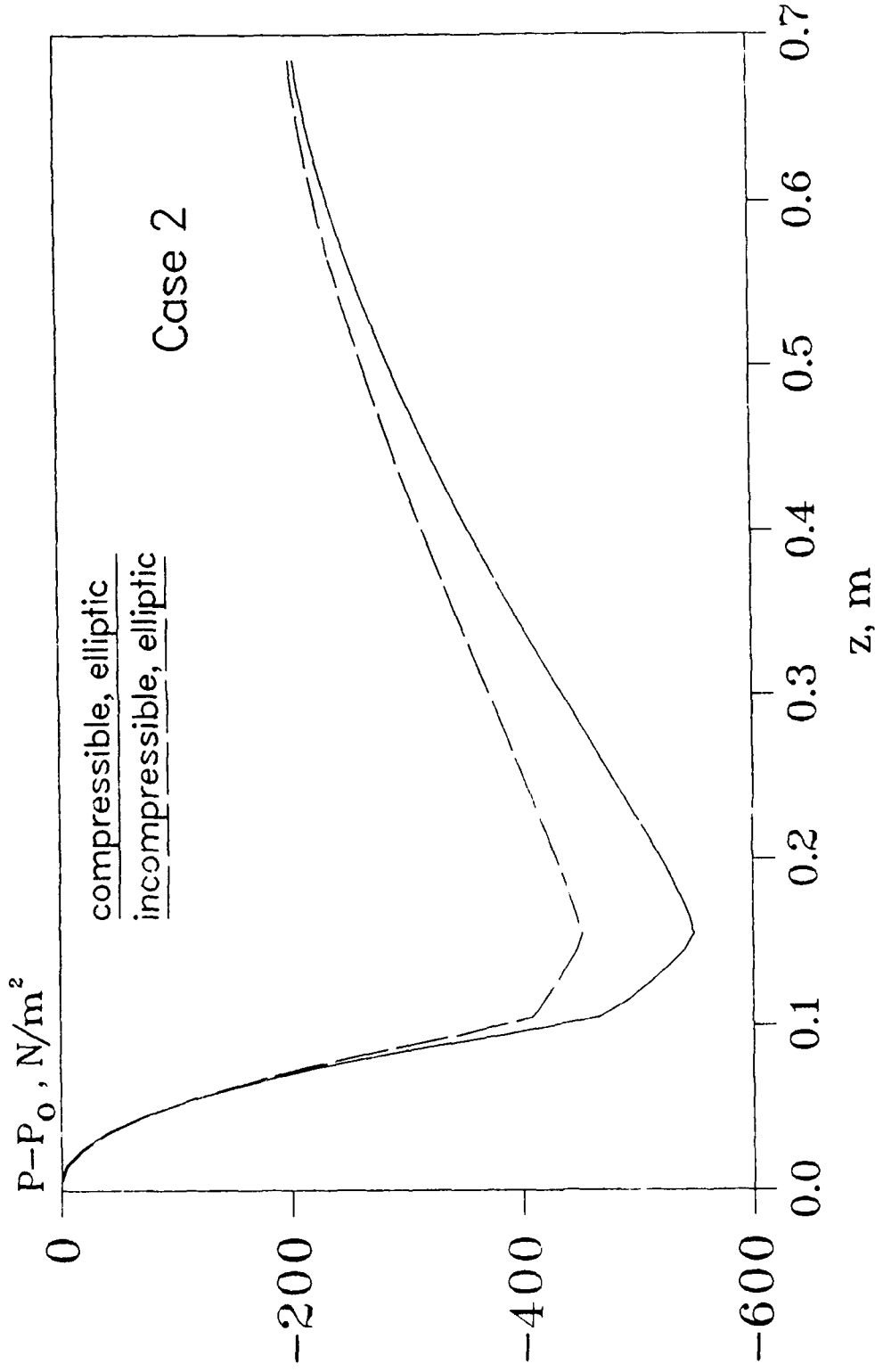
Fig. 1.6 The axial interface pressure profile along the sodium heat pipe
with Q=1000 W, R_v=0.007 m, L_e=0.1 m, L_a=0.05 m, L_c=0.55 m,
k_l=66.2 W/m^2-K, k_s=19.0 W/m^2-K δ_l=0.0005 m, δ_w=0.001 m
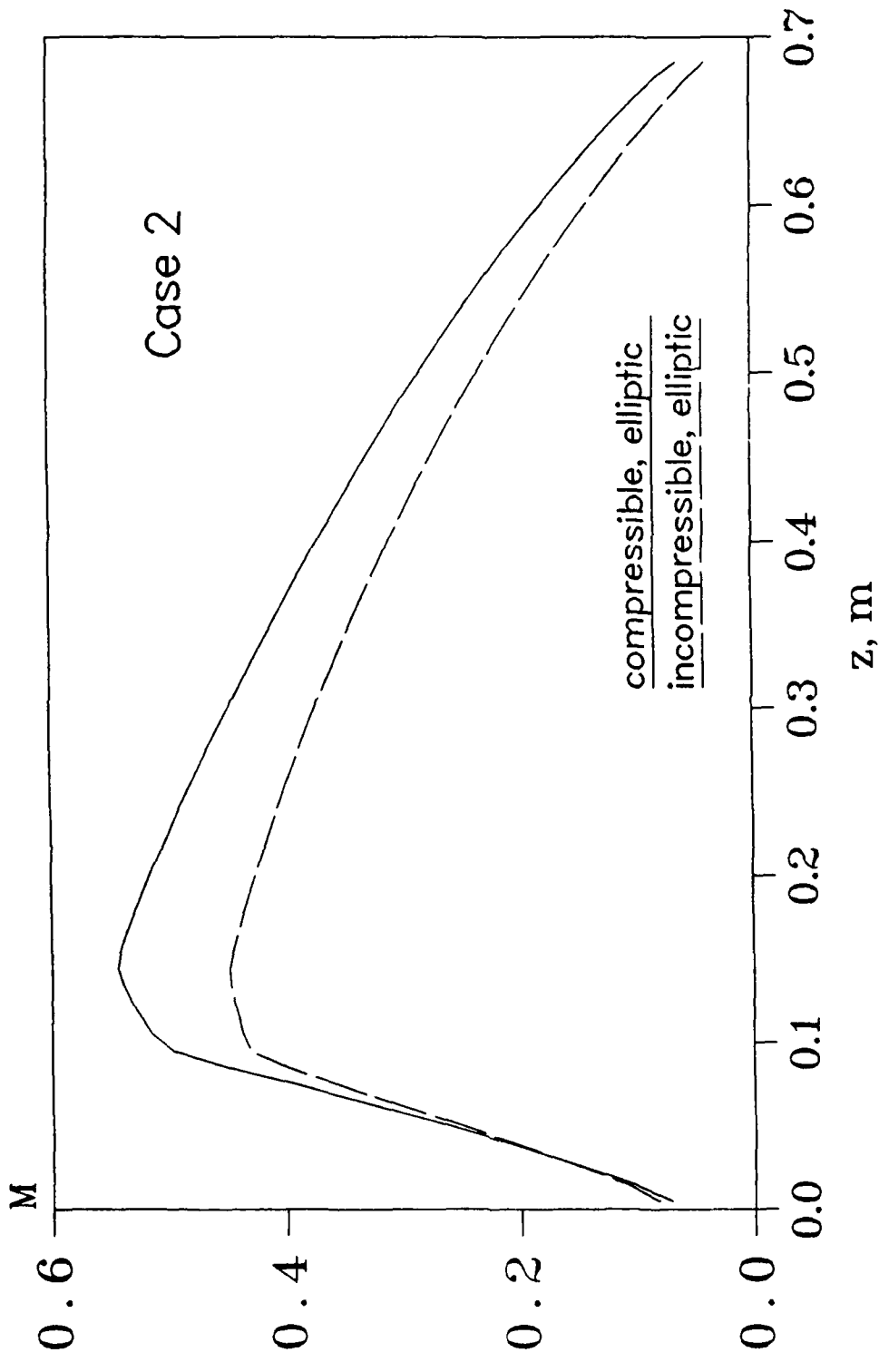
Fig. 1.7 The axial Mach number profile along centerline of the sodium heat pipe with Q=1000 W, $\dot{R}_v$=0.007 m, L_a=0.1 m, L_e=0.05 m, L_c=0.55 m, k_l=66.2 W/m²−K, k_s=19.0 W/m−K, δ_l=0.0005 m, δ_w=0.001 m

compared to the compressible model. Fig. 1.7 presents the Mach number variation obtained from the compressible model with the maximum Mach number of 0.54.

Figures 1.8 and 1.9 show the numerical results for the axial temperature and Mach number variations, respectively, which correspond to Case 3 of the experimental data by Kemme (1969). The heat pipe was about 1.3 m long and 5.7 mm I.D. with a screen wrap type wick of thickness $\delta_l =$ 0.15 mm and stainless steel wall of thickness $\delta_w = $ 0.9 mm. Heat was added to the evaporator section of the heat pipe with an induction coil while the heat was removed from the condenser section by conduction through a gas gap to a water calorimeter. The effective thermal conductivity of the wick is calculated from Eq. (1.7). For this case, three different sets of experimental data of the outer wall temperature were obtained for subsonic, sonic and supersonic vapor flow in the sodium heat pipe. During the experiment, the heat input was fixed to 6.4 kW and the working temperature was decreased by changing the cooling condition so the choking condition could be reached.

For the present numerical analysis, the temperature at the end cap of the evaporator is fixed to the experimental value of 692^{0}C, and one steady-state solution is obtained with a Mach number of 1.0 at the exit of the adiabatic section as shown in Fig. 1.9 for the compressible model. The maximum Mach number of 1.09 was found in the inlet region of the condenser. Fig. 1.8 presents the experimental data of the wall temperature and the numerical solutions of the compressible and incompressible models. The present results of both models are in general agreement with Kemme's data
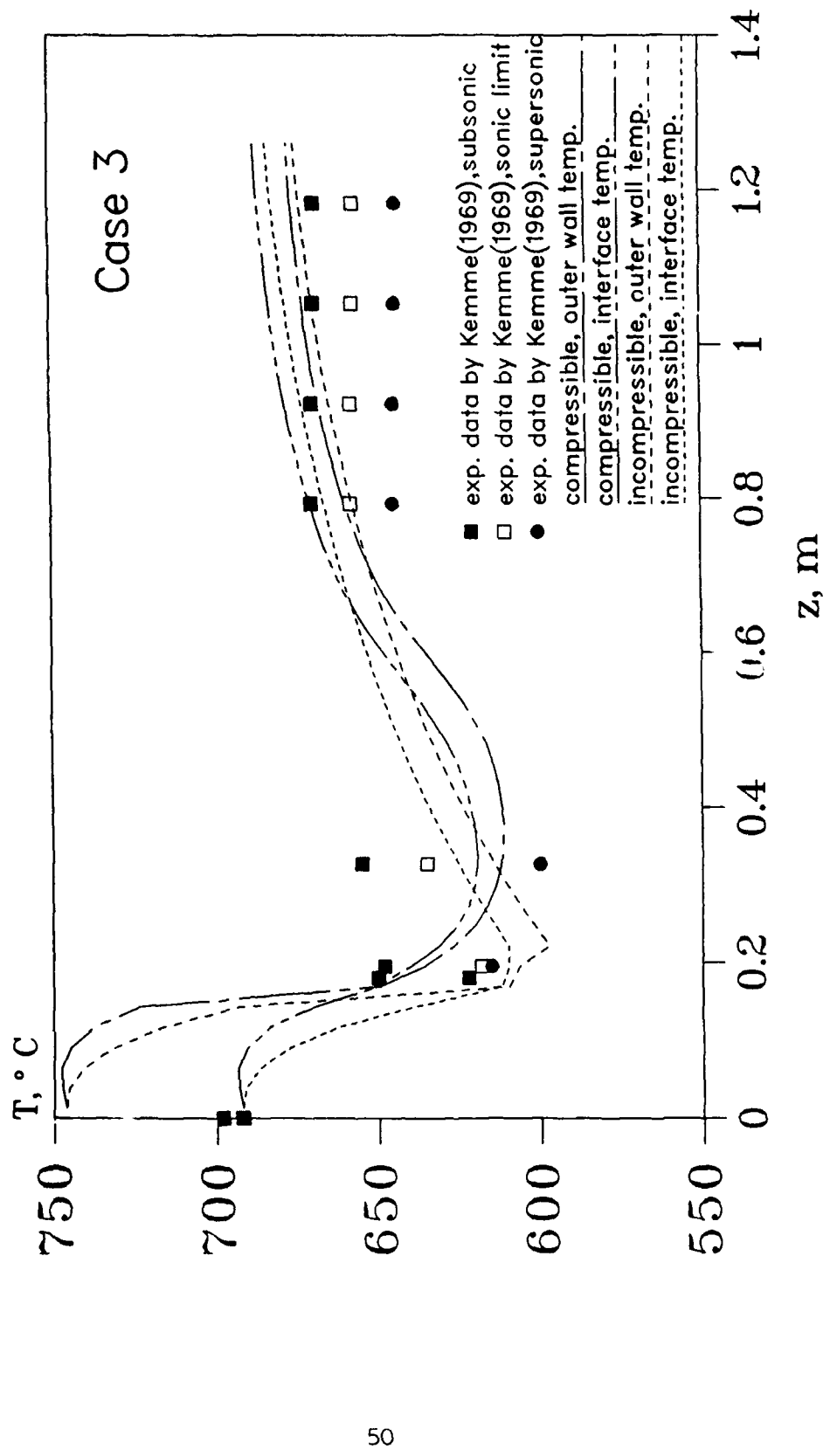
Fig. 1.8 The axial temperature profile along the sodium heat pipe with Q=6.4 KW, R_v=0.0057 m, L_e=0.143 m, L_a=0.06 m, L_c=1.08 m, k_l=59.5 W/m^2–K, k_s=19.0 W/m–K δ_l=0.00015 m, δ_w=0.0009 m
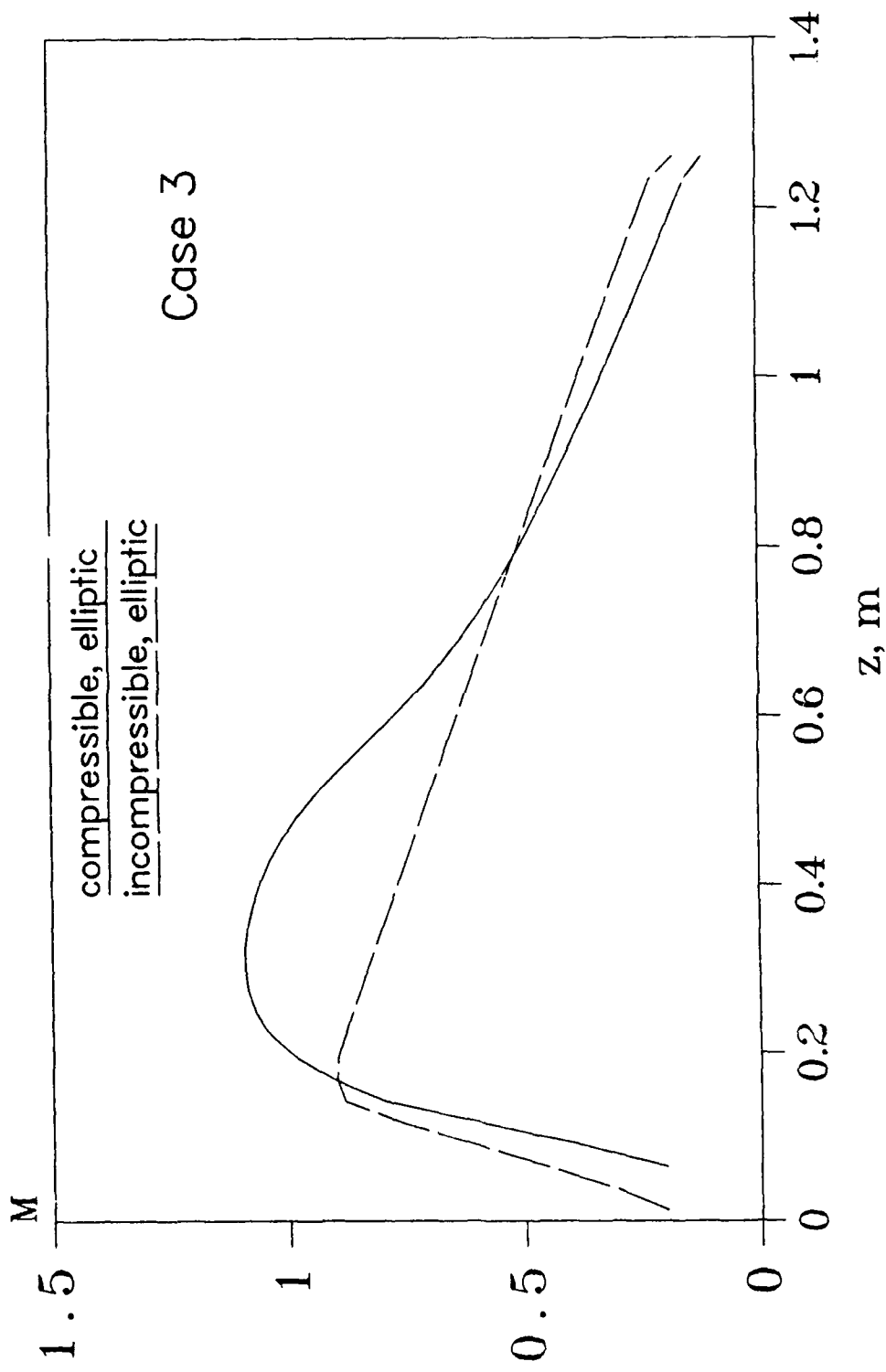
Fig. 1.9 The axial Mach number profile along the sodium heat pipe with Q=6.4 KW, R_v=0.0057 m, L_e=0.143 m, L_a=0.06 m, L_c=1.08 m k_l=59.5 W/m^2-K, k_s=19.0 W/m^2-K δ_l=0.00015 m, δ_w=0.0009 m

for the sonic limit case except that the condenser wall temperature is higher than the experimental data. This is probably because the condenser cooling may affect the accuracy of the thermocouple reading and makes the reading lower than the actual value. However, according to the comparison it seems that the present model can still predict the general trend of the heat pipe performance even if the Mach number of the vapor flow is high.

To further check the validity of the present numerical analysis, the code was also modified to predict the performance of the water heat pipe with multiple heat sources. The results were compared with the experimental data obtained by Gernert (1986). The experimental heat pipe under consideration had two evaporators and one condenser as illustrated in Fig. 1.10. The heat was provided at the evaporator by two electric heater blocks. The condenser section was fitted with a water cooled jacket. The heat pipe had a sintered powder wick and the effective thermal conductivity was calculated from the equation [Eq.(1.8)] proposed by Dunn and Reay (1982). A multipoint thermocouple was installed along the centerline of the vapor space to measure the variations of the vapor temperature. To measure the outer wall temperature, the outer wall of the evaporator and condenser sections were grooved, and thermocouples were soldered in the grooves to the pipe wall. According to the experimental conditions, two constant heat fluxes with heat inputs of 200 W and 800 W were specified at the two evaporator sections. For the condenser section, a constant heat flux based on the total heat input is also specified as a boundary condition for the numerical computation.
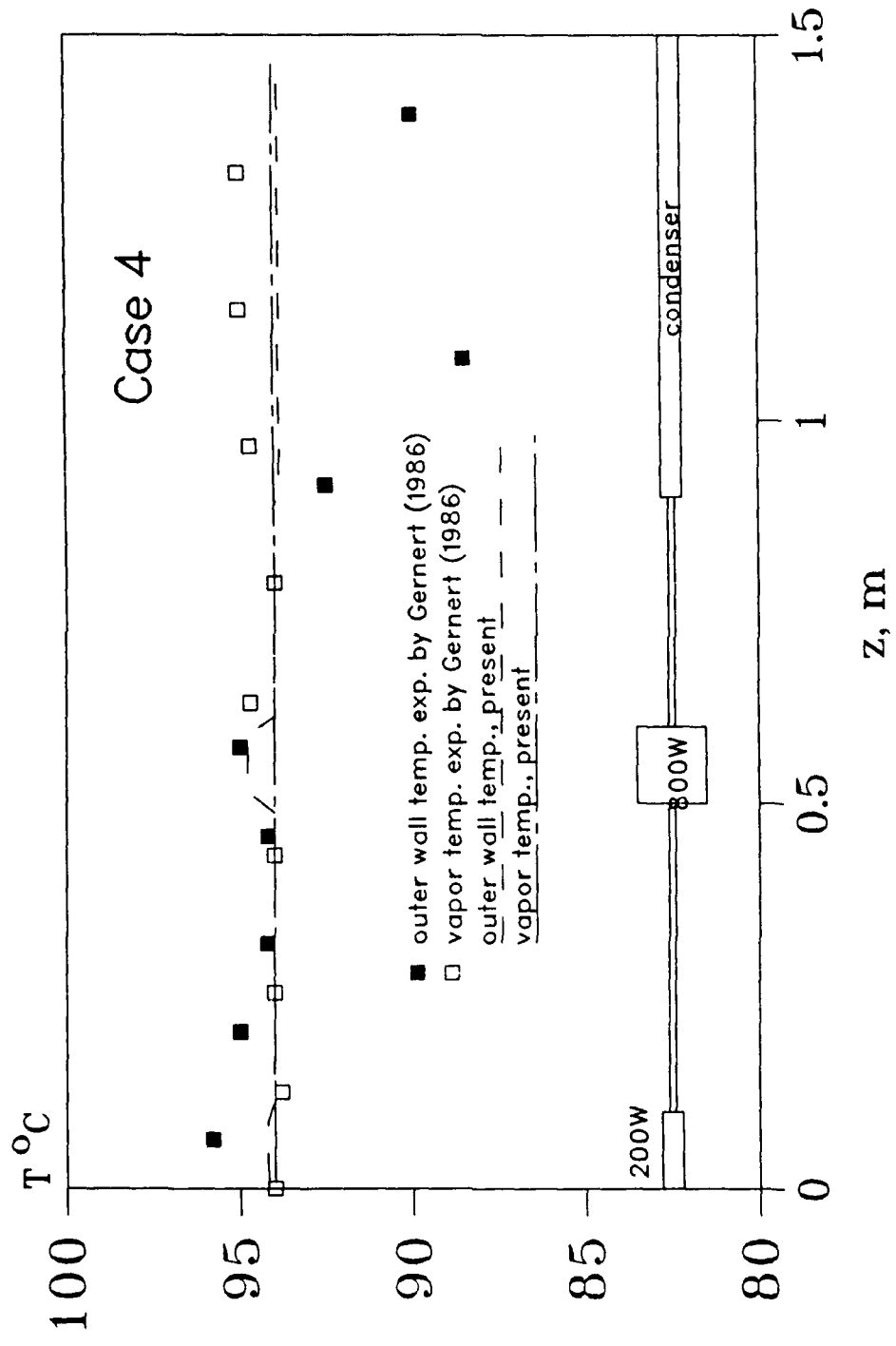
Fig. 1.10 The axial temperature profile along the water heat pipe
with multiple heat sources

Figure 1.10 shows the numerical results and the experimental data for the outer wall and the vapor temperature of the water heat pipe with multiple heat sources for Case 4. The present model gives a very uniform vapor temperature and a very small outer wall temperature variation. The measured vapor temperature is also fairly uniform with less than a $1^{0}C$ temperature difference along the pipe. The use of copper as the wall and wick materials and the sintered powder wick give a very good thermal conductivity, thus the radial temperature drop is very small through the wall and liquid-wick.

For the outer wall temperature, two experimental data points found in the adiabatic section and one in the 800 W evaporator are fairly close to the numerical solutions, but the temperature readings in the condenser section are almost $6^{0}C$ below the present predictions. Since the length of the condenser is much longer than that of the total length of the evaporator, the heat flux through the pipe wall of the condenser is smaller than that in the evaporator, which means that the heat flux through the pipe wall of the condenser is smaller than that in the evaporator with 800 W. Thus, it is expected to have a smaller temperature gradient through the pipe wall in the condenser section. It seems the measurements were not very accurate in the condenser section probably due to the influence of the cooling water on the thermocouple readings which resulted in the readings being lower than what is expected. Usually it is very difficult to measure the condenser and evaporator wall temperature because the cooling water may

lower the actual measurement while the heating may cause higher temperature readings. Furthermore, the accuracy of the thermocouple reading may also cause problems when the readings differ by only 1 or 2^{0}C.

Figure 1.11 shows the pressure variation along the vapor-liquid interface of the water heat pipe for Case 4. A very small pressure drop is noticed along the 200 W evaporator and the adjacent adiabatic section, but in the 800 W evaporator, the additional amount of heat flux causes more liquid to be evaporated into the vapor channel thus leading to a significant pressure drop along this section. In the condenser section, about 80% of the pressure drop is recovered. As the results show, the total pressure drop is very small which means that a very uniform vapor temperature profile can be obtained. The uniform temperature profile is a result of the thermodynamic equilibrium between the pressure and temperature at the liquid-vapor interface coupled with the fact that water has a high static vapor pressure and vapor density under normal working conditions. The phenomenon observed here is in general agreement with what is observed for a heat pipe with one evaporator section. We believe that the present model can predict the general performance of heat pipes with multiple heat sources and will also provide a guideline for future experiments in this respect.
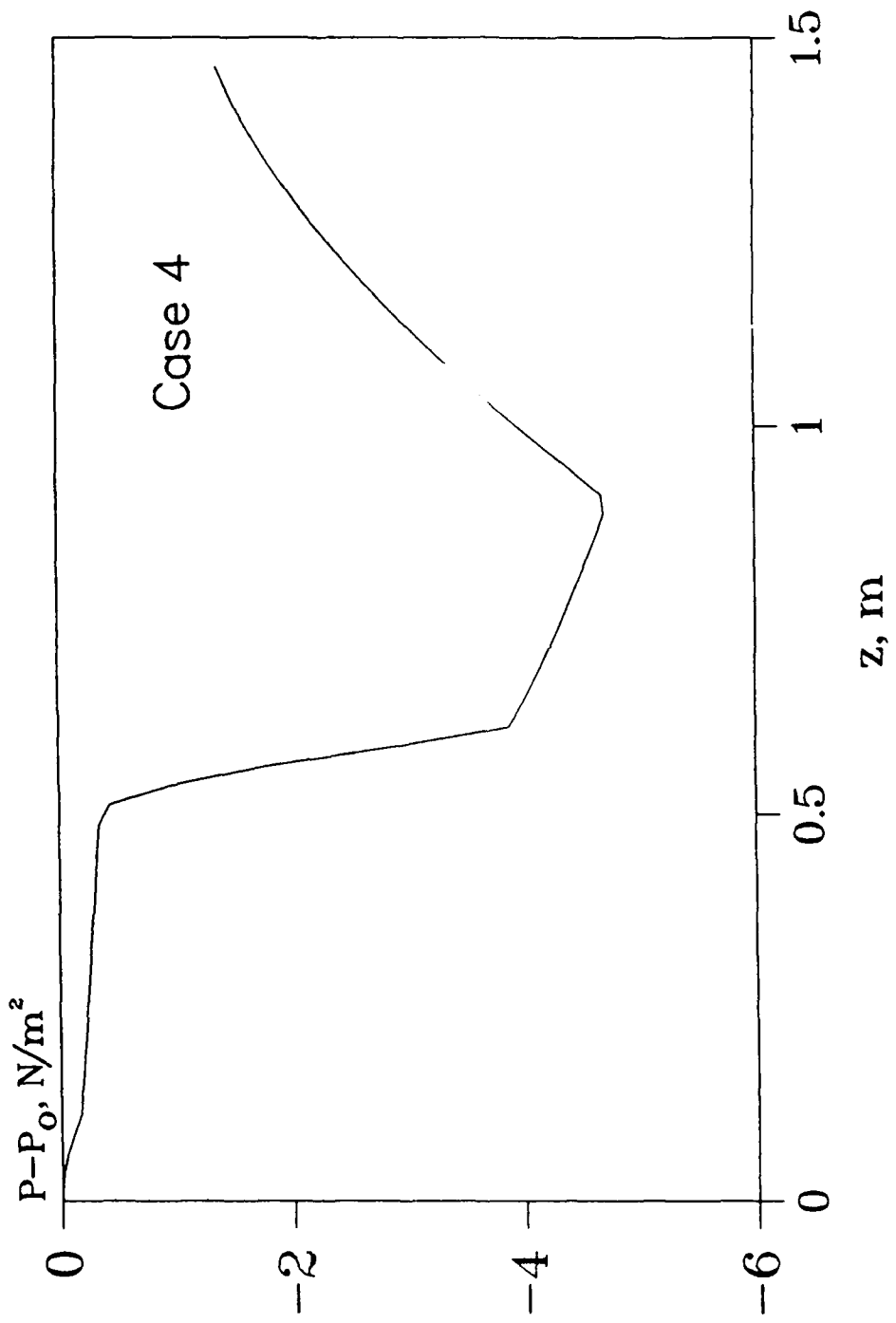
Fig. 1.11 The axial pressure profile along the vapor–liquid interface of the water heat pipe with multiple heat sources

Based on the comparisons of the present solutions with the experimental data, we believe that the present model can accurately predict heat pipe performance.

1.6 Parametric Analysis

The heat pipe under consideration for analysis in this section has an evaporator, adiabatic and condenser section each with a corresponding length of : L_e = 0.2 m, L_a = 0.1 m, L_c = 0.3 m. The dimensions of the pipe are vapor core radius R_v = 8.6 mm, wall thickness δ_w = 2 mm, liquid-wick thickness δ_l = 1.44 mm, total length L = 0.6 m. The wall and wick materials are assumed to be stainless steel with the screen wrap wick of porosity ϵ = 0.7. The cases presented in this section are listed in Table 1.6, and the corresponding properties are listed in Table 1.7. The properties are obtained at temperature T_0 and are assumed to be constant along the pipe. Since the radial Reynolds number along vapor-liquid interface changes, the average radial Reynolds numbers are calculated based on the total heat input at the outer wall of the heat pipe for the purpose of comparison, which are reported in Table 1.6. The heat input in the evaporator is chosen so that the Mach number has a wide range for the sodium heat pipe, and the total heat input is smaller than the heat pipe limits.

Table 1.6 Case Specifications for Parametric Analysis

Case no.	Working Fluid	Re_a	$Re_{r,e}$	$Re_{r,c}$	$Q(W)$	$T_0(^oC)$	$P_0(N/m^2)$
A	sodium	186	-2	1.33	213.4	535	1023
B	sodium	372.1	-4	2.67	426.7	535	1023
C	sodium	558.1	-6	4.0	640.2	535	1023
D	water	4419.0	-50	33.3	1647	100	101300

Table 1.7 Properties for Parametric Analysis

1. Sodium Heat Pipe (at $T_0 = 535^oC$)

$h_{fg}x10^{-6}$ (J/kg)	$\rho_v x10^2$ (kg/m^3)	$\mu_v x10^7$ (N·s/m^2)	c_{p_v} (J/kg-K)	k_s (W/m-K)	k_l (W/m-K)	$k_v x10^2$ (W/m-K)
4.237	3.713	207.5	2555	17.4	59.5	3.53

2. Water Heat Pipe (at $T_0 = 100^oC$)

$h_{fg}x10^{-6}$ (J/kg)	$\rho_v x10^2$ (kg/m^3)	$\mu_v x10^7$ (N·s/m^2)	c_{p_v} (J/kg-K)	k_s (W/m-K)	k_l (W/m-K)	$k_v x10^2$ (W/m-K)
2.257	59.77	120.3	2028	19	.685	2.479

1.6.1. Effect of Conjugate Axial Conduction

Table 1.8 shows the six cases which have been investigated for the conjugate heat transfer effect using the vapor properties of sodium. The property and parameter specifications needed for computation are the same as that of Case B (Table 1.6) except for the thermal conductivities and the wall and wick thicknesses. For all of the cases, the vapor thermal conductivity and vapor core radius are held constant, which are $k_v = 0.0353$ (W/m-K) and $R_v = 0.0086$ m.

Table 1.8 Case Specifications for Conjugate Effect Analysis

Case no.	K_{lv}	K_{wl}	Δ_1	Δ_w	Case No.	K_{lv}	K_{wl}	Δ_1	Δ_w
B	983.	0.69	0.084	0.116	B3	100	1000	0.1	0.1
B1	100	10	0.1	0.1	B4	100	10	0.2	0.2
B2	100	100	0.1	0.1	B5	100	10	0.01	0.01

Figures 1.12 and 1.13 show the effect of the thermal conductivity ratio K_{wl} on the performance of a sodium heat pipe with the pipe wall and liquid-wick dimensions held at $\Delta_w = \Delta_1 = 0.1$, $Re_{r,e} = -4.0$, and $K_{lv} = 100$. Fig. 1.12 presents the interfacial heat flux variation along the liquid-vapor interface with three different thermal conductivity ratios: $K_{wl} = 10, 100, 1000$ (Case B1, B2, B3). In addition, the solution for Case B is also presented. Fig. 1.13 shows the outer wall and interface temperature variations for the same cases. The effect of conjugate axial conduction becomes very significant as K_{wl} increases. When $K_{wl} = 10$, the results show a fairly uniform distribution of heat flux with the ratio
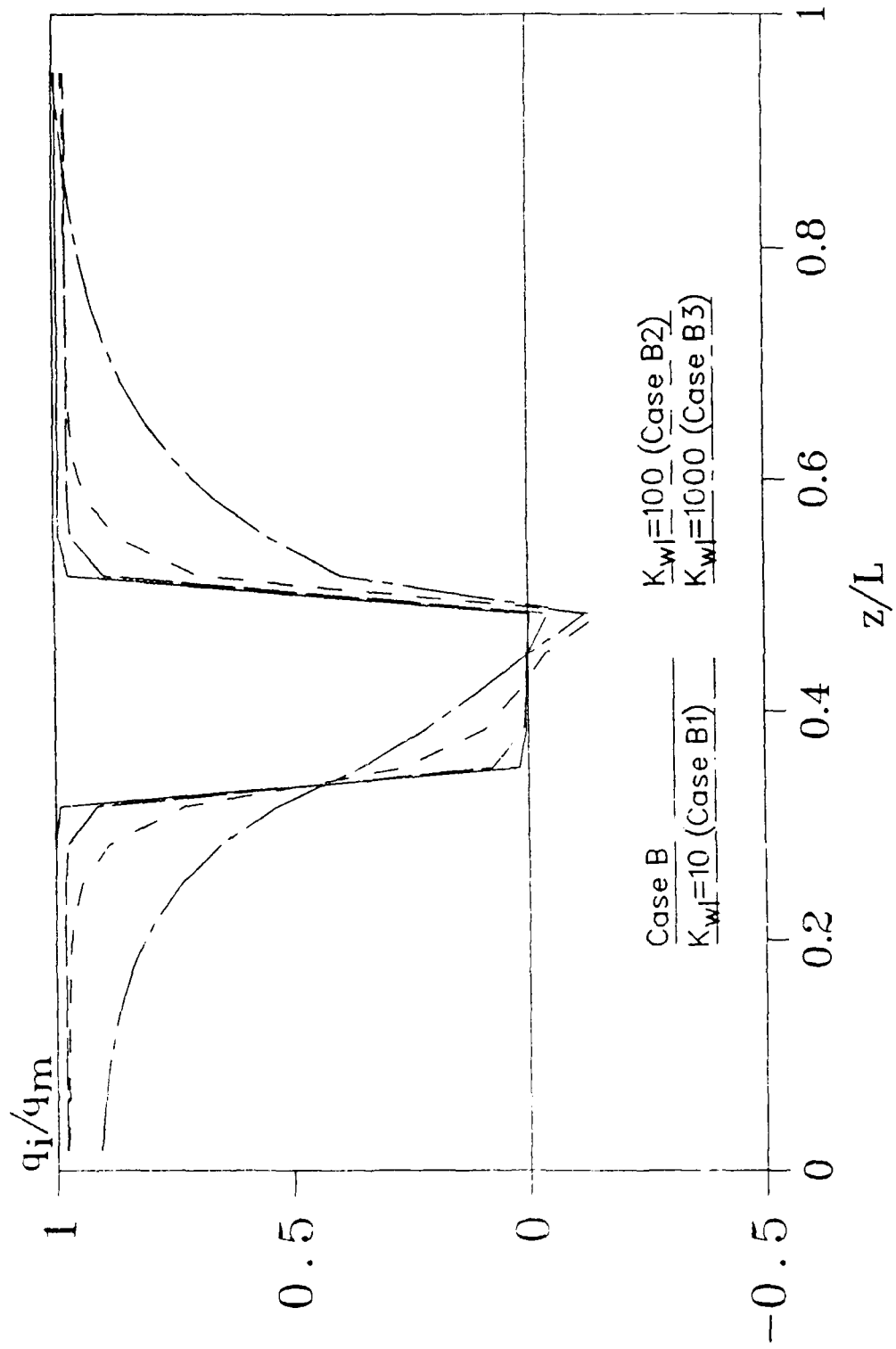
Fig. 1.12 The effect of the thermal conductivity ratio K_{wl} on the interfacial heat flux variations along the heat pipe with $Re_{r,e} = -4.0$
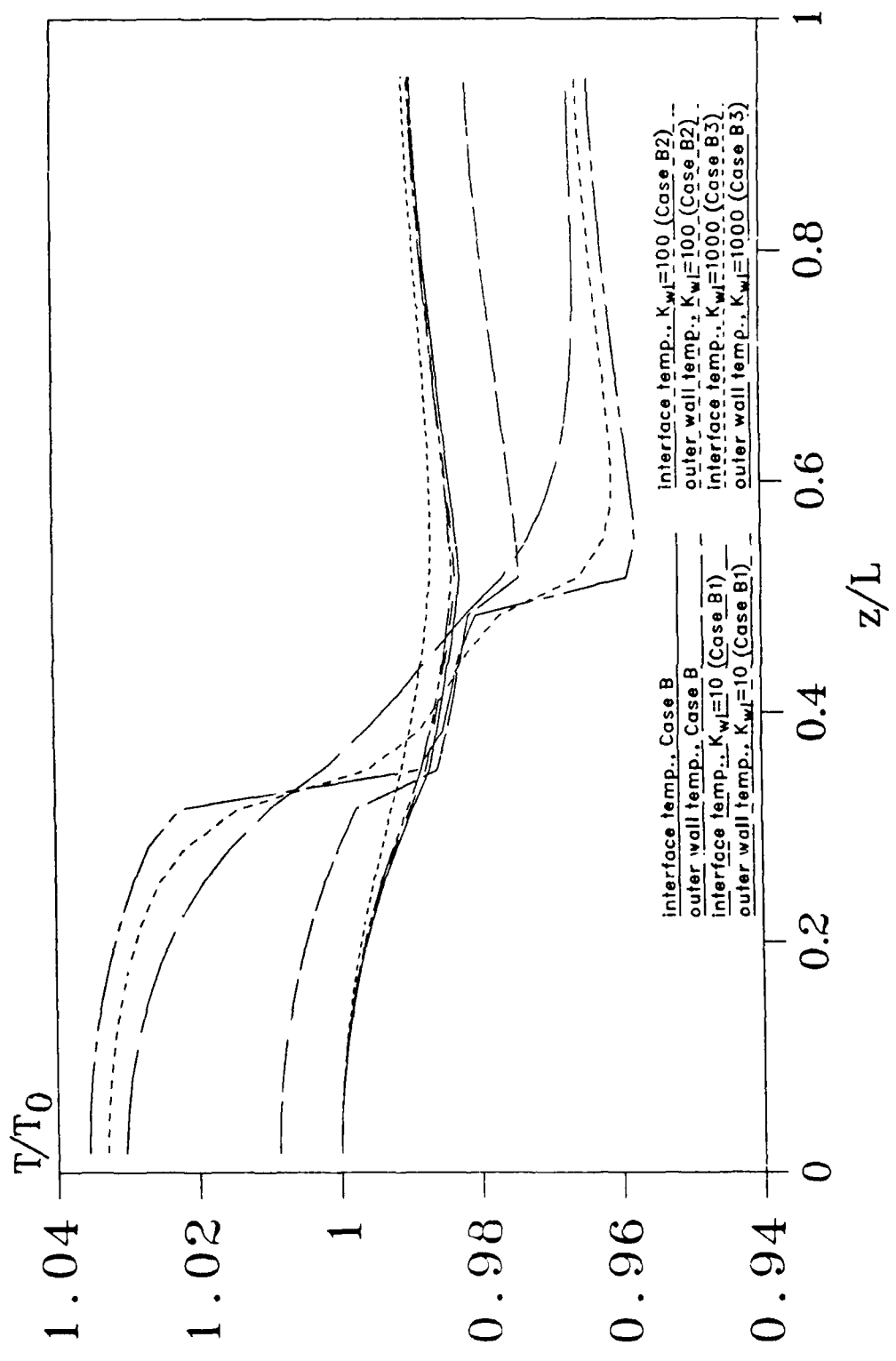
Fig. 1.13 The effect of the thermal conductivity ratio K on the axial temperature variation along the heat pipe with $\Delta_w = \Delta_l = 0.1$ and $Re_{r,e} = -4.0$

close to unity at both the evaporator and condenser, and zero in the adiabatic section. As K_{wl} increases, the results show that the conjugate effect makes the heat flux less uniform and the heat flux deviates from unity. The axial wall conduction in the evaporator tends to transfer the heat to the adiabatic section. Since the constant heat flux boundary condition is specified both at the outer wall of the evaporator and condenser, the interfacial heat flux in the evaporator becomes less than 1. In the condenser section, the heat is conducted from the evaporator, so that less heat flux is needed at the interface to satisfy the outer wall constant heat flux boundary condition. As the results show, the interfacial heat flux starts from a negative number at the end of the adiabatic section and gradually increases to unity at the end of the condenser. At $K_{wl} = 1000$, a significant variation of the interfacial heat flux can be noticed due to axial conduction. Obviously, the inclusion of axial wall and liquid-wick conduction is very important for this case. Also, the results for Case B are almost identical to this solution when no axial conduction is considered. Thus, the conjugate effect of this case can be excluded while discussing other effects.

The interfacial heat flux should be zero at the adiabatic section if there is no axial conduction, but because of the inclusion of axial conduction, the heat flux along the adiabatic section is no longer zero. Since the local q_m at the adiabatic section is zero, the q_m of the evaporator is used here for the calculation of q_i/q_m in the adiabatic section. The negative value of q_i/q_m in some regions of the adiabatic section is because the sign of q_i changes in the adiabatic section.

Actually, because of the axial conduction in the pipe, the region of the adiabatic section near the condenser acts as part of the condenser, likewise the region adjacent to the evaporator acts as part of the evaporator. Only one point in the adiabatic section is truly adiabatic.

For $K_{wl} = 1000$, the interface temperature distribution becomes more uniform and correspondingly, the outer wall temperature varies more smoothly as shown in Fig. 1.13. Therefore, it is always beneficial to have a large K_{wl} for better heat pipe performance.

Figures 1.14 and 1.15 show the effect of the wall and liquid-wick thicknesses on the heat pipe performance. Three different thicknesses $\Delta_w = \Delta_l = 0.2, 0.1, 0.01$ (Case B4, B1, B5) were chosen with $K_{lv} = 100$, $K_{wl} = 10$ and $Re_{r,e} = -4.0$. Fig. 1.14 presents the heat flux variation along the liquid-vapor interface. When the thickness is very small $(\Delta_w = \Delta_l = 0.01)$, the results show that the heat flux at both the evaporator and condenser almost equals unity which means the axial conduction is insignificant. As Δ increases, the effect of axial conduction becomes more pronounced. Fig. 1.15 gives the interface and outer wall temperature distribution. The outer wall temperature should be equal to the interface temperature at the adiabatic section if there is no axial conduction, but as the results show, there is a temperature difference for the cases presented and the case $\Delta_w = \Delta_l = 0.2$ has the largest difference. However, no significant effect of axial conduction is noticed within the range presented. It is confirmed here that for small values of Δ, the axial heat conduction through the wall and liquid-wick can be neglected because the results approach that of a constant heat flux at the interface. It is also interesting to note that

64
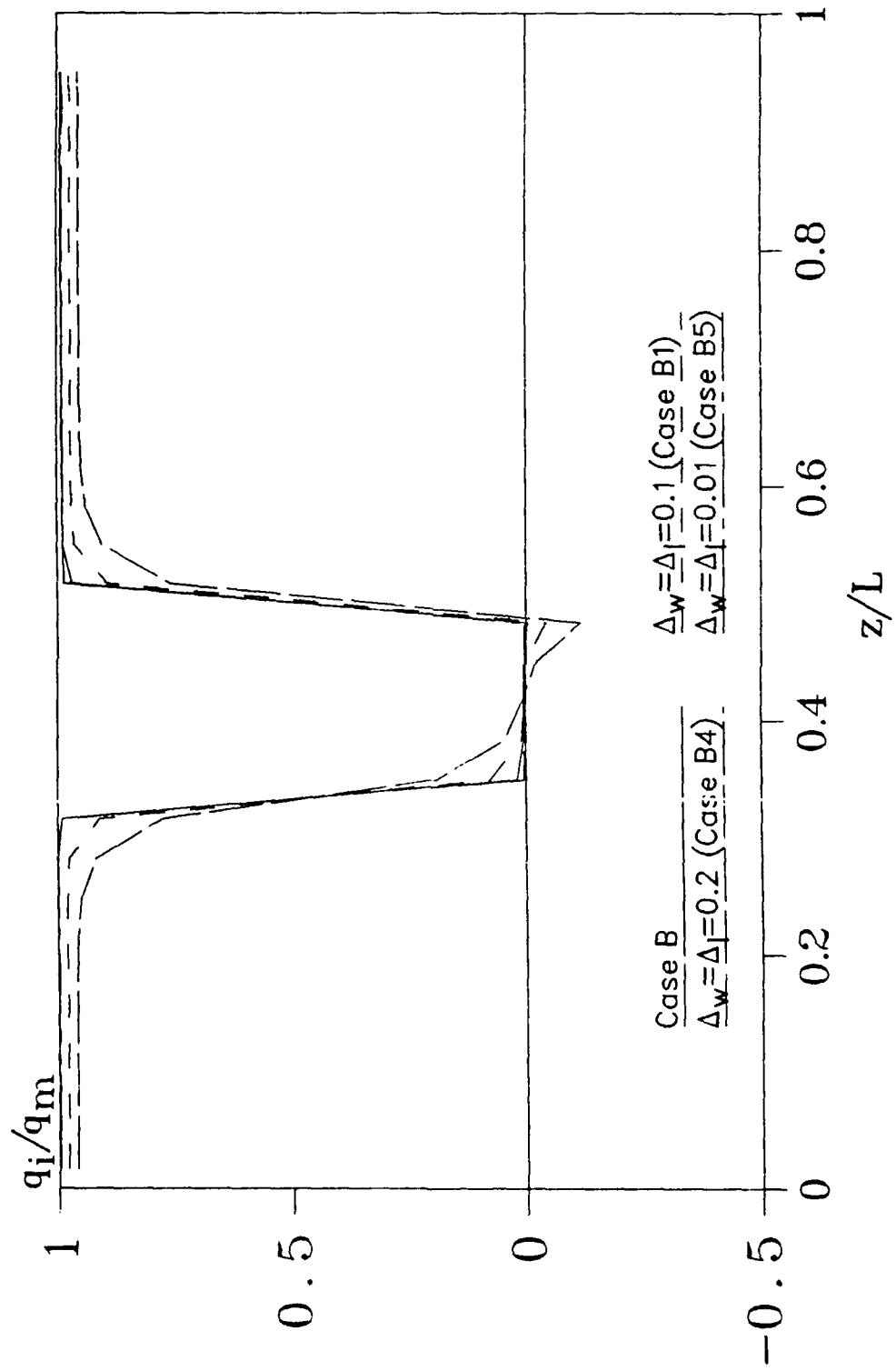
Fig. 1.14 The effect of the wall and liquid-wick thickness on the interfacial heat flux variation along the heat pipe with $Re_{r,e}=-4.0$
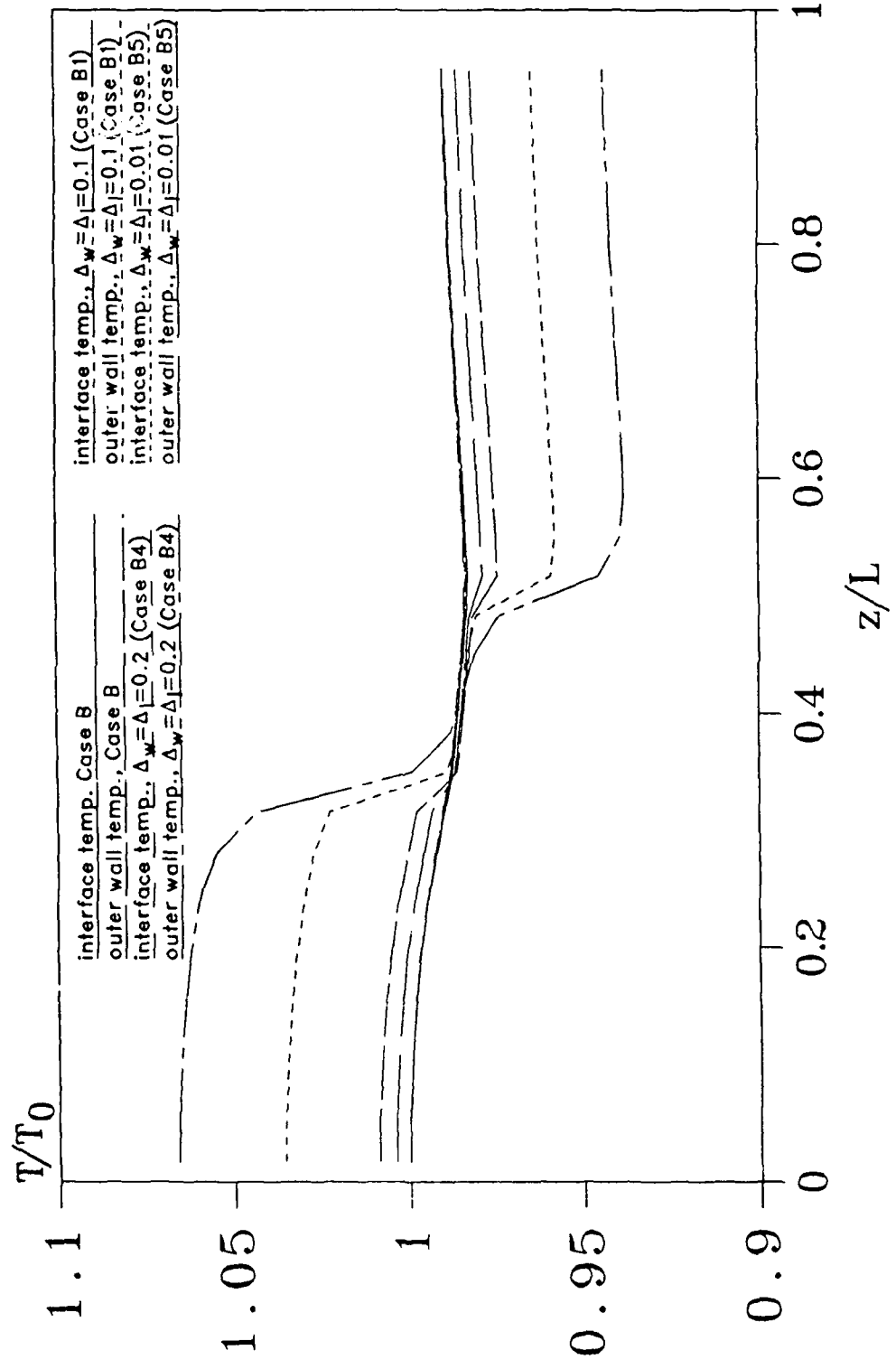
Fig. 1.15 The effect of the wall and liquid–wick thickness on the axial temperature variation along the heat pipe with $Re_{r,e} = -4.0$

the outer wall temperature in the middle of the adiabatic section is fairly close to the vapor temperature, which is a common practice to estimate the vapor temperature by measuring the outer wall temperature in the middle of the adiabatic section.

1.6.2 Effect of Vapor Compressibility

Figures 1.16 through 1.18 show the effect of compressibility on the sodium heat pipe vapor flow. Figure 1.16 gives the pressure variations along the liquid-vapor interface for three different vapor flow models: the present compressible and incompressible results, as well as the incompressible similarity solution by Faghri (1988). We found that the results for the incompressible similarity solution and the present incompressible numerical analysis are very close. The maximum deviations are less than 6% for all three cases presented. The comparison between the compressible and incompressible models shows a large deviation for the case of $Re_{r,e} = -6.0$ (Case C), which is about 24% at the inlet of the condenser. The maximum deviations for the case of $Re_{r,e} = -4.0$ (Case B) and $Re_{r,e} = -2.0$ (Case A) are about 11% and 3%, respectively, with very small deviations at the end of the condenser. Therefore, the compressibility of the vapor does not have a significant effect on the total vapor pressure drop.

The outer wall temperature uniformity is the major concern for heat pipe users and is easy to measure experimentally. The outer wall
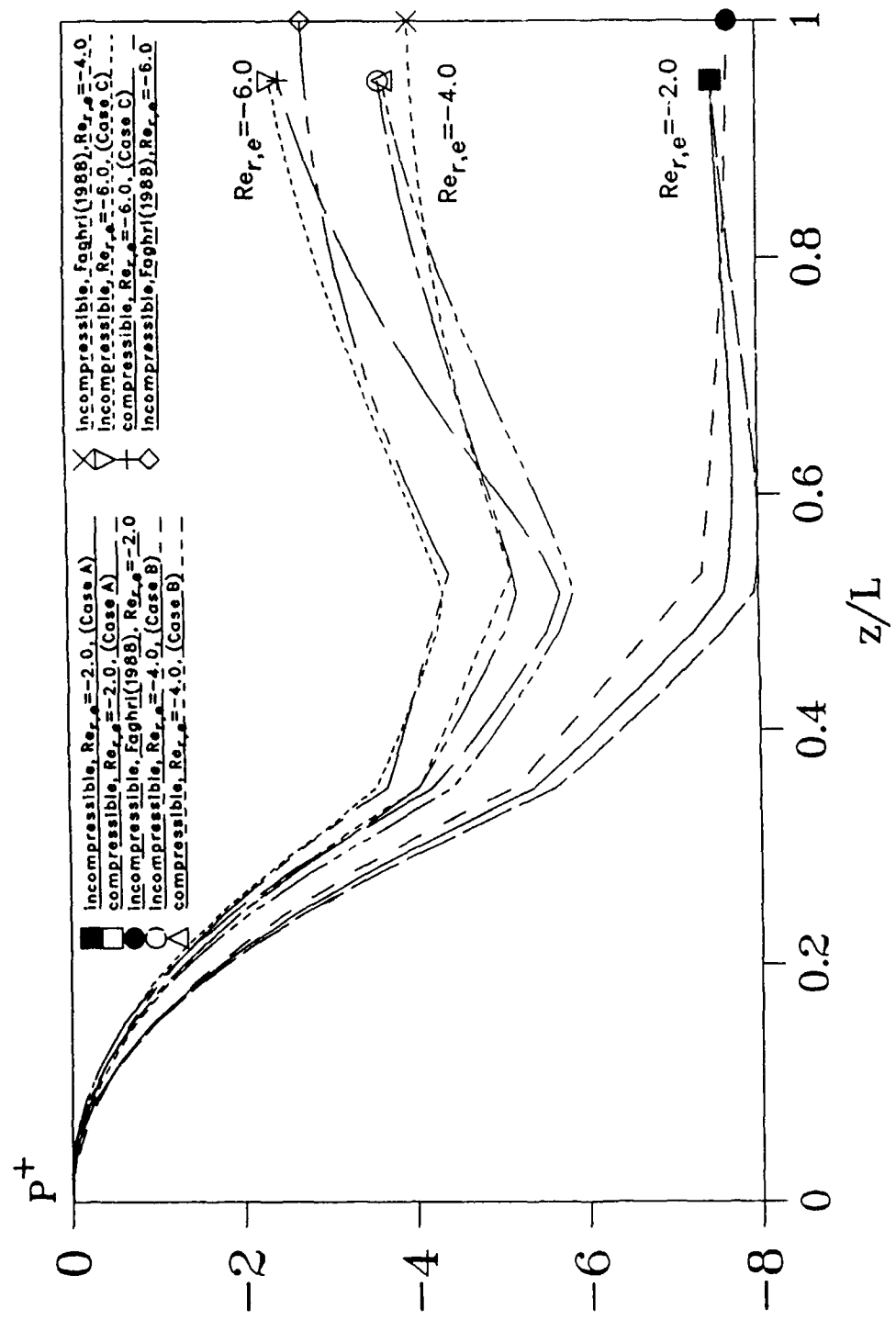
Fig. 1.16 The effect of compressibility on the axial pressure profile along the sodium heat pipe vapor–liquid interface
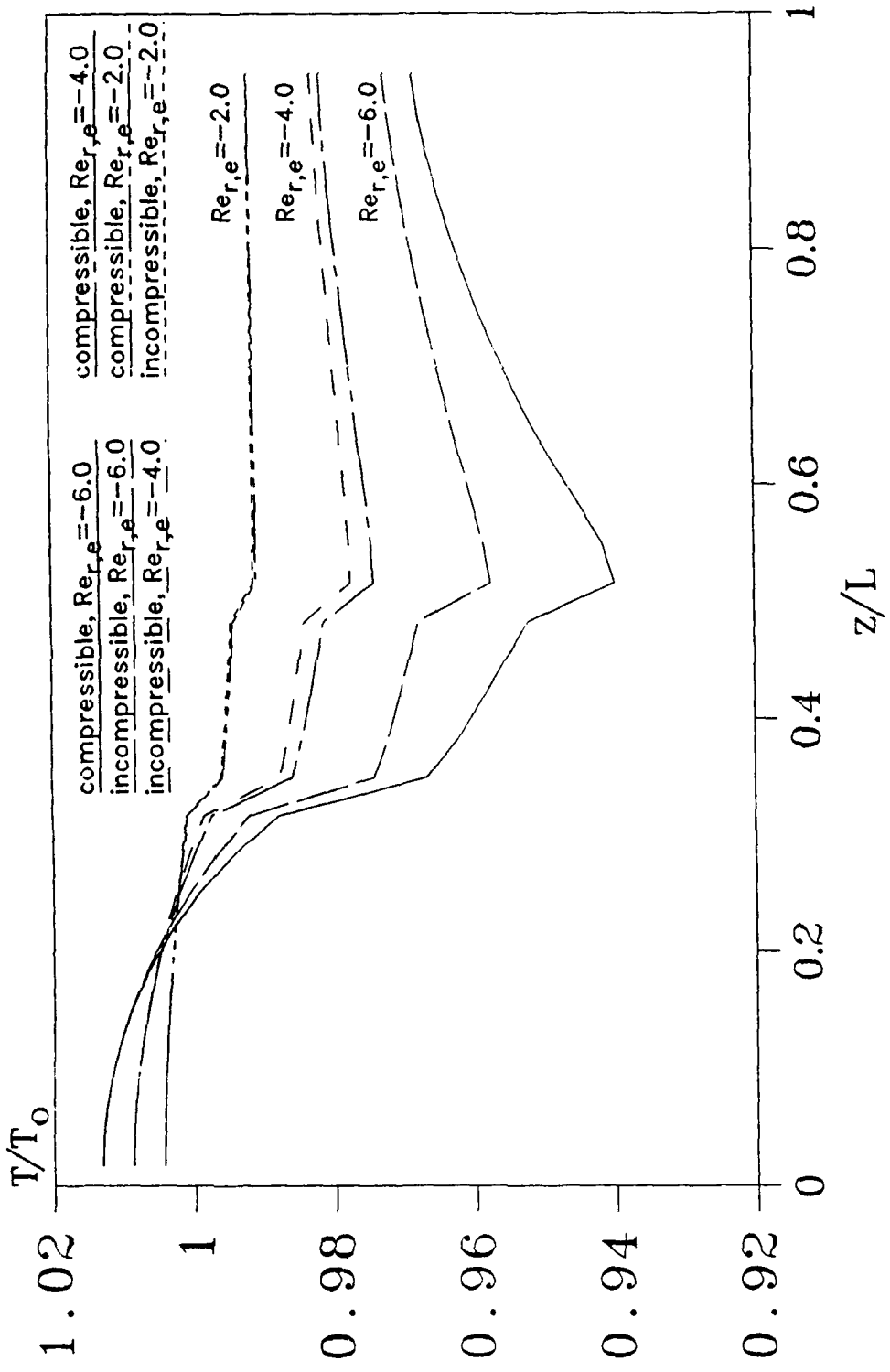
Fig. 1.17 The effect of compressibility on the outer wall temperature
variation along the sodium heat pipe
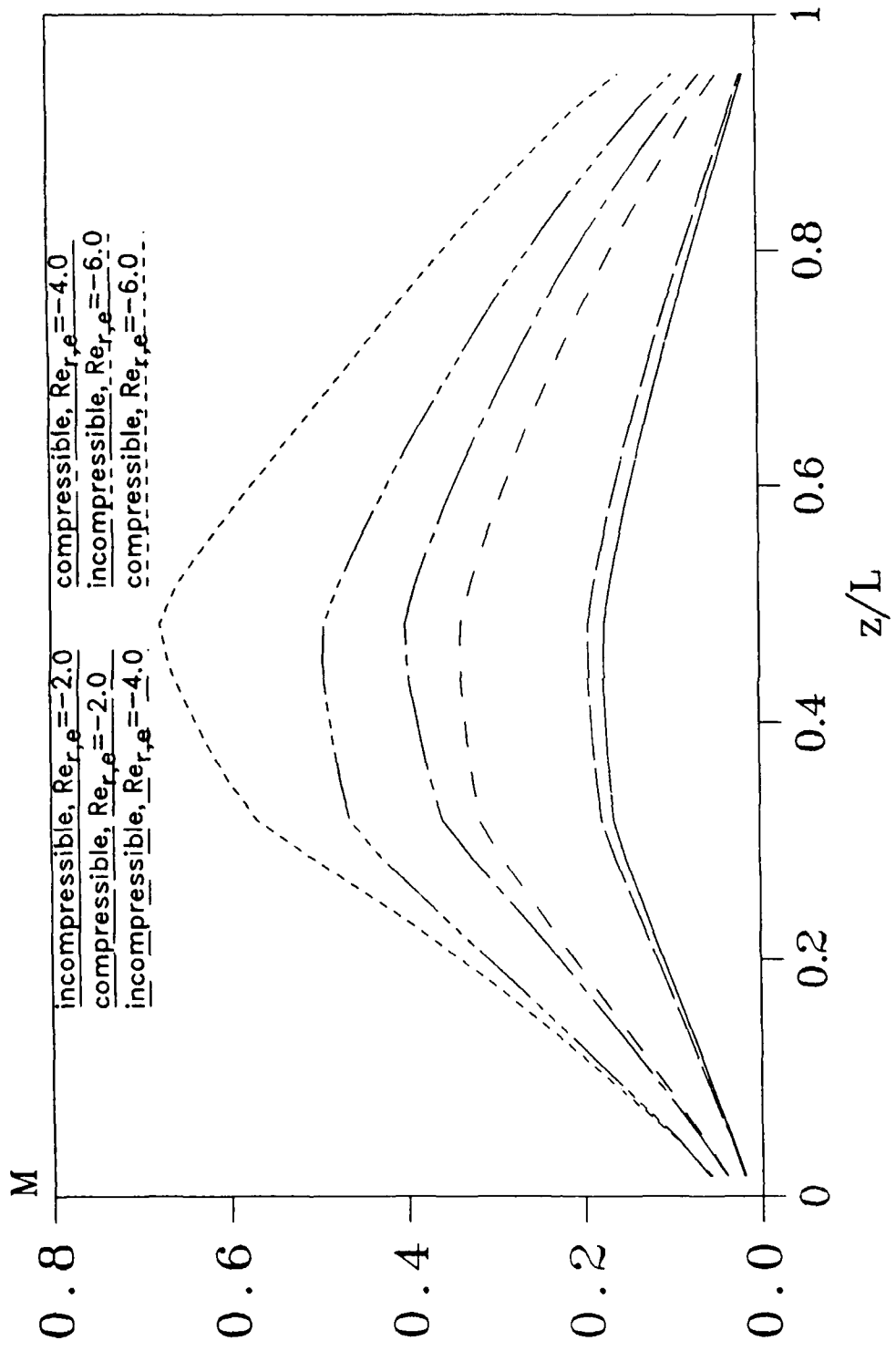
Fig. 1.18 The effect of compressibility on the axial Mach number variation along the centerline of the sodium heat pipe

Legend:
incompressible, $Re_{r,e} = -2.0$
compressible, $Re_{r,e} = -2.0$
incompressible, $Re_{r,e} = -4.0$
compressible, $Re_{r,e} = -4.0$
incompressible, $Re_{r,e} = -6.0$
compressible, $Re_{r,e} = -6.0$

Axes:
M (vertical axis, 0.0 to 0.8)
z/L (horizontal axis, 0 to 1)

temperature distribution is thus presented here in Fig. 1.17 to see the effect of compressibility. As the results show, a significant deviation exists between the compressible and incompressible models for the case of $Re_{r,e} = -6.0$ (Case C). The incompressible model gives a more uniform temperature profile than that of the compressible model. For the case of $T_0 = 535^0C$, the largest deviation of these two models is about 10^0C. The deviations are less significant for the results of $Re_{r,e} = -4.0$ (Case B) and $Re_{r,e} = -2.0$ (Case A).

Since the Mach number is a measure of the effect of the vapor compressibility, the variation of the Mach number, M, along the centerline of the pipe is shown in Fig. 1.18. The compressibility effect is important when M > 0.3 and is verified here from the present numerical results of the heat pipe analysis. We know from the case of $Re_{r,e} = -6.0$ (Case C) that when the Mach number is less than 0.2, very small deviations are noticed, but when M > 0.3, the deviation becomes significant. The maximum deviation of about 24% occurs at the exit of the adiabatic section with M=0.66. Comparing Fig. 1.18 with Figs. 1.16 and 1.17, we notice that the deviation of the models for the pressure and temperature variations correspond to the Mach number variation. As the Mach number increases, the deviation between the compressible and incompressible results increases.

Figures 1.19 and 1.20 show the effect of compressibility on the water heat pipe vapor flow (Case D). A comparatively large radial Reynolds number, $Re_{r,e} = -50$, is chosen to see the compressibility effect. Fig. 1.19 presents the pressure variation along the vapor-liquid interface for the compressible and incompressible models. The profiles almost overlap
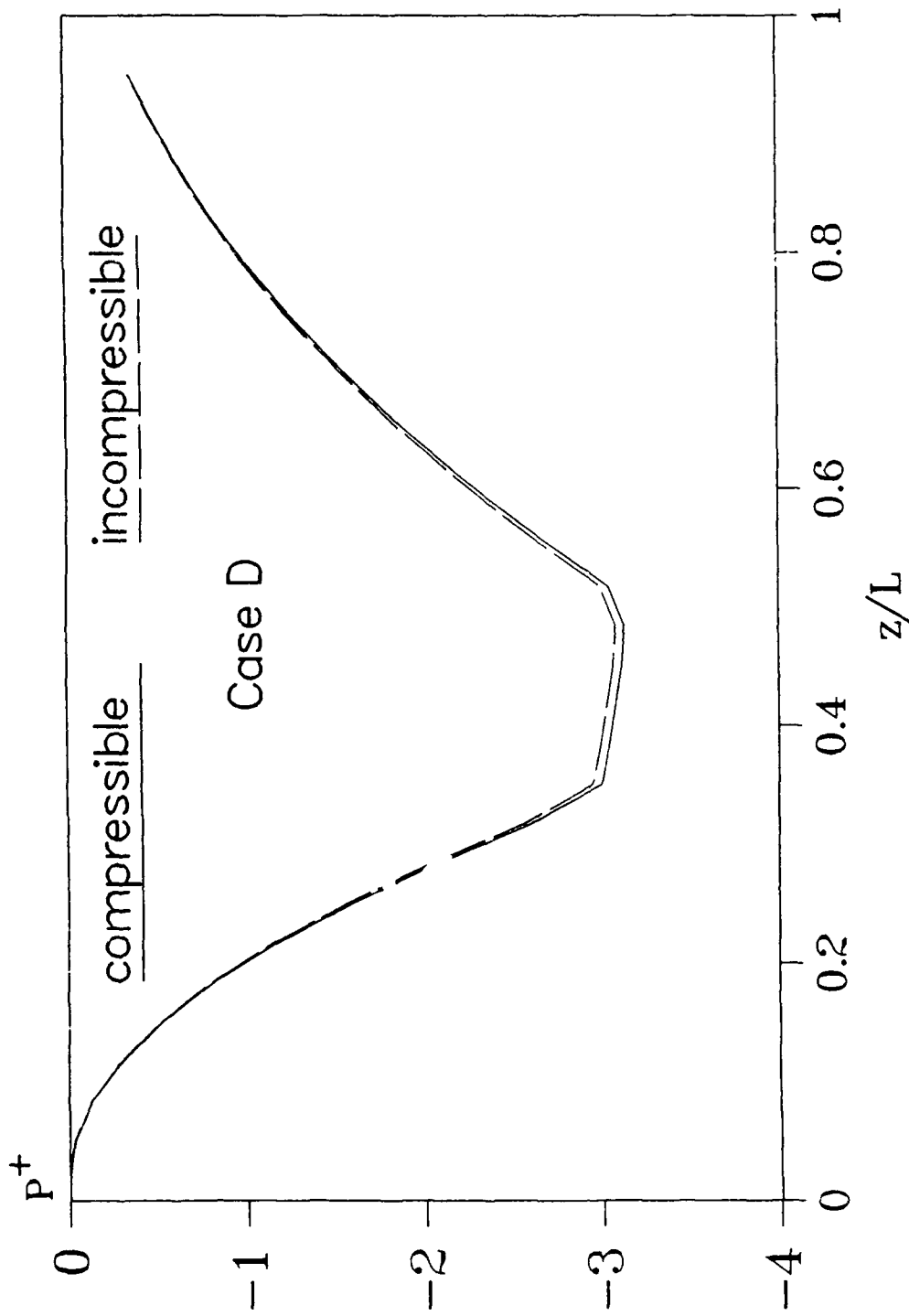
Fig. 1.19 The effect of the vapor compressibility on the axial pressure profile along the vapor–liquid interface of the water heat pipe
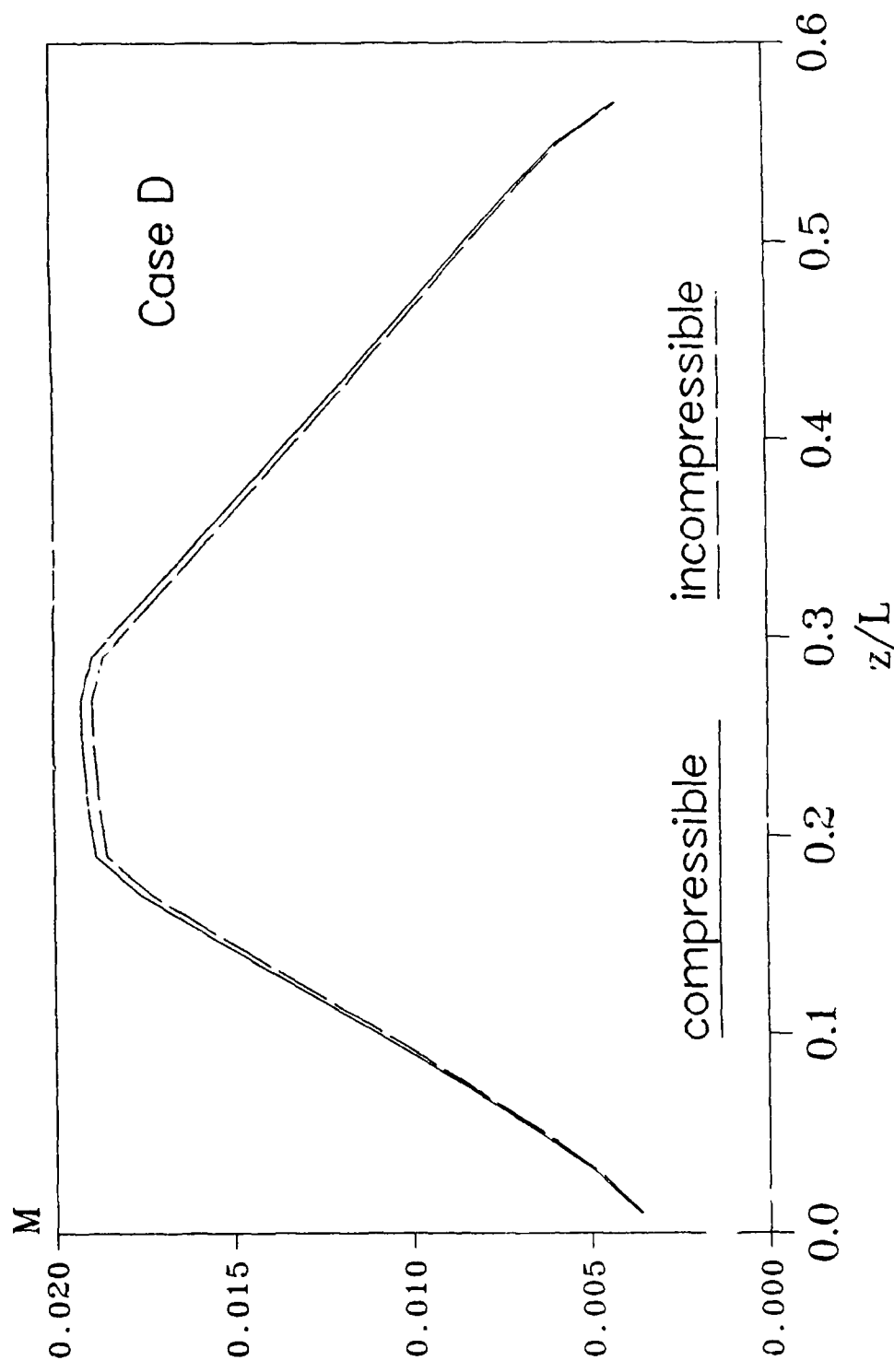
Fig. 1.20 The effect of the vapor compressibility on the Mach number variation along the centerline of the water heat pipe

along the evaporator and condenser sections with only a very small deviation of less than 1.5% in the adiabatic section. Fig. 1.20 shows the Mach number variation along the centerline of the vapor space. It shows that the maximum Mach number is only about 0.018 and the results for both cases are very close to each other. This is because for water as the working fluid, the vapor density is much greater than that of sodium vapor, so the vapor velocity is much smaller for the water heat pipe for a given heat input. Actually, Case D has a fairly high heat transfer rate, but the Mach number is still very small. Thus we concluded that the effect of vapor compressibility is not important for heat pipes using water as a working fluid.

1.6.3. Pressure Recovery and Flow Reversal

The pressure of the vapor in the evaporator decreases along the path of the vapor stream because of friction and acceleration of the flow as a result of the injection of vapor. In the condenser section, the extraction of mass leads to a deceleration of the flow, i.e., to an increase in pressure, while friction lowers the pressure of the vapor. The variation of pressure in the condenser section can be different, depending on the ratio of effects of friction and inertia. The results in Fig. 1.16 show that the extent of the pressure recovery increases as the condenser radial Reynolds number increases. For the case with $Re_{r,c} = 1.33$ (Case A), almost no pressure recovery can be noticed. This is a result of the viscous effect dominating with the small radial Reynolds number. For $Re_{r,c} = 2.67$ (Case B) and $Re_{r,c} = 4$ (Case C), the pressure recovery is approximately 35% and 55%, respectively. Fig. 1.19 shows a large pressure recovery in the

condenser section for the heat pipe using water as a working fluid (Case D). Up to 90% of the pressure drop in the evaporator and adiabatic sections were recovered at the end of the condenser.

We also found that flow reversal takes place in the condenser region when the pressure recovery is significant. Flow reversal was not found for the case of $Re_{r,c}$ = 1.33 (Case A), and a very slight amount of flow reversal at the end of condenser was noticed for $Re_{r,c}$ = 2.67 (Case B), which is in agreement with what Bankston and Smith (1973) observed. The dimensionless axial velocity profile for $Re_{r,c}$ = 4.0 at three different axial locations is plotted in Fig. 1.21. It shows clearly that the velocity in the condenser section is more extruded and flow reversal occurs near the wall region. Also, we found for water as the working fluid, a larger $Re_{r,c}$ compared with sodium as the working fluid has to be specified to get flow reversal. So for different working fluids, the starting point for flow reversal will depend on different $Re_{r,c}$ values.

1.6.4. Effect of Viscous Dissipation

The viscous dissipation term in the energy equation is included in the present analysis. We intend here to see the effect of this term on the sodium heat pipe vapor flow. For metallic working fluids, the density is extremely small at low vapor pressures and even for a relatively small heat transfer rate, the vapor velocity in the axial direction can be very large. The results presented in this section correspond to Case B in Table 1.6 for the compressible and incompressible models. Fig. 1.22 shows the axial dimensionless velocity profile in the radial direction at three different

75
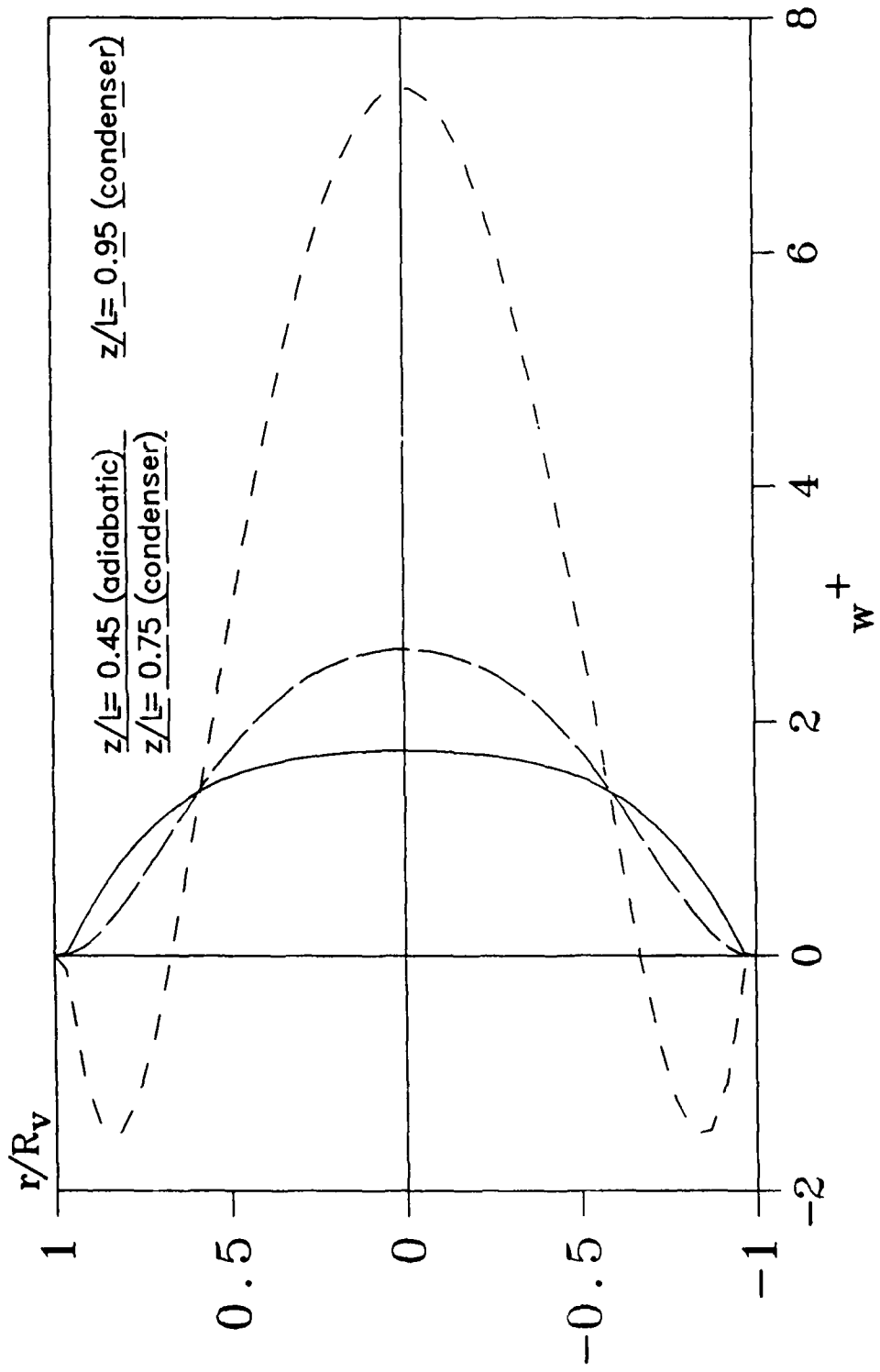
Fig. 1.21 The axial velocity profile at different axial locations of the compressible sodium heat pipe vapor flow with $Re_{r,e}=-6.0$ (Case C)
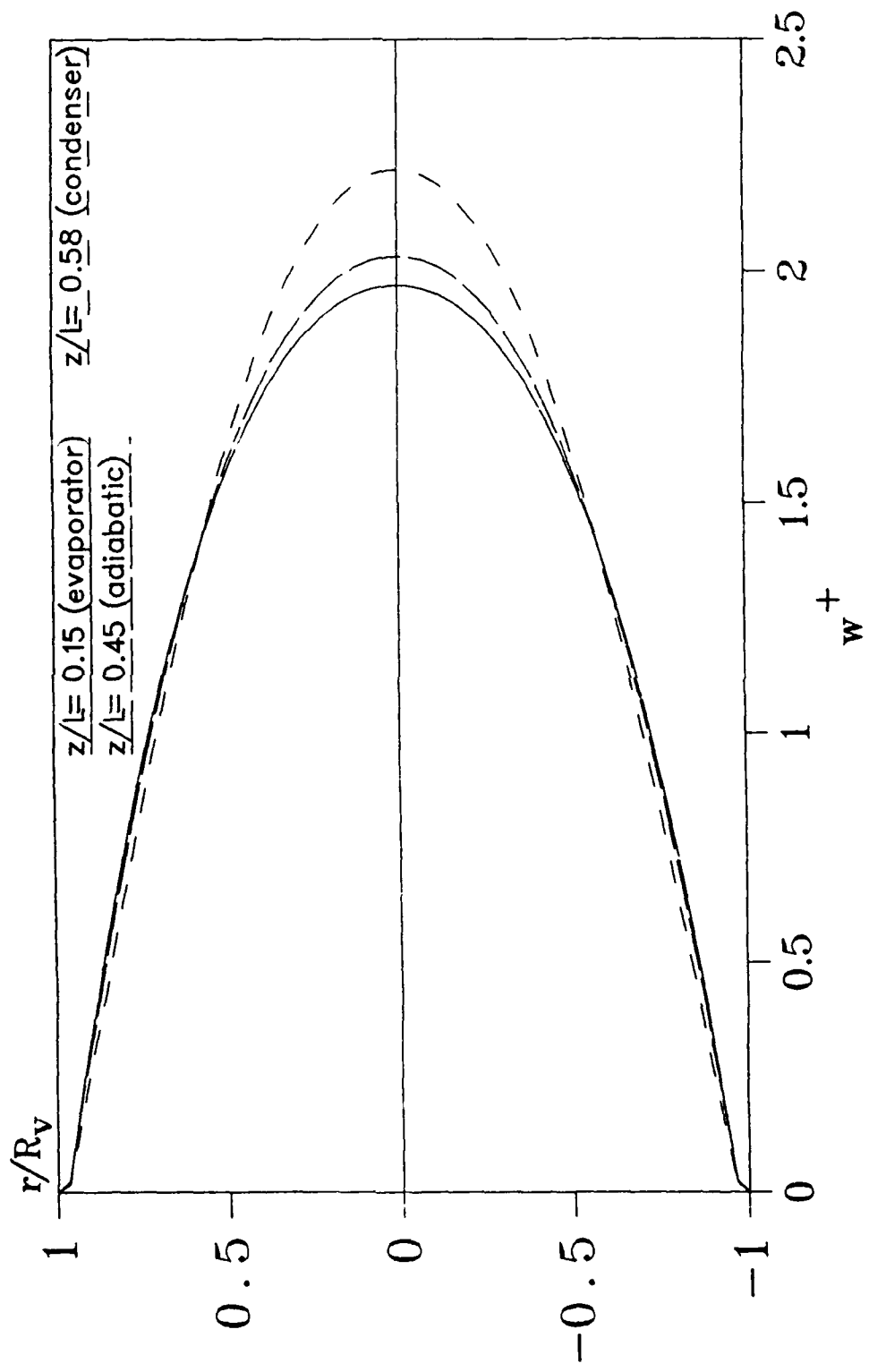
Fig. 122 The dimensionless axial velocity profile at different axial locations for the incompressible sodium heat pipe vapor flow with $Re_{r,e} = -4.0$ (Case B)

locations for Case B of the incompressible flow. Only the case with viscous dissipation is presented in this figure since the cases with and without viscous dissipation are almost identical. Since the dominant term in the viscous dissipation ϕ of Eq. (1.2.4) is $(\partial w_v/\partial r)^2$, it is helpful to have a velocity profile for discussion. From Fig. 1.22 the axial velocity profile in the evaporator is very close to that in the adiabatic section; this means that the velocity is nearly fully developed in the evaporator and adiabatic regions. In the condenser region, however, the mass extraction makes the profile extruded, which means that it has a larger velocity variation in the radial direction which had also been observed by Busse (1987a).

Figure 1.23 shows the effect of viscous dissipation on the radial temperature variation at three different axial locations for incompressible vapor flow in the sodium heat pipe for Case B. The temperature variations in the liquid-wick and wall regions are also presented in this figure. Fig. 1.23 also shows that the viscous dissipation can change the radial temperature distribution significantly. In the beginning of the evaporator, the two temperature curves are quite close, but in the adiabatic and condenser regions, the temperature difference between the curves which include and do not include viscous dissipation are much larger. For this particular case with $T_0 = 535^{\circ}C$, it can be as much as $8^{\circ}C$ difference. Also, the viscous dissipation term increases the temperature more near the wall because of the larger velocity gradient, as shown in Fig. 1.22.
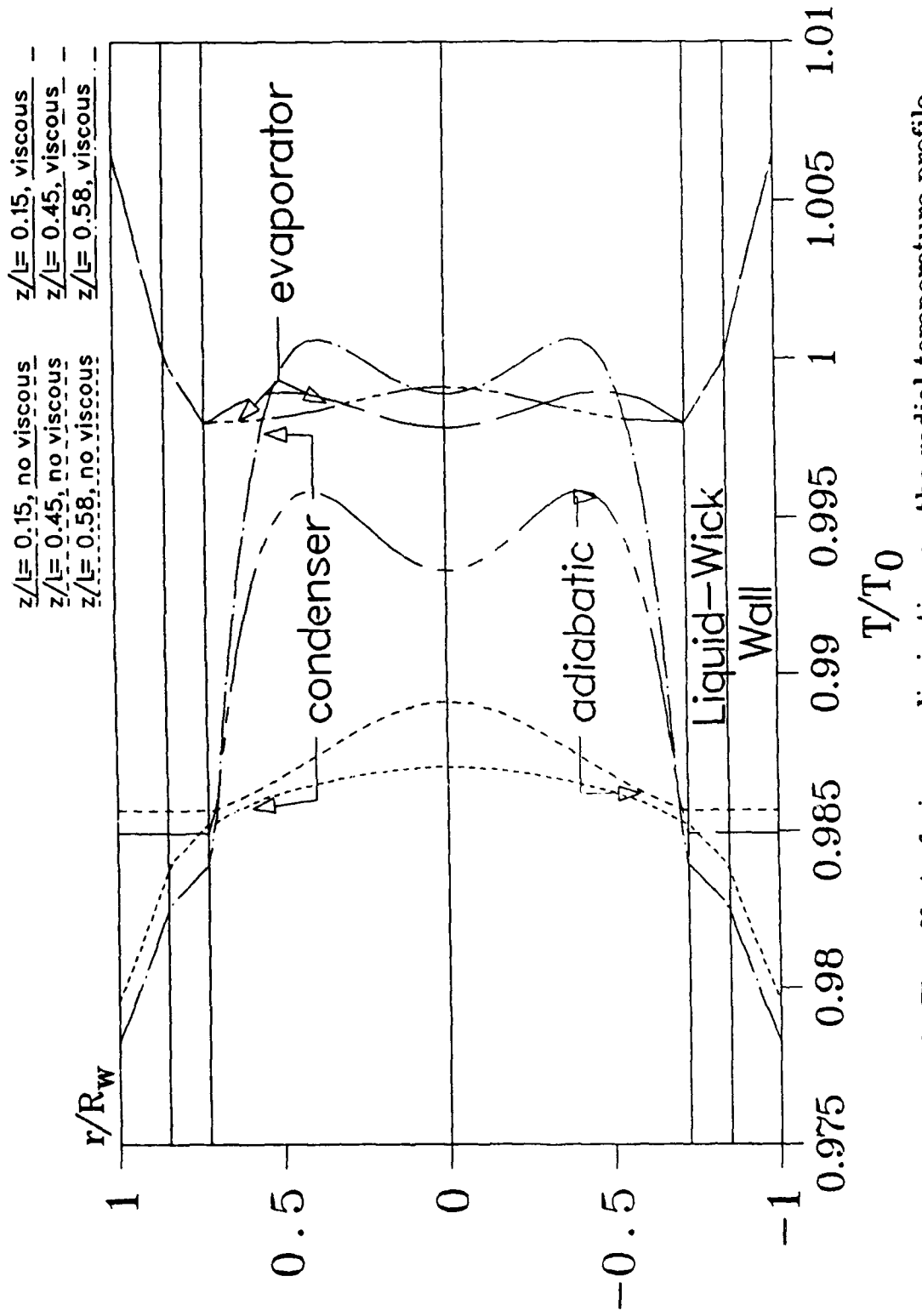
Fig. 1.23 The effect of viscous dissipation on the radial temperature profile at different axial locations for the incompressible sodium heat pipe vapor flow with $Re_{r,e} = -4.0$ (Case B)

Figure 1.24 presents the effect of viscous dissipation on the axial temperature variation. In PHOENICS, only the viscous dissipation term for incompressible flow can be controlled using one command. This is because another term DP/Dt is also involved in the same command for the compressible flow model. We cannot deactivate the viscous term alone. Therefore, the results are discussed based on the incompressible flow model, but the results with viscous dissipation for the compressible model are also presented for the axial temperature variations. The figure shows that for incompressible flow, the interface temperature almost remains the same both with and without the viscous dissipation terms. However, a large difference exists in the vapor temperature along the centerline of the pipe. In the evaporator, the two cases are close to each other but then start to deviate significantly from each other in the adiabatic section. This deviation continues through the heat pipe to the end of the condenser section. The largest deviation occurs near the end of the condenser. The centerline temperature for compressible flow is higher than that of the incompressible model, which means that the viscous term has a more significant effect on the compressible flow model. This is probably because the momentum equation is coupled with the energy equation by the density variation, so the viscous term will affect the pressure and velocity profiles and thus the overall temperature distribution. For the incompressible model, the only link between the momentum and energy equations is the vapor heat conduction term at the vapor-liquid interface in Eq. (1.15), but the effect is very small. Therefore, the velocity fields with and without the viscous terms are almost identical to each other.

T/T₀ axis values: 1.02, 1.01, 1, 0.99, 0.98

z/L axis values: 0, 0.2, 0.4, 0.6, 0.8, 1

Legend:
center temp. incompressible, no viscous
interface temp., incompressible, no viscous
center temp., incompressible, viscous
interface temp., incompressible, viscous
center temp., compressible, viscous
interface temp., compressible, viscous
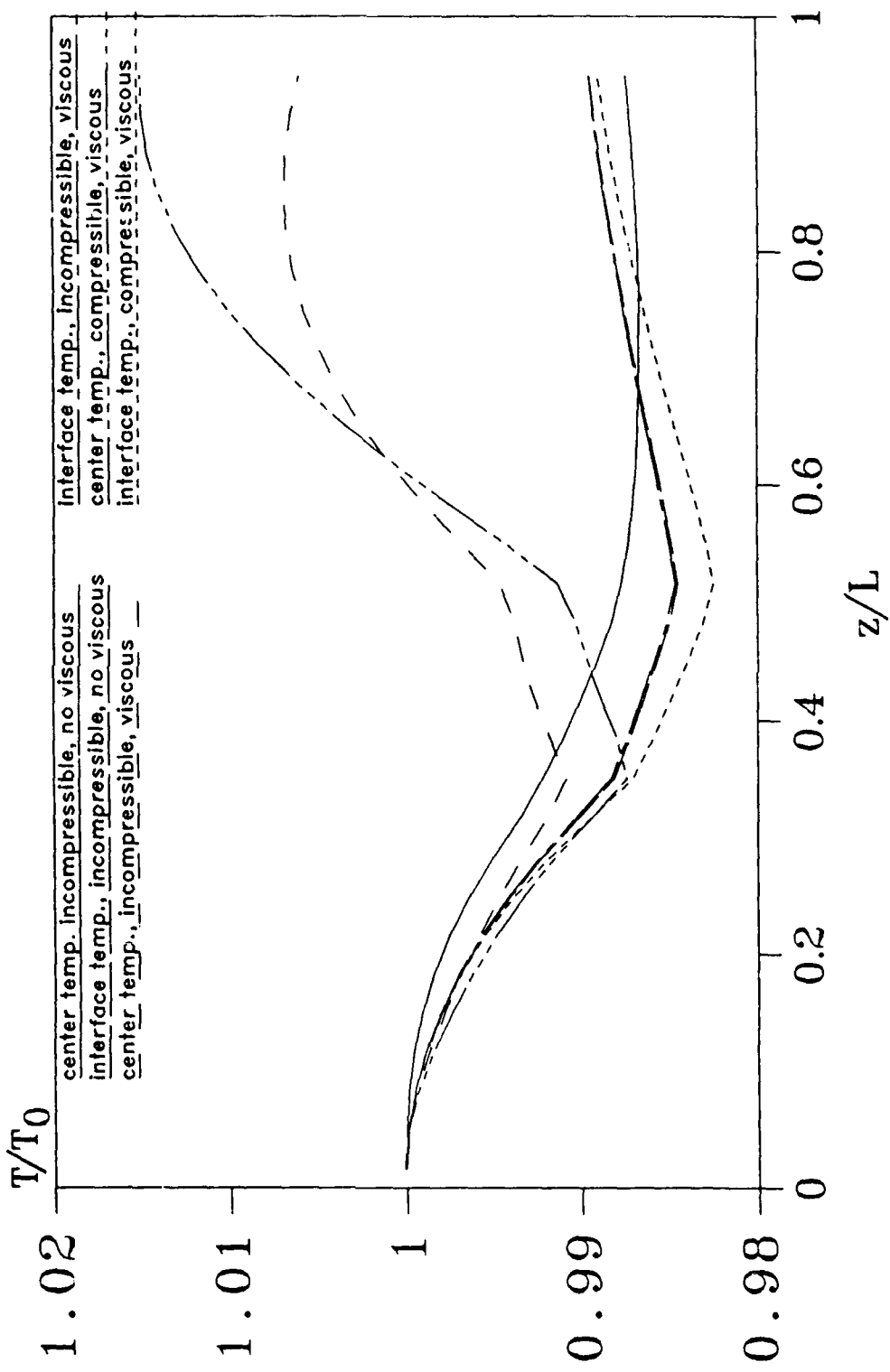
Fig. 1.24 The effect of viscous dissipation on the axial temperature profile along the sodium heat pipe with $Re_{r,e} = -4.0$ (Case B)

Since the temperature boundary condition at the interface is controlled by the Clapeyron correlation, the interface temperature variations are slightly different for both cases.

1.6.5. Elliptic and Parabolic Comparison

Figure 1.25 presents a comparison between the normalized pressure drop profiles of the elliptic and partially parabolic solutions for the compressible heat pipe vapor flow. For the partially parabolic solution, the axial diffusion terms are neglected in the governing equations. The results show that the partially parabolic solutions have larger pressure drops and the deviation ranges from 1-11% for the cases presented. For the case using water as the working fluid with a higher radial Reynolds number of $Re_{r,e} = -50$ (Case D), a larger deviation of 11% is noticed at the end of the condenser. For the case of a sodium heat pipe with a radial Reynolds number of $Re_{r,e} = -6.0$ (Case C), the deviation is about 7%. When the radial Reynolds number is decreased to $Re_{r,e} = -2.0$, the two curves almost overlap. This trend is similar to what Tien and Rohani (1974) observed, but the differences found here between these two models are not as large as what they observed. Faghri and Parvani (1988) did a comparison between the elliptic and partially parabolic solutions for the incompressible vapor flow in a concentric annular heat pipe. In that study, very small deviations were observed due to the incompressible flow analysis. However, the present results show that it is better to use the elliptic approach when the radial Reynolds number is large for the compressible model.
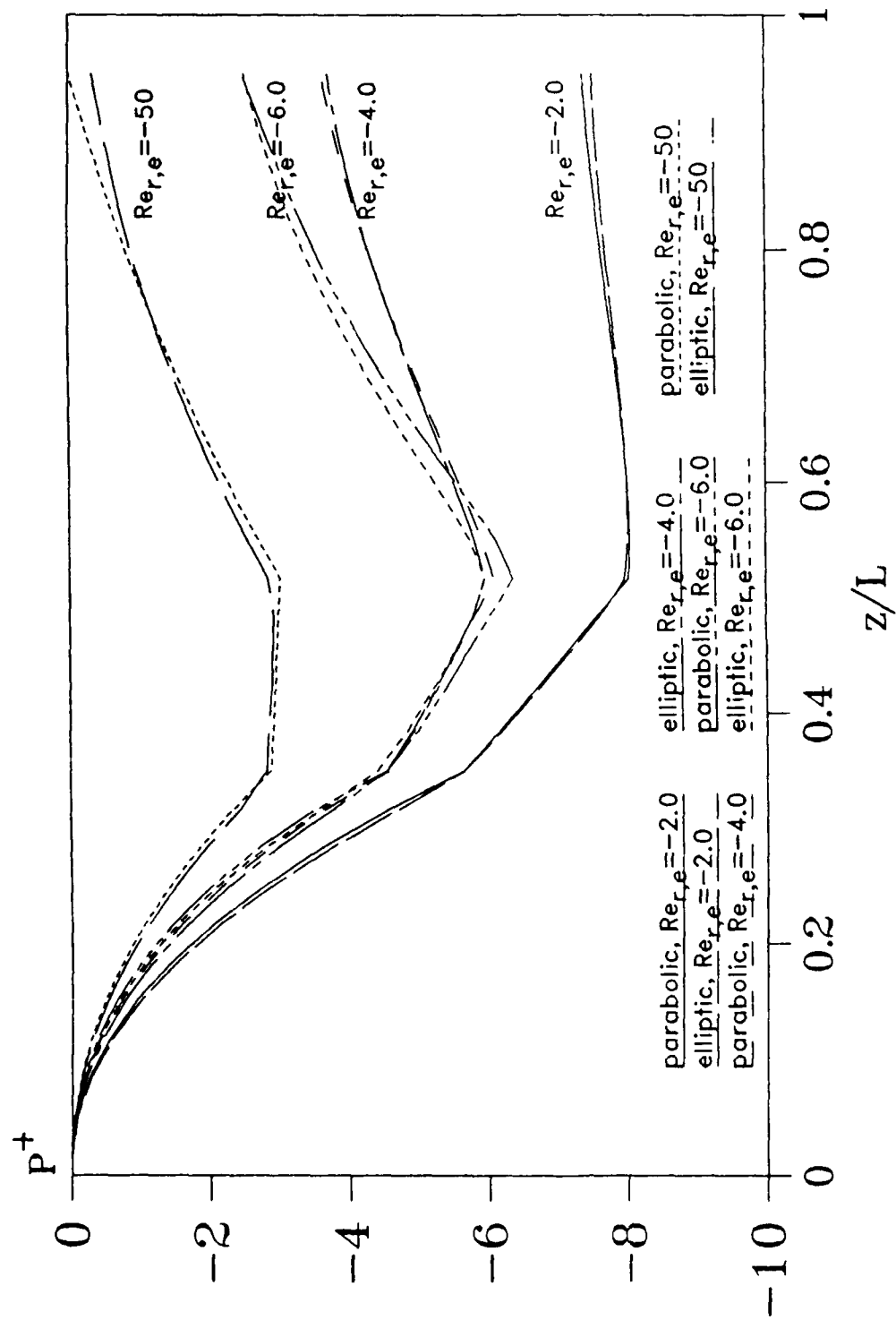
Fig. 125 The comparison between the elliptic and parabolic solutions for the axial pressure profile along the heat pipe vapor–liquid interface

Since no axial heat conduction through the wall is considered for the present partially parabolic solution, the total heat input at the liquid-vapor interface for the parabolic solution is greater than that of the elliptic solution. As a result, more liquid is evaporated and a larger pressure drop is expected for the partially parabolic solution. As expected, for the case with a high K_{wl} discussed in the section concerning the conjugate effect, the elliptic and partially parabolic solutions have larger deviations because of the significant axial heat conduction through the pipe wall. The maximum deviation of the pressure variation between the two solutions for $K_{wl} = 1000$ (Case B3) is about 12%.

1.7   Conclusions

The high and low temperature heat pipes have been studied numerically by using the generalized computer code PHOENICS for steady-state operation. The objective of this study is to find the effects of conjugate heat transfer and vapor compressibility. The following conclusions have been made:

1. The numerical results show a fairly good agreement compared with the experimental data at both low and high operating temperatures. It is also believed that the present model can predict the general performance of heat pipes with single or multiple heat sources.

2. The axial conduction through the wall and liquid-wick with large values of K_{wl} has a positive effect on the heat pipe performance. The conjugate axial conduction tends to make the outer wall and interface temperature more uniform. For the case with relatively small values of K_{wl} and Δ, the results approach the solution of the case when there is no axial conduction considered.

3. (a) The vapor compressibility can be important for the prediction of the sodium heat pipe temperature profile when the Mach number is greater than 0.3.

    (b) The compressible and incompressible models predict almost the same value for the total pressure drops.

(c) For the incompressible model, the similarity solution by Faghri (1988) shows a very good agreement (less than 1.5% deviation) for the pressure profile prediction compared with the present numerical results.

4. Up to 90% of the pressure recovery in the condenser section has been found for the heat pipe using water as a working fluid. The flow reversal for a sodium heat pipe vapor flow begins at $Re_{r,c} = 2.67$ (Case B) for the cases studied.

5. The viscous dissipation term in the energy equation does affect the temperature profile inside the vapor space, but has a very small effect on the interface temperature profile.

6. In general, the partially parabolic solutions are very close to the elliptic solutions except for the cases with a large radial Reynolds number at the interface or large values of K_{wl}.

7. For the heat pipe using water as the working fluid, the vapor temperature along the heat pipe is almost uniform. This is due to a very small pressure drop along the pipe compared with the static vapor pressure and also the thermodynamic equilibrium between the pressure and temperature at the liquid-vapor interface.

II. SIMULTANEOUS AXIAL CONDUCTION IN THE FLUID AND THE PIPE
FOR FORCED CONVECTIVE LAMINAR FLOW WITH BLOWING
AND SUCTION AT THE WALL

2.1 Summary

Numerical solutions are reported for conjugate heat transfer in a porous pipe having an internal laminar flow with blowing or suction at the inner surface of the pipe and constant heat flux at the outer surface of the pipe. The effect of the simultaneous axial conduction through the wall and the fluid has been studied for the combined hydrodynamic and thermal entry lengths. The results show that the ratio of the thermal conductivities of the pipe wall to the fluid and the thickness of the pipe wall may become significant factors on the heat transfer when the Peclet number is small, especially for the case when fluid is injected into the pipe. Also, the effect of axial wall conduction for the case of constant heat flux at the outer wall surface can be neglected when the wall thickness is small and the ratio of the conductivities of the wall to the fluid approaches unity.

2.2 Introduction

Conjugate heat transfer in a pipe with internal laminar fluid flow is a problem of considering the simultaneous heat transfer inside the fluid and the solid wall. In conventional convective heat transfer problems, the thermal boundary condition at the solid-fluid interface is assumed to be known, either in terms of the heat flux or the temperature. Some considerations have been given in the past concerning the errors that may be introduced by this assumption.

The primary research on the conjugate heat transfer problem for the circular tube was carried out by Luikov et al. (1971), but their closed-form solution involved highly complicated functions. Because of this fact, no numerical results were reported. A detailed solution was given by Mori et al. (1974, 1976) for constant heat flux and constant temperature at the outer surface of the pipe. The solution was obtained by assuming that the velocity profile was the fully developed parabolic profile and by neglecting the axial conduction of the fluid. Mori et al. (1974) also assumed the wall-fluid interfacial temperature distribution in the axial direction was in the form of a power series with unknown

coefficients. With this temperature distribution as the interfacial boundary condition, the analytical solution to the energy equation for the fluid was obtained using the Graetz solutions. The solution to the energy equation for the wall was then derived readily since all the boundary conditions were now known. Barozzi and Pagliarini (1985) employed a finite element method in conjuction with Duhamel's theorem to extend the results given by Mori et al. (1974) for different pipe lengths. Results by Mori (1974), and Barozzi and Pagliarini (1985) are applicable to cases with short heating sections due to the insulated boundary conditions imposed on the wall upstream and downstream of the heated section.

The coupled effect of axial conduction in the wall and the fluid in laminar pipe flow with an applied wall heat flux in the downstream region was studied for very long ducts numerically by Faghri and Sparrow (1980) and Zariffeh et al. (1982) and analytically by Campo and Rangel (1983) and Soliman (1984). In these analyses the pipe is extended indefinitely upstream and downstream of the heating section. Faghri and Sparrow (1980) investigated simultaneous wall and fluid axial conduction in laminar pipe flow with the assumption that the pipe wall was thin and the velocity profile was the fully developed parabolic profile. They observed that axial conduction inside the tube wall can cause a substantial preheating of both the wall and fluid in the upstream region where there is no external heat input. Conjugate heat transfer when the fluid is turbulent was investigated by Kuznetzov and Belousov (1974),

Sakakibara and Endoh (1977) and Lin and Chow (1984).

Recently, more attention has been given to the fluid flow and heat transfer in porous pipes with applications such as transpiration cooling and heat pipes. Usually, the porous pipe wall is of a significant thickness, so that axial wall conduction may have an influence on the heat transfer. In a heat pipe, the thin wick is attached to the inner wall of a thick tube to achieve the capillary force for the liquid return. Blowing and suction occurs because of the evaporation and condensation of the working fluid in the heating and cooling segments of the heat pipe. This application was the motivation for the present work. No literature has been found concerning the problem of conjugate heat transfer with blowing and suction at the wall. The objective of the present analysis is to investigate the effect of axial conduction in porous pipes in the combined hydrodynamic and thermal entry lengths with constant heat flux at the outer surface of the pipe wall. In addition, the influence of the Peclet number is stressed due to the inclusion of the axial conduction term in the fluid so as to complete the analysis given by Mori et al. (1974). The numerical solution relies on the control volume formulation by Patankar(1980) and an iterative scheme which dealt simultaneously with the fluid and the wall. The numerical results for the Nusselt number and temperature at the interface are presented as in by Mori (1974, 1976). In addition, the interfacial heat flux for both porous and impermeable wall cases are also given to make the results useful in engineering applications.

2.3 Mathematical Formulation

The model used for analysis is shown in Figure 2.1. A constant heat flux q_o is applied uniformly along the outer surface of the wall over a finite length L. The fluid enters the inlet of the pipe with a uniform velocity w_{in} and uniform temperature T_{in}. The injected and extracted fluid is the same as that of the main pipe flow and is at the interface temperature when it enters or leaves the walls. The equations governing the present problem are the conservation of mass, momentum and energy equations whereby assuming laminar, steady and incompressible flow with constant fluid properties are reduced to the following forms in cylindrical coordinates.

$$\frac{\partial v}{\partial r} + \frac{v}{r} + \frac{\partial w}{\partial z} = 0 \tag{2.1}$$

$$v\frac{\partial v}{\partial r} + w\frac{\partial v}{\partial z} = -\frac{1}{\rho}\frac{\partial p}{\partial r} + \nu\left[\frac{\partial}{\partial r}\left[\frac{1}{r}\frac{\partial}{\partial r}(rv)\right] + \left\{\frac{\partial^2 v}{\partial z^2}\right\}\right] \tag{2.2}$$

$$v\frac{\partial w}{\partial r} + w\frac{\partial w}{\partial z} = -\frac{1}{\rho}\frac{\partial p}{\partial z} + \nu\left[\frac{1}{r}\frac{\partial}{\partial r}\left[r\frac{\partial w}{\partial r}\right] + \left\{\frac{\partial^2 w}{\partial z^2}\right\}\right] \tag{2.3}$$

$$v\frac{\partial T}{\partial r} + w\frac{\partial T}{\partial z} = \frac{k}{\rho C_p}\left[\frac{1}{r}\frac{\partial}{\partial r}\left[r\frac{\partial T}{\partial r}\right] + \left\{\frac{\partial^2 T}{\partial z^2}\right\}\right] \tag{2.4}$$
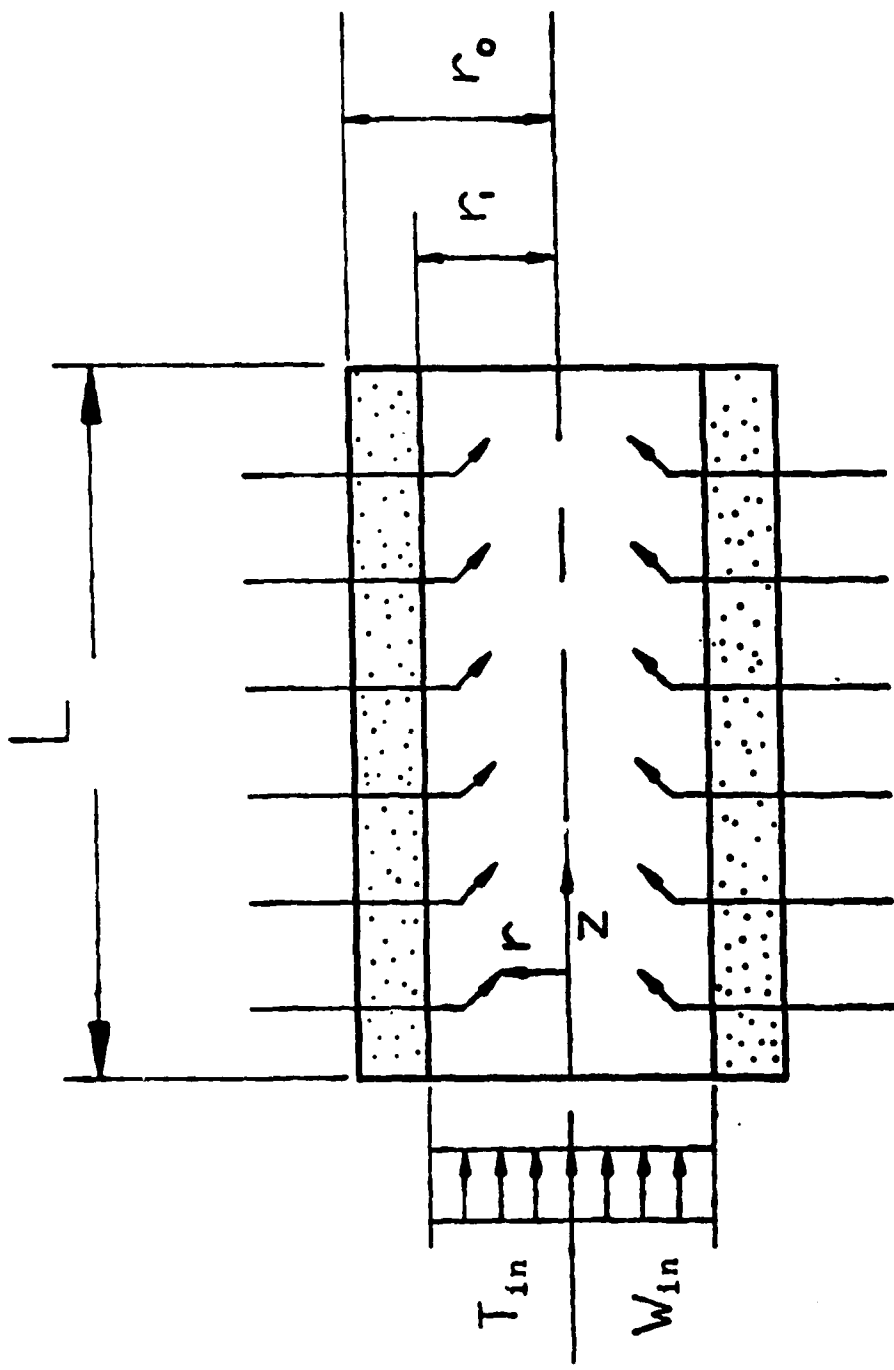
Fig.2.1 The schematic model of the heat transfer section of a porous pipe

We should note that in equations (2.2-2.4), the terms in braces {} are associated with axial diffusion terms. These terms are neglected when the partially parabolic version is considered but are accounted for in the elliptic case. The thermal conductivity k of the solid is in general different from that of the fluid. At the solid-fluid interface, the harmonic mean is used to determine the thermal conductivity.

The boundary conditions for the case of uniform inlet conditions and constant heat flux at the outer wall are defined as follows:

Inlet plane: $z = 0$, $0 < r < r_i$

$$w = w_{in}, \quad T = T_{in}, \quad v = 0 \qquad\qquad (2.5)$$

$$r_i < r < r_0, \qquad \frac{\partial T_w}{\partial z} = 0 \qquad\qquad (2.6)$$

Outer wall: $0 < z < L$, $r = r_0$

$$\frac{\partial T}{\partial r} \Big|_{wall} = q_0/k_w = constant \qquad\qquad (2.7)$$

Inner wall: $0 < z < L$, $r = r_i$

$$w = 0 \qquad\qquad (2.8)$$

$$v = v_i \begin{cases} v_i > 0 & \text{suction} \\ v_i < 0 & \text{blowing} \\ v_i = 0 & \text{impermeable wall} \end{cases} \qquad (2.9)$$

$$T_f = T_w \qquad (2.10)$$

$$k_f \frac{\partial T_f}{\partial r} = k_w \frac{\partial T_w}{\partial r} \qquad (2.11)$$

Outlet of the tube (elliptic solution): $z = L$

$$r_i < r < r_0, \qquad \frac{\partial T_w}{\partial z} = 0 \qquad (2.12)$$

$$0 < r < r_i, \qquad \frac{\partial T_f}{\partial z} = 0, \quad p = 0 \qquad (2.13)$$

We should emphasize that the physical situation corresponding to this problem is the one in which conduction is confined to a finite length of heated wall, with an adiabatic boundary condition imposed at the upstream and downstream ends of the heated segment. This constraint restricts the results to tubes with short heating sections.

The governing equations (2.1-2.4) with the appropriate boundary conditions (2.5-2.13) contain five independent parameters:

*   Peclet number of the fluid,

    $Pe = Re * Pr = 2\, r_i\, w_{in}\, \rho_f\, C_p / k_f$

* Radial Reynolds number at the solid-fluid interface,

$$Re_i = v_i \, r_i/\nu$$

* Wall-to-fluid thermal conductivity ratio,

$$K = k_w/k_f$$

* Thickness of the wall,

$$\Delta = (r_0 - r_i)/2r_i$$

* Heated length,

$$L^* = L/2r_i Pe$$

The computations are carried out for the Peclet number of the fluid of 100 and 1000 with Δ of 0.01 and 0.1 and K = 1, 500 and 5000 for different suction and blowing radial Reynolds numbers at the wall. This choice of parameters covers a wide range of possible combinations of fluid and pipe wall properties, flow rates and boundary condition specifications. The negative and positive radial Reynolds numbers at the wall indicate blowing and suction, respectively.

The numerical results can be presented for the following four dimensionless groups in terms of the dimensionless axial distance $z^* = \dfrac{z}{2r_i Pe}$:

* Interface temperature,

$$\theta_i = \frac{T_i - T_{in}}{q_0 \, r_i/k_f}$$

95

* Bulk Temperature,

$$\theta_b = \frac{T_b - T_{in}}{q_0 \, r_i / k_f}$$

* Nusselt number,

$$Nu_z = \frac{2r_i \left(\frac{\partial T}{\partial r}\right)_{r=r_i}}{T_i - T_b}$$

where

$$\left(\frac{\partial T}{\partial r}\right)_{r=r_i} = \frac{q_i}{k_f}$$

* Heat flux across the interface,

$$q_i / q_{mean}$$

Although the Nusselt number is traditionally the main dimensionless parameter used in presenting results for conventional convection problems, there is a good justification not to do so for conjugate heat transfer problems because q_i, T_b, T_i are all unknowns in the definition of the Nusselt number as given above. Mori et al. (1974) presented results only for Nu_z and θ_i, and therefore their results are of no use for direct engineering applications. From the engineering viewpoint, the most important information is the rate of heat transfer across the interface. So the results are presented in terms of the dimensionless

96

group q_i/q_{mean} as well as the Nusselt number. The local heat flux across the interface q_i is approximated by $\dfrac{k_h (T_{i,w} - T_{i,f})}{r_i \ln (r_{i,w}/r_{i,f})}$ with k_h being the harmonic mean of the thermal conductivities of the solid wall and the fluid which is defined as $2k_f \cdot k_w/(k_f + k_w)$ by Patankar (1978). The radial distance from the pipe axis to the interface is r_i and $T_{i,w}$ and $T_{i,f}$ are the temperatures at the grid nodes adjacent to the interface on the wall and the fluid sides, respectively. The constant mean heat flux at the interface without considering axial heat conduction in the tube wall q_{mean} is equal to:

$$q_{mean} = q_0 \frac{r_0}{r_i}$$

2.4 Solution Procedure

The problem is solved as a convection-conduction problem throughout the entire calculation domain, but since the velocities in the solid are zero, the analysis in the solid region was for a pure conduction problem. To account for the discontinuity in the value of the thermal conductivity at the wall-fluid interface, the transport coefficient in the energy equation is evaluated as the harmonic mean of the values on each side of the interface developed by Patankar (1980).

The finite difference iteration method of solution developed by Spalding et al. (1980) which is employed in the generalized PHOENICS Computational Code by Spalding and Rosten (1985) is used for the elliptic and partially parabolic solutions of equations (2.1-2.4) with the boundary specifications given in equations (2.5-2.13). By this method, the above equations are solved over a square mesh by the finite control volume method outlined by Patankar (1980). Finite control volume equations are derived by the integration of the differential equations over an elementary control volume or a cell surrounding a grid node. Upwind differencing is used for the convective terms.

Pressures are solved from a pressure correction equation which yields the pressure change needed to procure velocity changes to satisfy mass continuity. The 'SIMPLEST' practice by Spalding (1980) is employed for the momentum equations. The most significant difference between

'SIMPLEST' and the 'SIMPLE' algorithm by Patankar (1980) is that in the former the control volume formulation coefficients for momentum contain only diffusion contributions, the convection terms being added to the linearized source term of the equations.

The equations are solved by a line-by-line procedure which is similar to Stone's Strongly Implicit Method but is free from parameters requiring case-to-case adjustment and is therefore less complex. The temperature is solved in a whole-field manner, and the pressure correction equation is solved in a slab-by-slab manner.

The accuracy of the numerical solution was checked in two ways: the grid spacing was systematically varied and the results for different grid sizes were compared to the extrapolated results of the infinitesimal grid spacing, and the numerical results were compared with a known solution for uniform heat flux and temperature at the interface without axial conduction in the wall or the fluid and with no blowing or suction by Hornbeck (1966). The test was passed at a satisfactory level of agreement, within 1% for most of the results.

A number of different uniform grid sizes were chosen to test the accuracy of the solution. After considering the accuracy, computer time and the truncation error, the final grid sizes that were chosen for the presentation of results are as follows:

20x4x40 (radial fluid x radial solid x axial) for $\Delta = 0.01$
20x10x20 (radial fluid x radial solid x axial) for $\Delta = 0.1$

A converged solution was obtained by checking the variation of the residuals in terms of the sweep number. When increasing the sweep number to the extent that no further decrease of the residuals is observed, this means the results are converging. For this conjugate problem, 150 sweeps were adequate for convergence of the elliptic solution.

2.5 Results and Discussion

The numerical results were obtained for at least two different values of each of the dimensionless parameters in order to determine the importance of axial conduction. These parameters are the Peclet number of the fluid, the radial Reynolds number at the solid-fluid interface, the wall-to-fluid thermal conductivity ratio, and the dimensionless thickness of the pipe wall. In the present work, only one dimensionless pipe length $L^* = 0.05$ is chosen to avoid the excessive presentation of the results. Axial heat conduction along the pipe wall is usually neglected by practicing engineers when designing heat exchangers or other kinds of heat transfer devices because it is very difficult to deal with conjugate heat transfer. Therefore, it is of practical importance to know the errors that may be introduced by this assumption. The numerical results for the three dimensionless variables: the Nusselt number Nu_z, the interface temperature θ_i, and the heat flux across the interface q_i/q_{mean} are given in terms of z^* for different values of K, Δ, Pe and Re_i. The bulk temperature θ_b can be calculated from the information presented.

Figures 2.2 through 2.4 show the effect of the thermal conductivity ratio for $\Delta = 0.1$, Pe = 100 and $Re_i = 1.0, 0.0, -3.0$ on the axial variation of the Nusselt number, the interface temperature and the interfacial heat flux, respectively. The effect of axial conduction
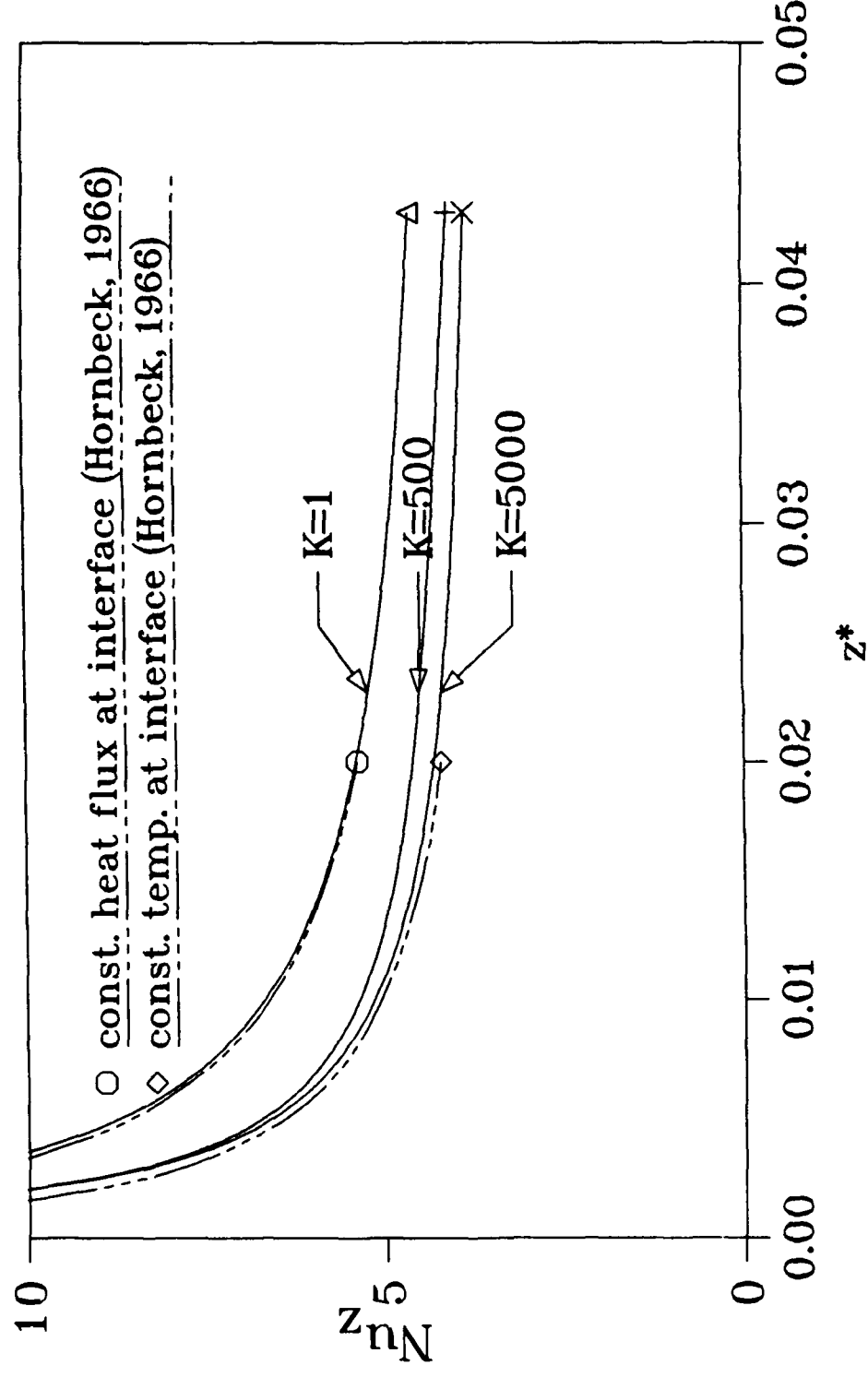
Fig. 2.2(a) The effect of the thermal conductivity ratio K on the Nusselt number at the interface for Pe=100, Δ=0.1 and Re_I=0.0
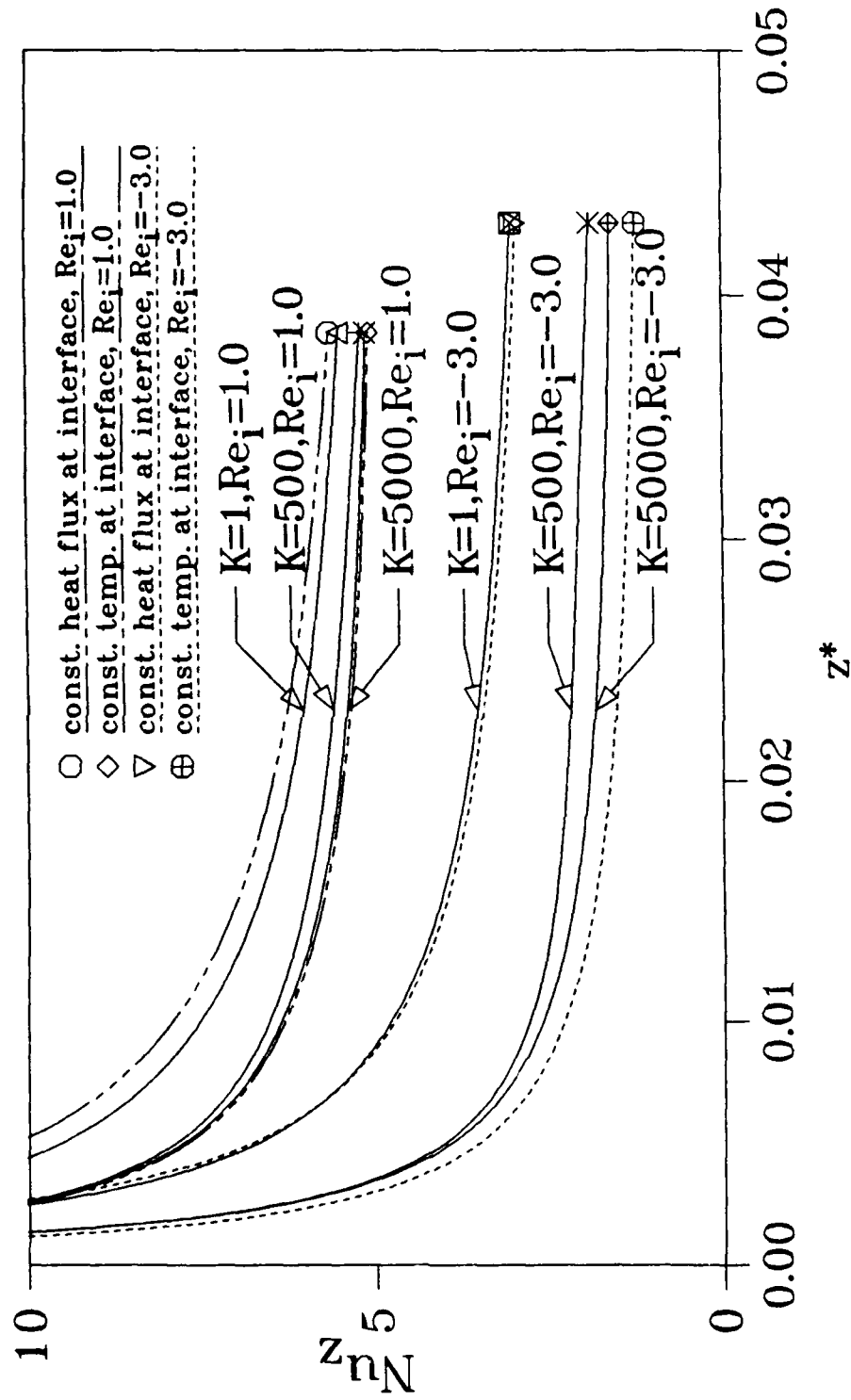
Fig. 2.2(b) The effect of the thermal conductivity ratio K on the Nusselt number at the interface for Pe=100 and Δ=0.1 with suction and blowing
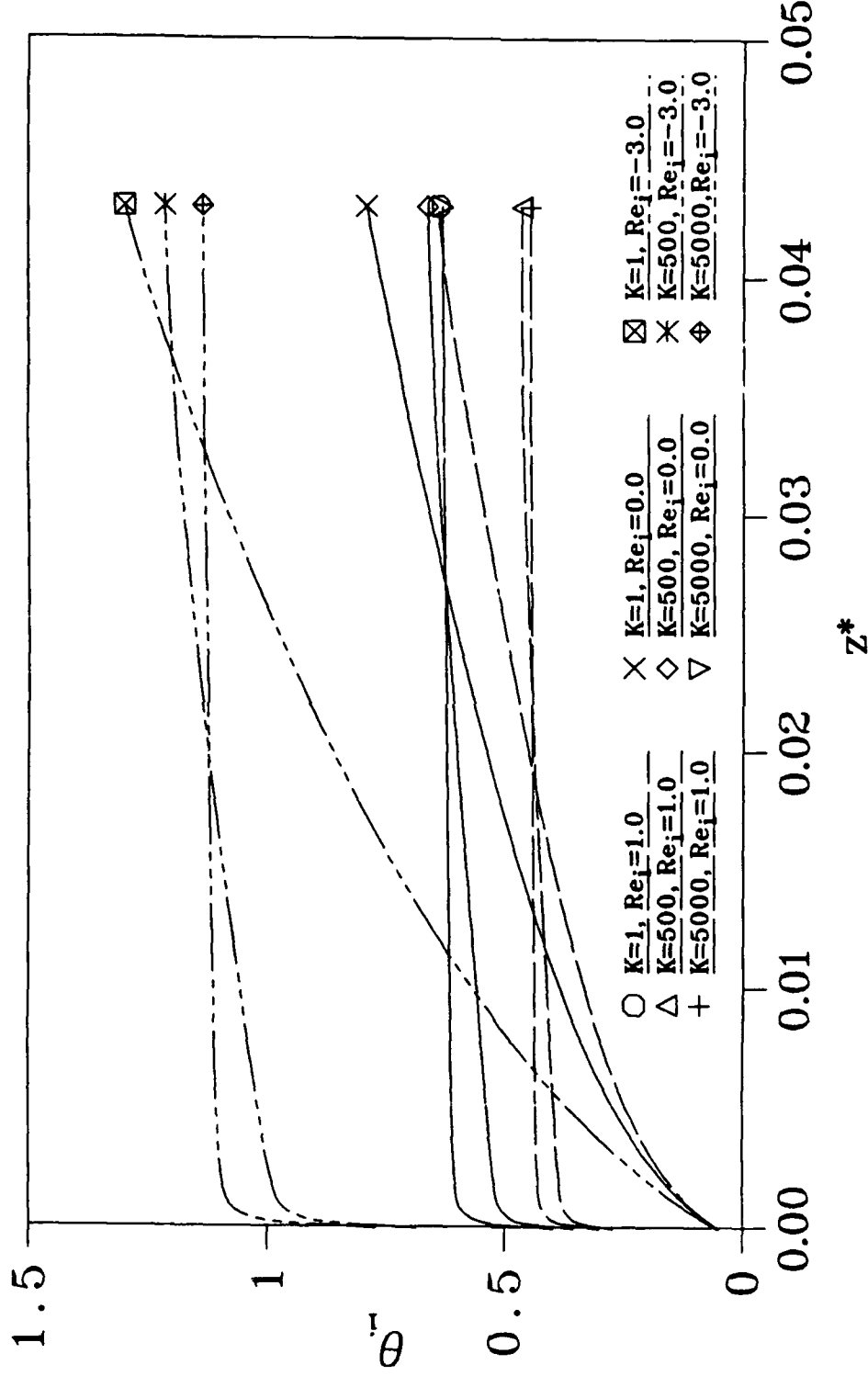
Fig. 2.3 The effect of the thermal conductivity ratio K on the interface temperature for Pe=100 and Δ=0.1
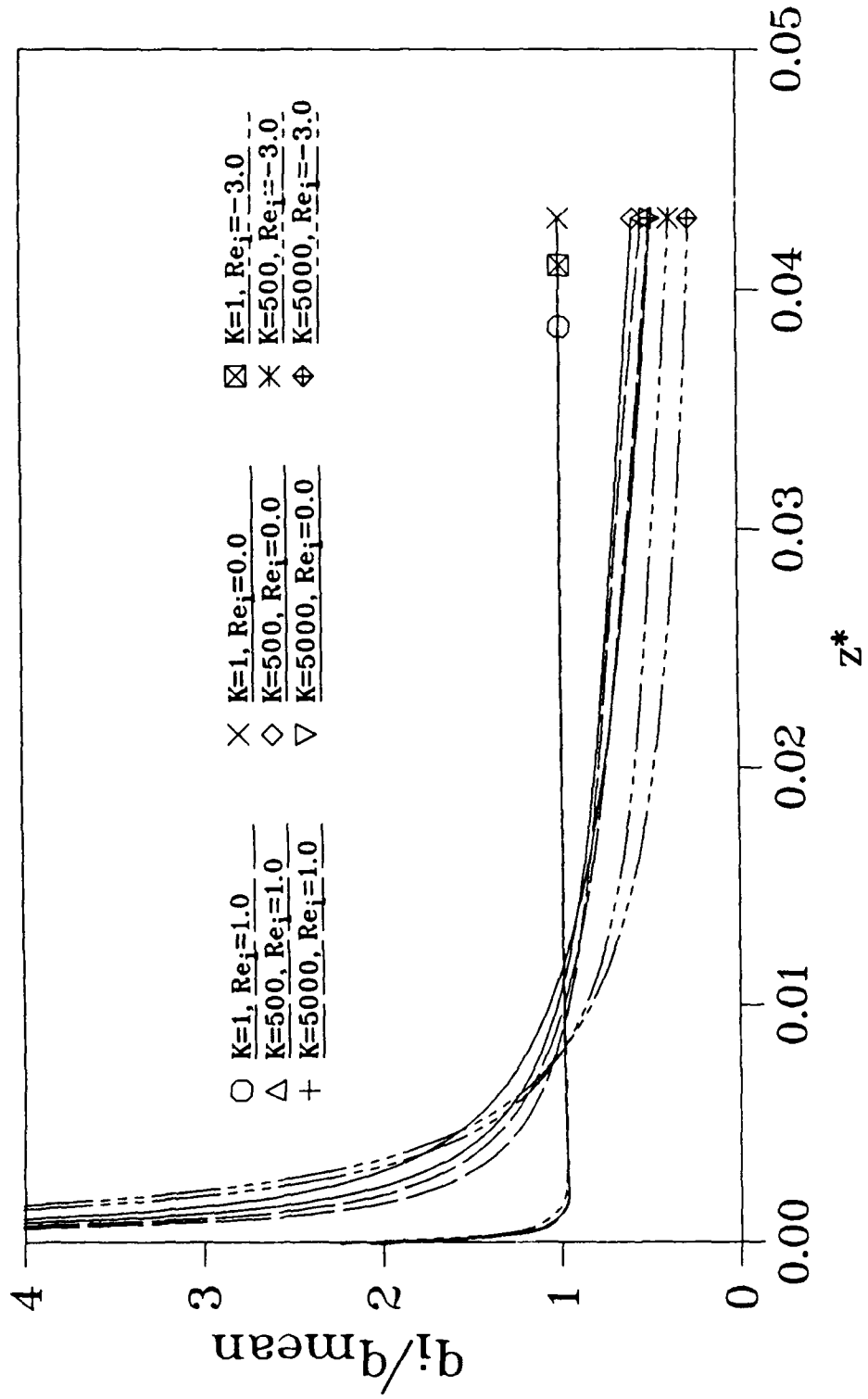
Fig. 2.4 The effect of the thermal conductivity ratio K on the interfacial heat flux for Pe=100 and Δ=0.1

becomes more important as the conductivity ratio, K, increases. As K increases, the results show that the interface temperature distribution changes gradually to a constant temperature along z^*, and the Nusselt number approaches that of a constant wall temperature. Physically, when K is very large the axial conduction in the wall has a tendency to make the wall temperature uniform. It is similar to the situation when condensation or evaporation at a wall occurs, which leads to a uniform wall temperature because of the high heat transfer coefficient. The blowing case has a higher interface temperature and the suction case has a lower interfacial temperature in comparison with the case in which the wall is impermeable. At K = 5000, the interface temperature distribution becomes constant except for the short entrance region and the Nusselt number also approaches the constant temperature results by Hornbeck (1966). It is noticed from the present results and those presented by Raithby (1971) for the case of no axial conduction that blowing at the wall caused a bigger difference between the Nusselt numbers for the cases of constant heat flux and constant wall temperature. So the effect of axial conduction is more pronounced in this case than in other cases. In general, as the thermal conductivity decreases, the Nusselt number increases and the interfacial heat flux tends to become more uniform. For K = 1, the results show that the interfacial heat flux almost becomes uniform for all three cases. Also, the Nusselt number approaches the case of constant heat flux at the interface. This is because the axial conduction causes both the interfacial temperature and bulk temperature

to increase at approximately the same rate, so that the difference of $T_i - T_b$ and $(\frac{\partial T}{\partial r})_{r=r_i}$ almost remains unchanged. The numerical results for constant heat flux and temperature at the interface for blowing and suction are computed with the consideration of axial conduction through the fluid. The numerical results for the Nusselt number for $K = 1$ without blowing and suction compares favorably with the numerical results for the case of constant heat flux at the interface as given by Hornbeck (1966). The Nusselt number for $K = 1$ with suction is slightly smaller than the results for constant heat flux at the interface and the results for the case of blowing is slightly greater than the results for constant heat flux at the interface. This is probably because the results for constant heat flux at the interface include the axial heat conduction through the fluid. The results for the Nusselt number with $K \geq 1$ are between two limiting cases: constant wall temperature and constant heat flux at the interface. This behavior was first noticed by Mori et al. (1974) for impermeable walls. The present analysis shows also the same general trend for the cases of blowing and suction. It appears that the influence of axial wall heat conduction must be accounted for if the value of K is large.

Figures 2.5 through 2.7 show the effect of varying the tube wall thickness on the Nusselt number, the interface temperature and the interfacial heat flux, respectively. From these results, we found that

107
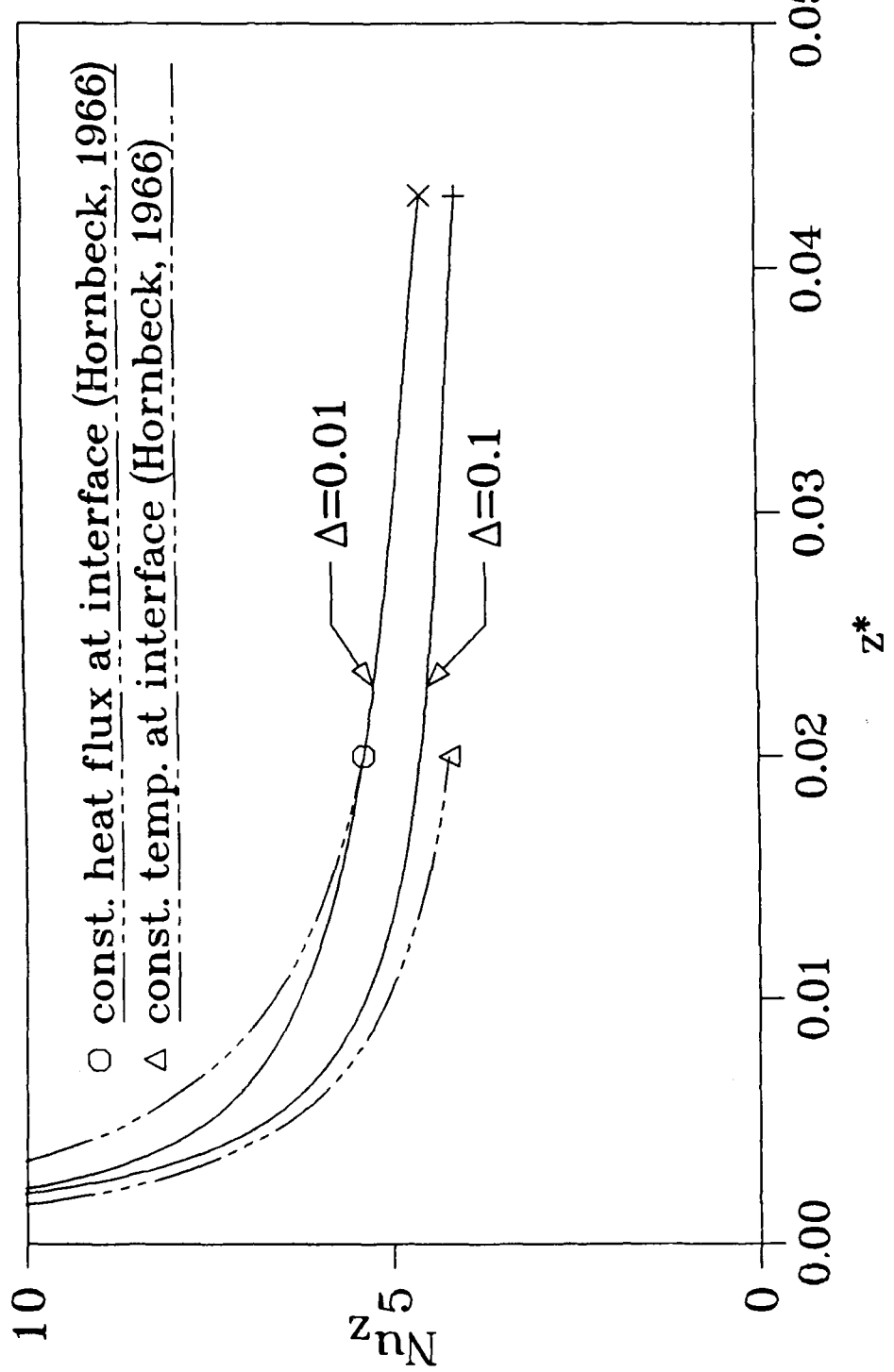
Fig. 2.5(a) The effect of wall thickness Δ on the Nusselt number at the interface for $Pe=100$, $K=500$ and $Re_i=0.0$
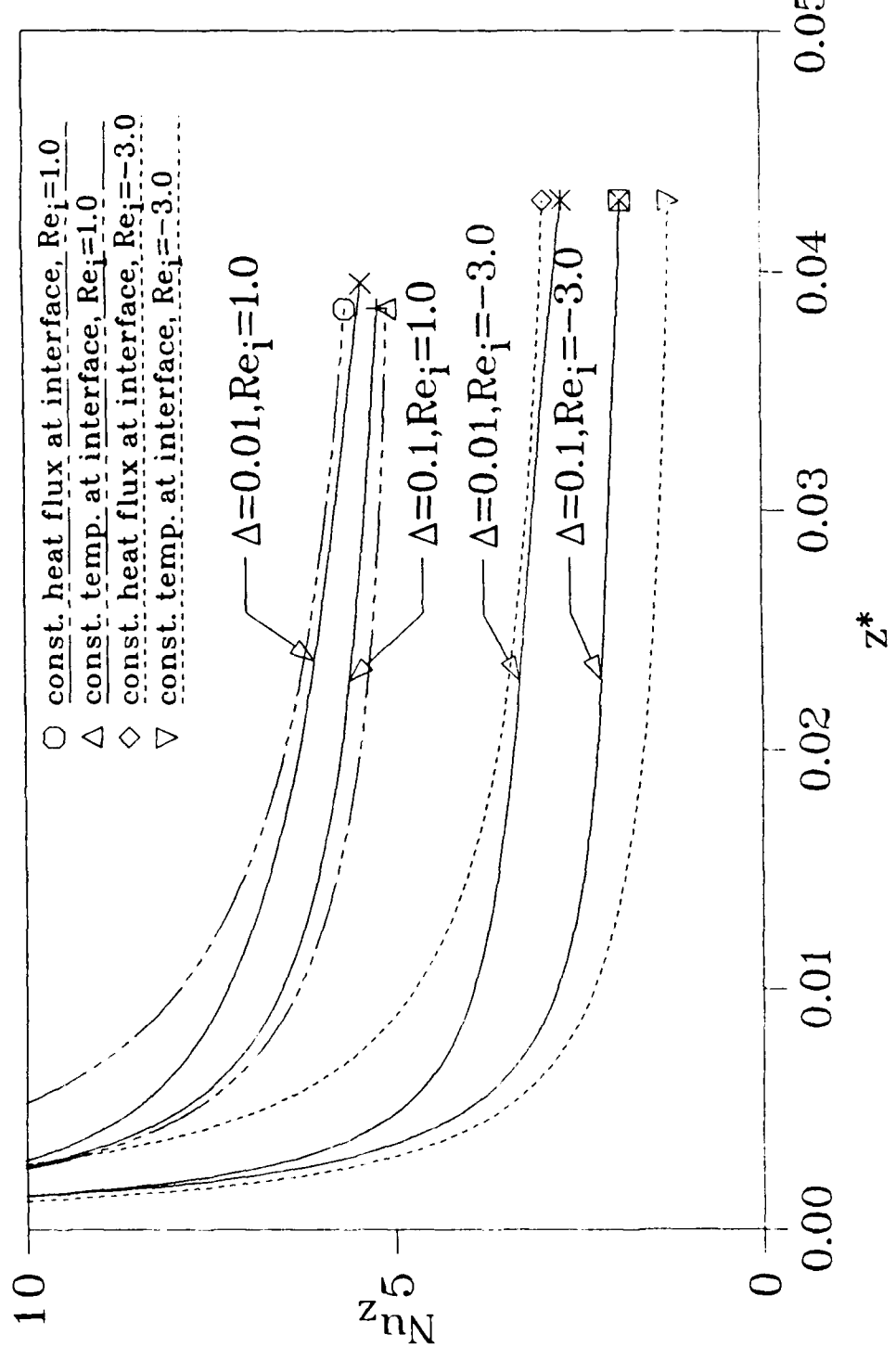
Fig. 2.5(b) The effect of wall thickness Δ on the Nusselt number at the interface for Pe=100 and K=500 with suction and blowing
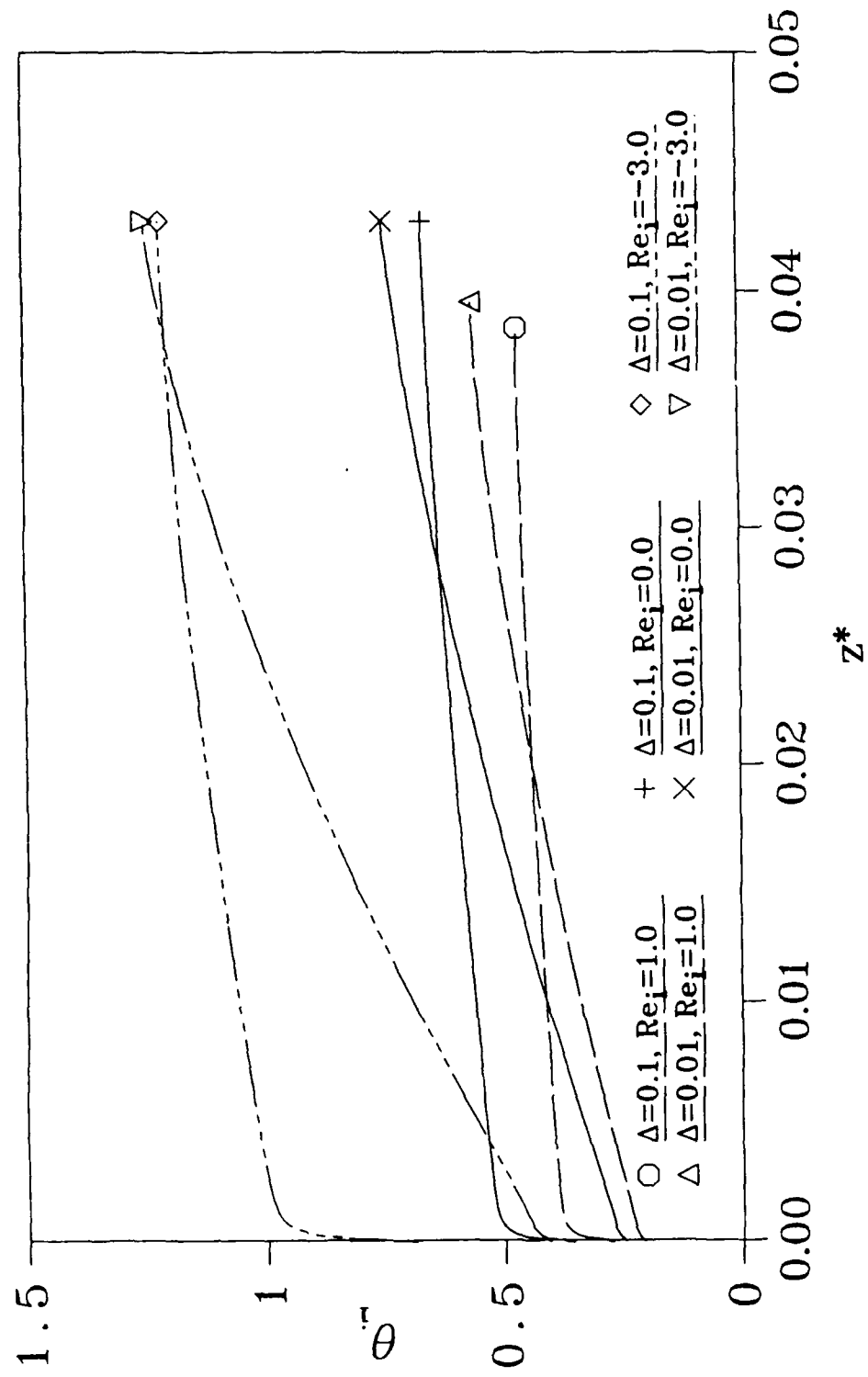
Fig. 2.6 The effect of the wall thickness Δ on the interface temperature for Pe=100 and K=500

Legend within figure:

○ Δ=0.1, Re$_i$=1.0   + Δ=0.1, Re$_i$=0.0   ◇ Δ=0.1, Re$_i$=-3.0
△ Δ=0.01, Re$_i$=1.0   × Δ=0.01, Re$_i$=0.0   ▽ Δ=0.01, Re$_i$=-3.0

Axis labels: z^*, θ_i
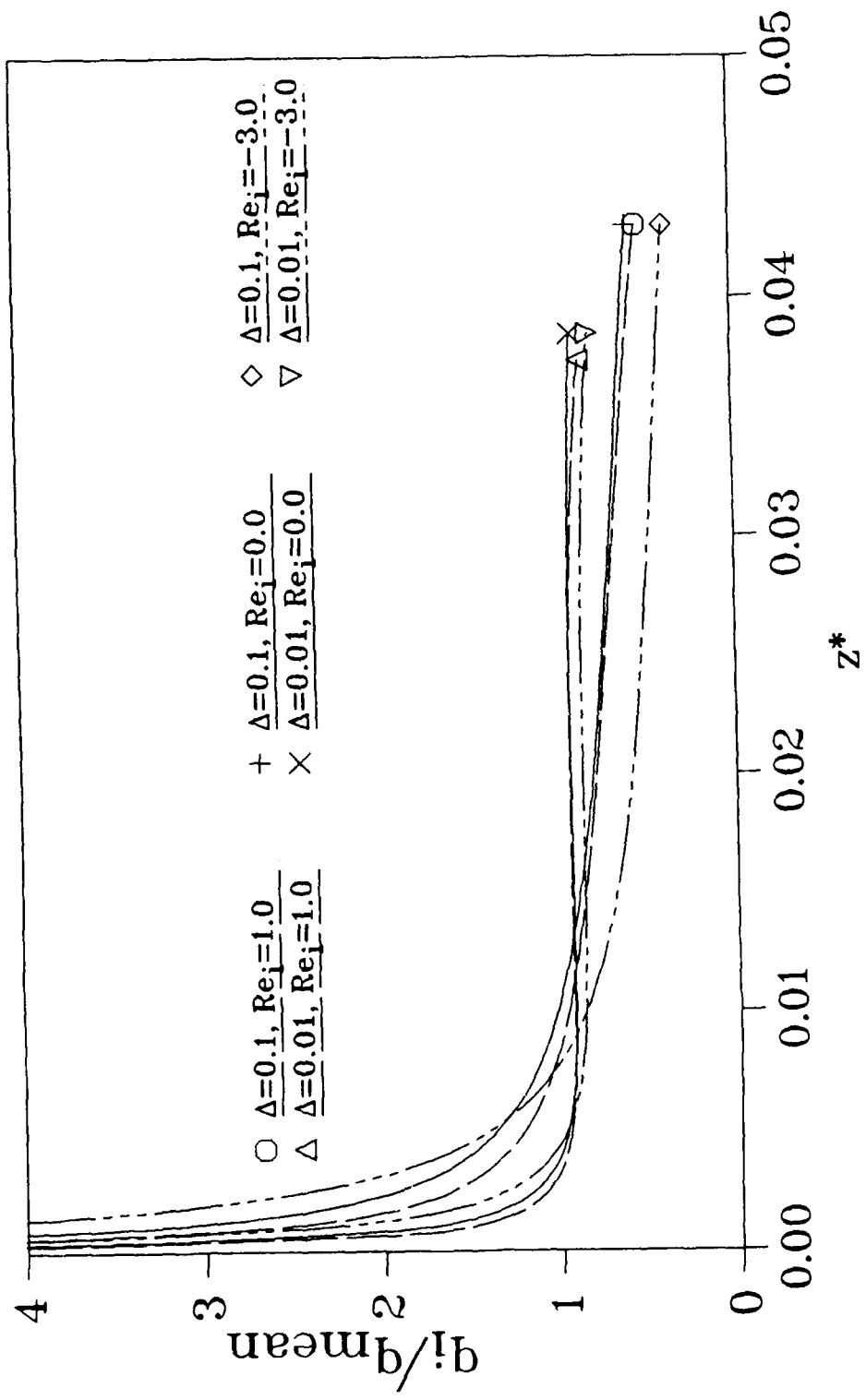
Fig. 2.7 The effect of the wall thickness on the interfacial heat flux for Pe=100 and K=500

Legend:

○ $\Delta=0.1$, $Re_i=1.0$
△ $\underline{\Delta=0.01}$, $\underline{Re_i=1.0}$

+ $\Delta=0.1$, $Re_i=0.0$
× $\underline{\Delta=0.01}$, $\underline{Re_i=0.0}$

◇ $\Delta=0.1$, $Re_i=-3.0$
▽ $\underline{\Delta=0.01}$, $\underline{Re_i=-3.0}$

Axis labels: q_i/q_{mean} (vertical), z^* (horizontal)

for small Δ the effect of axial heat conduction through the wall can be neglected since the results approach that of constant heat flux at the interface. Faghri and Sparrow (1980) assumed a thin-walled tube, so that all of the results for fully developed flow approach the results for a constant heat flux at the interface. We found that when the wall thickness increases, the axial wall conduction becomes more important, and the interface temperature becomes more uniform because axial heat conduction tends to level out the temperature along the pipe. These results also show that the interfacial heat flux tends to be uniform when the wall becomes thinner. It is interesting to notice that all of the results for different values of Δ are within the two limiting cases: constant heat flux at the interface and constant wall temperature at the interface. We should mention that when K → 1, the axial conduction becomes less important so that the influence of Δ will also become less important. When K → ∞ the influence of Δ will become pronounced. This seems quite reasonable from the physical viewpoint of the problem. Apparently from these results, we should pay more attention to the blowing case with large K. The trends of the results concerning the influence of the wall thickness agrees fairly well with those by Mori (1974) for the case of an impermeable wall.

Figures 2.8 through 2.10 show the comparison between the partially parabolic and the elliptic solution on the Nusselt number for different values of Pe and K. Figure 2.8 shows the values of the Nusselt number

112
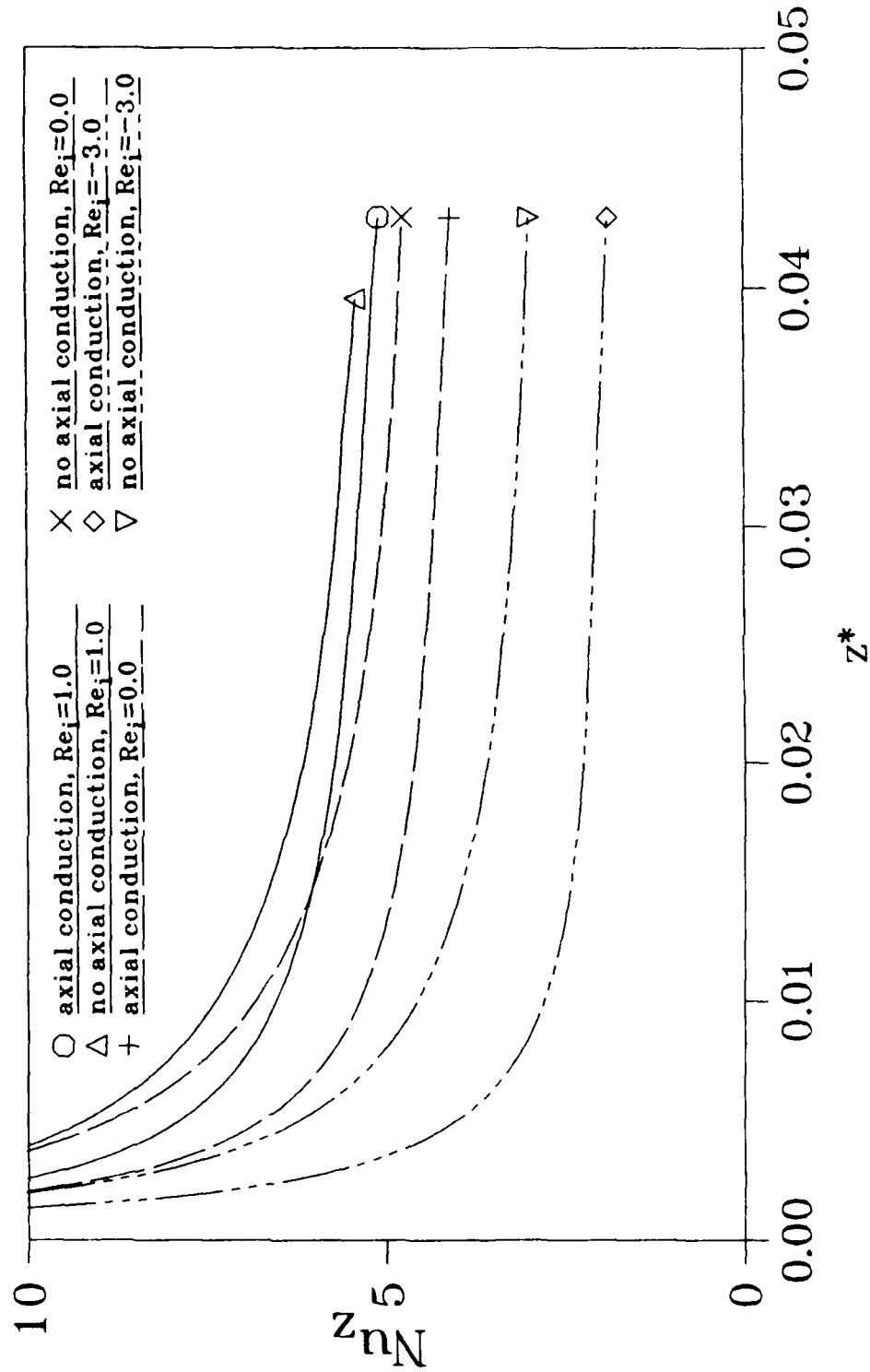
Fig. 2.8 The effect of axial heat conduction on the Nusselt number at the interface for Pe=100, K=500 and Δ=0.1
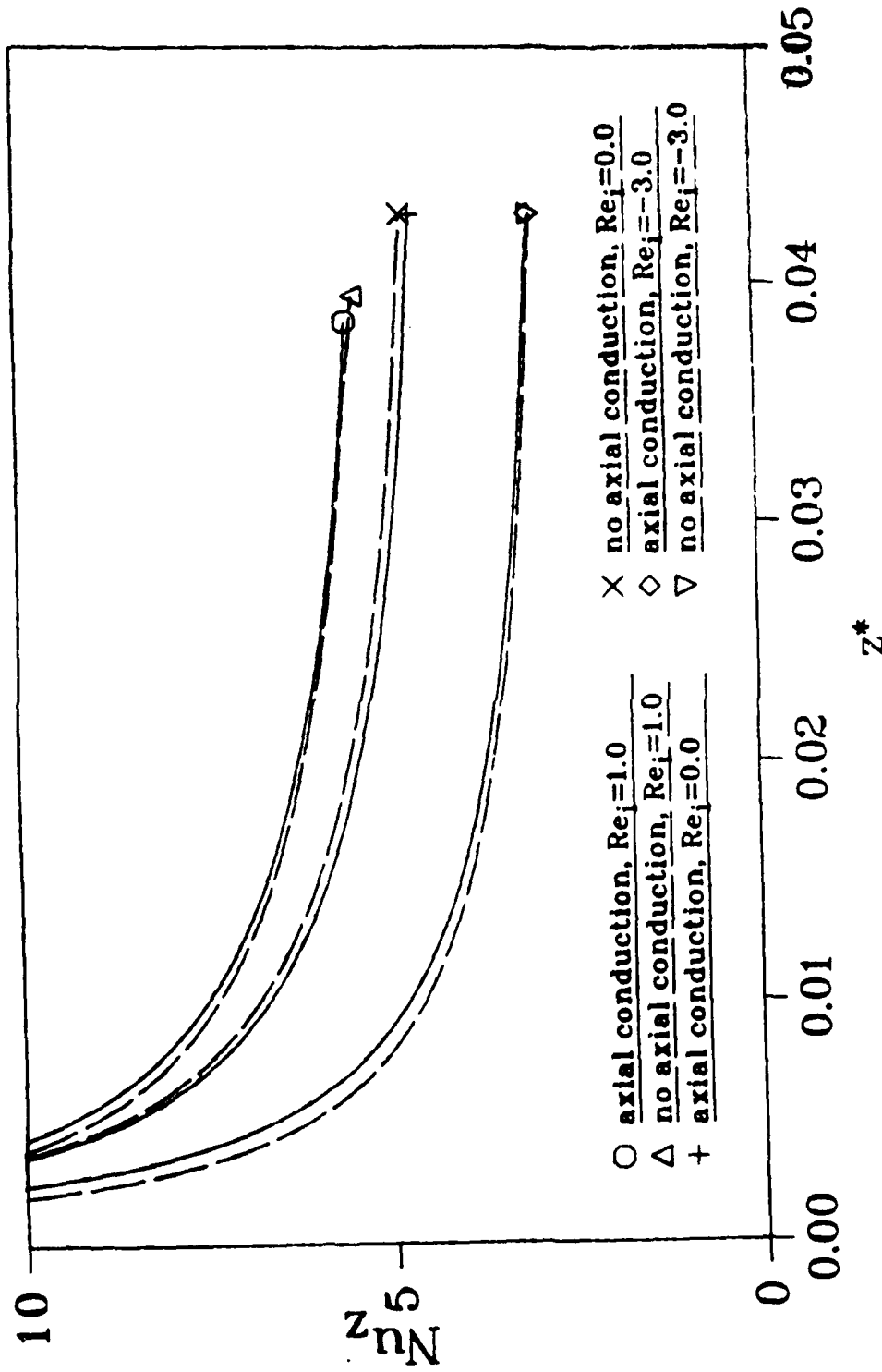
Fig. 2.9 The effect of axial heat conduction on the Nusselt number at the interface for Pe=100, K=1 and Δ=0.1

O axial conduction, Re_i=1.0   ✕ no axial conduction, Re_i=0.0
△ no axial conduction, Re_i=1.0   ◇ axial conduction, Re_i=-3.0
+ axial conduction, Re_i=0.0   ▽ no axial conduction, Re_i=-3.0

z^*

Nu_z
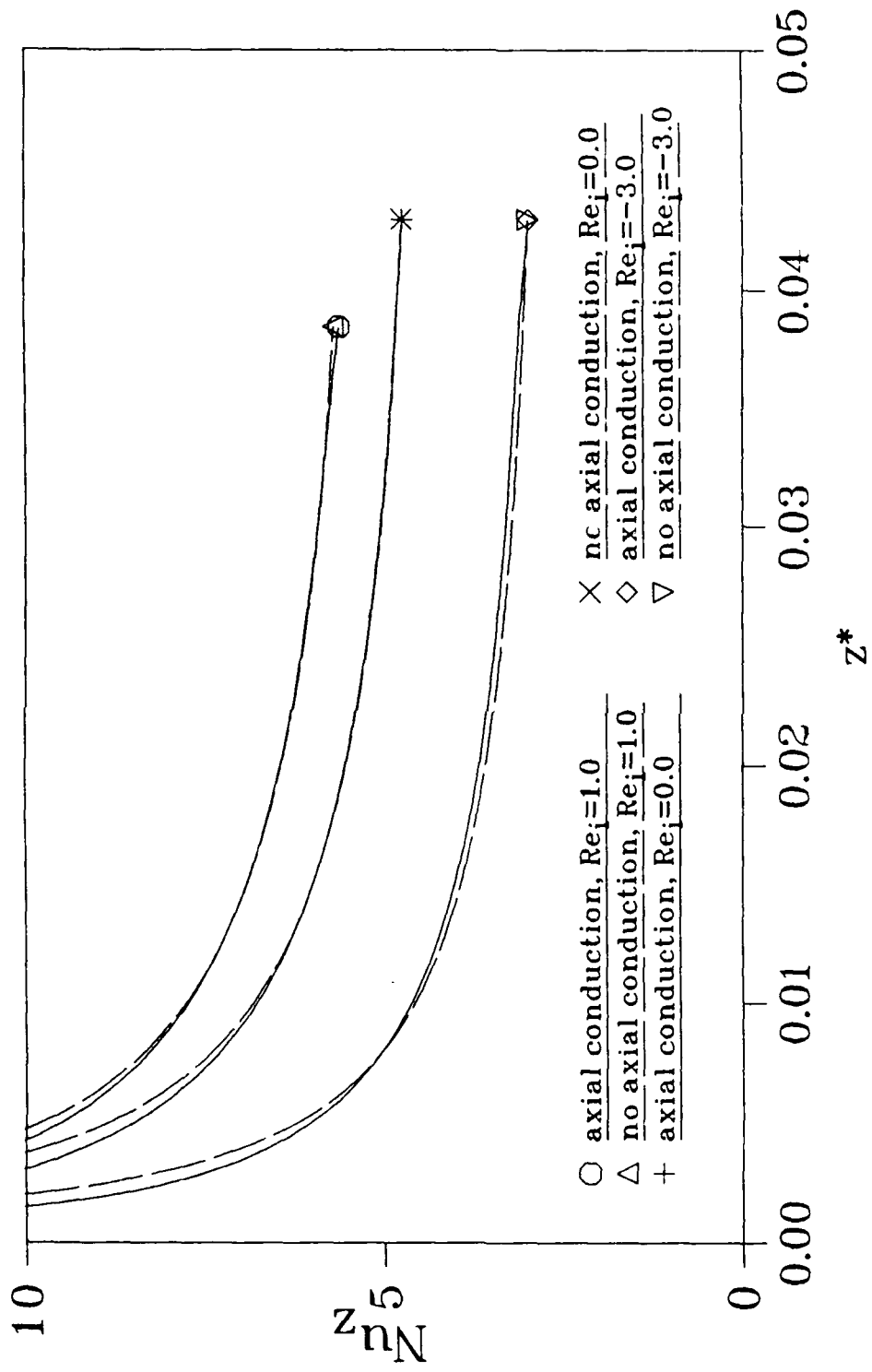
Fig. 2.10 The effect of axial heat conduction on the Nusselt number at the interface for $Pe=1000$, $K=500$ and $\Delta=0.1$

predicted with and without wall and fluid axial conduction for Pe = 100, Δ = 0.1, K = 500 and Re_i = 1.0, 0.0, -3.0. When axial conduction is neglected, the Nusselt number is overpredicted along the entire entry region. This effect diminishes as the wall-to-fluid conductivity ratio is reduced as shown in Figure 2.9. When the Peclet number is increased to 1000, smaller differences are observed.

2.6 Conclusions

The effect of axial heat conduction have been studied for cases with blowing and suction and with an impermeable wall. We concluded that large errors will arise in the solution when the axial wall conduction is neglected for blowing cases with large K. As K increases, the results approach the solution of constant wall temperature at the interface without axial wall conduction. For K = 1, the local Nusselt number approaches the solution of constant heat flux at the interface. It is confirmed that the effect of axial conduction in the wall can be neglected reasonably when the wall is very thin. But when the wall is very thick, the results approach the solution of constant wall temperature at the interface. Increasing Pe by a factor of 10 reduces the effect of axial conduction much more than a corresponding reduction of Δ or K.

III. THE THERMAL PERFORMANCE OF HEAT PIPES WITH LOCALIZED HEAT INPUT

3.1 Summary

The performance of heat pipes with localized heat input including the effects of axial and circumferential heat conduction under high and low working temperatures was investigated. The numerical results show that when heat pipes are spot heated, the peak temperature of the wall is greatly reduced and the surface can be protected from being burned out by the high heat flux. The boiling limitation becomes the most important limitation for this type of heat pipe. Numerical results for block heating a heat pipe with low working temperatures indicate a good agreement with existing experimental data. Also, most of the input heat passes through the wall beneath the heated block.

3.2 Introduction

Since the publication of the first paper on heat pipes, various kinds of heat pipes have been manufactured, tested, and put into operation. In the meantime, thousands of theoretical and experimental analyses dealing with the characteristics of heat pipes have been published. Among the special types of heat pipes, localized heat input or spot heated heat pipes have not been extensively studied. This is suprising since many high performance heat pipes are subjected to localized heating for a variety of applications. The study of spot heating heat pipes is important in research areas such as the cooling of leading edges on hypersonic aircraft, the protection of special surfaces from being attacked by very high heat flux sources such as a laser beam, cooling of microelectronic elements, etc.

According to the working conditions and the application, spot heated heat pipes can be classified into two major types: namely, heat pipes with low or moderate working temperatures mainly used for the purpose of energy conservation or electronic cooling, and heat pipes with high working temperatures used to protect a surf.ce from being burned out by a very high heat flux. Rosenfeld [1987] studied the performance of line heated heat pipes with low working temperatures analytically with a one-dimensional model (circumferential direction) and numerically with a two-dimensional model (radial and circumferential directions).

For the present analysis of spot heating or block heating, we should consider axial conduction, which has a much more pronounced effect than conduction in the radial direction. Furthermore, the effect of radiation

is included in the analysis of spot heated heat pipes with high working temperatures. In addition, the operating temperature of the heat pipe should be obtained by an overall energy balance rather than an input condition as done by Rosenfeld [1987] for the line heated heat pipe.

3.3 Analysis

3.3.1 Spot heated heat pipes with high working temperatures

Spot heated heat pipes should be used to protect a surface from being burned out by a very high heat flux by using the working fluid within the porous media inside the pipe as an evaporator to absorb the heat energy. The vapor flows to the rest of the porous surface and releases latent heat energy as it condenses. The energy is dissipated into space or to the environment by radiation from the outer surface. Because of the high latent heat of the working fluid, a large amount of incoming heat can be absorbed by evaporation, and spread to the surrounding surface of the wall to be dissipated into space, without causing the temperature in the wall to become too high and burn out. The positions of the evaporator and condenser are not fixed nor are their areas. These depend on where the pipe is hit by the incoming heat flux, and how large the surface area is that is being hit by the heat flux. Also, this kind of heat pipe has no adiabatic section (Fig. 3.1a). The end caps have been removed to demonstrate the typical interior structure and the vapor flow pattern. The origin of the coordinate system is set at the center of the heated spot. Figure 3.1b shows a typical wall temperature profile along the x axis at $y = 0$ and the vapor temperature T_s. If the temperature of the wall is higher than T_s, it serves as the evaporator; if the wall temperature is lower than T_s, it serves as the condenser. This particular phenomena is not observed for conventional heat pipes operated at a nearly constant wall temperature.

The present analysis is based on a number of physical assumptions.
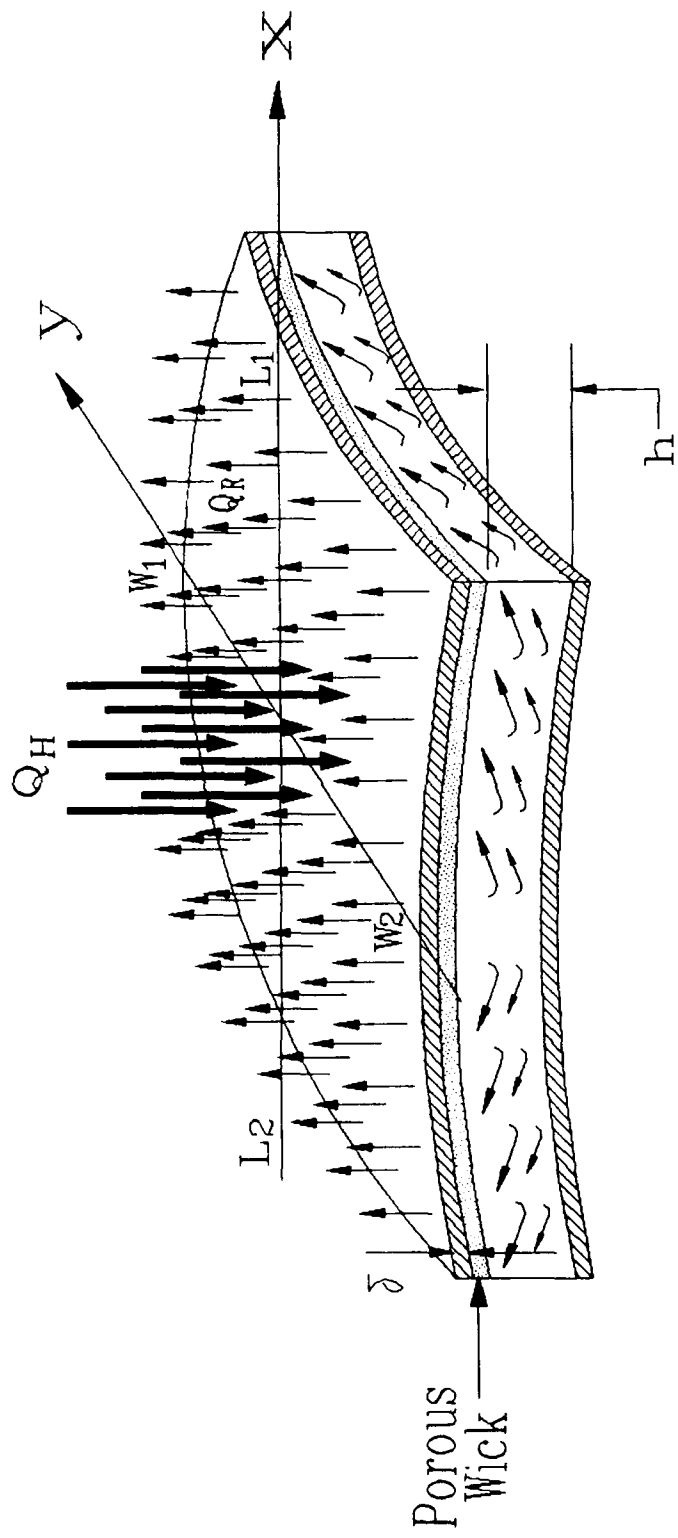
Fig. 3.1a Typical configuration of a spot heated heat pipe.
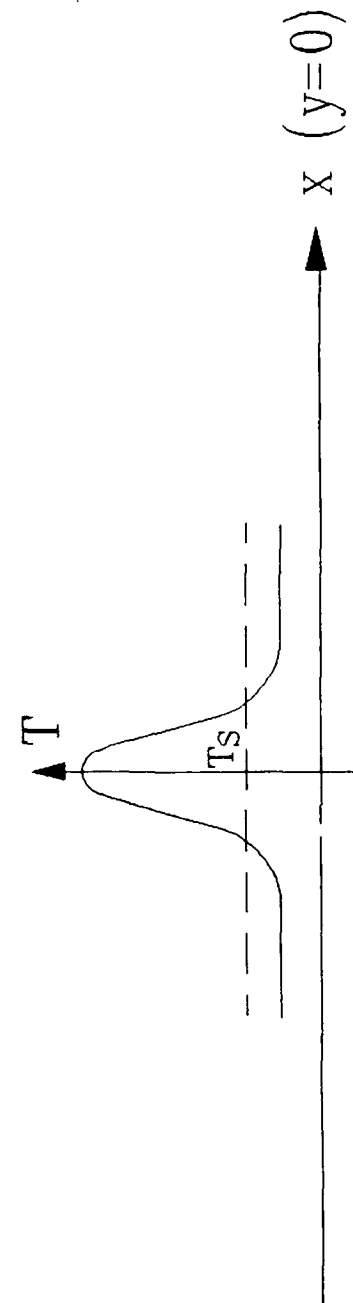
Fig. 3.1b Typical wall temperature profile at y=0.

We must emphasize the wall temperature in the analysis to prevent the heat pipe wall from melting. The heat pipe is assumed to contain only one fluid and is operating under steady-state conditions. This means that the vapor region is nearly isothermal, and the total energy input and output are equal. The wick-liquid matrix is assumed to be very thin, and its existence is represented by the evaporation heat transfer coefficient, H_E, and the condensation heat transfer coefficient, H_C. This is a good approach for the purpose of designing a heat pipe because in most cases, evaporation and condensation heat transfer coefficients in porous media can only be obtained from experimental data (Dunn and Reay [1982]; Groll et al. [1984]; Abhat and Seban [1974]). The common measurable parameters in experiments on heat pipes are T_S, H_E, H_C, and the wall temperature. The results of the analysis based on the above concept can be readily used as a guide when designing heat pipes. Finally, it is assumed that the wall thickness is thin, and the radius of curvature of the surface is much larger than h, so that the wall temperature does not vary substantially with radial position in the wall.

In the Cartesian coordinate system shown in Fig. 3.1a, the two-dimensional governing equations and boundary conditions for the wall can be written by an energy balance of the differential elements in each section of the heat pipe. For the evaporation section, except the surface beneath the heated spot, the governing equation is

$$\frac{\partial}{\partial x}\left[k\frac{\partial T}{\partial x}\right] + \frac{\partial}{\partial y}\left[k\frac{\partial T}{\partial y}\right] - \frac{\epsilon \sigma}{\delta}\left[T^4 - T_o^4\right] - \frac{q_E}{\delta} = 0 \qquad (3.1)$$

where $T = T_E$ at the junction of the evaporator and the condenser segments, ϵ is the emissivity, δ is the thickness of the wall, T_0 is the temperature of the environment, and q_E is the evaporation heat flux. We have shown that the evaporation heat transfer coefficient varies with heat flux because the menisci in a capillary evaporator recede as the heat flux increases. An examination of the reported data shows that a power-law boiling relation is appropriate for relating the heat flux to the evaporating temperature drop in a heat pipe (Rosenfeld [1987]; Dunn and Reay [1982]), i.e.;

$$q_E = a(T - T_s)^b \qquad (3.2)$$

The most common values of the exponent vary from 1.0 to 2.0, with that of liquid metal heat pipes remaining 1.0 and the coefficient $a = \bar{H}_E$ in many cases (Dunn and Reay [1982]; Groll et al. [1984]; Davis and Ferrell [1974]).

For the wall beneath the heated spot, the corresponding equation is

$$\frac{\partial}{\partial x}\left[k\frac{\partial T}{\partial x}\right] + \frac{\partial}{\partial y}\left[k\frac{\partial T}{\partial y}\right] + \frac{q_H}{\delta} - \frac{q_E}{\delta} = 0 \qquad (3.3)$$

where q_H is the incoming heat flux at the heated spot.

For the condenser segment, the governing equation is

$$\frac{\partial}{\partial x}\left[k\frac{\partial T}{\partial x}\right] + \frac{\partial}{\partial y}\left[k\frac{\partial T}{\partial y}\right] - \frac{\epsilon\sigma}{\delta}\left[T^4 - T_0^4\right] + H_C\left[T_s - T\right] = 0 \qquad (3.4)$$

With $T = T_C = T_E$ at the junction of the evaporator and the condenser

124

sections, and $\frac{\partial T}{\partial n} = 0$ at the peripheral boundary of the heat pipe where n is the normal direction of the periphery.

The vapor temperature, T_s, is an unknown in equation (3.4). The fact that the vapor temperature must be determined requires one more equation which is provided by an energy balance over the entire heat pipe. A steady-state operation has no energy and mass accumulations, and the vapor temperature will be adjusted according to the heat input and the ambient conditions. This means that the condensing heat transfer is equal to that of evaporation, and all the heat input is rejected to the ambient, i.e.;

$$\iint_{A_E} H_E(T - T_s)dA = \iint_{A_C} H_C(T_s - T)dA \qquad (3.5)$$

$$Q_H = \iint_A \epsilon\sigma(T^4 - T_0^4)dA \qquad (3.6)$$

where Q_H is the heat input through the spot; A_E and A_C are the evaporator surface area and the condenser surface area inside the heat pipe, respectively; A is the outer radiation surface area. Note that A is not necessarily equal to A_C. When spot heating heat pipes, the evaporator and condenser are not prescribed. Usually, the heated area is small, and a large amount of heat needs to be spread to the surrounding surfaces to be dissipated. Therefore, A_E is larger than the spot heating area A_H and as a result, $A > A_C$.

3.3.2 Block heated heat pipes with low or moderate working temperatures

Block heated heat pipes are normally used to transport energy from

125

one place to another to conserve energy or to cool electronic components. The evaporator and condenser segments are normally separated, which is similar to conventional heat pipes except for the localized heating. The working temperature is comparatively low or moderate, which means that radiation heat transfer is not important in the analysis of these heat pipes.

Consider the heat pipe shown in Fig. 3.2. It has an evaporator section of length, L_E, a wall thickness, δ, an outside radius, R, and a block heated area of width, W_H, and length, L_H.

The analysis here is based on similar assumptions used for spot heated heat pipes with high operating temperatures. With a thin wall and a large pipe diameter, the problem can be investigated in Cartesian coordinates.

In the evaporator section, the governing equation for the pipe wall that is not underneath the heated block is

$$\frac{\partial^2 T}{\partial x^2} + \frac{\partial^2 T}{\partial s^2} - \frac{a}{k\delta}(T - T_s)^b = 0 \qquad (3.7)$$

and the governing equation for the wall beneath the heated block is

$$\frac{\partial^2 T}{\partial x^2} + \frac{\partial^2 T}{\partial s^2} - \frac{a}{k\delta}(T - T_s)^b + \frac{q_H}{k\delta} = 0 \qquad (3.8)$$

In equation (3.8), we have employed the power-law relation for the boiling heat flux. In this situation, b is greater than 1.0. The boundary conditions for this problem are
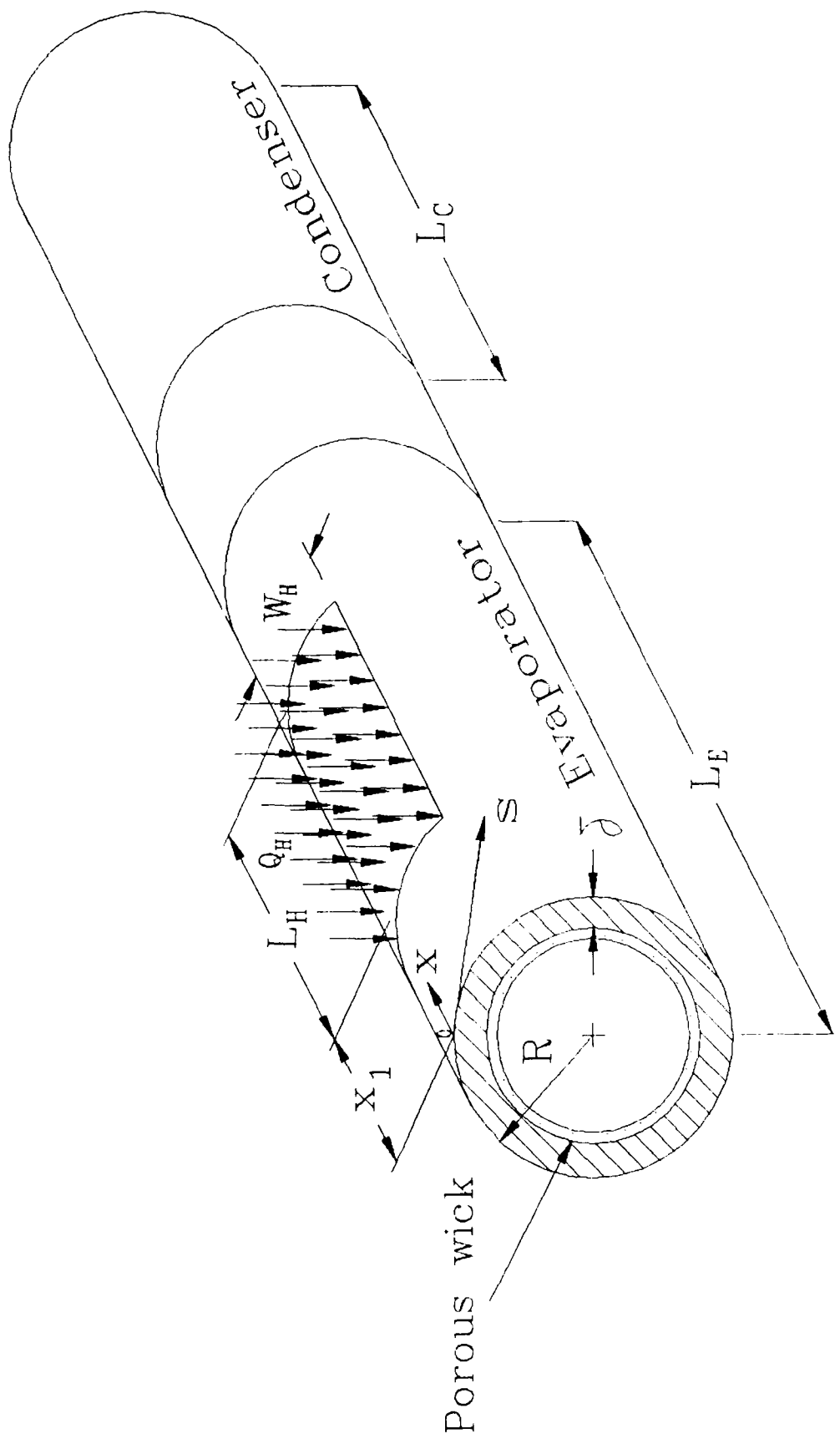
Fig. 3.2   A general configuration of a block heated heat pipe.

$$\frac{\partial T}{\partial x} = 0 \quad \text{at } x = 0 \text{ and } x = L_E \qquad\qquad (3.9)$$

$$\frac{\partial T}{\partial s} = 0 \quad \text{at } s = 0 \text{ and } s = \pi R \qquad\qquad (3.10)$$

Equation (3.9) defines an insulated boundary condition, and equation (3.10) is true due to symmetry.

Equations (3.9) and (3.10) can be nondimensionalized with the following variables:

$$T^* = (T - T_s)/T_H, \quad X = x/\pi R, \quad Y = s/\pi R$$

The resulting nondimensional equations are

$$\frac{\partial^2 T^*}{\partial X^2} + \frac{\partial^2 T^*}{\partial Y^2} + C_1 T^{*b} = 0 \qquad\qquad (3.9a)$$

$$\frac{\partial^2 T^*}{\partial X^2} + \frac{\partial^2 T^*}{\partial Y^2} + C_1 T^{*b} + C_2 q_H = 0 \qquad\qquad (3.10a)$$

where $C_1 = -a(\pi R)^2 T_H^{b-1}/\delta k$, $C_2 = (\pi R)^2/T_H \delta k$ and T_H is the reference temperature.

The above model is justified because since the main purpose is to transport energy from one place to another, the heat dissipation to the ambient from the evaporator section is negligible. Also, because of the large evaporation heat transfer coefficient, very little heat is transported from the evaporator to the condenser through the pipe wall. Section 3.4 shows the numerical results.

3.4 Numerical Results and Discussion

The governing equations for spot heated and block heated heat pipes are nonlinear and nonhomogeneous and require an iterative procedure. The problems were solved by using the finite-difference method based on the control-volume formulation (Patankar [1980]). A combination of the direct method (TDMA) and the Gauss-Seidel method was employed to solve the discretization equations. In some special cases, under-relaxation parameters were used to control the advancement of the solutions. The grid size employed in the program varies from 20 x 70 to 70 x 300 depending on the computational domain. To determine a suitable grid size, the computed temperature profiles are compared for a number of different grid sizes for the same problem. The maximum errors among these grid sizes are less than 1.0%. Also, an energy balance over the entire computational domain was checked for every computed temperature field, the maximum error of which was at most 0.1%.

Figure 3.3 shows the numerical results for spot heated heat pipes with high working temperatures. Like conventional heat pipes, the heat input has a strong influence on the heat pipe performance. As the heat input increases, the peak wall temperature increases. For example, the peak temperature with Q_H = 8000 W is more than twice as high as that with Q_H = 2000 W.

In conventional heat pipes, the area available for heat input is comparatively large, the input heat flux is comparatively low, and the working limitation is mainly determined by the total energy input. With spot heated heat pipes, the situation is different. Figure 3.4 shows the temperature distribution of the wall with a very high incoming heat flux
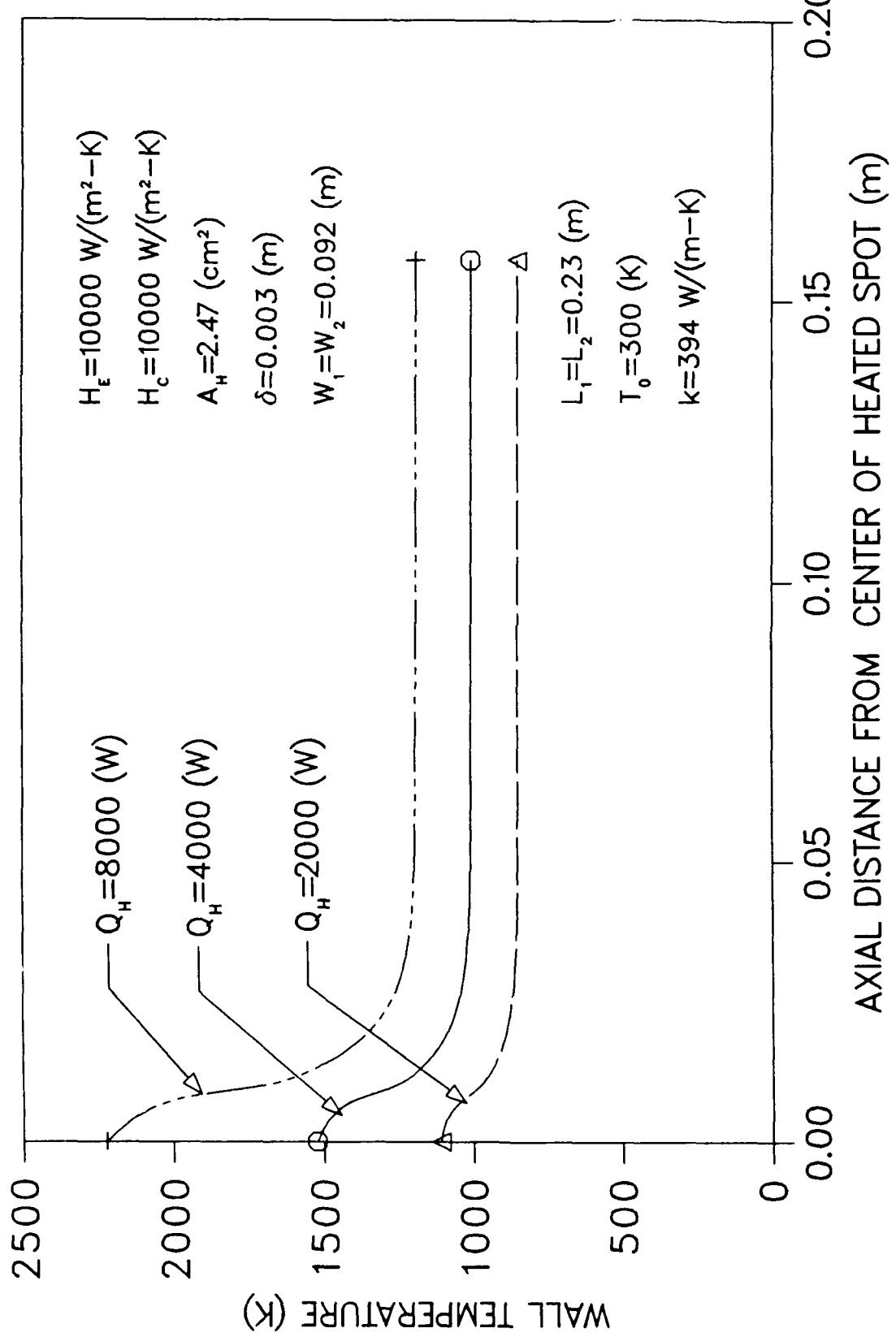
FIG.3.3 THE VARIATION OF THE WALL TEMPERATURE WITH INPUT HEAT

130
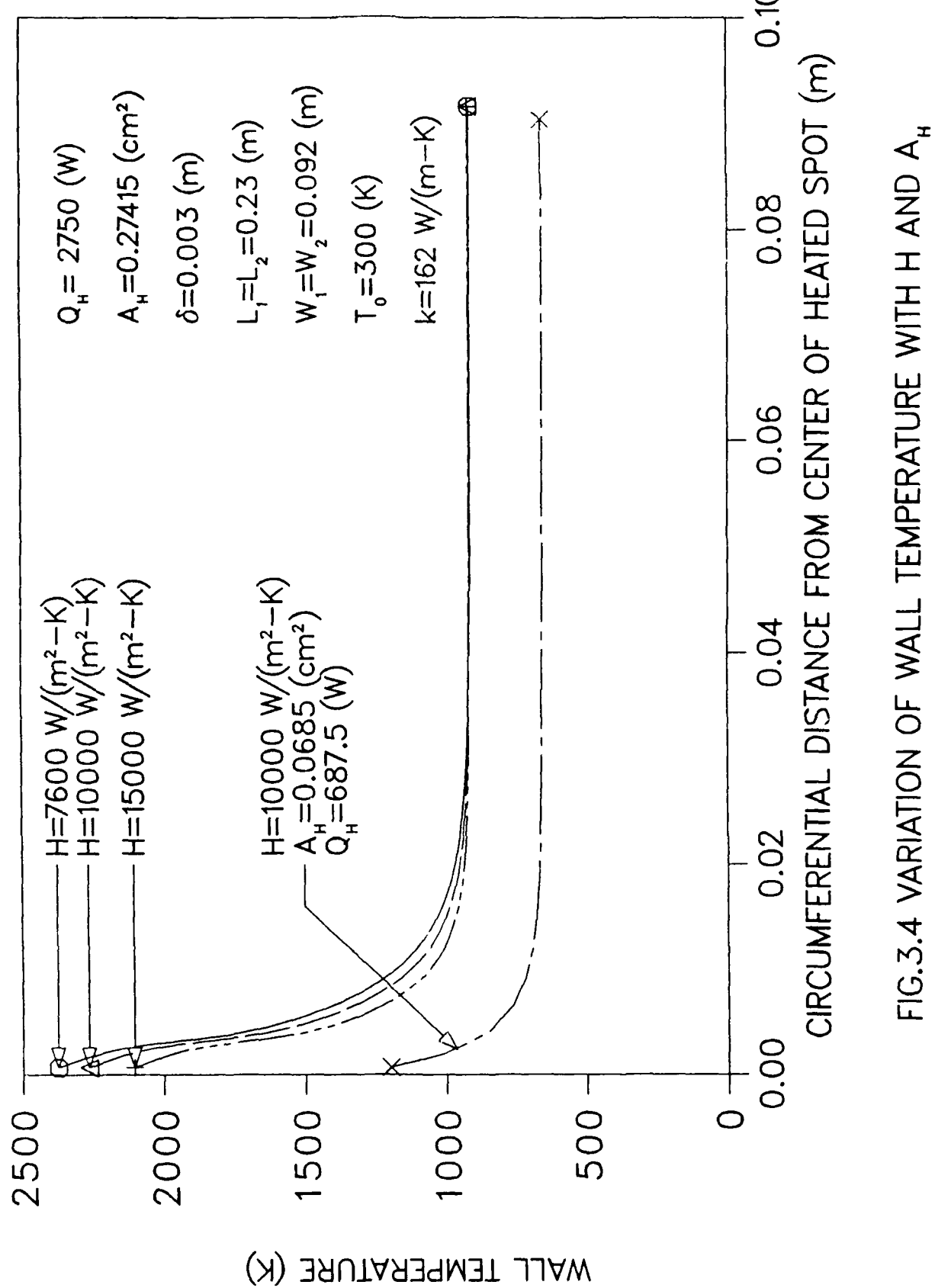
FIG.3.4 VARIATION OF WALL TEMPERATURE WITH H AND A_H

The figure plots WALL TEMPERATURE (K) on the vertical axis (0 to 2500) against CIRCUMFERENTIAL DISTANCE FROM CENTER OF HEATED SPOT (m) on the horizontal axis (0.00 to 0.10).

Legend:
- H=7600 W/(m²−K)
- H=10000 W/(m²−K)
- H=15000 W/(m²−K)

- H=10000 W/(m²−K)
- A_H=0.0685 (cm²)
- Q_H=687.5 (W)

Parameters:
- Q_H = 2750 (W)
- A_H=0.27415 (cm²)
- δ=0.003 (m)
- L_1=L_2=0.23 (m)
- W_1=W_2=0.092 (m)
- T_0=300 (K)
- k=162 W/(m−K)

(as high as 10 kW/cm^2). Comparing the curve of $H = H_E = H_C = 10,000$ W/(m^2-K) and $Q_H = 2,750$ W in Fig. 3.4 with that of $Q_H = 4000$ W in Fig. 3.3, we know that even though the heat input $Q_H = 2750$ W in Fig. 3.4 is less than that of $Q_H = 4000$ W in Fig. 3.3, its peak temperature is still several hundred degrees higher because of the smaller area that is heated. On the other hand, Fig. 3.4 shows that a higher heat transfer coefficient can reduce the peak temperature, as is expected.

Also shown in Fig. 3.4 is the influence of A_H on the peak wall temperature. The curve with a much lower peak wall temperature in Fig. 3.4 is subject to the same heat flux as that of the other three curves ($q_E = 10$ kW/cm^2), but a smaller heating area (Q_H is also smaller). The resultant peak wall temperature is almost 1,000 degrees lower than that with the larger heating area. In this study, the heating area is square. Because of the small heating areas, its shape is less important.

Unlike conventional heat pipes, the thermal conductivity of the wall influences the wall temperature distribution greatly for spot heated heat pipes, especially in the case of a very high incoming heat flux, as shown in Fig. 3.5. When the thermal conductivity of the wall is small, the peak temperature would jump intolerably high and the surface would be burned out. On the other hand, with a large wall thermal conductivity, the peak temperature decreases sharply. This is not surprising because a large amount of heat needs to be transferred to the surrounding wall through a very small area by conduction.

In conventional heat pipes, better cooling conditions and a larger cooling surface can ameliorate the performance and result in a lower working temperature. This is also true for spot heated heat pipes. The trend is well illustrated in Fig. 3.6, where a larger surface area

132
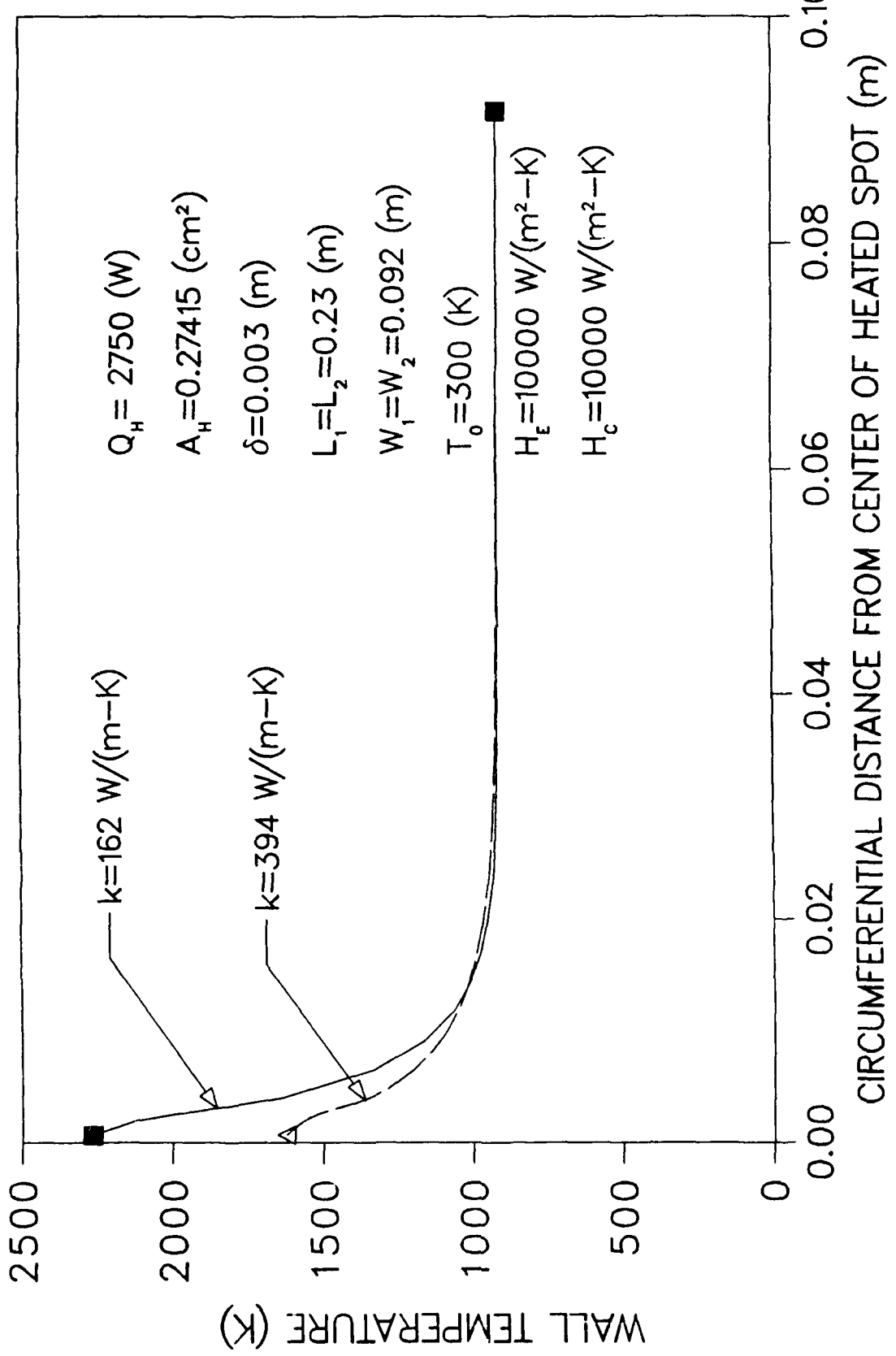
FIG.3.5 VARIATION OF WALL TEMPERATURE WITH THERMAL CONDUCTIVITY k
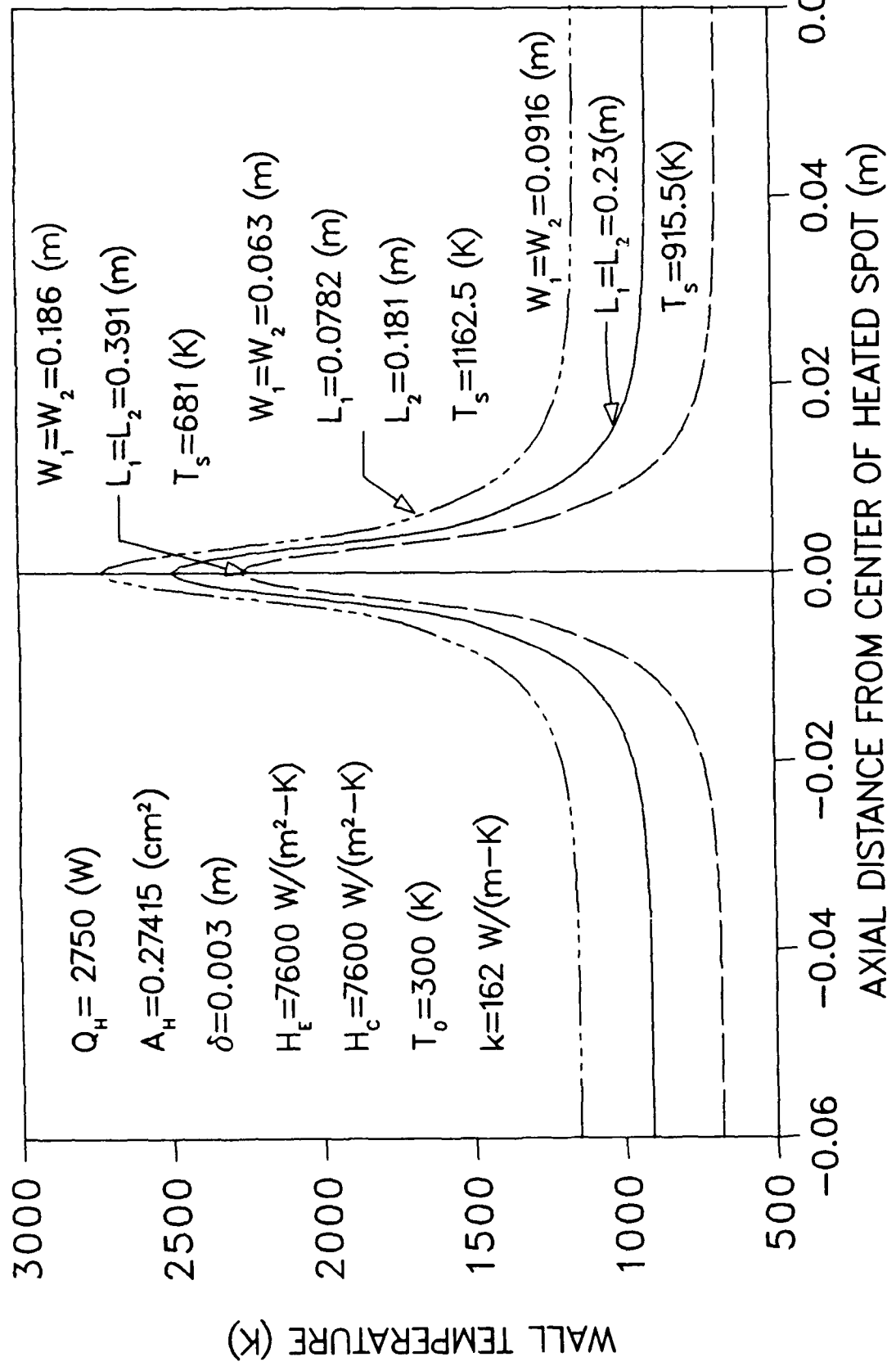
FIG.3.6 VARIATION OF WALL TEMPERATURE WITH HEAT PIPE SURFACE AREA

Plot parameters:

$Q_H = 2750$ (W)
$A_H = 0.27415$ (cm²)
$\delta = 0.003$ (m)
$H_E = 7600$ W/(m²−K)
$H_c = 7600$ W/(m²−K)
$T_o = 300$ (K)
$k = 162$ W/(m−K)

$W_1 = W_2 = 0.186$ (m)
$L_1 = L_2 = 0.391$ (m)
$T_s = 681$ (K)

$W_1 = W_2 = 0.063$ (m)
$L_1 = 0.0782$ (m)
$L_2 = 0.181$ (m)
$T_s = 1162.5$ (K)

$W_1 = W_2 = 0.0916$ (m)
$L_1 = L_2 = 0.23$ (m)
$T_s = 915.5$ (K)

AXIAL DISTANCE FROM CENTER OF HEATED SPOT (m)

WALL TEMPERATURE (K)

134

(radiation heat transfer area) corresponds to a lower working temperature T_s. Also, the peak wall temperature is decreased accordingly. But, if we pay attention to the area around the center of the heated spot, we may notice that the temperature difference between the peak temperature and the working temperature for different curves almost remains the same. This local phenomenon obviously results from the localized heat input characteristics of the heat pipe. The most important factor which determines the performance is the working conditions at the heated spot.

To estimate the validity of spot heating heat pipes to reduce the wall temperature, we compared the wall temperature of a plate that is not a heat pipe with that of a plate heat pipe. The curve with the solid circle legend in Fig. 3.7 is the wall temperature profile of a spot heated heat pipe under normal working conditions, while the curve indicated with $H = 0$ is the temperature profile of a plate that is not a heat pipe ($H_E = H_C = H = 0$), with other conditions being the same. Obviously, the peak wall temperature of the surface adopting heat pipe technology is reduced significantly.

When we compare the conventional heat pipes, it is clear that spot heated heat pipes have small evaporator surfaces, very high evaporation heat fluxes, large condenser surfaces and vapor passages. Because of these factors, the boiling limit becomes the most important operating limit of these heat pipes. In Fig. 3.7, the curve indicated with $\Delta T_C = 100$ K assumes that the boiling limitation is reached for the local evaporating surface when $T - T_s > \Delta T_C = 100$ K. When this occurs, the porous media at that point is assumed to be completely dry, and no evaporation takes place. For the curve with the solid circle legend, this restriction has not been imposed on ΔT, and the pipe works properly
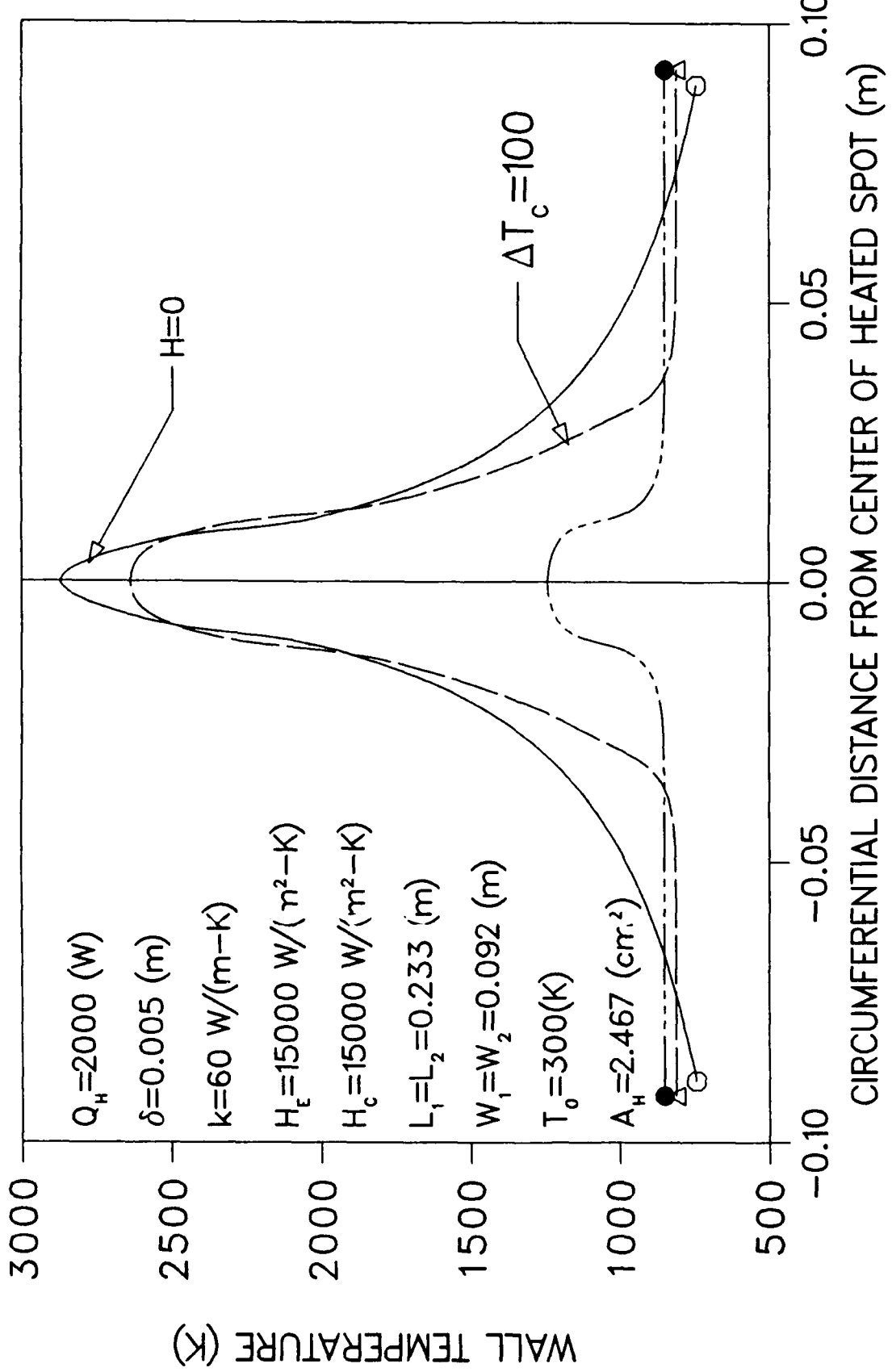
FIG.3.7 TEMPERATURE PROFILES WITH DIFFERENT WORKING CONDITIONS

Q_H=2000 (W)

δ=0.005 (m)

k=60 W/(m–K)

H_E=15000 W/(m²–K)

H_c=15000 W/(m²–K)

L_1=L_2=0.233 (m)

W_1=W_2=0.092 (m)

T_o=300(K)

A_H=2.467 (cm²)

H=0

ΔT_c=100

WALL TEMPERATURE (K)

CIRCUMFERENTIAL DISTANCE FROM CENTER OF HEATED SPOT (m)

136

with the other conditions being the same. Once the boiling limitation is reached and evaporating surface becomes dry, the wall temperature at the heated spot will jump thousands of degrees higher than that of heat pipes under normal working conditions. From the viewpoint of heat pipe design, most difficulties arise from the avoidance of the incipience of boiling in the porous wick of the pipe. Special care must be taken to properly design the structure of the porous media, to choose suitable working fluids, and to insure the wettability of the wick and the wall to increase the boiling limitation.

In addition, the emissivity of the surface and the thickness of the wall have strong effects on the temperature profile of the wall. Increasing the emissivity will reduce the working temperature, and therefore the peak wall temperature. The value of ϵ in this numerical calculation was taken as 0.8. Also, a larger thickness of the wall will alleviate the temperature jumps at the center of the heated spot, but this is not practical in many applications.

Figures 3.8 through 3.10 show the numerical results for heat pipes with localized heat input working under low or moderate temperatures. In this situation, the heated area is comparatively large, and the heat flux is comparatively low, so that the temperature jump is not so severe as that for spot heating heat pipes with high working temperatures.

Figure 3.8 shows the comparison of the numerical results of the circumferential wall temperature profile with the experimental data from the paper by Rosenfeld [1987]. The experiment was conducted with a narrow line heater at the evaporation section of the heat pipe. The evaporation heat flux relation is also taken from that experiment, with

FIG.3.8 COMPARISION OF THE NUMERICAL RESULT WITH THE EXPERIMENTAL DATA

Q_H=950 (W)

δ=0.003175 (m)

L_E=L_H=0.1 (m)

W_H=0.02 (m)

k=230 W/(m−°C)

a=17330

b=1.215

X axis: CIRCUMFERENTIAL DISTANCE FROM CENTER OF HEATED BLOCK (m)

Y axis: WALL TEMPERATURE (°C)

138
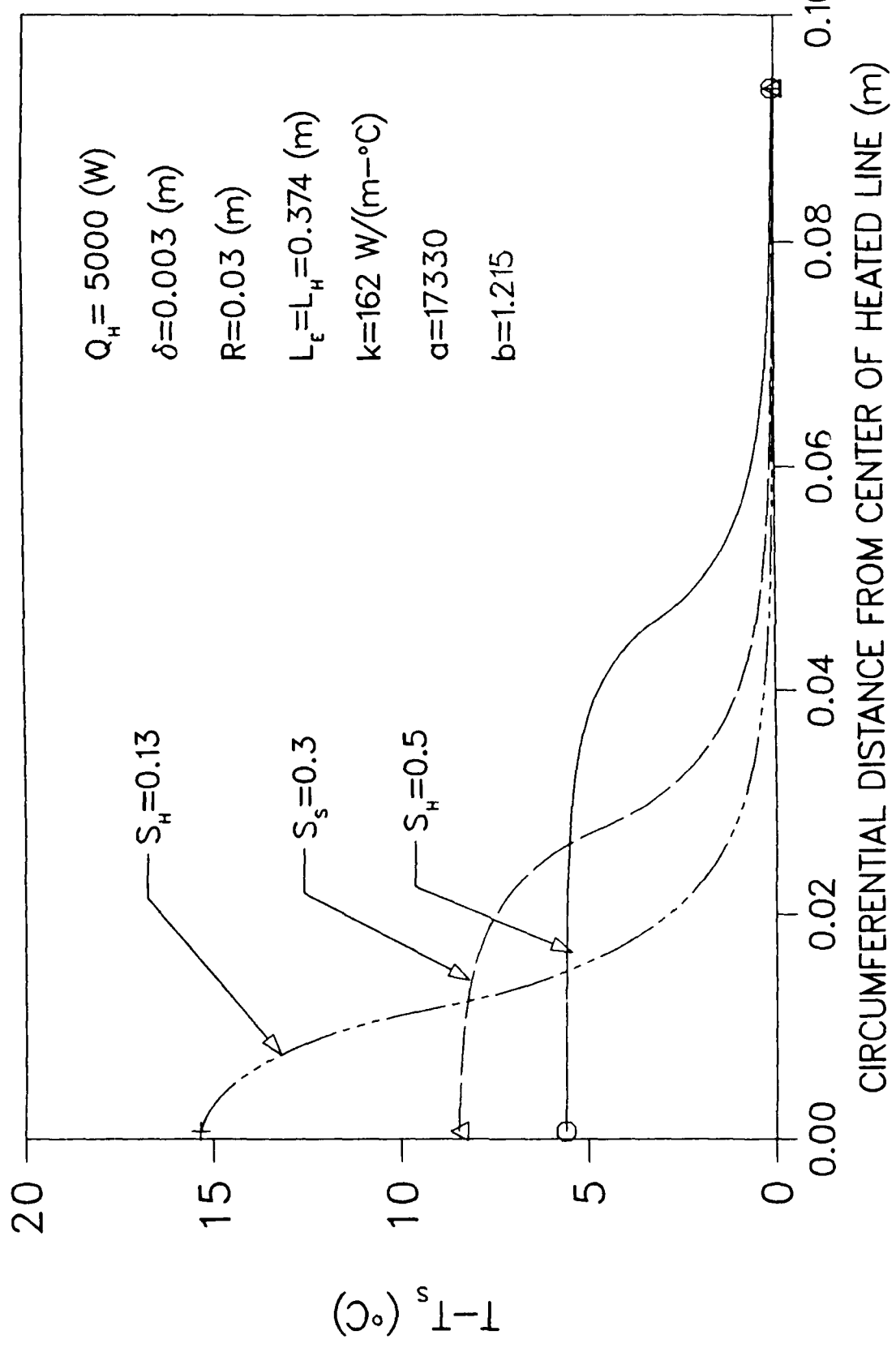
FIG.3.9 VARIATION OF THE TEMPERATURE DIFFERENCE T-T$_s$ WITH THE DIMENSIONLESS WIDTH S$_H$

Plot axes and annotations:

- Y-axis: T-T$_s$ (°C), scale 0 to 20
- X-axis: CIRCUMFERENTIAL DISTANCE FROM CENTER OF HEATED LINE (m), scale 0.00 to 0.10

Parameters:
- Q$_H$ = 5000 (W)
- δ = 0.003 (m)
- R = 0.03 (m)
- L$_\epsilon$ = L$_H$ = 0.374 (m)
- k = 162 W/(m-°C)
- a = 17330
- b = 1.215

Curve labels:
- S$_H$ = 0.13
- S$_s$ = 0.3
- S$_H$ = 0.5
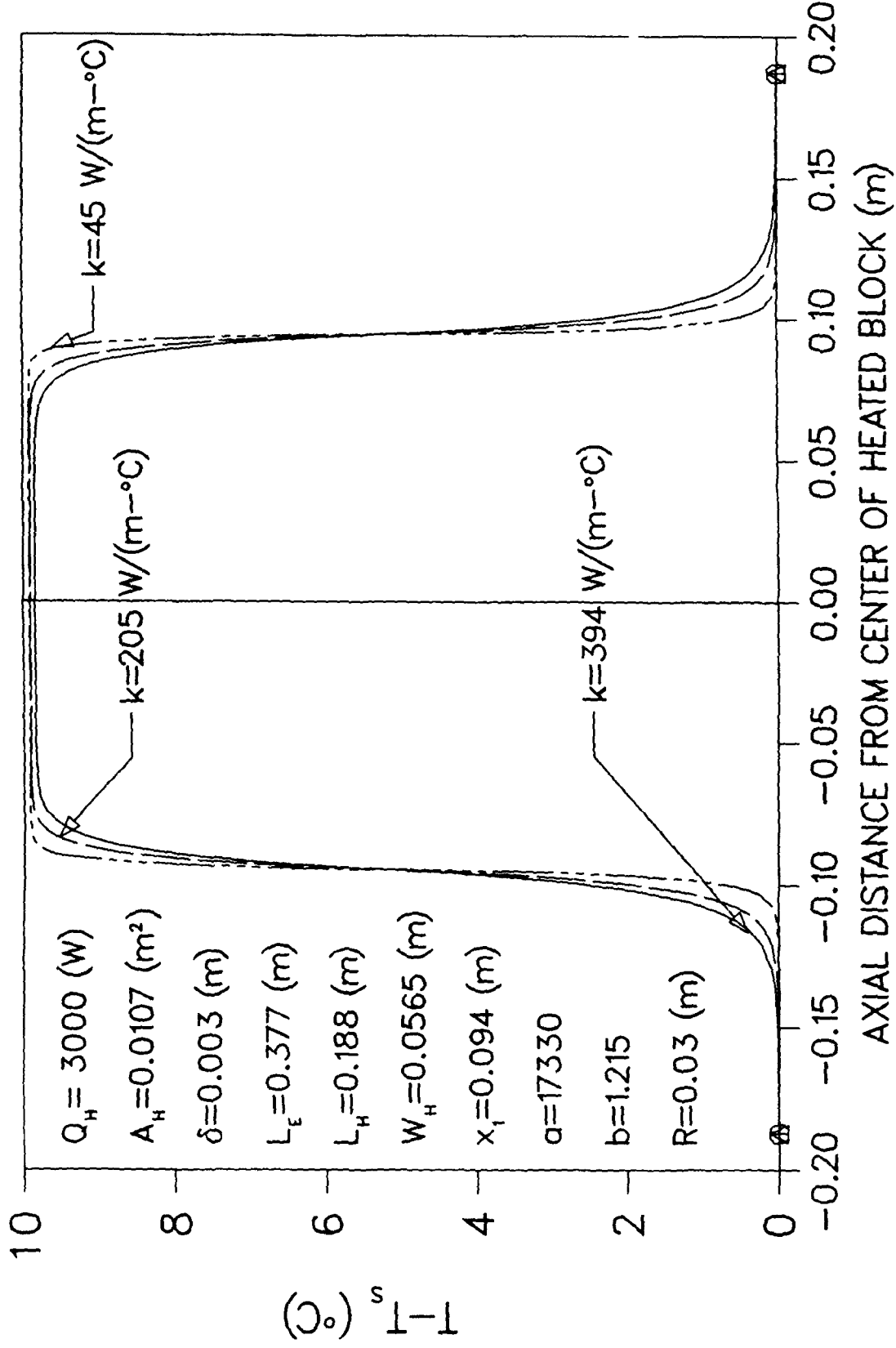
FIG.3.10 VARIATION OF $T-T_s$ WITH THERMAL CONDUCTIVITY k

$Q_H = 3000$ (W)
$A_H = 0.0107$ (m²)
$\delta = 0.003$ (m)
$L_\epsilon = 0.377$ (m)
$L_H = 0.188$ (m)
$W_H = 0.0565$ (m)
$x_1 = 0.094$ (m)
$a = 17330$
$b = 1.215$
$R = 0.03$ (m)

k=45 W/(m—°C)

k=205 W/(m—°C)

k=394 W/(m—°C)

$$q_E = a(T - T_s)^b$$

where a = 17330, and b = 1.215.

The agreement between the numerical results and the experimental data is excellent. The line width surely influences the performance of the heat pipe. With the width of the heated line becoming larger, the temperature distribution along the circumferential direction becomes smoother, as shown in Fig. 3.9. Among the different heating widths, half heating (s_H = $W_H/\pi R$ = 0.5) is of special interest in many applications. Obviously with a uniform input heat flux and a large evaporation heat transfer coefficient, the temperature profile of the wall beneath the heated block is nearly smooth, and the working conditions of this half of the evaporator are nearly the same as that of heat pipes with a uniform heat input.

Figure 3.10 shows the performance of block heated heat pipes for different values of the wall thermal conductivity. Unlike the spot heated heat pipes shown in Fig. 3.5, the thermal conductivity of the wall has little effect on the temperature distribution. The reason is that, because of the large boiling heat transfer coefficient, most of the input heat was absorbed by the evaporating surface beneath the heated block, and only a small amount of heat is spread to the wall that is not heated. This is more pronounced as the wall thermal conductivity decreases. For the working conditions indicated in Fig. 3.10, with k = 394 W/(m-K), 86.2% of the heat passes through the wall under the heated block, while with k = 45 W/(m-K), 96% of the heat passes through the wall under the heated block.

3.5 Conclusions and Remarks

1. The use of a heat pipe is an excellent method to protect a surface from burning out when the surface is spot heated. The peak wall temperature is greatly reduced due to the operation of the heat pipe. The parameters which influence the performance are Q_H, k, H_E, H_C, A_H, ϵ and δ. For a fixed heat input Q_H, larger values of k, A_H, H_E, H_C, or δ can reduce the peak wall temperature, and larger values of ϵ and the heat pipe surface area result in a lower working temperature. Because of the localized heating characteristics of heat pipes, a temperature jump is inevitable at the center of the heated spot and results in a large ΔT and a high q_E at the heated location. Special measures must be taken to increase the boiling limitation of the heat pipe. Otherwise, the temperature at the heated location will jump intolerably high. More work needs to be done on the structure of the porous media, the wettability of the wick and wall, and the vapor flow pattern in the pipe for this special kind of heat pipe.

2. The numerical results for localized heat input heat pipes working under low or moderate temperatures agree well with the existing experimental data and can be used to improve the prediction of heat pipe performance under localized heating. With a large evaporation heat transfer coefficient, most of the input heat passes through the wall under the heated block.

IV. A NUMERICAL ANALYSIS OF STEFAN PROBLEMS FCR GENERALIZED MULTI-DIMENSIONAL PHASE-CHANGE STRUCTURES USING THE ENTHALPY TRANSFORMING MODEL

4.1 Summary

An enthalpy transforming scheme is proposed to convert the energy equation into a nonlinear equation with the enthalpy, E, being the single dependent variable. The existing control-volume finite-difference approach has been modified to apply it to the numerical performance of Stefan problems. The model has been tested by applying it to a three-dimensional freezing problem. The numerical results are in good agreement with those existing in the literature. The model and its algorithm are further applied to a three-dimensional moving heat source problem showing that the methodology is capable of handling complicated phase-change problems with fixed grids.

4.2 Introduction

Heat flow and diffusion with melting and solidification are of great importance in many industrial applications. Examples are casting, welding, thermal energy storage units, heat pipe start-up from frozen state, etc. The last two operations were the major motivation for the present study. Phase-change processes may produce solid and liquid phase regions which have extremely complex appearances. Also, it is not possible to predict a priori what the phase-change front evolving in time will look like. Therefore, exact analytical solutions for these types of nonlinear problems are available only for some simplified and idealized systems. Apparently, numerical methods are the only practical method to handle the general melting and freezing problems providing that we can successfully trace the moving interface.

The numerical methods used to solve phase-change problems might be divided into two main groups. The first group is called strong numerical solutions. The focus here is on applying finite-difference techniques to the strong formulation of the pro ess, locating fronts and finding temperature distributions at each time step or employing a transformed coordinate system to immobilize the moving interfaces (Okada [1984], Ho and Chen [1986]). These methods are applicable to those processes involving one or two phases in one space dimension which, with the use of cumbersome schemes, are being applied to two-dimensional cases as well.

The second group is called weak numerical solutions (Shamsundar and Sparrow [1975], Crowley [1978], Voller and Cross [1981], Hsiao and Chung

144

[1984], Keung [1980], and Hsiao [1984]). These methods allow us to avoid paying explicit attention to the nature of the phase-change front. They appear to have great flexibility and are easily extended to multi-dimensional problems. In this group, the most important and widely used method is the enthalpy method. The advantages of the enthalpy reformulation are that the problem to be solved is formulated in a fixed region, and no modification of the numerical scheme is necessary to satisfy the conditions at the moving phase-change interface. Furthermore, this method is especially suitable both for the problems where the phase change occurs at a single temperature and the problems where the phase change occurs over a temperature range.

Most of the previous enthalpy models usually treated the enthalpy as a dependent variable in addition to the temperature and discretized the energy equation into a set of equations which contain both E and T. For the implicit schemes, they actually treated all of the terms containing T = T(E) as a constant heat source term in the energy equation during iterations at each time step. This may cause some problems for convergence when T = T(E) is complicated and physical properties change significantly as is the case of frozen heat pipe start-up, or when boundary conditions are severe. Furthermore, when the energy equation contains a convective term, the previous methods have difficulties in handling the relationship between the convective and diffusive terms because of the two dependent variable nature of the equation.

In this section, a simple strategy is proposed to transform the energy equation into a nonlinear equation with a single dependent

145

variable E. Thus, solving a phase-change problem is equivalent to solving a nonlinear enthalpy equation, and existing algorithms are readily applicable with some modifications.

4.3 Enthalpy Transformation of the Energy Equation

The energy equation governing three-dimensional laminar flow with no viscous dissipation and with incorporating the continuity equation in the Cartesian coordinate system (Kays and Crawford [1980], Patankar [1980]) is

$$\frac{\partial(\rho E)}{\partial t} + \frac{\partial}{\partial x}(\rho u E) + \frac{\partial}{\partial y}(\rho v E) + \frac{\partial}{\partial z}(\rho w E) = \frac{\partial}{\partial x}\left(k\frac{\partial T}{\partial x}\right) + \frac{\partial}{\partial y}\left(k\frac{\partial T}{\partial y}\right) + \frac{\partial}{\partial z}\left(k\frac{\partial T}{\partial z}\right)$$

$$(4.1)$$

with the state equation

$$\frac{dE}{dT} = c(T) \qquad\qquad (4.2)$$

In the case of constant specific heats for each phase, and that the phase change occurs at a single temperature, we have

$$T = \begin{cases} T_m + E/c_s & E \leq 0 & \text{(solid phase)} \\ T_m & 0 < E < H & \text{(mushy phase)} \\ T_m + (E - H)/c_\ell & E \geq H & \text{(liquid phase)} \end{cases} \qquad (4.3)$$

where T_m is the melting temperature. In the above relation, we have selected $E = 0$ to correspond to phase-change materials in their solid state at temperature T_m.

The "Kirchoff" temperature (Solomon et al. [1966]) is introduced as follows

$$T^+ = \int_{T_m}^{T} k(\eta)d\eta = \begin{cases} k_s(T - T_m) & T < T_m \\ 0 & T = T_m \\ k_\ell(T - T_m) & T > T_m \end{cases} \qquad (4.4)$$

Transforming eq. (4.3) with the definition given in eq. (4.4) results in

$$T^* = \begin{cases} k_s E/c_s & E \leq 0 \\ 0 & 0 < E < H \\ k_\ell(E - H)/c_\ell & E \geq H \end{cases} \qquad (4.5)$$

and eq. (4.1) becomes

$$\frac{\partial(\rho E)}{\partial t} + \frac{\partial}{\partial x}(\rho u E) + \frac{\partial}{\partial y}(\rho v E) + \frac{\partial}{\partial z}(\rho w E) = \frac{\partial^2 T^*}{\partial x^2} + \frac{\partial^2 T^*}{\partial y^2} + \frac{\partial^2 T^*}{\partial z^2} \qquad (4.6)$$

Now, let us introduce an enthalpy function as follows

$$T^* = \Gamma(E)E + S(E) \qquad (4.7)$$

For the phase change occurring at a single temperature, we have

$$\Gamma(E) = \begin{cases} k_s/c_s & E \leq 0 \\ 0 & 0 < E < H \\ k_\ell/c_\ell & E \geq H \end{cases} \qquad (4.8)$$

148

and

$$
S(E) = \begin{cases} 0 & E \leq 0 \\ 0 & 0 < E < H \\ -Hk_\ell/c_\ell & E \geq H \end{cases} \tag{4.9}
$$

Upon substituting eq. (4.7) into eq. (4.6) and noticing that, for example,

$$
\frac{\partial^2 T^*}{\partial x^2} = \frac{\partial}{\partial x}\left[\frac{\partial(\Gamma E + S)}{\partial x}\right] = \frac{\partial^2}{\partial x^2}(\Gamma E) + \frac{\partial^2 S}{\partial x^2}
$$

we have

$$
\frac{\partial(\rho E)}{\partial t} + \frac{\partial}{\partial x}(\rho u E) + \frac{\partial}{\partial y}(\rho v E) + \frac{\partial}{\partial z}(\rho w E) = \frac{\partial^2 \Gamma E}{\partial x^2} + \frac{\partial^2 \Gamma E}{\partial y^2} + \frac{\partial^2 \Gamma E}{\partial z^2} + P \tag{4.10}
$$

with

$$
p = \frac{\partial^2 S}{\partial x^2} + \frac{\partial^2 S}{\partial y^2} + \frac{\partial^2 S}{\partial z^2} , \quad \Gamma = \Gamma(E) , \quad \text{and } S = S(E).
$$

The energy equation has been transformed into a nonlinear equation with single dependent E. The nonlinearity of the phase-change problem is evident in the above equation.

In the liquid region away from the moving front as indicated in the numerical domain of Fig. 4.1, eq. (4.10) reduces to the normal linear energy equation as
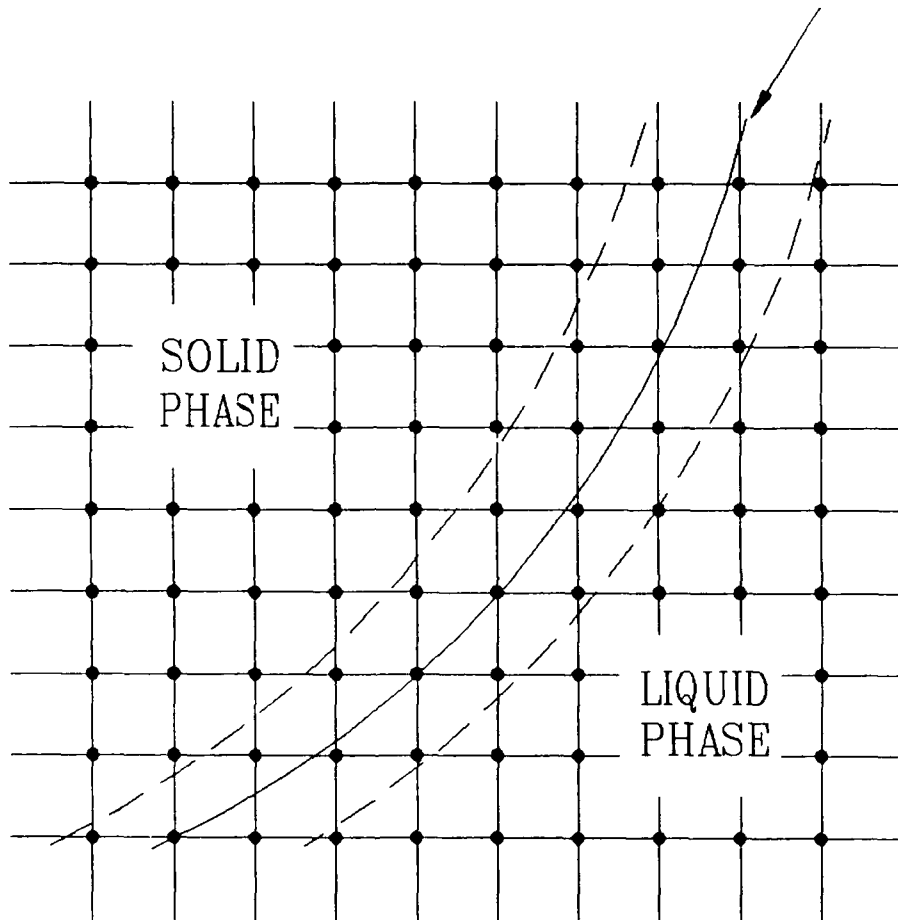
FIG. 4.1 DIFFERENT REGIONS IN A NUMERICAL DOMAIN

$$\frac{\partial(\rho_\ell E)}{\partial t} + \frac{\partial}{\partial x}(\rho_\ell uE) + \frac{\partial}{\partial y}(\rho_\ell vE) + \frac{\partial}{\partial z}(\rho_\ell wE) = \frac{\partial}{\partial x}(k_\ell \frac{\partial T}{\partial x}) + \frac{\partial}{\partial y}(k_\ell \frac{\partial T}{\partial y}) + \frac{\partial}{\partial z}(k_\ell$$
$$\frac{\partial T}{\partial z})$$
$$(4.11)$$

Also, in the solid region eq. (4.10) reduces to

$$\frac{\partial(\rho_s E)}{\partial t} + \frac{\partial}{\partial x}(\rho_s uE) + \frac{\partial}{\partial y}(\rho_s vE) + \frac{\partial}{\partial z}(\rho_s wE) = \frac{\partial}{\partial x}(k_s \frac{\partial T}{\partial x}) + \frac{\partial}{\partial y}(k_s \frac{\partial T}{\partial y}) + \frac{\partial}{\partial z}(k_s \frac{\partial T}{\partial z})$$
$$(4.12)$$

In the moving front region (the region between the two dashed lines as indicated in Fig. (4.1), eq. (4.10) is nonlinear. This agrees with the well-known fact that the nonlinearity of phase-change problems is due to the existence of a moving interface (Ozisik [1980]).

The method proposed is not restricted to the forms for $\Gamma(E)$ and $S(E)$ given by eq. (4.8) and eq. (4.9). With different conditions and assumptions, they have different expressions. For example, if phase changes occur over a temperature range (such as alloys), as shown in Fig. 4.2, with constant specific heats for each phase, we have

$$T - T_1 = \begin{cases} E/c_s & E \leq 0 & \text{(solid phase)} \\ \Delta T E/(H + c_m \Delta T) & 0 < E < H + c_m \Delta T & \text{(mushy phase)} \\ E/c_\ell - [H + (c_m - c_\ell)\Delta T]/c_\ell & E \geq H + c_m \Delta T & \text{(liquid phase)} \end{cases} \quad (4.13)$$

Here, we have selected $E = 0$ to correspond to phase-change materials in their solid state at temperature T_1. Then $T_m = (T_1 + T_2)/2$ is defined as the melting temperature, $\Delta T = T_2 - T_1$ is the melting temperature
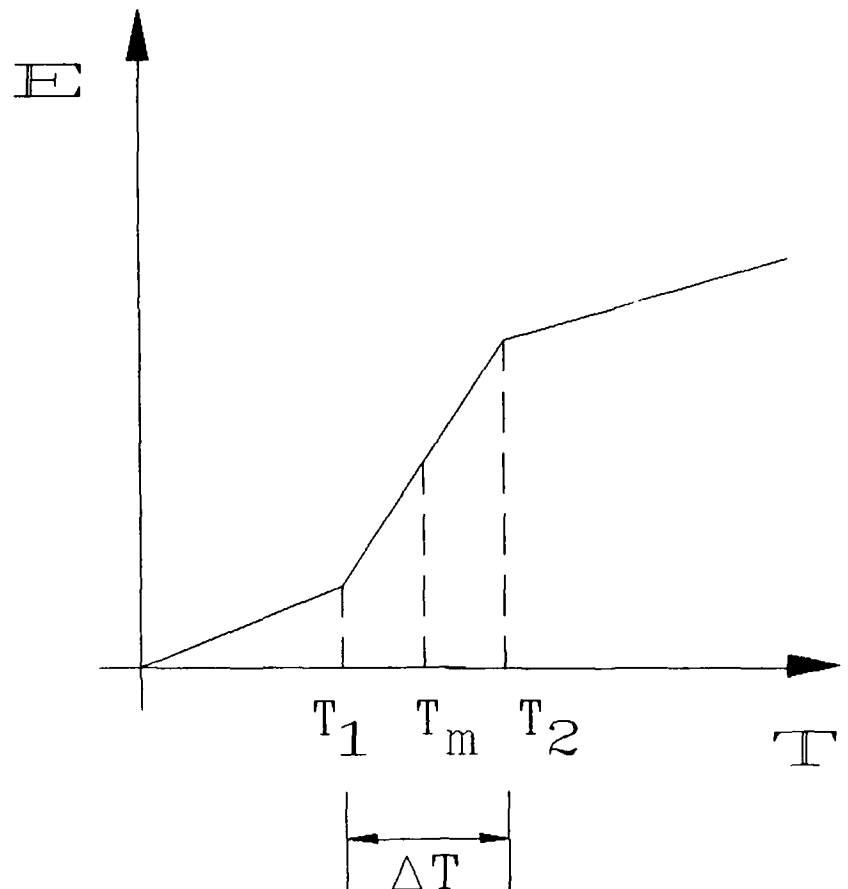
FIG. 4.2 RELATION BETWEEN T AND E WITH PHASE-CHANGE
TEMPERATURE RANGE

range, and C_m is the specific heat for the mushy phase.

The "Kirchoff" temperature is introduced as

$$T^+ = \int_{T_1}^{T} k(\eta)\, d\eta = \begin{cases} k_s\,(T\text{-}T_1) & T \leq T_1 \\ k_m\,(T\text{-}T_1) & T_1 < T < T_2 \\ k_\ell\,(T\text{-}T_1) & T \geq T_2 \end{cases} \qquad (4.14)$$

where k_m is the thermal conductivity for the mushy phase. The transformation procedure is the same as that of phase change at a single temperature, and the resulting equation is still eq. (4.10) with different expressions for $\Gamma(E)$ and $S(E)$.

$$\Gamma(E) = \begin{cases} k_s/c_s & E \leq 0 \\ k_m \Delta T/(H + c_m \Delta T) & 0 < E < H + c_m \Delta T \\ k_\ell/c_\ell & E \geq H + c_m \Delta T \end{cases} \qquad (4.15)$$

$$S(E) = \begin{cases} 0 & E \leq 0 \\ 0 & 0 < E < H + c_m \Delta T \\ -\,k_\ell\,[H + (c_m - c_\ell)\Delta T]/c_\ell & E \geq H + c_m \Delta T \end{cases} \qquad (4.16)$$

In the above relations for the mushy region, a linear change was assumed. In real systems, they may take more complicated forms. However, this is outside the scope of this report.

4.4 Numerical Scheme

4.4.1 Phase change without convective terms

To demonstrate the methodology, let us consider a phase-change problem in one space dimension. In this case, eq. (4.10) reduces to

$$\rho \frac{\partial E}{\partial t} = \frac{\partial^2}{\partial x^2} (\Gamma E) + \frac{\partial^2 S}{\partial x^2} \qquad (4.17)$$

with $\Gamma = \Gamma(E)$ and $S = S(E)$

The discretization of the above equation employs the control-volume finite-difference approach described by Patankar [1980]. In this methodology, the discretization equations are obtained by applying conservation laws over finite size control volumes surrounding the grid nodes, and integrating the equation over the control volumes, i.e.

$$\iiint_{\Delta V} \rho \frac{\partial E}{\partial t} dV = \iiint_{\Delta V} \left(\frac{\partial^2 (\Gamma E)}{\partial x^2} + \frac{\partial^2 S}{\partial x^2} \right) dV \qquad (4.18)$$

Using a fully implicit scheme and referring to Fig. 4.3, we have

$$\iiint_{\Delta V} \rho \frac{\partial E}{\partial t} dV = \rho \Delta x \frac{E_P - E_P^0}{\Delta t} \qquad (4.19)$$

$$\iiint_{\Delta V} \frac{\partial^2}{\partial x^2} (\Gamma E) dV = \left(\frac{\partial \Gamma E}{\partial x} \right)_e - \left(\frac{\partial \Gamma E}{\partial x} \right)_w = \frac{\Gamma_E E_E - \Gamma_P E_P}{(\delta x)_e} - \frac{\Gamma_P E_P - \Gamma_W E_W}{(\delta x)_w} \qquad (4.20)$$

$$\iiint_{\Delta V} \frac{\partial^2 S}{\partial x^2} dV = \frac{S_E - S_P}{(\delta x)_e} - \frac{S_P - S_W}{(\delta x)_w} \qquad (4.21)$$

154
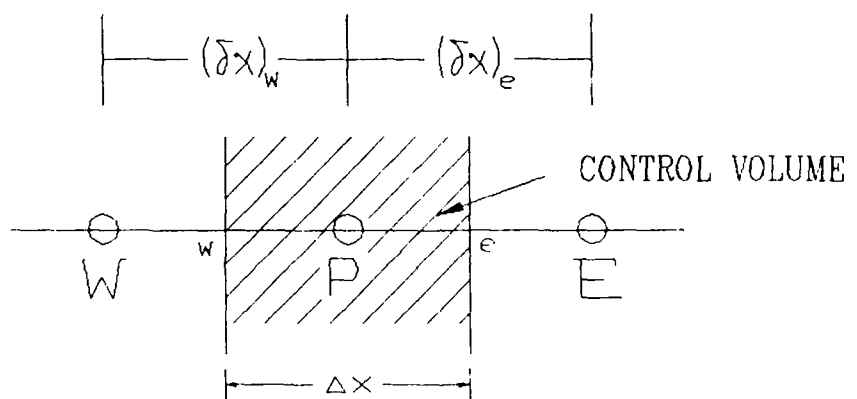
FIG. 4.3 GRID-POINT CLUSTER FOR THE
ONE-DIMENSIONAL PROBLEM

Thus

$$a_P E_P = a_E E_E + a_W E_W + b \tag{4.22}$$

with E_P^0 denoting the old value of E at grid point P

$$a_E = \frac{\Gamma_E}{(\delta x)_e} \quad , \quad a_W = \frac{\Gamma_W}{(\delta x)_w} \quad , \quad b = \frac{\rho \Delta x E_P^0}{\Delta t} + \frac{S_E - S_P}{(\delta x)_e} - \frac{S_P - S_W}{(\delta x)_w} \quad , \tag{4.22a}$$

and

$$a_P = \frac{\Gamma_P}{(\delta x)_e} - \frac{\Gamma_P}{(\delta x)_w} + \frac{\rho \Delta x}{\Delta t} \tag{4.22b}$$

4.4.2 Phase change with convective terms

In this case, a one space dimensional problem will also be considered as a demonstrative example. The governing equation is

$$\frac{\partial \rho E}{\partial t} + \frac{\partial}{\partial x} (\rho u E) = \frac{\partial^2}{\partial x^2} (\Gamma E) + \frac{\partial^2 S}{\partial x^2} \tag{4.23}$$

Since the total flux in the above equation $J = \rho v E - \frac{\partial}{\partial x}(\Gamma E)$ is different from the conventional total flux $J = \rho u \phi - \Gamma \frac{\partial \phi}{\partial x}$, the usual method to obtain the convection-diffusion expression is not applicable. Also, the coefficient Γ is small in most cases. To handle convection-diffusion situations and ensure physically realistic solutions, we employed a scheme similar to the upwind scheme. The discretization equation is written as

$$a_P E_P = a_E E_E + a_W E_W + b \tag{4.24}$$

156

where

$$a_P = a_{PE} + a_{PW} + \frac{\Delta x}{\Delta t} \rho_P^0$$

$$a_E = \Gamma_E D_e + \max\left[-F_e, \, 0\right], \quad a_{PE} = \Gamma_p D_e + \max\left[-F_e, \, 0\right]$$

$$a_W = \Gamma_W D_W + \max\left[F_W, \, 0\right], \quad a_{PW} = \Gamma_p D_W + \max\left[F_W, \, 0\right]$$

$$b = \frac{\rho_P^0 \, \Delta x E_P^0}{\Delta t} + \frac{S_E - S_P}{(\delta x)_e} - \frac{S_P - S_W}{(\delta x)_W}$$

$$D_e = 1/(\delta x)_e, \quad F_e = (\rho u)_e, \quad D_W = 1/(\delta x)_W, \quad F_W = (\rho u)_W$$

The greater of a and b is given by $\max\left[a, \, b\right]$, E_P^0 denotes the old value of E at grid point P, and ρ_P^0 denotes the old value of ρ at grid point P. Clearly, no special treatment is needed for solving the velocity using momentum equations.

4.4.3 Phase change for multi-dimensional problems

Having described the discretization equation for one space dimensional problems, we can now write a discretization equation based on the general differential equation (4.10) for multi dimensional problems, with E, W, N, S, T, and B representing the "east," "west," "north," "south," "top," and "bottom" neighbors of node P, respectively. The corresponding discretization equation is

$$a_P E_P = a_E E_E + a_W E_W + a_N E_N + a_S E_S + a_T E_T + a_B E_B + b \qquad (4.25)$$

where

$$a_P = a_{PE} + a_{PW} + a_{PN} + a_{PS} + a_{PB} + a_{PT} + \frac{\Delta x \, \Delta y \, \Delta z}{\Delta t} \rho_P^0$$

$$a_E = \Gamma_E D_e + \max\ [-F_e,\ 0],\ \ a_{PE} = \Gamma_P D_e + \max\ [-F_e,\ 0]$$

$$a_W = \Gamma_W D_w + \max\ [F_w,\ 0],\ \ \ a_{PW} = \Gamma_P D_w + \max\ [F_w,\ 0]$$

$$a_N = \Gamma_N D_n + \max\ [-F_n,\ 0],\ \ a_{PN} = \Gamma_P D_n + \max\ [-F_n,\ 0]$$

$$a_S = \Gamma_S D_s + \max\ [F_s,\ 0],\ \ \ a_{PS} = \Gamma_P D_s + \max\ [F_s,\ 0]$$

$$a_T = \Gamma_T D_t + \max\ [-F_t,\ 0],\ \ a_{PT} = \Gamma_P D_t + \max\ [-F_t,\ 0]$$

$$a_B = \Gamma_B D_b + \max\ [F_b,\ 0],\ \ \ a_{PB} = \Gamma_P D_b + \max\ [F_b,\ 0]$$

$$b = \frac{\Delta x \Delta y \Delta z \rho_P^0}{\Delta t}\ E_P^0 + D_e(S_E - S_P) - D_w(S_P - S_W) + D_n(S_N - S_P) -$$

$$D_s(S_P - S_S) + D_t(S_T - S_P) - D_b(S_P - S_B)$$

The flow rates and conductances are defined as

$$
\begin{aligned}
F_e &= (\rho u)_e\ \Delta y \Delta z & D_e &= \frac{\Delta y \Delta z}{(\delta x)_e}\\[6pt]
F_w &= (\rho u)_w\ \Delta y \Delta z & D_w &= \frac{\Delta y \Delta z}{(\delta x)_w}\\[6pt]
F_n &= (\rho v)_n\ \Delta z \Delta x & D_n &= \frac{\Delta z \Delta x}{(\delta y)_n}\\[6pt]
F_s &= (\rho v)_s\ \Delta z \Delta x & D_s &= \frac{\Delta z \Delta x}{(\delta y)_s}\\[6pt]
F_t &= (\rho w)_t\ \Delta x \Delta y & D_t &= \frac{\Delta x \Delta y}{(\delta z)_t}\\[6pt]
F_b &= (\rho w)_b\ \Delta x \Delta y & D_b &= \frac{\Delta x \Delta y}{(\delta z)_b}
\end{aligned}
\tag{4.26}
$$

Because of the nonlinearity of the above equation and the implicit nature of the scheme, iterations are needed at each time step. This procedure is the same as that which solves a nonlinear equation, and is as follows:

1) Let E^k represent the E field as it exists at the beginning of the kth iteration.

2) From these values, calculate tentative values of Γ and S according to their relations with E, using eqs. (4.8) and (4.9), or eqs. (4.15) and (4.16).

3) Solve the nominally linear set of discretization equations to get new values of E^{k+1}.

4) Return to step 1 and repeat the process until further iterations cease to produce any significant change in the values of E.

## 4.5 Application of the Methodology to the Example Problems

To demonstrate the present scheme, the proposed methodology has been applied to two separate phase-change problems. The first is a three-dimensional freezing problem, and the other is a three-dimensional moving heat source problem. In the two problems considered herein, the thermal physical properties such as k and C are assumed to be constant in each phase but may differ among the solid, mushy and liquid phases, while the density, ρ, is considered the same for each phase.

4.5.1 The three-dimensional freezing problem

Consider a liquid initially at its melting temperature, T_m, in a bar with a uniform square cross section and adiabatic ends as shown in Fig. 4.4a. The surface is suddenly exposed to a uniform wall temperature below the fusion temperature and freezing takes place immediately. Because of the symmetry of the geometry, only a quarter of the bar is considered as shown in Fig. 4.4b. To facilitate comparison, the dimensionless parameters are chosen to be the same as those used by Hsiao and Chung [1984], i.e.

$$\theta_0 = (T_i - T_w) / (T_m - T_w) = 1 \text{ and } St = c_s(T_m - T_w) / H = 1.$$

At the middle plane of the bar in the z-direction, the temperature distribution is two-dimensional. Figure 4.5 shows the interface position as a function of time along the diagonal for the present three-dimensional modeling. The two-dimensional results given by Hsiao and Chung [1984] using the equivalent heat capacity model and given by

160
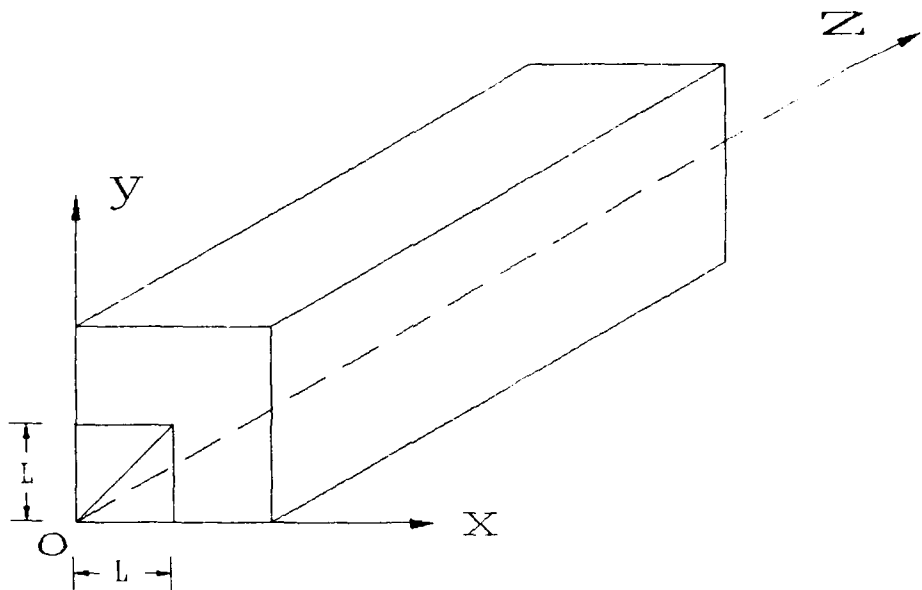
(a) Bar of liquid with an uniform square cross section
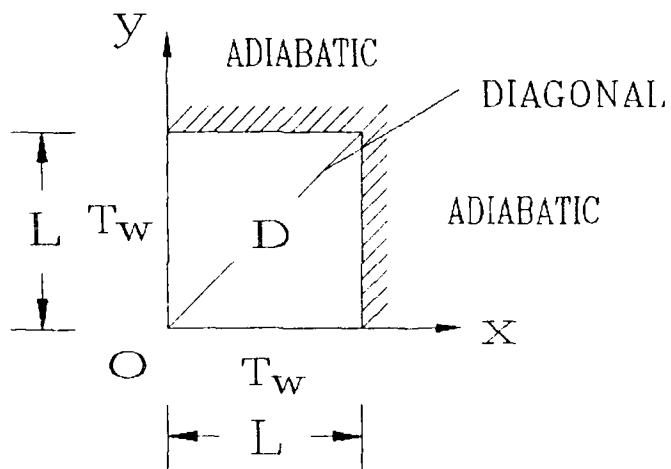
(b) One-quarter of the bar used for the computational
domain due to the symmetry of the problem.

FIG. 4.4 DESCRIPTION OF THE GEOMETRY AND BOUNDARY CONDITIONS
FOR THE TWO-DIMENSIONAL FREEZING PROBLEM.
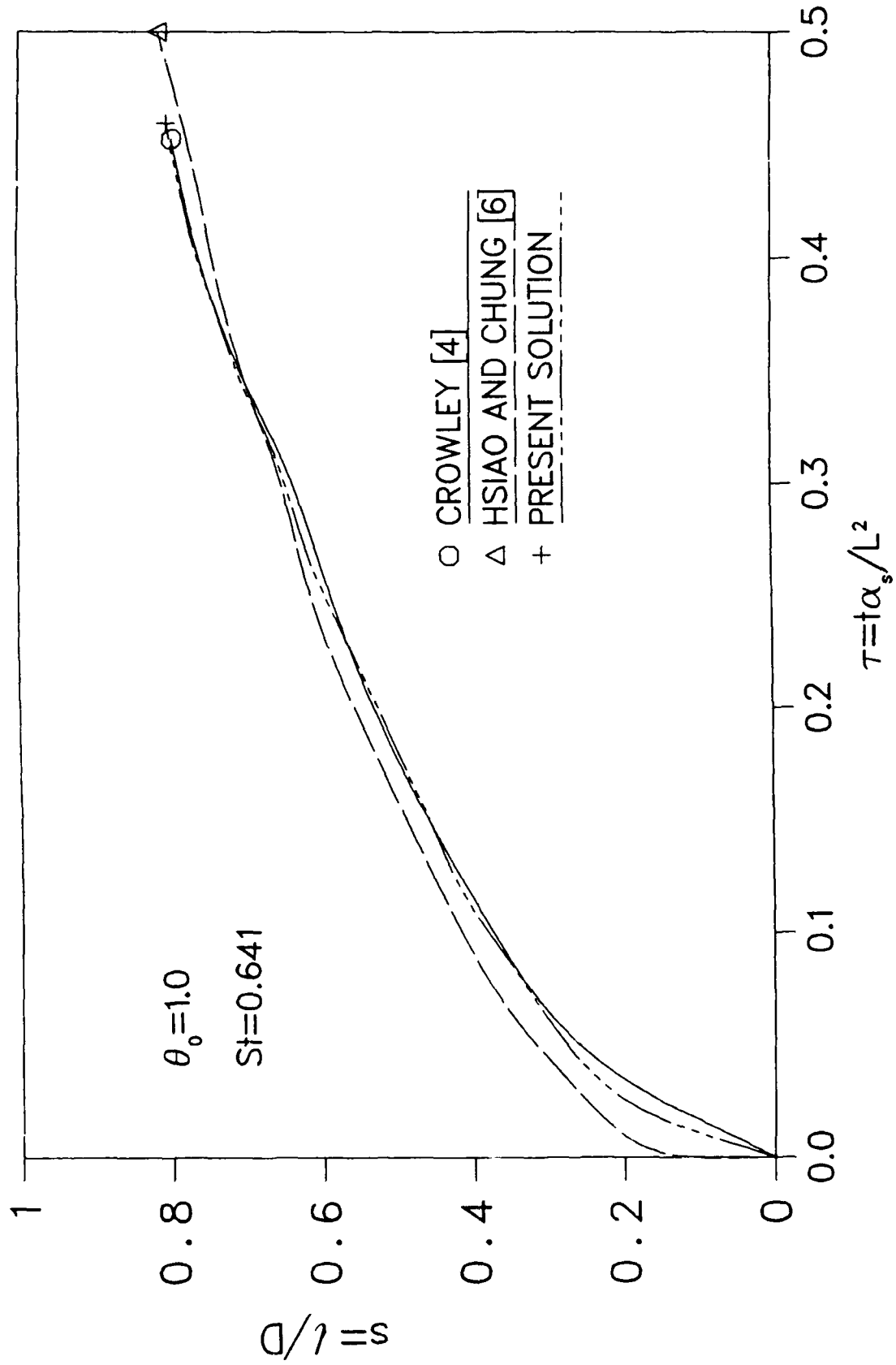
FIG.4.5 INTERFACE POSITION ALONG THE DIAGONAL FOR SOLIDIFICATION OF A SATURATED LIQUID

Crowley [1978] using the enthalpy model are also included in the same figure. The agreement among these solutions is excellent.

Consider the same problem with different initial conditions and physical properties. The dimensionless parameters are $k_\ell/k_s = 0.9$, $a_\ell/a_s = 0.9$, $\theta_0 = (T_i - T_w)/(T_m - T_w) = 9/7$, and $St = c_s(T_m - T_w)/H = 2$. Figure 4.6 shows the interface position as a function of time along the diagonal. Also included in Fig. 4.6 are solutions obtained by Hsiao and Chung [1984], and by Keung [1980]. Again, the present three-dimensional solution agrees well with the results of those two-dimensional studies.

We base the above calculation on the phase change which occurs at a single temperature. Assuming that the phase change takes place over a temperature range of $\Delta T = 20$ K, the same calculation is conducted, as also shown in Fig. 4.6. Plainly, the present model is insensitive to the phase-change temperature range. If the temperature range is small enough, we can expect the same result as that of the single temperature case. This is the case for the present model. The calculation is conducted with $\Delta T = 2$ K, and the result is almost identical with that of the single temperature case in Fig. 4.6.

The grid size employed in the above two cases is 20 x 20 x 30, and the discretization equations are solved by the Gauss-Seidel method. The physical properties of the mushy phase are taken as the average of those of the solid and liquid phases. The time step limit is not encountered
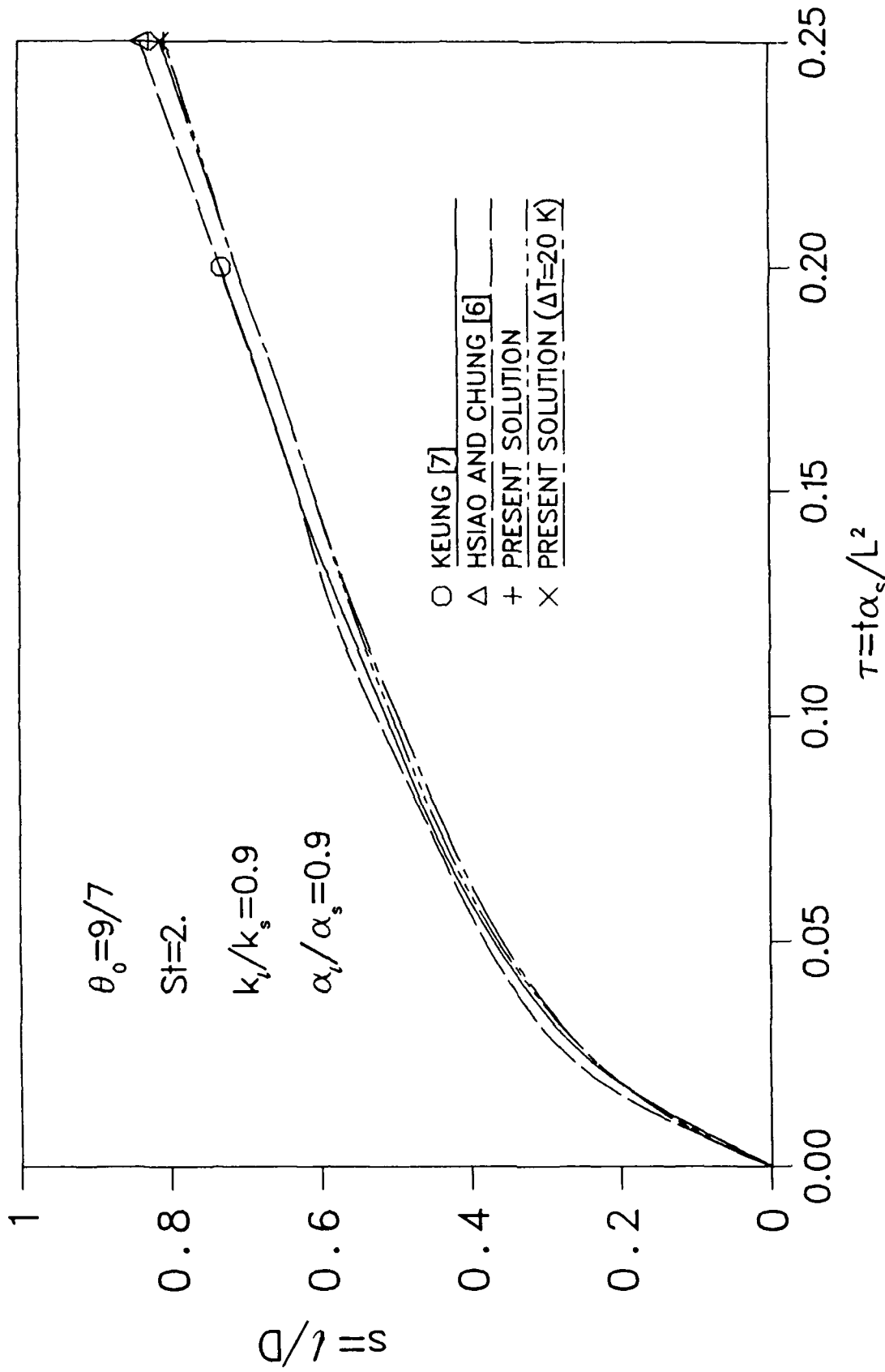
FIG.4.6 INTERFACE POSITION ALONG THE DIAGONAL WITH PRESCRIBED BOUNDARY TEMPERATURE

in the calculations. The dimensionless time steps can be on the order of 0.1, and real time steps can be as large as several days.

4.5.2 Three-dimensional phase-change problem with moving heat source

As indicated in Fig. 4.7, a source of heat moves over the surface of the plate with speed U. Because of intense heating, the material under the heat source melts. It is important to determine the molten depth for the given velocity, heat source power and its diameter, as well as the material properties.

With the coordinates fixed at the center of the moving heat source, eq. (4.10) is applicable for this problem. To simulate the circular heat source, the equation has been transformed into the form for the cylindrical-polar coordinate system.

The governing equation is

$$
\frac{\partial(E\rho)}{\partial t} + \frac{1}{r} \frac{\partial(r v_r \rho E)}{\partial r} + \frac{1}{r} \frac{\partial(v_\theta \rho E)}{\partial \theta} = \frac{1}{r} \frac{\partial}{\partial r}\left[r \frac{\partial(\Gamma E)}{\partial r} \right] + \frac{1}{r} \frac{\partial}{\partial \theta}\left[\frac{1}{r} \frac{\partial(\Gamma E)}{\partial \theta} \right]
$$
$$
+ \frac{\partial}{\partial z}\left[\frac{\partial(\Gamma E)}{\partial z} \right] + P \tag{4.27}
$$

where

$$
P = \frac{1}{r} \frac{\partial}{\partial r}\left[r \frac{\partial S}{\partial r} \right] + \frac{1}{r} \frac{\partial}{\partial \theta}\left[\frac{1}{r} \frac{\partial S}{\partial \theta} \right] + \frac{\partial^2 S}{\partial z^2}
$$

$$
v_r = -U\cos\theta \ , \quad v_\theta = U\sin\theta
$$
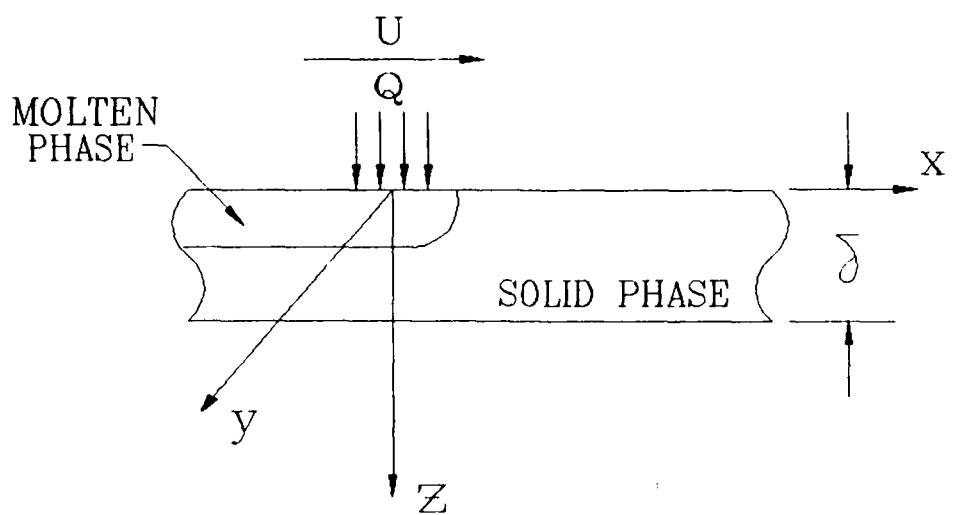
(a) Side-View of the Computational Domain with the Heat Source Moving at Speed U.
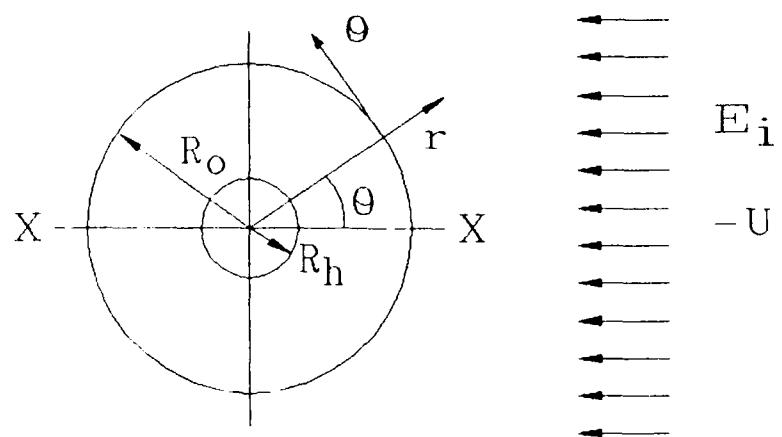
(b) Top-View of the Computational Domain with the Heat source stationary and the Computational Domain moving at speed −U.

FIG. 4.7 PICTORIAL DESCRIPTION OF MOVING HEAT SOURCE PROBLEM.

$\Gamma = \Gamma(E)$, $S = S(E)$ are given by eqs. (4.8) and (4.9), respectively.

The initial and boundary conditions are as follows

$$E_i = c_s (T_i - T_m) \qquad\qquad t = 0$$

$$q = q_h \qquad\qquad z = 0 , \quad r < R_h$$

$$q = 0 \qquad\qquad z = 0 , \quad r > R_h$$

$$q = 0 \qquad\qquad z = \delta$$

$$E = E_i \qquad\qquad r = R_0 , \quad -90^0 < \theta < 90^0$$

$$\frac{\partial(\Gamma E + S)}{\partial r} = 0 \qquad\qquad r = R_0 , \quad 90^0 < \theta < 270^0$$

The radius R_0 must be sufficiently large such that the region $r \geq R_0$, $-90^0 < \theta < 90^0$ is unaffected by the moving heat source. Also, the last boundary condition implies that the upwind scheme is used, and the diffusive term is neglected for the outflow boundary. The calculation proceeds with grid size 32 x 50 x 12 and time step 0.1 second. Other parameters are

$$U = 0.3 \text{ m/s}, \quad a_s/a_\ell = 1.44, \quad St = c_s(T_m - T_i)/H = 0.126$$

$$R_h = 0.005 \text{ m}, \quad R_0 = 0.25 \text{ m}, \quad Q = 11.80 \text{ kW}$$

Figure 4.8 shows isotherms of the dimensionless temperature $\theta_d = $ (T - T_i)/ (T_m - T_i) for t = 0.1 second at the x - x plane indicated in Fig. 4.7 (b) (i.e., θ = 0°, and θ = 180°). The center of the heat source is located at x = 0.0. The solid line labelled with 0 indicates the melting front at this time, while the dashed line labelled with -1 is a boundary beyond which the temperature field is unaffected by the moving heat source. After about 0.5 second, the steady-state condition is reached. Figure 4.9 shows the steady-state isotherms of the dimensionless temperature at the same plane. The melting front line becomes flat in the portion of x < 0.
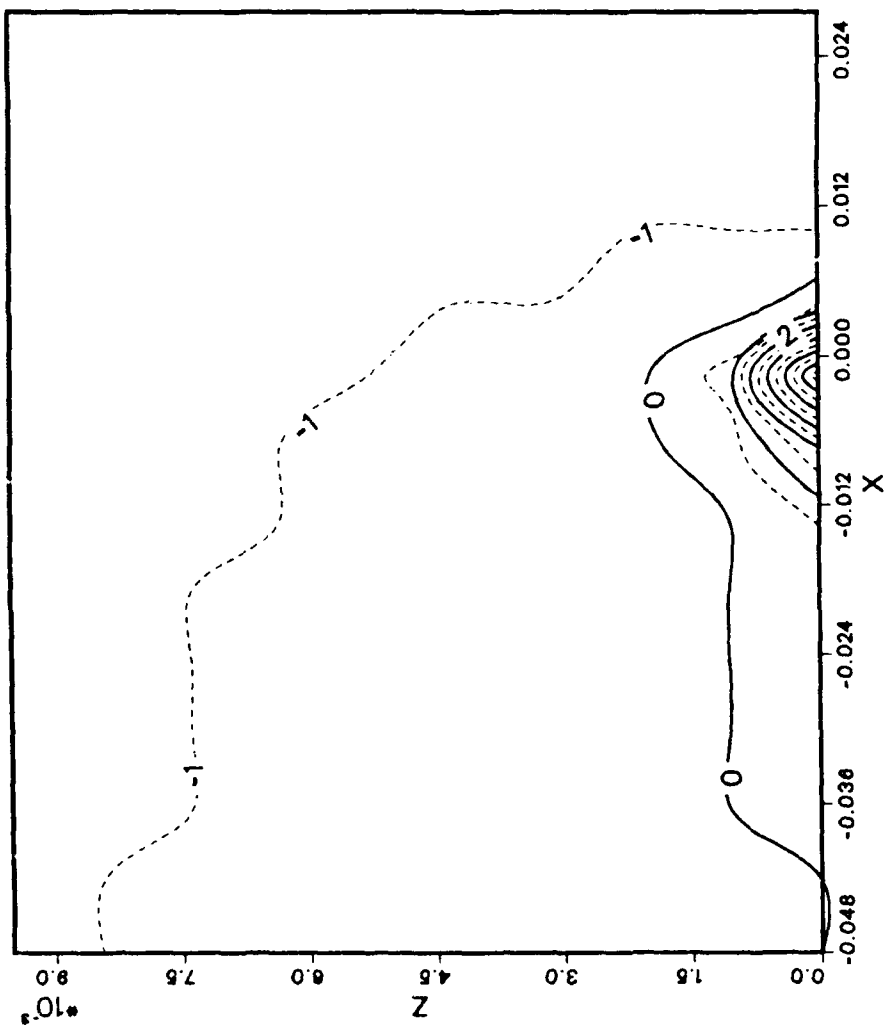
FIG.4.8 ISOTHERMS OF THE SOLUTION FOR t=0.1s AT X-X PLANE
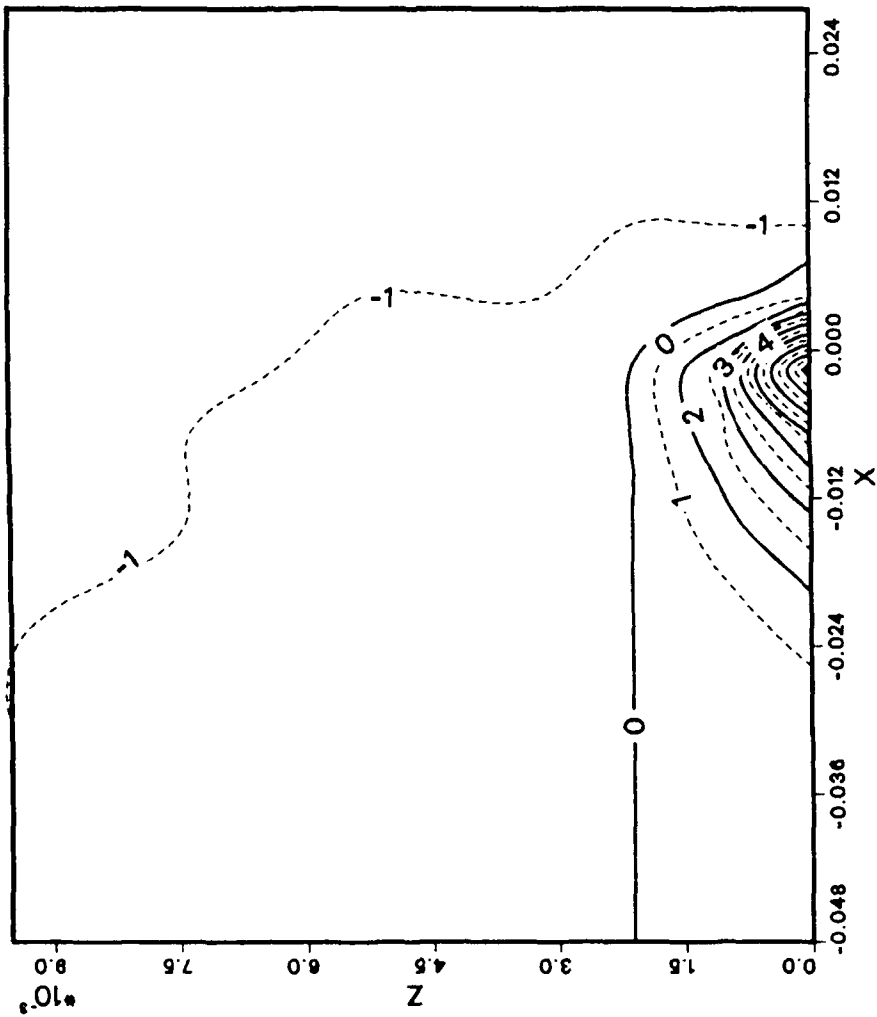
FIG.4.9 STEADY STATE ISOTHERMS OF THE SOLUTION AT X-X PLANE

4.6 Conclusions

The enthalpy transforming model proposed in this section proves to be capable of handling complicated phase-change problems occurring both at a single temperature and a temperature range with fixed grids. Due to the one dependent variable nature of the transformed equation, the convection and diffusion situations can be handled with appropriate algorithms. We have compared the numerical results existing in the literature with good agreement, showing that the present model can properly predict the phase-change processes. The advantage of this model based on enthalpy is that it allows us to avoid paying explicit attention to the nature of the phase-change front and can be extended to complicated multi-dimensional problems with convective terms without involving cumbersome mathematical schemes.

V. THERMAL PROTECTION FROM INTENSE LOCALIZED MOVING HEAT FLUXES USING PHASE-CHANGE MATERIALS

5.1 Summary

Various technologies which protect a wall from being burned out by an intense localized moving heat source have been reviewed, and a solution to this problem is proposed in which a phase-change material (PCM) is placed underneath the wall to absorb the high heat flux. The three-dimensional melting problem is nondimensionalized and modelled with a new enthalpy transforming scheme. The numerical results show that the proposed solution reduces the peak wall temperature significantly. The method of coating the PCM on the wall surface is also employed, which can maintain the surface temperature below the melting temperature of the PCM.

5.2 Introduction

Heat Transfer in a body resulting from a moving heat source is a well-known heat transfer problem and has had broad applications in the fields of welding, laser and electron beam surface processing (Eckert and Drake [1972], Festa et al. [1988]), etc. In these cases, a surface is subjected to a localized heat input, and the incoming heat flux moves relatively to the surface. The interest for the above applications is how to heat the surface effectively. However, in some applications a surface is hit by a moving high intensity heat source, as shown in Fig. 5.1. The major concern here is how to protect the surface from being burned out by the moving heat flux. This is indeed a problem of concern in laser thermal threats and re-entry situations and has been one of the motivations of the present study.

The methods used to protect surfaces from being burned out by a high heat flux are usually ablation and heat pipe technologies. Most of the previous studies on ablation concentrated on a stationary heat input with a large heating area. The major concern for this problem is the total energy which must be absorbed during a given time period. In the ablation technology which is used in missile re-entry situations, the body surface is coated with a solid material which is exposed to the high heat flux and is allowed to melt and blow away. Thus, a large amount of the incoming heat is expended in melting the material rather than being conducted into the interior of the vehicle, so that the temperature of the vehicle surface is reduced. The thickness of the coated material must be greater than the melted thickness during this time period. The
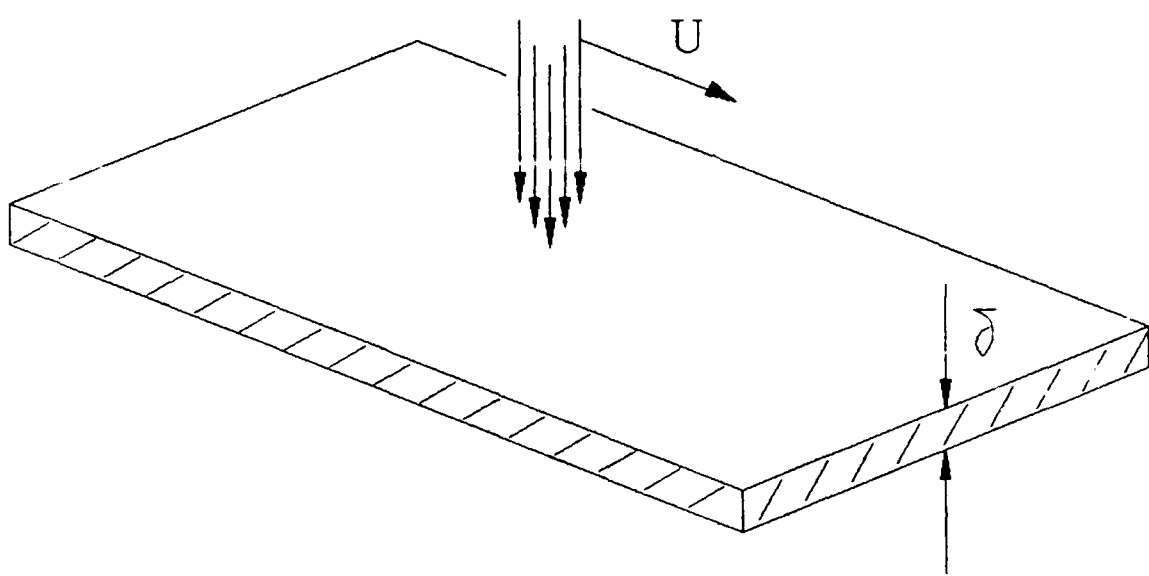
FIG. 5.1 A WALL SURFACE SUBJECT TO AN INTENSE
LOCALIZED MOVING HEAT SOURCE.

drawback of this technology is that once the coated material is melted, it is immediately blown away. The coated surface can be used only once, and for the next mission we must coat the surface again. For vehicles which have frequent missions such as airplanes, this situation may be intolerable. Moreover, high speed vehicles require a smooth surface to reduce the flow resistance and to reject the incoming heat; coated or ablated surfaces may have difficulties in reaching this goal. Nevertheless, due to the simplicity and effectiveness of this method, it still remains an alternative to protecting the surface and may be adopted to the case of a moving heat source.

Heat pipe technology is a good means of protecting a surface from attack by a high heat flux. For the present moving heat source problem, however, the heat pipe may only work under melting or free molecular conditions. Furthermore, a heat pipe is an integral vessel which cannot allow vapor leakage, which means that the present manufacturing technology would not be easily adapted to vehicles that have a large surface area. For these reasons, the adoption of heat pipe technology for the present problem is not economical.

Recently, the study of phase-change materials is active due to applications to space-based power plants and the utilization of solar energy. Phase-change materials (PCM) have a large melting heat, so it is an efficient way to absorb the heat energy during the time period when the materials are subject to heat input and to release it afterward at a relatively constant temperature. It is advantageous to incorporate the merits of the above technologies and propose another alternative to

175

protect the surface from attack by a high heat flux for the present problem, as shown in Fig. 5.2. There, the incoming heat input moves along the surface with speed $\vec{U}$ and the heat is conducted through the outside wall to the PCM. The PCM beneath the surface melts and absorbs a large amount of the incoming heat. Because of the large melting latent heat of the PCM and the constant melting temperature T_m, the peak wall temperature will be maintained at a temperature moderately higher than T_m. With a low or moderate T_m, the reduction of the peak wall temperature is evident. The dividing sheet, the soft insulating material, and the supporting plate may be used to prevent the separation of the PCM from the surface wall during the melting process, and to prevent the incoming heat from being conducted into the cabin. Because the density of liquid PCM is different from that of solid PCM, the solid PCM tends to separate from the outside wall, or to form voids near the wall, which reduces the heat transfer into the PCM. If the thickness of the PCM is thin and the density difference is not large, this situation will not be very severe.

The method proposed above imposes few difficulties on the present manufacturing technology and might also be used to cool the leading edges of space vehicles in re-entry situations. Since the re-entry time is short, a moderate thickness of the PCM will greatly reduce the temperature jump at the leading edges.

Section 5.3 gives a numerical analysis of this problem and discusses the important parameters to protect surfaces from an intense localized moving heat flux using PCM.

INCOMING HEAT

RADIATION $\vec{U}$ OUTSIDE WALL

PCM (LIQUID)

PCM (SOLID)

DIVIDING SHEET

INNER SUPPORTING PLATE SPONGY INSULATING MATERIAL
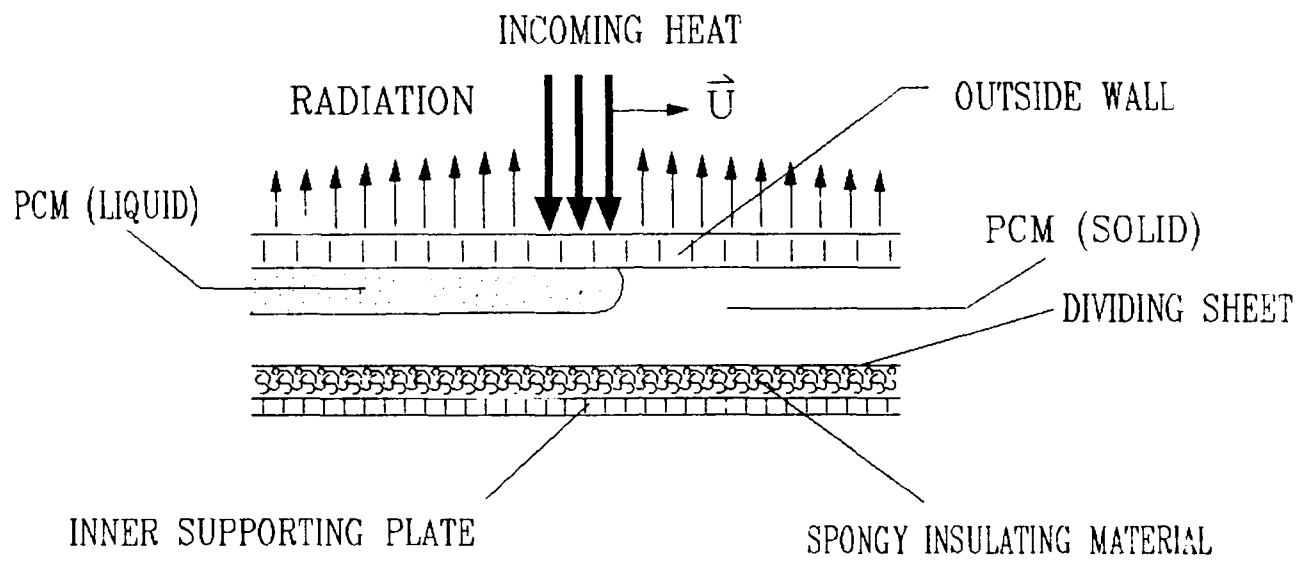
FIG. 5.2 CONFIGURATION TO PROTECT SURFACES FROM ATTACK BY HIGH HEAT FLUXES.

5.3 Analysis of Phase Change with a Moving Heat Source

The present problem mentioned previously is a three-dimensional phase-change problem with a moving heat source. Since the focus here is on space applications and the PCM thickness is comparatively thin, the natural convection due to gravity will not be considered. Also, since the layer of the PCM is thin, the influence of the density change between the solid and the liquid phases is expected to be small, and will be ignored.

In a Cartesian coordinate system (x', y', z') fixed at the outside wall as shown in Fig. 5.3, the heat source moves relatively to the plate with speed $\vec{U}$ on the surface. The appropriate energy equation is (Kays and Crawford [1980])

$$\rho \frac{\partial E}{\partial t} = \frac{\partial}{\partial x'} \left(k \frac{\partial T}{\partial x'}\right) + \frac{\partial}{\partial y'} \left(k \frac{\partial T}{\partial y'}\right) + \frac{\partial}{\partial z'} \left(k \frac{\partial T}{\partial z'}\right) \tag{5.1}$$

where the relation between E and T is given by the equation of state, $\frac{dE}{dT} = c$. This equation is applicable to the three different regions, namely, the wall, the solid PCM, and the liquid PCM with different relations between the enthalpy E, the temperature T, and the appropriate physical properties.

An analysis in a fixed coordinate system is difficult for this problem. It is convenient to study it in a moving coordinate system where the origin is fixed at the heated spot. Imagine an observer riding
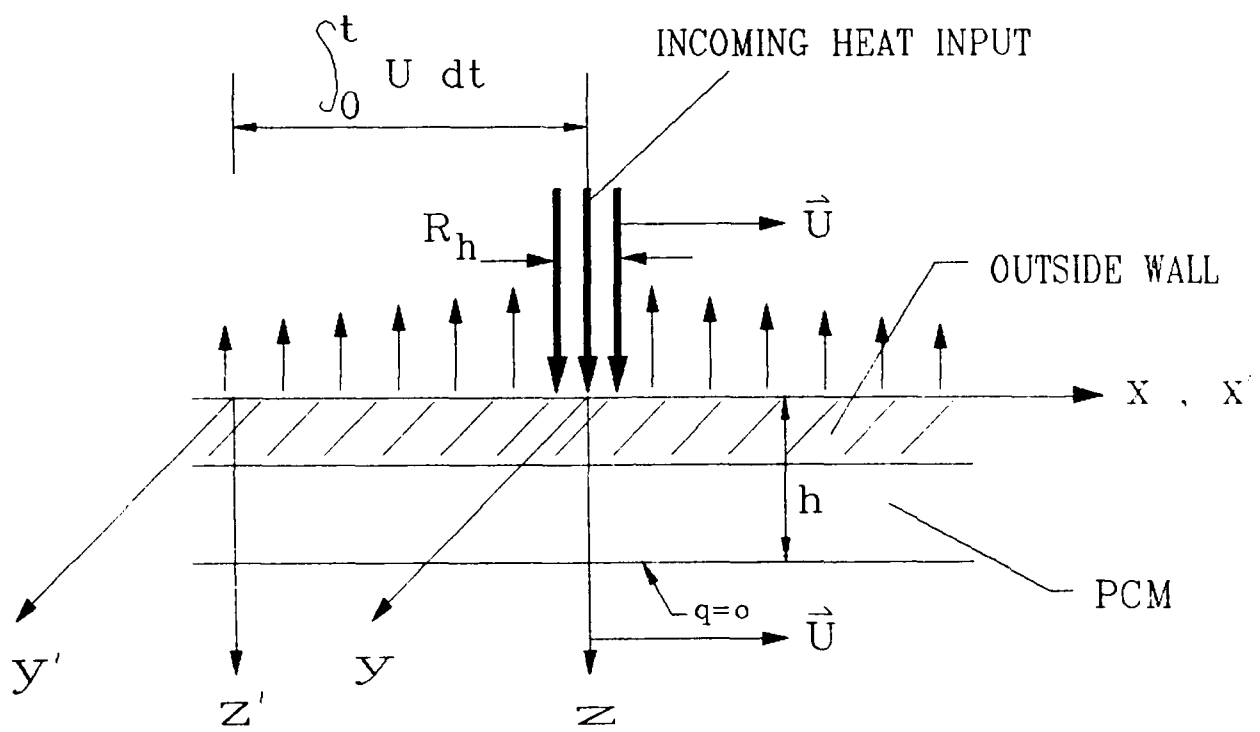
FIG. 5.3 DESCRIPTION OF DIFFERENT COORDINATE
SYSTEMS AND THEIR RELATIONSHIPS.

along with the incoming heat beam. The outside wall and the PCM will travel by at the same speed - $\vec{U}$. If we fix a moving coordinate system (x, y, z) to the center of the beam, the system will appear in reference to the fixed coordinate system as shown in Fig. 5.3.

In the moving coordinate system, the problem becomes a convective and diffusive heat transfer problem. The governing equation according to Kays and Crawford [1980] is

$$\rho \frac{DE}{Dt} = \frac{\partial}{\partial x} \left(k \frac{\partial T}{\partial x} \right) + \frac{\partial}{\partial y} \left(k \frac{\partial T}{\partial y} \right) + \frac{\partial}{\partial z} \left(k \frac{\partial T}{\partial z} \right) \tag{5.2}$$

With u = -U, v = w = 0, we have

$$\rho \frac{DE}{Dt} = \rho \frac{\partial E}{\partial t} - \rho U \frac{\partial E}{\partial x} \tag{5.3}$$

Equation (5.2) then becomes

$$\rho \frac{\partial E}{\partial t} - \rho U \frac{\partial E}{\partial x} = \frac{\partial}{\partial x} \left(k \frac{\partial T}{\partial x} \right) + \frac{\partial}{\partial y} \left(k \frac{\partial T}{\partial y} \right) + \frac{\partial}{\partial z} \left(k \frac{\partial T}{\partial z} \right) \tag{5.4}$$

The second term on the left-hand side of the equation is a convective term, while the terms on the right-hand side are diffusive terms.

The relations between the variables of the two coordinate systems are evident, i.e., $y = y'$, $z - z'$ and $x = x' - \int_0^t U \, dt$. When U is a constant, $x = x' - Ut$.

In the case of constant physical properties for the wall, the solid PCM and the liquid PCM, the phase change occurs at a single temperature. Equation (5.4) can be written for each region as

$$\frac{C_w}{k_w}\frac{\partial T}{\partial t} - \frac{C_w}{k_w}U\frac{\partial T}{\partial x} = \frac{\partial^2 T}{\partial x^2} + \frac{\partial^2 T}{\partial y^2} + \frac{\partial^2 T}{\partial z^2} \qquad \text{(wall)}$$

$$\frac{C_s}{k_s}\frac{\partial T}{\partial t} - \frac{C_s}{k_s}U\frac{\partial T}{\partial x} = \frac{\partial^2 T}{\partial x^2} + \frac{\partial^2 T}{\partial y^2} + \frac{\partial^2 T}{\partial z^2} \qquad \text{(solid PCM)} \qquad (5.5)$$

$$\frac{C_\ell}{k_\ell}\frac{\partial T}{\partial t} - \frac{C_\ell}{k_\ell}U\frac{\partial T}{\partial x} = \frac{\partial^2 T}{\partial x^2} + \frac{\partial^2 T}{\partial y^2} + \frac{\partial^2 T}{\partial z^2} \qquad \text{(liquid PCM)}$$

where $C_w = c_w\rho_w$, $C_s = c_s\rho_s$ and $C_\ell = c_\ell\rho_\ell$. The initial and boundary conditions are

$$t = 0, \quad T = T_i, \ 0 \leq z \leq h, \ -\infty < x < \infty, \quad -\infty < y < \infty$$

$t > 0$

$$k_w\frac{\partial T}{\partial z} = q_h, \quad z = 0, \quad \sqrt{x^2 + y^2} \leq R_h$$

$$k_w\frac{\partial T}{\partial z} = \sigma\epsilon T^4, \quad z = 0, \quad \sqrt{x^2 + y^2} > R_h$$

$$q\big|_{\delta^-} = q\big|_{\delta^+}, \quad z = \delta, \ -\infty < x < \infty, \quad -\infty < y < \infty \qquad (5.6)$$

$$\frac{\partial T}{\partial z} = 0, \quad z = h, \quad -\infty < x < \infty, \quad -\infty < y < \infty$$

181

$$T = T_i, \quad 0 \leq z \leq h, \quad |x| \to \infty, \quad |y| \to \infty$$

$$u = U, \quad w = v = 0, \quad 0 \leq z \leq h, \quad -\infty < x < \infty, \quad -\infty < y < \infty$$

At the liquid and solid interface within the PCM, we have

$$T_s = T_\ell = T_m$$

$$-k_\ell \frac{\partial T_\ell}{\partial n} + k_s \frac{\partial T_s}{\partial n} = H v_n \rho \qquad (5.7)$$

To reduce the number of parameters that have to be specified for the numerical solutions, the following dimensionless variables are introduced:

$$x^* = \frac{x}{R_h}, \quad y^* = \frac{y}{R_h}, \quad z^* = \frac{z}{R_h}, \quad T^* = \frac{T - T_i}{T_m - T_i}, \quad U^* = \frac{C_w U}{k_w} R_h,$$

$$t^* = \frac{k_w t}{C_w R_h^2} \qquad (5.8)$$

Equations (5.5-5.7) are nondimensionalized as

$$\frac{\partial T^*}{\partial t^*} - U^* \frac{\partial T^*}{\partial x^*} = \frac{\partial^2 T^*}{\partial x^{*2}} + \frac{\partial^2 T^*}{\partial y^{*2}} + \frac{\partial^2 T^*}{\partial z^{*2}} \qquad \text{(wall)}$$

$$\frac{C_s}{C_w} \frac{k_w}{k_s} \frac{\partial T^*}{\partial t^*} - \frac{C_s}{C_w} \frac{k_w}{k_s} U^* \frac{\partial T^*}{\partial x^*} = \frac{\partial^2 T^*}{\partial x^{*2}} + \frac{\partial^2 T^*}{\partial y^{*2}} + \frac{\partial^2 T^*}{\partial z^{*2}} \qquad \text{(solid PCM)} \qquad (5.9)$$

182

$$\frac{C_\ell}{C_w} \frac{k_w}{k_\ell} \frac{\partial T^*}{\partial t^*} - \frac{C_\ell}{C_w} \frac{k_w}{k_\ell} U^* \frac{\partial T^*}{\partial x^*} = \frac{\partial^2 T^*}{\partial x^{*2}} + \frac{\partial^2 T^*}{\partial y^{*2}} + \frac{\partial^2 T^*}{\partial z^{*2}} \qquad \text{(liquid PCM)}$$

$$t^* = 0, \quad T^* = 0, \quad 0 \leq z^* \leq h^*, \quad -\infty < x^* < \infty, \quad -\infty < y^* < \infty$$

$$t^* > 0$$

$$-\frac{\partial T^*}{\partial z^*} = \frac{q_h \, R_h}{(T_m - T_i) \, k_w}, \quad z^* = 0, \quad \sqrt{x^{*2} + y^{*2}} \leq 1$$

$$\frac{\partial T^*}{\partial z^*} = \frac{R_h \, (T_m - T_i)^3 \, \sigma\epsilon}{k_w} \left(T^* + \frac{T_i}{T_m - T_i}\right)^4, \quad z^* = 0, \quad \sqrt{x^{*2} + y^{*2}} > 1 \qquad (5.10)$$

$$q|_{\delta^*_-} = q|_{\delta^*_+}, \quad z^* = \delta^* = \frac{\delta}{R_h}, \quad -\infty < x^* < \infty, \quad -\infty < y^* < \infty$$

$$\frac{\partial T^*}{\partial z^*} = 0, \quad z^* = h^* = \frac{h}{R_h}, \quad -\infty < x^* < \infty, \quad -\infty < y^* < \infty$$

$$T^* = 0, \quad 0 \leq z^* \leq h^*, \quad |x^*| \to \infty, \quad |y^*| \to \infty$$
$$u^* = U^*, \quad v^* = w^* = 0, \quad 0 \leq z^* \leq h^*, \quad -\infty < x^* < \infty, \quad -\infty < y^* < \infty$$

At the interface of the liquid and solid in the PCM

$$T_s^* = T_\ell^* = 1$$

$$(5.11)$$

$$\frac{c_s \, (T_m - T_i)}{H} \left(-\frac{k_\ell}{k_w} \frac{\partial T_\ell^*}{\partial n^*} + \frac{k_s}{k_w} \frac{\partial T_s^*}{\partial n^*} \right) = \frac{C_s \, R_h}{k_w} \, v_n$$

The independent dimensionless parameters in addition to those in eq. (5.8) above are

$$\frac{C_s}{C_w}, \ \frac{C_\ell}{C_w}, \ \frac{k_s}{k_w}, \ \frac{k_\ell}{k_w}, \ \ \frac{q_h R_h}{(T_m - T_i) k_w}, \ \ \ \delta^*, \ h^*, \ \frac{R_h (T_m - T_i)^3}{k_w} \ \sigma \ \epsilon,$$

$$\frac{T_i}{T_m - T_i}, \ \ \frac{c_s (T_m - T_i)}{H}$$

Upon combining $\dfrac{C_w U R_h}{k_w}$ with $\dfrac{q_h R_h}{(T_m - T_i) k_w}$, we get a new dimensionless parameter $\dfrac{U C_w (T_m - T_i)}{q_h}$ which may be used to replace the dimensionless number $C_w U R_h / k_w$. Also, since $h^* = \delta^* + \delta_p^*$, the independent variable h^* may be replaced by δ_p^*. Thus, we have

$$T^* = f (N_v, \ N_Q, \ St, \ t^*, \ N_r, \ N_t, \ C_{sw}, \ C_{\ell w}, \ K_{\ell w}, \ K_{sw}, \ \delta^*, \ \delta_p^*, \ x^*, \ y^*, \ z^*)$$

$$(5.12)$$

where $\quad T^* = (T - T_i)/(T_m - T_i)$

$\qquad\qquad N_v = U C_w (T_m - T_i)/q_h$

$\qquad\qquad N_Q = q_h R_h / (T_m - T_i) k_w$

$\qquad\qquad St = c_s (T_m - T_i)/H$

$\qquad\qquad t^* = k_w t/(C_w R_h^2)$

$\qquad\qquad N_r = R_h (T_m - T_i)^3 \ \sigma \ \epsilon / k_w$

$\qquad\qquad N_t = T_i/(T_m - T_i)$

$\qquad\qquad C_{sw} = C_s/C_w$

$\qquad\qquad C_{\ell w} = C_\ell/C_w$

$\qquad\qquad K_{sw} = k_s/k_w$

184

$$K_{\ell w} = k_\ell / k_w$$

$$\delta^* = \delta / R_h$$

$$\delta_p^* = \delta_p / R_h$$

$$x^* \quad x / R_h$$

$$y^* = y / R_h$$

$$z^* \quad z / R_h$$

5.4 Numerical Model and Solution Procedure

This problem is nonlinear due to the moving front, so that exact analytical solutions for this type of nonlinear problems are available only for some simplified and idealized systems. Numerical methods appear to be the only practical approach for handling this three-dimensional melting problem with a moving heat source.

The numerical methods used to solve phase-change problems might be divided into two main groups. The first group is called strong numerical solutions; examples are given by Okada [1984], and Ho and Chen [1986]. These methods are only applicable to processes involving one or two space dimensions. The second group is called weak numerical solutions (Shamsunder and Sparrow [1975], Voller and Cross [1981], Cao et al. [1988], Solomon et al. [1986]). These methods allow us to avoid paying explicit attention to the nature of the phase-change front. Recently, Cao et al. [1988] proposed a new enthalpy transforming model which starts from eq. (5.4) and transforms the equation into a nonlinear equation with a single dependent variable E. The existing algorithms were modified to facilitate the numerical calculations. The numerical schemes are flexible and can handle three-dimensional problems without difficulty.

To simulate the circular heat source, eq. (5.4) needs to be transformed into the form for the cylindrical coordinate system. Referring to Fig. 5.4 and introducing $x = r \cos \theta$, $y = r \sin \theta$, we get

186
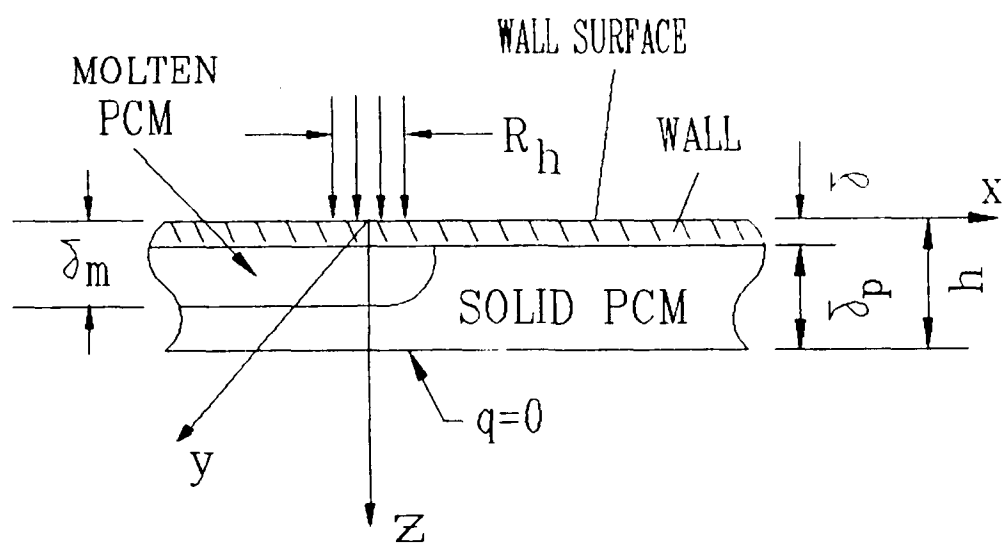
(a) Side-View of the Computational Domain of the
WALL – PCM Module.
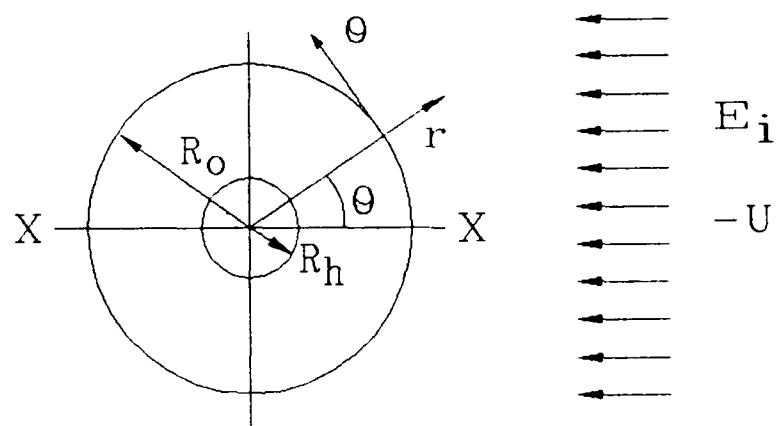
(b) Top-View of the Computational Domain of the
WALL – PCM Module.

FIG. 5.4 PICTORIAL DESCRIPTION OF THE COMPUTATIONAL DOMAIN FOR THE WALL – PCM MODULE.

$$\rho \frac{\partial E}{\partial t} + v_r \rho \frac{\partial E}{\partial r} + \rho v_\theta \frac{\partial E}{r \partial \theta} = \frac{1}{r} \frac{\partial}{\partial r} \left(rk \frac{\partial T}{\partial r} \right) + \frac{1}{r} \frac{\partial}{\partial \theta} \left(\frac{k}{r} \frac{\partial T}{\partial \theta} \right) + \frac{\partial}{\partial z} \left(k \frac{\partial T}{\partial z} \right) \quad (5.13)$$

with $v_r = -U \cos \theta$, $v_\theta = U \sin \theta$, $v_z = 0$.

Incorporating the continuity equation

$$\frac{1}{r} \frac{\partial}{\partial r} (r \rho v_r) + \frac{1}{r} \frac{\partial (v_\theta \rho)}{\partial \theta} + \frac{\partial \rho}{\partial t} = 0 \quad (5.14)$$

we obtain

$$\frac{\partial \rho E}{\partial t} + \frac{1}{r} \frac{\partial (r v_r \rho E)}{\partial r} + \frac{1}{r} \frac{\partial (v_\theta \rho E)}{\partial \theta} = \frac{1}{r} \frac{\partial}{\partial r} \left(rk \frac{\partial T}{\partial r} \right) + \frac{1}{r} \frac{\partial}{\partial \theta} \left(\frac{k \partial T}{r \partial \theta} \right) +$$

$$\frac{\partial}{\partial z} \left(k \frac{\partial T}{\partial z} \right) \quad (5.15)$$

with the state equation $\frac{dE}{dT} = c(T)$. Following the analysis given by Cao et al. [1988], the transforming method is described as follows.

In the case of constant specific heats for each phase and that the phase change occurs at a single temperature, the relation between temperature and enthalpy can be expressed as follows

$$T = \begin{cases} T_m + E/c_s & E \leq 0 \quad \text{(solid phase)} \\ T_m & 0 < E < H \quad \text{(mushy phase)} \\ T_m + (E - H)/c_\ell & E \geq H \quad \text{(liquid phase)} \end{cases} \quad (5.16)$$

Here, $E = 0$ has been selected to correspond to phase-change materials in their solid state at temperature T_m.

The "Kirchoff" temperature is introduced as

$$T^+ = \int_{T_m}^T k(\eta) \, d\eta = \begin{cases} k_s \, (T - T_m) & T < T_m \\ 0 & T = T_m \\ k_\ell \, (T - T_m) & T > T_m \end{cases} \qquad (5.17)$$

Transforming eq. (5.16) with the definition given in eq. (5.17) results in

$$T^+ = \begin{cases} k_s \, E/c_s & E \leq 0 \\ 0 & 0 < E < H \\ k_\ell \, (E - H)/c_\ell & E \geq H \end{cases} \qquad (5.18)$$

An enthalpy function is introduced as follows

$$T^+ = \Gamma(E) \, E + S(E) \qquad (5.19)$$

Eq. (5.15) is transformed into a nonlinear equation with a single dependent variable E.

$$\frac{\partial(E\rho)}{\partial t} + \frac{1}{r}\frac{\partial(rv_r\rho E)}{\partial r} + \frac{1}{r}\frac{\partial(v_\theta\rho E)}{\partial\theta} = \frac{1}{r}\frac{\partial}{\partial r}\left(r\frac{\partial(\Gamma E)}{\partial r}\right) + \frac{1}{r}\frac{\partial}{\partial\theta}\left(\frac{1}{r}\frac{\partial(\Gamma E)}{\partial\theta}\right)$$

$$+ \frac{\partial}{\partial z}\left(\frac{\partial(\Gamma E)}{\partial z}\right) + P \qquad\qquad (5.20)$$

where

$$P = \frac{1}{r}\frac{\partial}{\partial r}\left[r\frac{\partial S}{\partial r}\right] + \frac{1}{r}\frac{\partial}{\partial\theta}\left[\frac{1}{r}\frac{\partial S}{\partial\theta}\right] + \frac{\partial^2 S}{\partial z^2}$$

$$v_r = -U\cos\theta, \quad v_\theta = U\sin\theta$$

$$\Gamma = \Gamma(E) = \begin{cases} k_s/c_s & E \leq 0 \\ 0 & 0 < E < H \\ k_\ell/c_\ell & E \geq H \end{cases} \qquad\qquad (5.21)$$

and

$$S = S(E) = \begin{cases} 0 & E \leq 0 \\ 0 & 0 < E < H \\ -H\,k_\ell/c_\ell & E \geq H \end{cases} \qquad\qquad (5.22)$$

For the wall, no phase change occurs and therefore

$$E = c_w T, \quad \Gamma \equiv k_w/c_w, \quad \text{and } S \equiv 0 \qquad\qquad (5.23)$$

with eq. (5.20) still being applicable.

The initial and boundary conditions for the numerical domain in Fig. 5.4 are as follows:

$t = 0$

$E_i = c_w T_i$ $0 \leq z \leq \delta$, $0 \leq r < \infty$, $0 \leq \theta \leq 360^0$

$E_i = c_s (T_i - T_m)$ $\delta < z \leq h$, $0 \leq r < \infty$, $0 \leq \theta \leq 360^0$

$t > 0$

$-\dfrac{k_w}{c_w} \dfrac{\partial E}{\partial z} = q_h$ $z = 0$, $r \leq R_h$, $0 \leq \theta \leq 360^0$

$\dfrac{k_w}{c_w} \dfrac{\partial E}{\partial z} = \sigma \epsilon (E/c_w)^4$ $z = 0$, $r > R_h$, $0 \leq \theta \leq 360^0$

$q|_{\delta+} = q|_{\delta-}$ $z = \delta$, $0 \leq r < \infty$, $0 \leq \theta \leq 360^0$

$q = 0$ $z = h$, $0 \leq r < \infty$, $0 \leq \theta \leq 360^0$

$E = E_i$ $0 \leq z \leq h$, $r = R_0$, $-90^0 \leq \theta \leq 90^0$

$\dfrac{\partial E}{\partial r} = 0$ $0 \leq z \leq \delta$, $r = R_0$, $90^0 < \theta < 270^0$

$\dfrac{\partial (\Gamma E + S)}{\partial r} = 0$ $\delta < z \leq h$, $r = R_0$, $90^0 < \theta < 270^0$

The radius R_0 must be sufficiently large such that the region $r \geq R_0$, $-90^0 \leq \theta \leq 90^0$ is unaffected by the moving heat source. The last two boundary conditions imply that the upwind scheme is used, and the diffusive term is neglected for the outflow boundary.

Equation (5.20) is discretized with the numerical scheme proposed by Cao et al. [1988], which is based on the control-volume finite-difference approach described by Patankar [1980]. The general three-dimensional

191

discretization equation for the phase-change problem with a fully implicit scheme in the cylindrical coordinate system is

$$a_P E_P = a_E E_E + a_W E_W + a_N E_N + a_S E_S + a_T E_T + a_E E_E + b \qquad (5.24)$$

where

$$a_P = a_{PE} + a_{PW} + a_{PN} + a_{PS} + a_{PB} + a_{PT} + \frac{\Delta V}{\Delta t}\rho_P^0$$

$$a_E = \Gamma_E D_e + \max\left[-F_e,\ 0\right], \quad a_{PE} = \Gamma_P D_e + \max\left[-F_e,\ 0\right]$$

$$a_W = \Gamma_W D_w + \max\left[F_w,\ 0\right], \quad a_{PW} = \Gamma_P D_w + \max\left[F_w,\ 0\right]$$

$$a_N = \Gamma_N D_n + \max\left[-F_n,\ 0\right], \quad a_{PN} = \Gamma_P D_n + \max\left[-F_n,\ 0\right]$$

$$a_S = \Gamma_S D_s + \max\left[F_s,\ 0\right], \quad a_{PS} = \Gamma_P D_s + \max\left[F_s,\ 0\right]$$

$$a_T = \Gamma_T D_t + \max\left[-F_t,\ 0\right], \quad a_{PT} = \Gamma_P D_t + \max\left[-F_t,\ 0\right]$$

$$a_B = \Gamma_B D_b + \max\left[F_b,\ 0\right], \quad a_{PB} = \Gamma_P D_b + \max\left[F_b,\ 0\right]$$

$$b = \frac{\Delta V \rho_P^0}{\Delta t} E_P^0 + D_e(S_E - S_P) - D_w(S_P - S_W) + D_n(S_N - S_P) - D_s(S_P - S_S) +$$

$$D_t(S_T - S_P) - D_b(S_P - S_B)$$

where ΔV is the volume of the control volume, $\Delta\theta\ \Delta z\ (r_n + r_s)/2$, the greater of a and b is given by $\max[a,b]$, E_P^0 denotes the old value (at time t) of E at grid point p, and ρ_P^0 denotes the old value of ρ at grid point p. The flow rates and conductances are defined as

$$F_e = (\rho v_\theta)_e\ \Delta r \Delta z, \quad D_e = \frac{\Delta r \Delta z}{r_e(\delta\theta)_e}$$

$$F_w = (\rho v_\theta)_w\ \Delta r \Delta z, \quad D_w = \frac{\Delta r \Delta z}{r_w(\delta\theta)_w}$$

$$F_n = (\rho v_r)_n \, \Delta z r_n \Delta \theta, \quad D_n = \frac{\Delta z r_n \Delta \theta}{(\delta r)_n}$$

$$F_s = (\rho v_r)_s \, \Delta z r_s \Delta \theta, \quad D_s = \frac{\Delta z r_s \Delta \theta}{(\delta r)_s}$$

$$F_t = (\rho v_z)_t \, r_p \Delta \theta \Delta r, \quad D_t = \frac{r_p \Delta \theta \Delta r}{(\delta z)_t}$$

$$F_b = (\rho v_z)_b \, r_p \Delta \theta \Delta r, \quad D_b = \frac{r_p \Delta \theta \Delta r}{(\delta z)_b}$$

Because of the nonlinearity of the above equation and the implicit nature of the scheme, iterations are needed at each time step. This procedure is the same as those which solve a normal nonlinear equation.

Since the dimensionless parameters in the last section are independent of the coordinate system, eq. (5.12) is still applicable to the problem in the cylindrical coordinate system of this section.

5.5 Numerical Results and Discussion

The discretization equations above are solved with the Gauss-Seidel method. The grid size employed is 32 x 30 x 20 with the grid size near the wall surface being finer. To check the validity of the computer program, the calculation has been made with a moving heat source without phase change, i.e., a pure wall without PCM, and the steady-state surface temperature along the X-X plane (the X-X plane corresponds to the plane defined by $\theta = 0^0$ and $\theta = 180^0$ in cylindrical coordinates or y = 0 in Cartesian coordinates) was compared with the analytical result of a point source moving on the surface of a semi-infinite medium by Eckert and Drake [1972], as shown in Fig. 5.5. The steady-state analytical result has the form

$$T - T_i = (Q/2\pi k_w r)e^{-(U/2\alpha_w)(r+x)} \tag{5.25}$$

The above equation was obtained from a moving Cartesian coordinate system (x, y, z) with the point heat source at the origin and $r = \sqrt{x^2 + y^2 + z^2}$.

The discrepancy between the two results near x = 0 is due to the nature of the heat source that was modeled in each case. The analytical result has an infinitesimal heat source at x = 0, while the numerical one has a heat source of finite radius R_h. Considering this, the accuracy of the numerical results is very good. The numerical results with radiation ($\epsilon = 1$) into space for the surface other than the heated spot is also

Q=28.3 (W)
U=0.5 (m/s)
k=120 (W/(m-K))
α=1.07E-4 (m²/s)
δ=14.0E-3 (m)
R_h=3.E-4 (m)

△ NUMERICAL RESULT (ε=0.)
● ANALYTICAL RESULT [1]
+ NUMERICAL RESULT (ε=1.)

TEMPERATURE (K)

DISTANCE ALONG THE X-X PLANE AT Z=0, X(m)
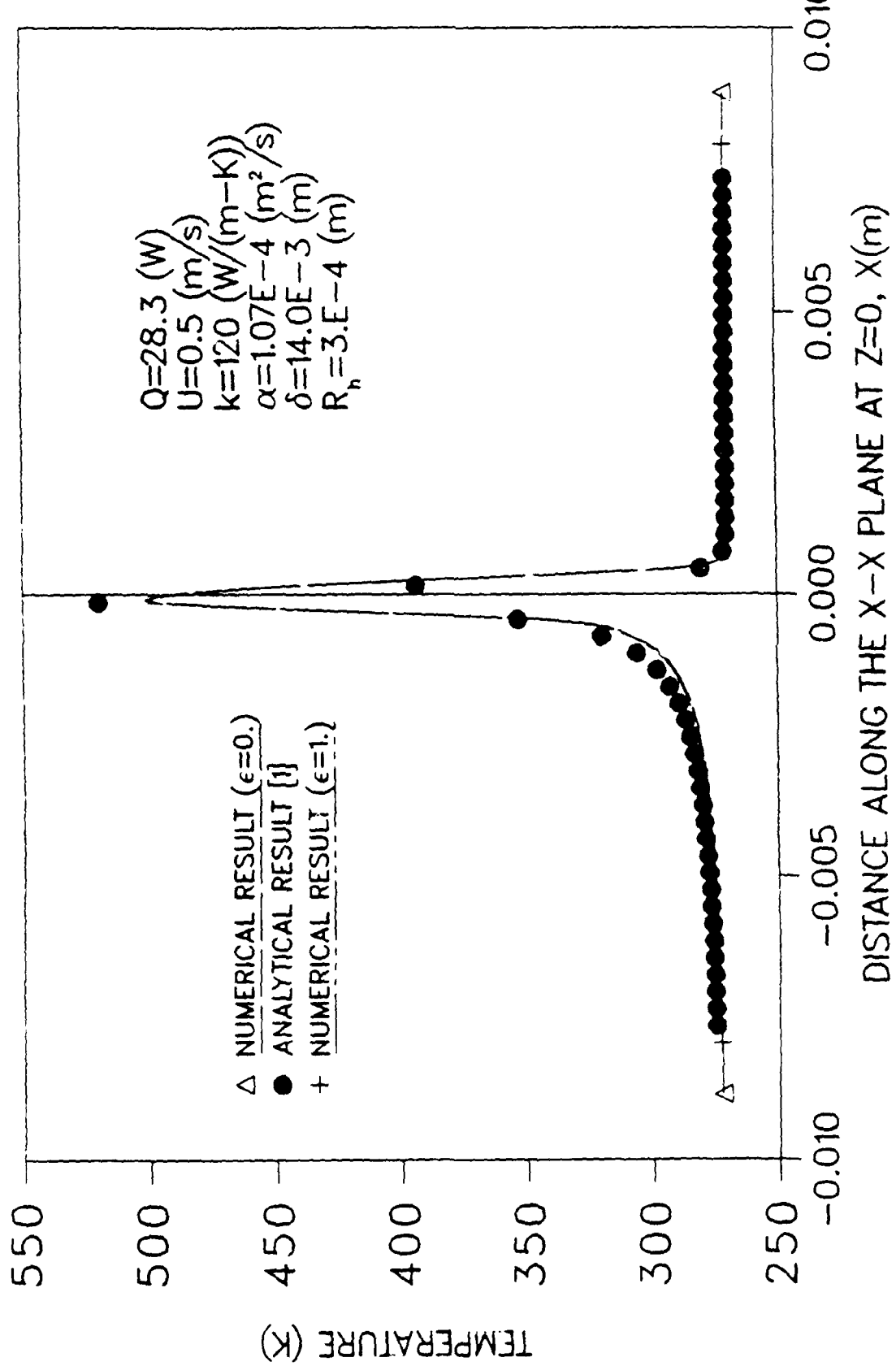
FIG.5.5 COMPARISION BETWEEN ANALYTICAL AND NUMERICAL RESULTS WITHOUT PHASE CHANGE

included in Fig. 5.5. The radiation plays no significant role in the temperature distribution of the wall near the heat source, and therefore will not be included in the next discussion, and the radiation parameters N_r and N_t will be dropped.

Figure 5.6 shows the general temperature distribution trend on the surface as a three-dimensional plot. The temperature falls off sharply in the portion of $x^* > 0$, while it falls off gradually for $x^* < 0$. Also, the symmetry of the temperature distribution to the X-X plane indicated in Fig. 5.4 is evident. Therefore, the representation of the temperature distributions will focus on the X-X plane for simplicity.

5.5.1 Moving heat source without phase change

As a first step, a pure wall without PCM is studied. In this situation, eq. (5.12) reduces to

$$T^* = f(N_v, N_Q, t^*, \delta^*, x^*, y^*, z^*) \tag{5.26}$$

Since the problem is now independent of T_m, $(T_m - T_i)$ is chosen as unity for convenience.

Figure 5.7 shows the variation of the steady-state wall surface temperature with different values of N_v. A larger N_v reduces the peak wall temperature significantly, while a small N_v may result in an intolerably high peak wall temperature. The dimensionless number N_Q has an opposite effect on the wall temperature, as shown in Fig. 5.8. A smaller N_Q corresponds to a lower peak wall temperature, while a larger

196

FIG.5.6 GRAPH OF THE SURFACE TEMPERATURE DISTRIBUTION TREND

197
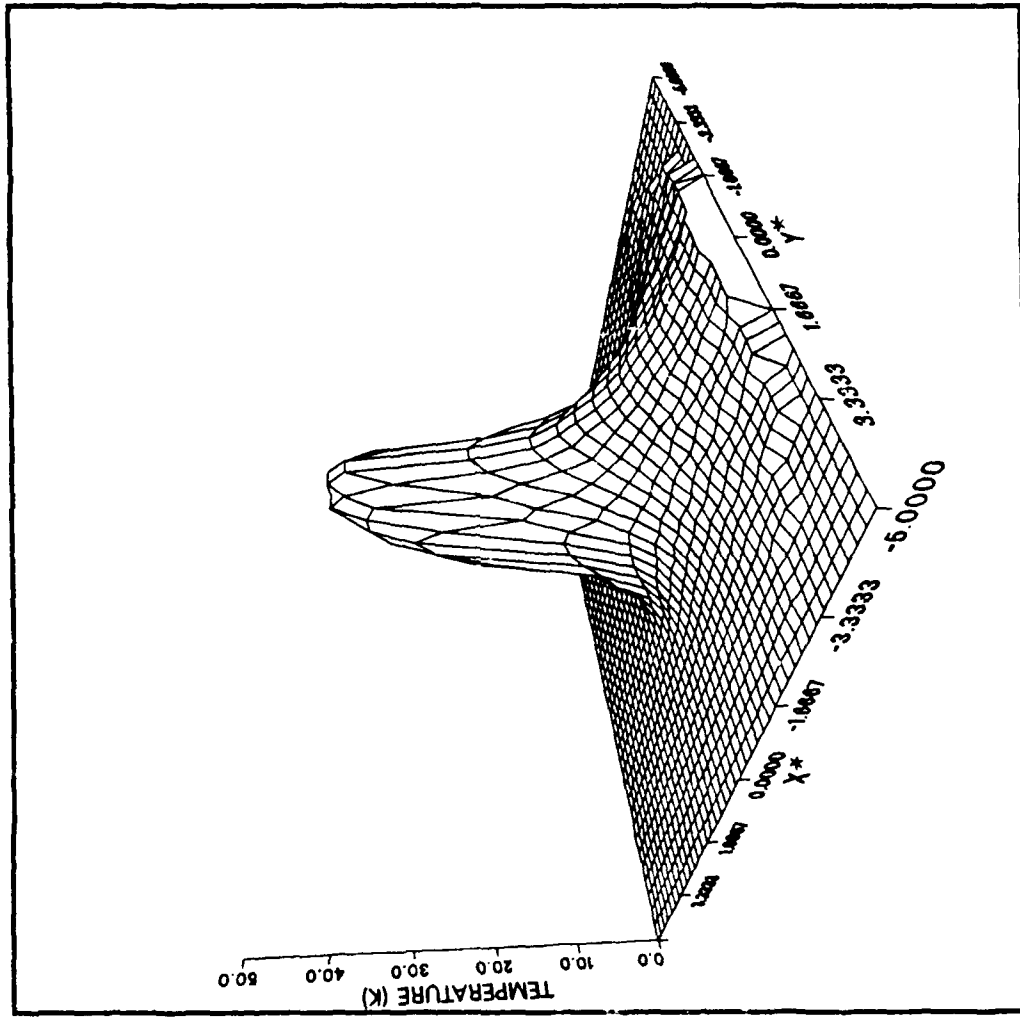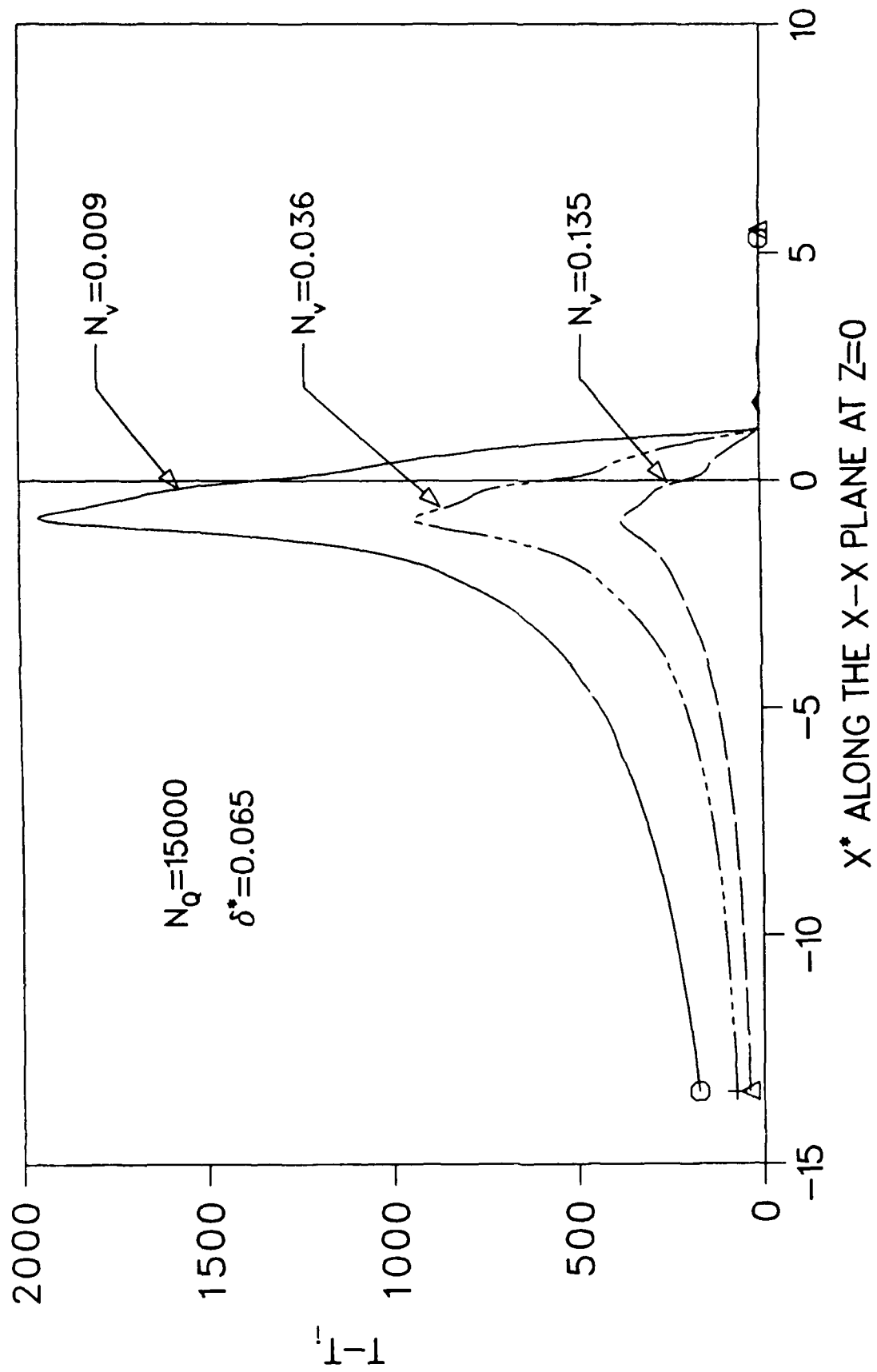
FIG.5.7 STEADY STATE TEMPERATURE PROFILES WITH DIFFERENT N_v WITHOUT PCM
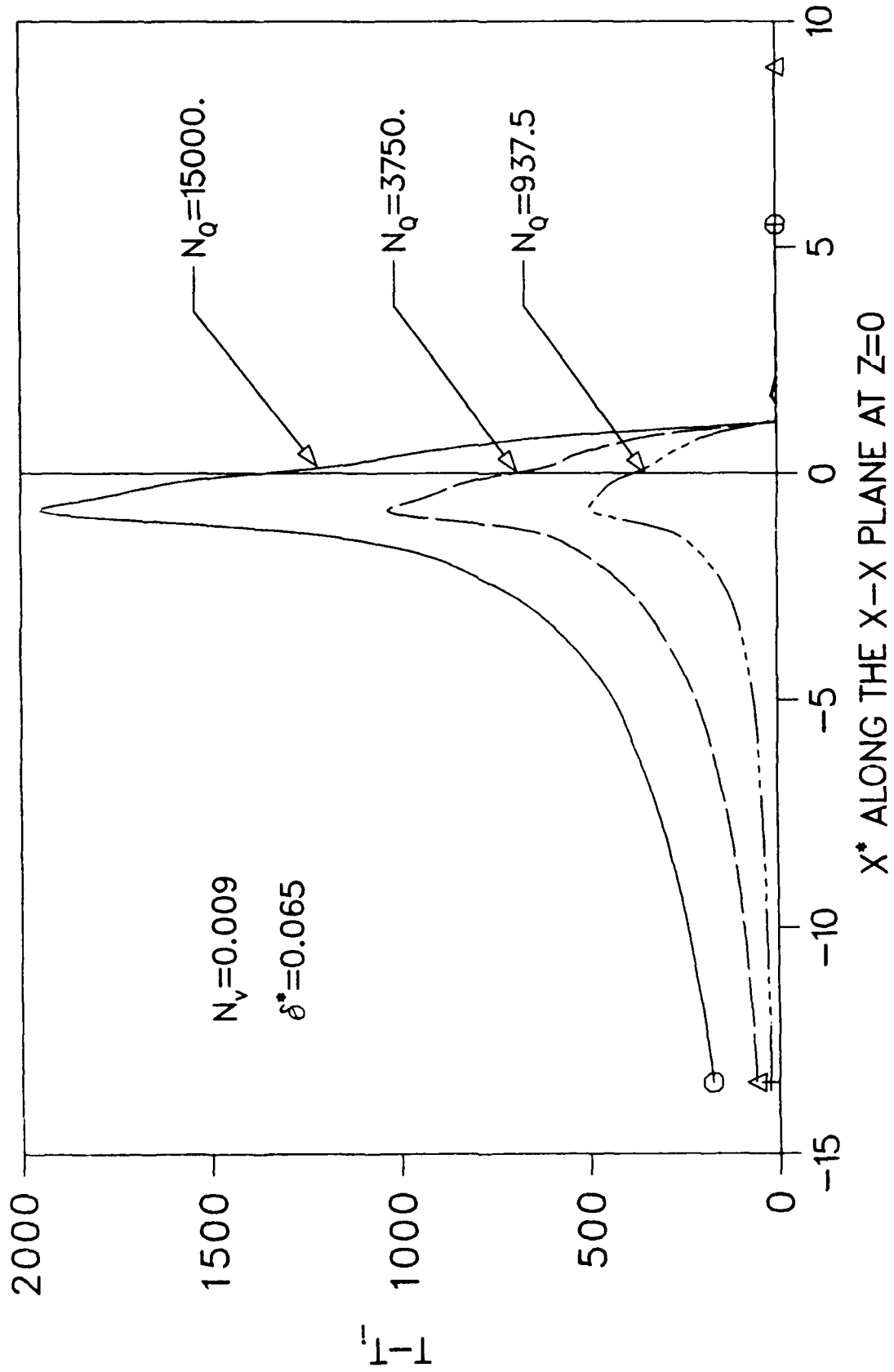
FIG.5.8 STEADY STATE TEMPERATURE PROFILES WITH DIFFERENT N_Q WITHOUT PCM

N_Q corresponds to a higher peak wall temperature. We can conclude that with a certain δ^*, when N_v is large enough or N_Q is small enough, the peak wall temperature is low and the wall does not need to be protected. When N_v is small or N_Q is large, something must be done to protect the wall, otherwise the wall will be burned out. Also, a larger δ^* has the effect of relieving the peak wall temperature, but is often not practical in space applications.

5.5.2 Moving heat source with PCM underneath the wall

As mentioned before, one of the alternatives of protecting the wall is to put the PCM beneath the wall as shown in Figs. 5.2 and 5.4. Figure 5.9 shows the numerical isotherms of the dimensionless temperature $T^* = (T - T_i)/(T_m - T_i)$ for $t = 0.1$ second along the X-X plane. Other parameters are $N_v = 1.2$, $N_Q = 60$, St $= 0.001$, $C_{sw} = 0.94$, $C_{\ell w} = 1.38$, $K_{\ell w} = K_{sw} = 0.65$, $\delta^* = 0.51$, and $h^* = 1.45$. The center of the heat source is located at $x = 0.0$. The solid line labelled with 1.0 indicates the melting front at this time. After about 0.5 second, the steady-state condition is reached. Figure 5.10 shows the corresponding steady-state isotherms of the dimensionless temperature at the same plane. The melting front is also labelled with 1.0.

Figure 5.11 shows the steady state wall surface temperature along the X-X plane with different Stefan numbers, St $= c_s(T_m - T_i)/H$. Also shown in the figure is that of a pure wall (without PCM) having the same weight per unit surface area as that of the wall-PCM module. The reduction of the peak wall temperature is significant. In the figure, $\delta_m^* = \delta_m/R_h$ is the dimensionless maximum melting front depth, where δ_m is

200
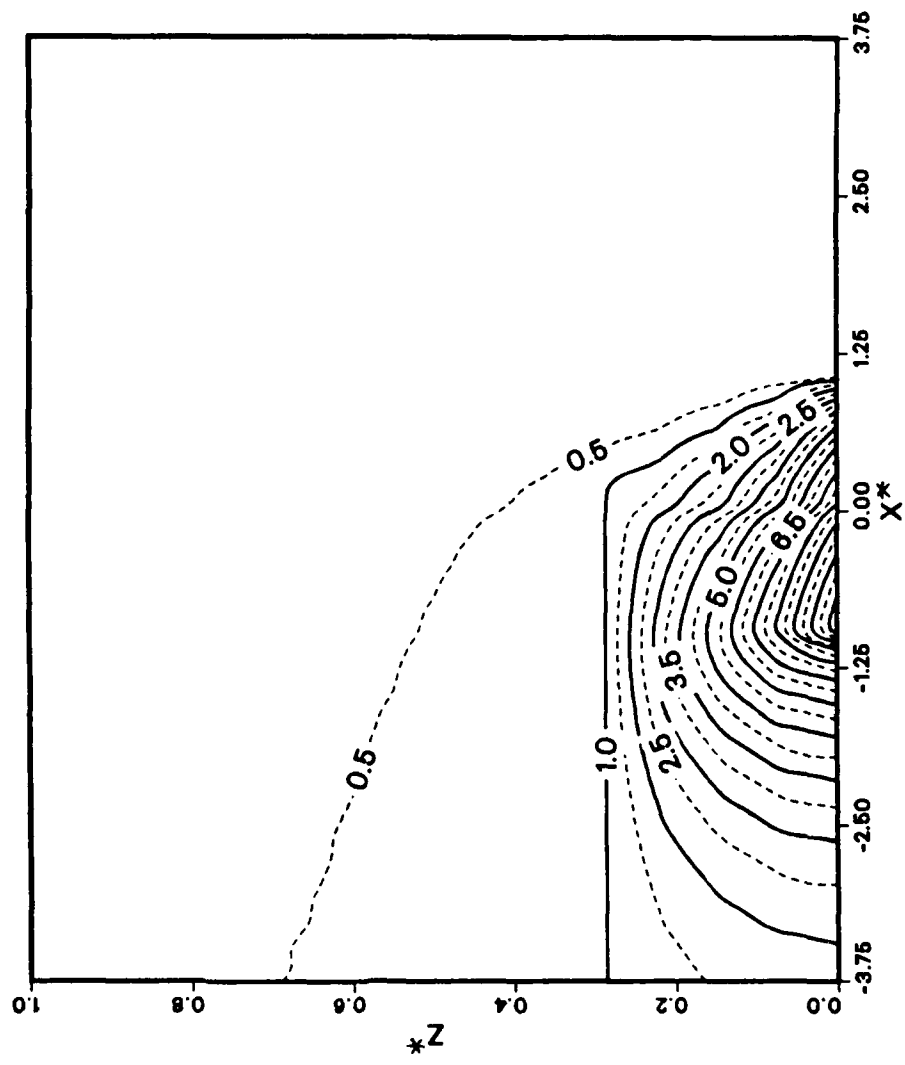
FIG.5.9 ISOTHERMS OF THE SOLUTION for t=0.1s AT X-X PLANE
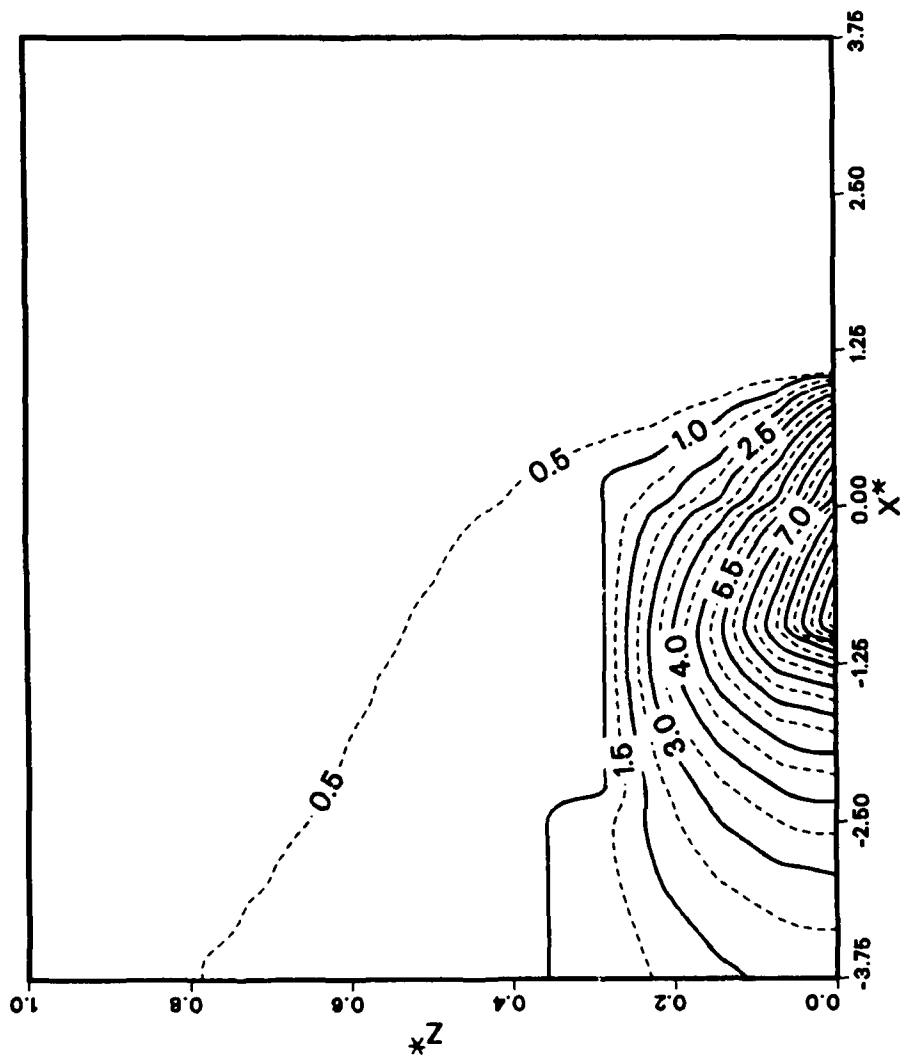
FIG.5.10 STEADY STATE ISOTHERMS OF THE SOLUTION AT X-X PLANE
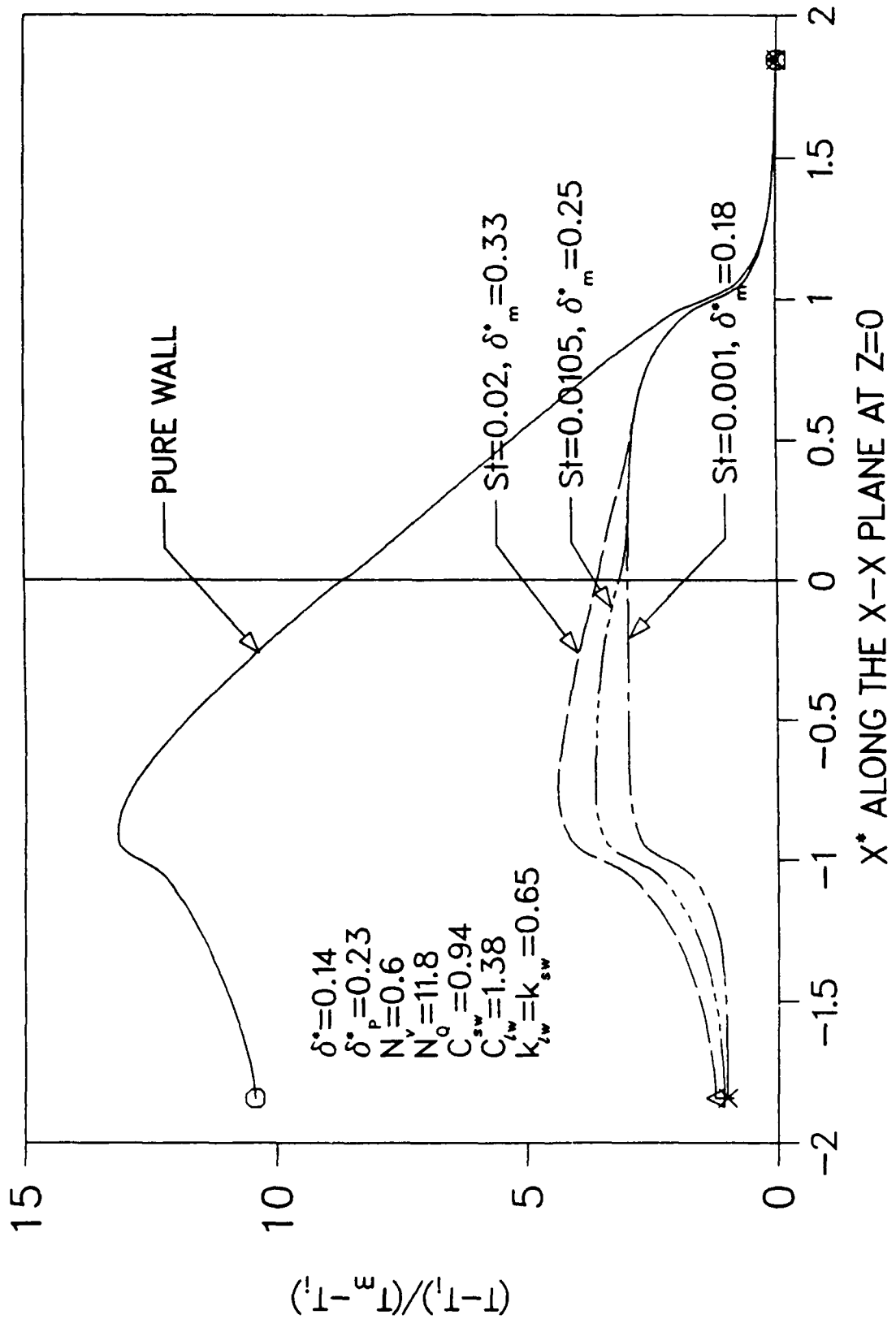
FIG.5.11 STEADY STATE TEMPERATURE PROFILES WITH DIFFERENT St

the maximum melting front depth from the wall surface corresponding to the steady state.

The dimensionless wall thickness δ^* has a significant influence on the temperature distribution. With a smaller δ^* the reduction of the peak wall temperature is more evident, as shown in Fig. 5.12.

Like the moving heat source problem without phase change, when N_v is small enough and N_Q is large enough the dimensionless temperature will become high, as shown in Fig. 5.13. The case with $N_v = 0.3$ and $N_Q = 60$ has a peak wall temperature almost four times as high as that with $N_v = 2.4$ and $N_Q = 30$. In this situation, perhaps we have to resort to another alternative.

5.5.3 Moving heat source with PCM coated on the surface

The configuration of this technology of protecting the surface is illustrated in Fig. 5.14. The numerical procedure is similar to that with PCM beneath the wall. The calculation is conducted with three different Stefan numbers and the results are shown in Fig. 5.15. The liquid phase in the numerical domain is assumed not to be blown away in this situation. Also shown in the figure is the temperature distribution of a pure plate (without PCM) having the same weight per unit surface area as that of the PCM-wall module indicated in Fig. 5.14. It is evident that the dimensionless temperature of the wall surface with PCM coated on it has no way to exceed one, which means that the wall surface temperature will be less than T_m, provided than the maximum melting front depth is less that the thickness of the PCM coat on the surface.

204

FIG.5.12 STEADY STATE TEMPERATURE PROFILES WITH DIFFERENT δ^*

X* ALONG THE X–X PLANE AT Z=0

$(T-T_i)/(T_m-T_i)$

PURE WALL, δ^*=0.145

δ^*=0.488

δ^*=0.3

δ^*=0.145

δ_p^*=0.23
St=0.001
N_v=0.6
N_o=11.8
C_{sw}=0.94
C_{tw}=1.38
$k_{tw}=k_{sw}$=0.65
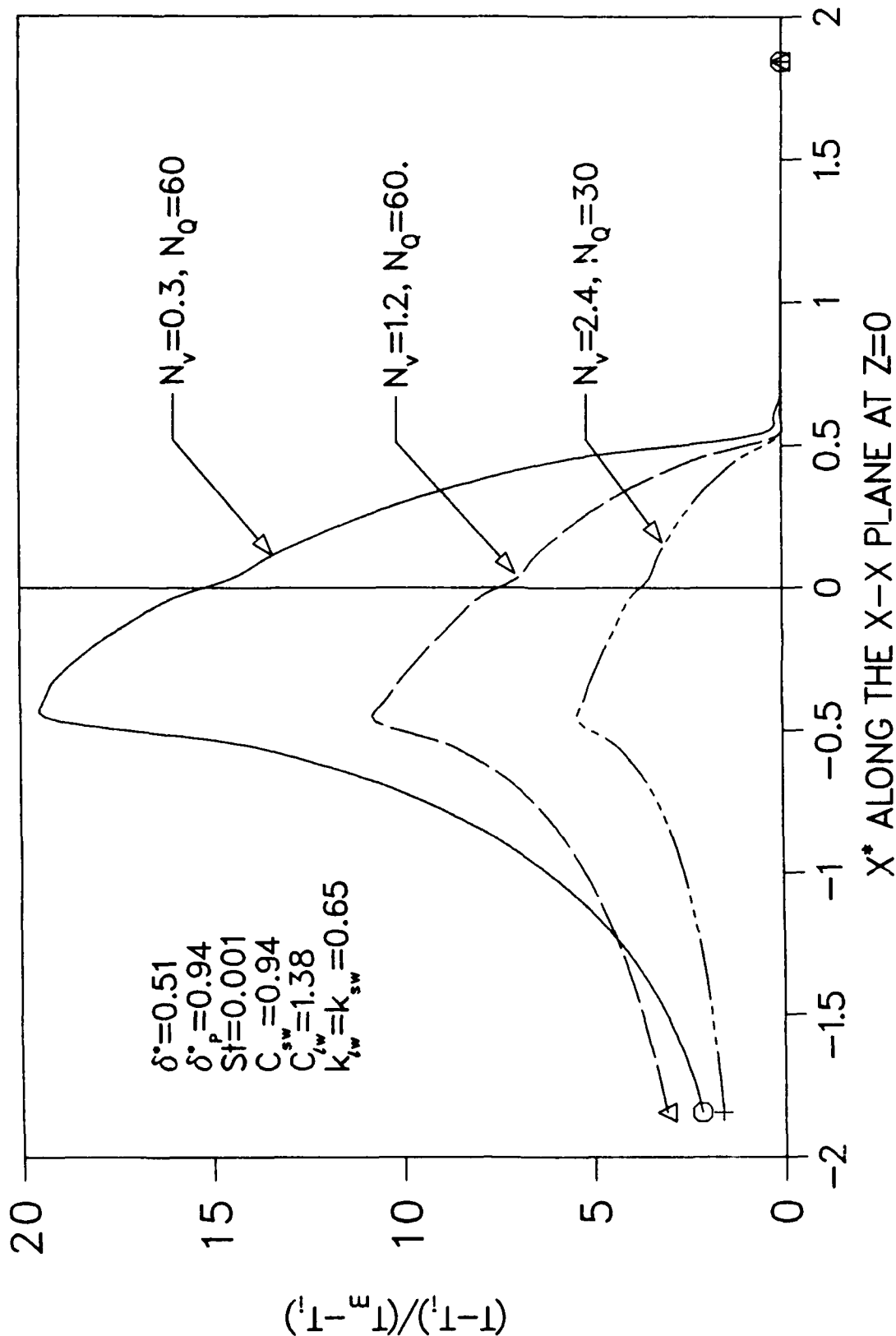
FIG.5.13 STEADY STATE TEMPERATURE PROFILES WITH DIFFERENT N_v AND N_Q
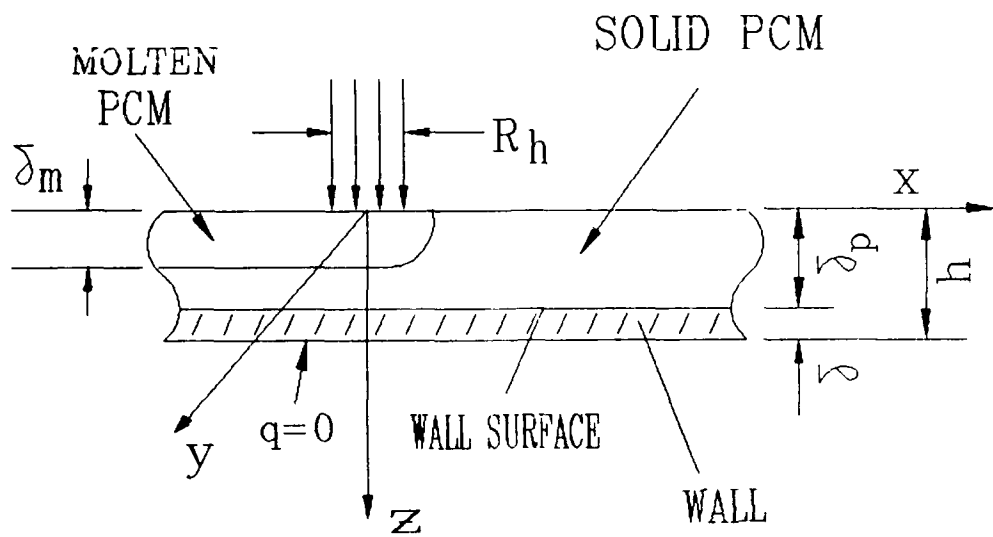
(a) Side-View of the Computational Domain of the PCM – WALL Module.
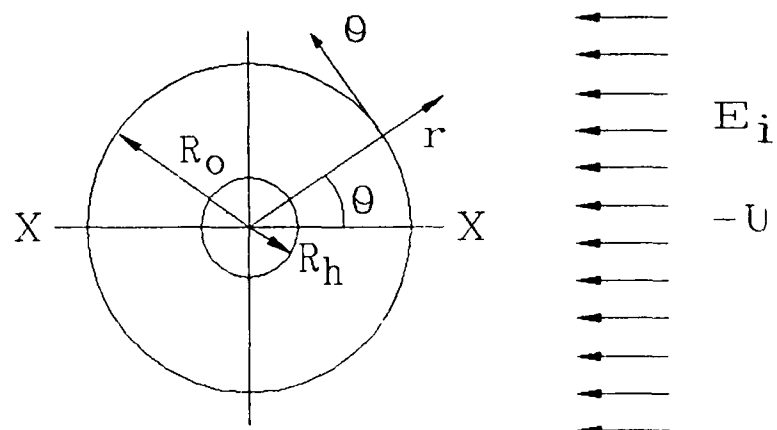
(b) Top-View of the Computational Domain of the PCM – WALL Module.

FIG. 5.14 PICTORIAL DESCRIPTION OF THE COMPUTATIONAL DOMAIN FOR THE PCM – WALL MODULE.
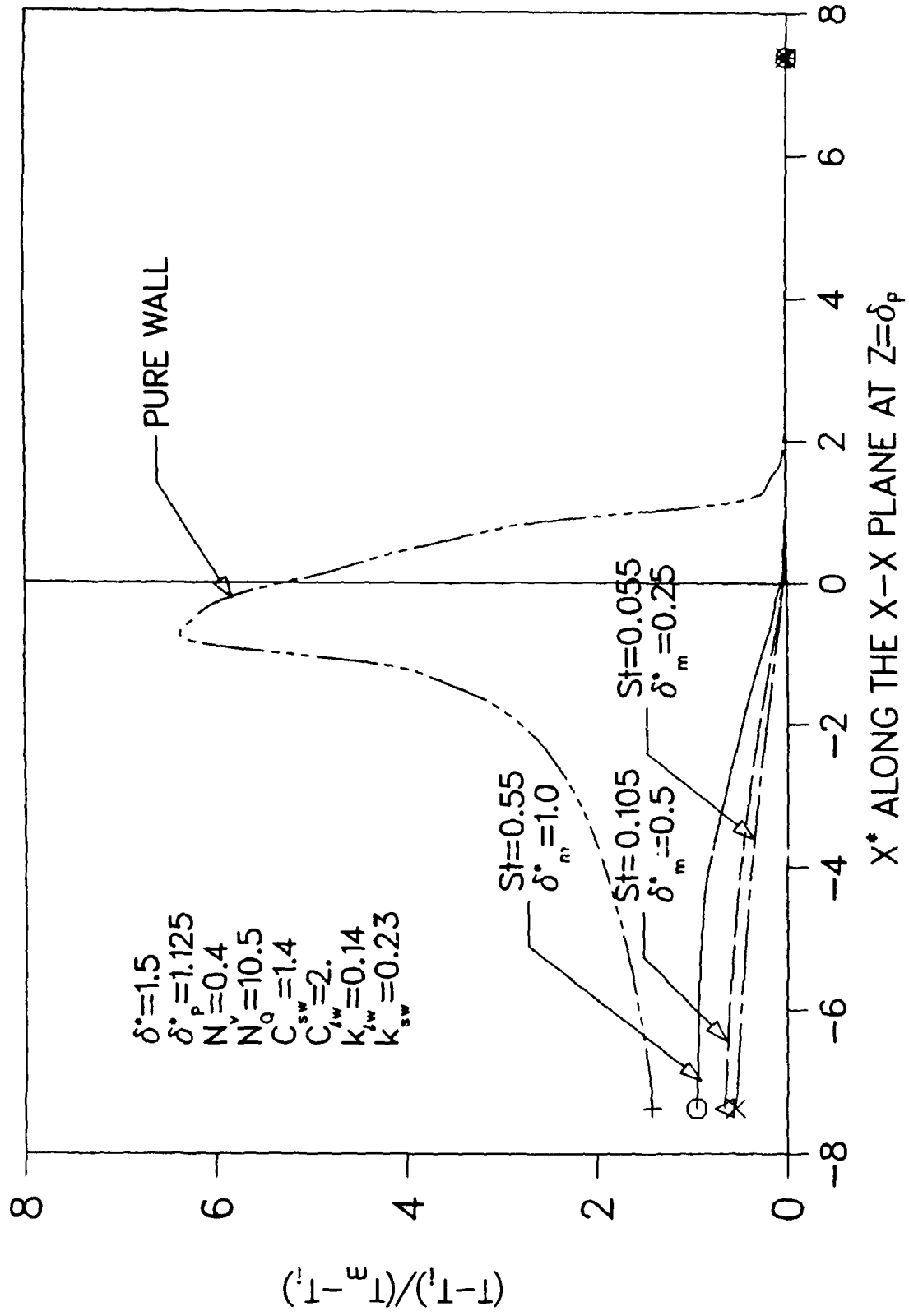
FIG.5.15 STEADY STATE TEMPERATURE VARIATION OF WALL SURFACE WITH St

X^* ALONG THE X–X PLANE AT Z=δ_P

PURE WALL

St=0.55
δ^*_m=1.0

St=0.105
δ^*_m=0.5

St=0.055
δ^*_m=0.25

δ^*=1.5
δ^*_p=1.125
N_v=0.4
N_o=10.5
C_{sw}=1.4
C_{tw}=2.
k_{tw}=0.14
k_{sw}=0.23

$(T-T_i)/(T_m-T_i)$

208

5.6 Conclusions and Remarks

If a wall surface is subject to an intense moving heat flux, and with a large N_Q and a small N_v, the surface is prone to be burned out unless some measure is taken to protect it. The use of PCM proves to be a good means of protecting the surface in this respect. One way to protect the surface is to put the PCM underneath the wall. This method is more efficient with smaller St and δ^*. With N_Q increasing and N_v decreasing further, the method of coating the PCM on the surface is needed to protect the surface. In this situation, the wall surface temperature will be less than T_m provided that the maximum melting depth is less than the thickness of the PCM coat on the surface. We should point out that both methods have advantages and disadvantages. Even if the method of putting the PCM underneath the wall is less efficient when N_Q and N_v are beyond some limits, it is ready to be used again and puts no restrictions on the wall surface. In these cases, a trade-off will be reached when selecting the protective technology.

REFERENCES

Abhat, A., and Seban, R.A., 1974, "Boiling and Evaporation from Heat Pipe Wicks with Water and Acetone," ASME J. Heat Transfer, Vol. 96, No. 3, p. 331.

Bankston, C.A., and Smith, H.J., 1971, "Incompressible Laminar Flow in Cylindrical Heat Pipes," ASME Paper 71-WA/HT.

Bankston, C.A. and Smith, H.J., 1973, "Vapor Flow in Cylindrical Heat Pipes," ASME J. Heat Transfer, Vol. 95, No. 3, pp. 371-376.

Barozzi, G.S., and Pagliarini, G., 1985, "A Method to Solve Conjugate Heat-Transfer Problems: The Case of Fully Developed Laminar Flow in a Pipe," ASME J. Heat Transfer, Vol. 107, No. 1, pp. 77-83.

Bejan, A., 1984, Convection Heat Transfer, John Wiley & Sons, Inc., Chapter 1.

Bird, R.B., Stewart, W.E. and Lightfoot, E.N., 1960, Transport Phenomena, John Wiley & Sons, Inc., Appendix A.

210

Bianchi, A.M., 1987, "Finite Element Method Application to the Vapor Flow Study in a Cylindrical Wick Heat Pipe," 6th Int. Heat Pipe Conf., France, Vol. 1, pp. 86-92.

Bowman, J. and Hitchcock, J., 1988, "Transient Compressible Heat Pipe Vapor Dynamics," Proc. 24th ASME National Heat Transfer Conference, Houston, Vol. 1, pp. 329-338.

Busse, C.A., 1967, "Pressure Drop in the Vapor Phase of Long Heat Pipes," Thermionic Conversion Specialist Conference, Palo Alto, Calif., pp. 391-398.

Busse, C.A., 1973, "Theory of the Ultimate Heat Transfer Limit of Cylindrical Heat Pipes," Int. J. Heat Mass Transfer, Vol. 16, No. 1, pp. 169-186.

Busse, C.A. and Prenger, F.C., 1984, "Numerical Analysis of the Vapor Flow in Cylindrical Heat Pipes," Research and Development of Heat Pipe Technology, Japan, pp. 214-219.

Busse, C.A., 1987, "On the Development of Laminar Flows with Mass Injection and Extraction," J. Fluids Engineering, Vol. 109, pp. 448-452.

Busse, C.A., 1989, "Subsonic Pressure Recovery in Cylindrical Condensers," ASME J. Heat Transfer, Vol. 111, No. 2, pp. 533-537.

Bystrov, P.I., and Popov, A.N., 1976, "A Study of the Characteristics of Heat Pipes with Liquid Metal Working Fluids in Low Temperature Regimes," Teplofiz. Vys. Temp. (USSR), Vol. 14, pp. 629-637.

Bystrov, P.I., and Mikhailov, V.S., 1982, "Laminar Flow of Vapor Flux in the Condensation Region of the Heat Tubes," Teplofiz. Vys. Temp. (USSR), Vol. 20, No. 2, pp. 311-316.

Campo, A., and Rangel R., 1983, "Lumped-System Analysis for the Simultaneous Wall and Fluid Axial Conduction in Laminar Pipe-Flow Heat Transfer," Physico Chemical Hydrodynamics, Vol. 4, No. 2, pp. 163-173.

Cao, Y., Faghri, A., and Chang, W.S., 1988, "A Numerical Analysis of Stefan Problems for Generalized Multi-Dimensional Phase-Change Structures using the Enthalpy Transforming Model," Submitted to Int. J. Heat Mass Transfer.

Cao, Y., and Faghri, A., 1989, "A Transient Two-Dimensional Compressible Analysis for High Temperature Heat Pipes with a Pulsed Heat Input," submitted to Int. J. Heat Mass Transfer.

Chang, W.S., 1987, "Effective Thermal Conductivity of Wire Screens," 24th ASME/AIChE National Heat Transfer Conference, Pittsburgh, PA.

Chi, S.W., 1976, Heat Pipe Theory and Practice, Hemisphere Publishing Corp., Washington, D.C.

Colwell, G.T., Jang, J.H., and Camarda, C.J., 1987, "Modeling of Startup from the Frozen State," 6th Int. Heat Pipe Conference, France, Vol. 1, pp. 165-170.

Cotter, T.P., 1965, "Theory of Heat Pipes," Report LA-3246-MS.

Crowley, A.B., 1978, "Numerical Solution of Stefan Problems," Int. J. Heat Mass Transfer, Vol. 21, No. 2, pp. 215-218.

Davis, V.R., and Ferrell, J.K., 1974, "Evaporative Heat Transfer of Liquid Potassium in Porous Media," AIAA/ASME Thermophysics and Heat Transfer Conference, Boston, Mass.

Dunn, P.D., and Reay, D.A., 1982, Heat Pipes, 3rd Edition, Pergamon Press, Oxford.

Eckert, E.R.G., and Drake, R.M., Jr., 1972, Analysis of Heat and Mass Transfer, McGraw-Hill.

Faghri, M., and Sparrow, E.M., 1980, "Simultaneous Wall and Fluid Axial Conduction in Laminar Pipe-Flow Heat Transfer," ASME J. Heat Transfer, Vol. 102, No. 1, pp. 58-62.

Faghri, A., 1986, "Vapor Flow Analysis in a Double-Walled Concentric Heat Pipe," Numerical Heat Transfer, Vol. 10, pp. 583-595.

Faghri, A., and Parvani, S., 1988, "Numerical Analysis of Laminar Flow in a Double-Walled Annular Heat Pipe," J. Thermophysics, Vol. 2, No. 2, pp. 165-171.

Faghri, A., and Thomas, S., 1988, "Performance Characteristics of a Concentric Annular Heat Pipe, Part I. Experimental Prediction and Analysis of the Capillary Limit," Proc. 24th ASME National Heat Transfer Conference, Houston, Vol. 1, pp. 379-387.

Faghri, A., 1988, "Performance Characteristics of a Concentric Annular Heat Pipe, Part II. Vapor Flow Analysis," Proc. 24th ASME National Heat Transfer Conference, Houston, Vol. 1, pp. 389-396.

Festa, R., Manca, O., and Naso, V., 1988, "A Comparison Between Models of Thermal Fields in Laser and Electron Beam Surface Processing," Int. J. Heat Mass Transfer, Vol. 13, No. 1, pp. 90-105.

Gaugler, R.S., 1944, "Heat Transfer Device," US patent No. 2350348, Appl. 21 December, 1942, Published 6 June, 1944.

Gernert, N.J., 1986, "Analysis and Performance Evaluation of Heat Pipes with Multiple Heat Sources," AIAA/ASME 4th Joint Thermophysics and Heat Transfer Conference, Boston, Mass.

Groll, M., Brost, O., Mack, H., and Shevchuk, E.N., 1984, "Evaporation Heat Transfer of Sodium from Capillary Structures," Research and Development of Heat Pipe Technology, Supplement, Japan, pp. 21-27.

214

Grover, G.M., 1963, "Evaporation Condensation Heat Transfer Device," US patent No. 3229759, Appl. 2 Dec., 1963, Published 18 January, 1966.

Grover, G.M., Cotter, T.P., and Erikson, G.F., 1964, "Structure of Very High Thermal Conduction," J. Appl. Phys., Vol. 35, No. 6, pp. 1990-1991.

Ho, C.J., and Chen, S., 1986, "Numerical Simulation of Melting of Ice around a Horizontal Cylinder," Int. J. Heat Mass Transfer, Vol. 29, No. 9, pp. 1359-1368.

Hornbeck, R.W., 1966, "An All-Numerical Method for Heat Transfer in the Inlet of a Tube," Mech. Eng., Vol. 88, No. 1, p. 76.

Hsiao, J.S., 1984, "An Efficient Algorithm for Finite Difference Analysis of Heat Transfer with Melting and Solidification," ASME paper no. 84-WA/HT-42.

Hsiao, J.S., and Chung, B.T.F., 1984, "An Efficient Algorithm for Finite Element Solution to Two-Dimensional Heat Transfer with Melting and Freezing," ASME paper no. 84-HT-2.

Ismail, K.A.R., Zanardi, M.A., and Liu, C.Y., 1987, "Two-Dimensional Analysis of Flow and Heat Transfer in a Porous Heat Pipe," 6th Int. Heat Pipe Conf., France, pp. 164-167.

Issacci, F., Catton, I., Heiss, A., and Ghoniem, N.M., 1988, "Analysis of Heat Pipe Vapor Dynamics," <u>Proc. 24th ASME National Heat Transfer Conf.</u>, Houston, Vol. 1, pp. 361-366.

Ivanovskii, M.N., Sorokin, V.P., and Yagodkin, I.V., 1982, <u>The Physical Principles of Heat Pipes</u>, Oxford University Press, Chapter 2.

Jang, J.H., Faghri, A., and Chang, W.S., "Analysis of the Transient Compressible Vapor Flow in Heat Pipes," <u>Proc. 1989 ASME National Heat Transfer Conf.</u>, Philadelphia, Aug. 1989.

Jang, J.H., Faghri, A., Chang, W.S., and Mahefkey, E.T., "Mathematical Modeling and Analysis of Heat Pipe Start-Up From the Frozen State," <u>Proc. 1989 ASME Annual Conf.</u>, San Francisco, Dec. 1989.

Kadaner, Ya.S., and Rassadkin, Yu.P., 1975, "Laminar Vapor Flow in a Heat Pipe," <u>Inzhenerno-Fizicheskii Zhurnal</u>, Vol. 28, No. 2, pp. 208-216.

Kays, W.M., and Crawford, M.E., 1980, <u>Convective Heat and Mass Transfer</u>, Second Edition, McGraw-Hill Book Company.

Kemme, J.E., 1969, "Ultimate Heat-Pipe Performance," <u>IEEE Transactions on Electronic Devices</u>, Vol. ED16, No. 8, pp. 717-723.

Keung, C.S., 1980, "The Use of Sources and Sinks in Solving Two-Dimensional Heat Conduction Problems with Change of Phase in Arbitrary Domains," Ph.D. Dissertation, Columbia University.

Koening, D.R., 1985, "Heat Pipe Reactor Designs for Space Power," Space Nuclear Power Systems, 1984, M.S. El-Crenk and M.D. Hoover, eds., Vol. 1, pp. 217-228, Orbit Book Company, Malabar, FL.

Kuznetzov, Y.N., and Belousov, V.P., 1974, "Unsteady Turbulent Conjugated Heat Transfer in Tubes," Paper FC 9.3, Proc. 5th Heat Transfer Conf., Vol. II, pp. 349-352.

Levy, E.K., 1968, "Theoretical Investigation of Heat Pipes Operating at Low Vapor Pressure," J. Engineering for Industry, Vol. 90, Series B, No. 4, pp. 547-552.

Lin, Y.K., and Chow, L.C., 1984, "Effects of Wall Conduction on Heat-Transfer for Turbulent-Flow in a Circular Tube," ASME J. Heat Transfer, Vol. 106, No. 3, pp. 597-604.

Luikov, A.V., Aleksashenko, V.A., and Aleksashenko, A.A., 1971, "Analytical Methods of Solution of Conjugated Problems in Convective Heat-Transfer," Int. J. Heat Mass Transfer, Vol. 14, No. 8, pp. 1047-1056.

Markatos, N.C., Malin, M.R., and Cox, G., 1982, "Mathematical Modeling of Buoyancy-Induced Smoke Flow in Enclosures," Int. J. Heat Mass Transfer, Vol. 25, No. 1, pp. 63-75.

Merrigan, M.A., Keddy, E.S., and Sena, J.T., 1986, "Transient Performance Investigation of a Space Power System Heat Pipe," AIAA Paper No. 86-1273, Proc. AIAA/ASME 4th Joint Thermophysics and Heat Transfer Conference, Boston.

Mori, S., Shinke, T., Sakakibara, M., and Tanimoto, A., 1976, "Steady Heat Transfer to Laminar Flow Between Parallel Plates with Conduction in Wall," Heat Transfer, Japanese Research, Vol. 5, No. 4, pp. 17-25.

Mori, S., Sakakibara, M., and Tanimoto, A., 1974, "Steady Heat Transfer to Laminar Flow in a Circular Tube with Conduction in the Tube Wall," Heat Transfer, Japanese Research, Vol. 3, No. 2, pp. 37-46.

Narayana, K.B., 1986, "Vapor Flow Characteristics of Slender Cylindrical Heat Pipes - A Numerical Approach," Numerical Heat Transfer, Vol. 10, No. 1, pp. 79-93.

Okada, M., 1984, "Analysis of Heat Transfer During Melting from a Vertical Wall," Int. J. Heat Mass Transfer, Vol. 27, No. 11, pp. 2057-2066.

Ozisik, M.N., 1980, Heat Conduction, John Wiley and Sons, New York.

Patankar, S.V, 1978, "A Numerical Method for Conduction in Composite Materials, Flow in Irregular Geometries and Conjugate Heat Transfer," Proc. 6th Int. Heat Transfer Conference, Toronto, Vol. 3, pp. 297-302.

Patankar, S.V., 1980, Numerical Heat Transfer and Fluid Flow, McGraw-Hill, New York.

Perkins, L.P., and Buck, W.E., 1892, "Improvement in Devices for the Diffusion or Transference of Heat," UK patent No. 22272, London.

Ponnappan, R., and Mahefkey, E.T., 1984, "Improved Double-Wall Artery Heat Pipe," Research and Development of Heat Pipe Technology, Japan, pp. 36-40.

Quaile, J.P. and Levy, E.K., 1972, "Pressure Variations in an Incompressible Laminar Tube Flow with Uniform Suction," Proc. AIAA 7th Thermophysics Conference, San Antonio, Texas.

Raithby, G., 1971, "Laminar Heat Transfer in the Thermal Entrance Region of Circular Tubes and Two-Dimensional Rectangular Ducts with Wall Suction and Injection," Int. J. Heat Mass Transfer, Vol. 14, No. 2, pp. 223-243.

Rohani, A.R., and Tien, C.L., 1973, "Steady Two-Dimensional Heat and Mass-Transfer in the Vapor-Gas Region of a Gas-Loaded Heat Pipe," ASME J. Heat Transfer, Vol. 95, No. 3, pp. 377-382.

Rosenfeld, J.H., 1987, "Modeling of Heat Transfer into a Heat Pipe for a Localized Heat Input Zone," AIChE Symposium Series, Heat Transfer - Pittsburgh, Vol. 83, pp. 71-76.

Sakakibara, M., and Endoh, K., 1977, "Effect of Conduction in Wall on Heat Transfer with Turbulent Flow Between Parallel Plates," Int. J. Heat Mass Transfer, Vol. 20, No. 5, pp. 507-516.

Seo, J.T., and El-Genk, M.S., 1988, "A Transient Model for Liquid Metal Heat Pipes," 5th Symposium on Space Nuclear Power Systems, Albuquerque, New Mexico.

Shamsunder, N., and Sparrow, E.M., 1975, "Analysis of Multidimensional Conduction Phase-Change via the Enthalpy Model," ASME J. Heat Transfer, Vol. 97, No. 3, pp. 333-340.

Silverstein, C.C., 1971, "A Feasibility Study of Heat-Pipe-Cooled Leading Edges for Hypersonic Cruise Aircraft," NASA CR-1857.

Soliman, H.M., 1984, "Analysis of Low-Peclet Heat-Transfer during Slug Flow in Tubes with Axial Wall Conduction," ASME J. Heat Transfer, Vol. 106, No. 4, pp. 782-788.

Solomon, A.D., Morris, M.D., Martin, J., and Olszewski, M., 1986, "The Development of a Simulation Code for a Latent Heat Thermal Energy Storage System in a Space Station," Technical Report ORNL-6213.

Spalding, D.B., 1980, "Mathematical Modeling of Fluid-Mechanics, Heat Transfer and Chemical-Reaction Processes," a lecture course, CFDU Report HTS/80/1, Imperial College, London.

Spalding, D.B., Rosten, H.I., 1985, PHOENICS-Beginner's Guide, CHAM Limited.

Tien, C.L., and Rohani, A.R., 1974, "Analysis of the Effect of Vapor-Pressure Drop on Heat Pipe Performance," Int. J. Heat Mass Transfer, Vol. 17, No. 1, pp. 61-67.

Van Ooijen, H., and Hoogendoom, C.J., 1979, "Vapor Flow Calculations in a Flat-Plate Heat Pipe," AIAA Journal, Vol. 17, No. 11, pp. 1251-1259.

Voller, V.R., and Cross, M., 1981, "Estimating the Solidification/Melting Times of Cylindrically Symmetric Regions," Int. J. Heat Mass Transfer, Vol. 24, No. 9, pp. 1457-1462.

Weissberg, H., 1959, "Laminar Flow in the Entrance Region of a Porous Pipe," Physics of Fluids, Vol. 2, No. 5, pp. 510-516.

Zariffeh, E.K., Soliman, H.M., and Trupp, A.C, 1982, "The Combined Effects of Wall and Fluid Axial Conduction on Laminar Heat Transfer in Circular Tubes," Paper FC-23, Proc. 7th Heat Transfer Conf., Vol. IV, pp. 131-136.

END

FILMED

10-89

DTIC